

**UNSTEADY DYNAMICS OF SHOCK-WAVE
BOUNDARY-LAYER INTERACTIONS**

by

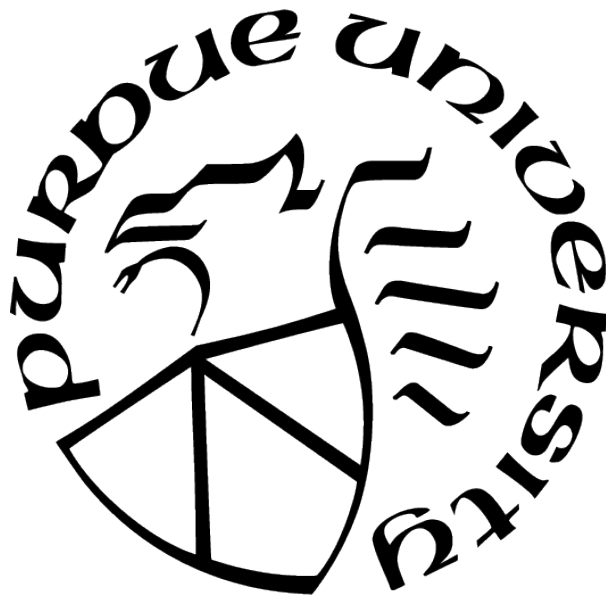
Akshay S. Deshpande

A Dissertation

Submitted to the Faculty of Purdue University

In Partial Fulfillment of the Requirements for the degree of

Doctor of Philosophy



School of Aeronautics and Astronautics

West Lafayette, Indiana

August 2021

**THE PURDUE UNIVERSITY GRADUATE SCHOOL
STATEMENT OF COMMITTEE APPROVAL**

Dr. Jonathan Poggie, Chair

School of Aeronautics and Astronautics

Dr. Gregory Blaisdell

School of Aeronautics and Astronautics

Dr. Tom Shih

School of Aeronautics and Astronautics

Dr. Guillermo Paniagua

School of Mechanical Engineering

Approved by:

Dr. Gregory Blaisdell

To Aai, Baba, and Aditya

To work alone you have the right, and not to the fruits. Do not be impelled by the fruits of work. Nor have attachment to inaction.

—Bhagavad Gita, 2:47

ACKNOWLEDGMENTS

First of all, I would like to thank my parents for constantly supporting me during my graduate studies at Purdue. I would like to thank my advisor, Dr. Jonathan Poggie, for providing me the opportunity to work on this project and be a part of his research group. His constant motivation and tutelage has contributed greatly towards my research on unsteadiness of shock-wave boundary-layer interactions. I thank Dr. Gregory Blaisdell, Dr. Tom Shih, and Dr. Guillermo Paniagua for serving on my thesis committee.

Thanks are also due my colleagues, Geoffrey Andrews, Tugba Piskin, Ian Hall, and Robert Alviani for their academic consultations and encouragement during my PhD research. I am also grateful to Dr. Timothy Leger at AFRL for providing some of the required computational data used for analysis in this document.

Support for this work was provided by Purdue University, by AFOSR Grant No. FA9550-17-1-0153, by ONR Grant N000141712374, by an award of computer time provided by the DoE INCITE program, and by computer time provided under a DoD HPCMP Frontier Project. This research used resources of the Argonne Leadership Computing Facility, which is a DOE Office of Science User Facility supported under Contract No. DE-AC02-06CH11357.

TABLE OF CONTENTS

LIST OF TABLES	8
LIST OF FIGURES	9
LIST OF SYMBOLS	16
ABBREVIATIONS	18
ABSTRACT	19
1 INTRODUCTION	21
1.1 General Overview of Shock-Wave/Turbulent Boundary-Layer Interactions	21
1.2 Compressible Reattaching Shear-Layers	24
1.3 Compression Ramp Flow with Sidewalls	28
1.4 High-Frequency Forcing of Shear-Layers	31
1.5 Thesis Summary	32
2 METHODOLOGY	34
2.1 Delayed Detached-Eddy Simulations	35
2.2 Implicit Large-Eddy Simulations	38
2.3 Governing Equations	41
2.3.1 Compressible Navier-Stokes Equations	41
2.3.2 S-A turbulence model	42
2.3.3 Smagorinsky Sub-Grid Scale Model	44
2.3.4 Padé-type Non-Dispersive Spatial Filters	44
2.4 Computational Setup	47
2.4.1 Case 1: Compressible Reattaching Shear-Layer	47
2.4.2 Case 2: Compression Ramp Flow With Sidewalls	53
2.5 Data Analysis	56
2.5.1 Statistical Methods	56
2.5.2 Dynamic Mode Decomposition	57

3	COMPRESSIBLE REATTACHING SHEAR-LAYER	62
3.1	Flowfield structure	62
3.2	Unsteadiness of the interaction	70
3.3	Large-scale structures	78
3.4	Shear-layer flapping, separation-bubble breathing, and reattachment shock motion	88
3.5	Unsteadiness of the reattachment shock	96
3.6	Unsteadiness at the mean reattachment location	100
3.7	Summary	103
4	COMPRESSION RAMP FLOW WITH SIDEWALLS	105
4.1	Flowfield structure	105
4.2	Unsteadiness of the flowfield	117
4.3	Unsteadiness of the shock front	122
4.4	Unsteadiness of the centerline separation bubble	129
4.5	Coupling between centerline, corner, and sidewall interactions	134
4.6	Dynamic Mode Decomposition	140
4.6.1	Centerplane	140
4.6.2	Ramp-normal plane	145
4.6.3	Wall and sidewalls	149
4.7	Summary	156
5	HIGH-FREQUENCY FORCING OF SHEAR-LAYERS	158
5.1	Actuator Formulation	158
5.2	Flowfield Structure	161
5.3	Unsteadiness of the interaction	165
5.4	Summary	178
6	CONCLUSIONS	179
6.1	Compressible Reattaching Shear-Layer	179
6.2	Compression Ramp Flow with Sidewalls	182

6.3	High-Frequency Forcing of Reattaching Shear-Layers	185
6.4	Prospects of Future Study	186
	REFERENCES	188

LIST OF TABLES

2.1	List of calculations for Case 1.	48
2.2	Flow conditions for Case 1.	49
2.3	Grid details for Case 1.	50
2.4	Time-stepping details for Case 1.	52
2.5	Flow conditions for Case 2.	53
2.6	Locations of data extraction for Case 1.	61
5.1	Amplitude values.	161

LIST OF FIGURES

2.1	Fourier wave number analysis of central and compact discretization schemes. Black solid line represents the exact solution, $\widehat{k} = k$	40
2.2	Filter transfer function. Black dashed line represents no filtering of the variables.	46
2.3	Geometry used in experiments [28].	48
2.4	Extracted data locations (Case 1.) (a) Sampling stations [28] (Reprinted with permission from the author) (b) Division of grid on the centerplane.	50
2.5	Computational grid; every 32^{nd} point shown for clarity.	54
2.6	Sampled planes (near surface omitted).	55
3.1	Mean density field (from OVERFLOW.) The mean reattachment location is marked at $x_R/D = 4.69$ for reference.	63
3.2	Resolved Reynolds stresses (from OVERFLOW.) (a) $R_{33} = \langle w' \rangle^2$ component (b) $R_{12} = \langle u'v' \rangle$ component. The mean reattachment location is marked at $x_R/D = 4.69$ for reference.	63
3.3	Comparison of mean velocity profiles in the shear-layer at (a) $x/D = 0.5$ (b) $x/D = 1.5$ (c) $x/D = 2.5$ (d) $x/D = 3.5$	64
3.4	Comparison of shear-layer growth rates between SU2 (—), OVERFLOW (—), and HOPS (—) for (a) Momentum thickness (b) Vorticity thickness.	65
3.5	Surface quantities of (a) Wall-pressure (b) Skin-friction coefficient.	66
3.6	Comparison of normalized mean-squared streamwise momentum fluctuations in the shear-layer between SU2 (—), HOPS (—), OVERFLOW (∇), and experimental data (\circ) [31].	67
3.7	Snapshots of instantaneous flowfields for (a) OVERFLOW case (b) SU2 case (c) HOPS case.	69
3.8	Pre-multiplied wall pressure spectra in the cavity region for the OVERFLOW case in parts (a)–(c). (a) Contour plot (b) Spectral plots in the first half of the cavity; the local peaks that may correspond to Rossiter modes are labeled as P_1 , P_2 , and P_3 (c) Spectral plots in the second half of the cavity (d) Comparison of spectra at $x/D \approx 1.07$ (e) Comparison of spectra at $x/D \approx 2.44$. For reference, the ramp starts at $x_R/D = 2.44$ and mean reattachment occurs at $x_R/D = 4.69$	72
3.9	Premultiplied wall pressure spectra on the ramp for the OVERFLOW case in parts (a)–(c). (a) Contour plot (b) Spectral plots upstream of mean-reattachment (c) Spectral plots downstream of mean-reattachment (d) Comparison of spectra at $x/D \approx 3.81$. The ramp starts at $x_R/D = 2.44$ and the mean reattachment location is marked at $x_R/D = 4.69$ for reference. Symbols indicate experimental results of Shen et al. [140] at $x/D = 5.21$	76

3.10	Comparison of Pressure spectra between SU2 (—), OVERFLOW (—), and HOPS (—) at (a) SH-1 (b) SH-2 (c) SH-3 (d) RZ-1 (e) RZ-2.	78
3.11	Two-point correlations for the OVERFLOW case on the centerplane ($z/D = 0$) using (a) Streamwise velocity fluctuations (u); colored dashed lines are contours of non-dimensional mean u -velocity. (b) Density fluctuations $(x/D, y/D)_{ref} = (2.66, -0.012)$. (c) Density fluctuations $(x/D, y/D)_{ref} = (2.66, 0.055)$. Dashed lines indicate experimental correlations obtained by Poggie and Smits [145]; y_0 is the height of zero mean velocity line and δ is the thickness of the undisturbed shear-layer at $x/D = 2.79$	80
3.12	Space-time correlation of streamwise velocity fluctuations in the shear-layer for the OVERFLOW case.	81
3.13	Spanwise space-time correlations for the OVERFLOW case of (a) streamwise velocity fluctuations between SH-1 (dashed red lines) and SH-3 (flooded contours) (b) RZ-1 (dashed red lines) and RZ-2 (flooded contours).	82
3.14	Comparison of spanwise wavenumber spectra of (a) streamwise velocity fluctuations between OVERFLOW (—) and HOPS (—) at SH-1 (—), SH-2 (— — —), and SH-3 (— — —). Arrow indicates the downstream direction.	83
3.15	(a) Space-time correlations of wall pressure fluctuations for the OVERFLOW on the ramp at Pos-1 (flooded contours) and Pos-2 (dashed red lines). (b) Convection velocities on the ramp. (Bottom-left) Nested hairpin model [147] (Reproduced with permission from J. Fluid Mech. (2000), 422, pp.1-54. Copyright 2000 Cambridge University Press).	84
3.16	Space-time correlations of wall pressure fluctuations on the ramp for the OVERFLOW case at (a) $(x/D, y/D)_{ref} = (4.83, -0.13)$ (b) $(x/D, y/D)_{ref} = (6.24, 0.38)$; δ_R is the experimentally measured boundary layer thickness at the mean reattachment location. Symbols indicate experimental results of Shen et al. [140].	86
3.17	Comparison of spanwise wavenumber spectra ($E_p(k_3)$) of wall-pressure fluctuations between SU2 (—) and HOPS (—) at (a) $x/D = 1.07$ (—) and $x/D = 2.44$ (— — —) (b) $x/D = 3.81$ (— — —) and $x/D = 5.18$ (— · · —). Arrow indicates the downstream direction.	87
3.18	Space-time correlations of p and v for the OVERFLOW case. (Top-left) Contour plot of local speed of sound.	89
3.19	Two-point correlations of p_w at a given streamwise station x/D and v in the shear-layer at the same station for the OVERFLOW case. Colored dashed lines are contours of non-dimensional mean density.	91

3.20	Contours of u/U_∞ describing the shear-layer flapping motion and separation bubble breathing cycle for the OVERFLOW case. (a) Mean location/Equilibrium. (b) Downward movement/Bubble contraction. (c) Mean location/Equilibrium. (d) Upward movement/Bubble expansion. Dashed line indicates the mean reattachment location.	92
3.21	Spectrum of separation bubble mass for SU2 (—) and OVERFLOW (—).	94
3.22	Spectra of shock location and separation bubble mass for the OVERFLOW case in (a) log-log coordinates (b) semilog coordinates.	95
3.23	Coherence of shock position relative to (a) SH-1 (—), SH-2 (—), and SH-3 (—) (b) RZ-1 (—) and RZ-2 (—) for the OVERFLOW case.	97
3.24	Coherence of shock position with the mass history of separation bubble for the OVERFLOW case.	98
3.25	Conditionally averaged streamwise component of the density gradient on the centerplane ($z/D = 0$) for the OVERFLOW case, based on instantaneous mass of the separation bubble. (a) Bubble contraction phase. (b) Equilibrium phase. (c) Bubble expansion phase.	100
3.26	Plots of coherence of wall pressure fluctuations at mean reattachment for the OVERFLOW case with (a) wall pressure fluctuations on the ramp, (b) Wall-normal velocity fluctuations in the shear-layer, and (c) Pressure fluctuations in the recirculation zone. Phase plots of wall pressure fluctuations at mean reattachment with (d) wall pressure fluctuations on the ramp, (e) Wall-normal velocity fluctuations in the shear-layer, and (f) Pressure fluctuations in the recirculation zone. In parts (b) and (e) SH-1 (—), SH-2 (—), and SH-3 (—). In parts (c) and (f) RZ-1 (—) and RZ-2 (—).	102
4.1	Contours of mean wall-pressure (a) Three-dimensional view (b) Projection on the ramp surface (Plane 1) (c) Projection on the left-sidewall (Plane 2). The ramp corner lies at $X = 100$	106
4.2	Contours of mean density. (a) Three-dimensional view (b) Projection on the centerplane at $Z = 10$ (Plane 6) (c) Projection on the streamwise plane at $X = 80$ (Plane 4) (d) Projection on the ramp-normal plane (Plane 5).	108
4.3	Contours of RMS pressure. Black solid lines represent the $c_{f_x} = 0$ contour level.	109
4.4	Instantaneous flowfield. (a) Iso-surfaces of $u = 0$ colored with the magnitude of non-dimensional pressure. Contours of density gradient magnitude are shown on the centerplane ($Z = 0$) and colored streamwise planes at (b) $X = 95$ (red) (c) $X = 103$ (green) (d) $X = 110$ (blue) (e) $X = 117$ (orange).	113
4.5	Contours of instantaneous density gradient magnitude ($ \nabla\rho $) on inclined planes (at constant j -values) (a) Location of extracted planes in the domain (b) $j = 620$ (red) (c) $j = 750$ (green) (d) $j = 1000$ (blue) (e) $j = 1270$ (orange).	115

4.6	Characterization of large-scale structure by correlations of streamwise velocity fluctuations (a) Two-point correlations (b) Space-time correlations of streamwise velocity fluctuations.	116
4.7	Premultiplied pressure spectra on the floor, left sidewall, and ramp-normal plane (a) $St = 0.03$ (b) $St = 0.12$ (c) $St = 0.54$. The $c_{f_x} = 0$ contour is shown as a white solid line. Limiting streamlines in orange are included for reference. Mean density contours (white lines) are shown on the ramp-normal plane.	118
4.8	Contours of premultiplied pressure spectra ($fG(f)/\sigma_p^2$) on the centerplane ($Z = 10$) (a) $St = 0.03$ (b) $St = 0.12$ (c) $St = 0.54$. Solid and dashed black lines indicate the mean dividing streamline ($u/U_\infty = 0$) and the sonic line, respectively. The dashed-dotted line in part (c) highlights the boundary layer edge upstream of the interaction.	122
4.9	Spectra of shock oscillations.	123
4.10	Coherence of centerline shock oscillations with pressure fluctuations for frequency component: (a,b) $St = 0.03$ (c,d) $St = 0.06$. In parts (a) and (c), the solid black and white lines on the floor and left sidewall represent the limiting streamlines and $c_{f_x} = 0$ contour, respectively. Solid black lines on the ramp-normal plane indicate the mean density contours. Solid and dashed black lines on the centerplane in parts (b) and (d) indicate the mean dividing streamline ($u/U_\infty = 0$) and the sonic line, respectively.	126
4.11	Upstream influence of large-scale structures on separation shock motion.	128
4.12	Spectra of centerline separation bubble unsteadiness.	129
4.13	Coherence of oscillations of centerline separation bubble with pressure fluctuations for (a,b) $St = 0.03$ (c,d) $St = 0.12$. In parts (a) and (c), the solid black and white lines on the floor and left sidewall represent the limiting streamlines and $c_{f_x} = 0$ contour, respectively. Solid black lines on the ramp-normal plane indicate the mean density contours. Solid and dashed black lines on the centerplane in parts (b) and (d) indicate the mean dividing streamline ($u/U_\infty = 0$) and the sonic line, respectively.	131
4.14	Contours of low-pass filtered streamwise velocity field (u/U_∞) on the ramp-normal plane at (a) $t \approx 145 \mu s$; larger right separation bubble (b) $t \approx 332 \mu s$; mean location/equilibrium (c) $t \approx 798 \mu s$; larger left separation bubble (d) $t \approx 871 \mu s$; mean location/equilibrium. Black and white solid lines indicate instantaneous and mean contour levels of: $u/U_\infty = 0.2, 0.8, \text{ and } 0.9$, respectively.	132
4.15	Space-time correlation of centerline shock oscillations and separation bubble breathing.	134

4.16	Space-time correlations with reference point at $X \approx 92$ and (a) at the centerline ($Z = 10$) (b) close to the left sidewall ($Z \approx 1.5$) (c) close to the right sidewall ($Z \approx 19.2$). Solid lines represent the $R = 0.25$ contour level. Dotted lines in (b) and (c) represent the $R = 0.25$ contour level in (a).	136
4.17	Space-time correlation between (a) pressure fluctuations on the centerline and left sidewall (b) pressure fluctuations on the left and right sidewall.	137
4.18	DMD modes on the centerplane (a) Eigenspectrum (b) Mode amplitudes. Red markers indicate dominant modes obtained from SPDMD.	141
4.19	Contours of \hat{u}/U_∞ describing the low-frequency breathing of the separated zone and oscillations of the compression-ramp shock. Orange and white solid lines represent the mean and instantaneous mean dividing streamline ($\hat{u}/U_\infty = 0$). . .	142
4.20	Contours of \hat{u}/U_∞ depicting the low-mid frequency flapping of the separated zone. Red and black solid lines represent the mean and instantaneous contour levels of $\hat{u}/U_\infty = 0.3, 0.4, 0.5$, and 0.6	144
4.21	Contours of \hat{p}/ρ_∞ showing the mid-frequency vortex shedding. The black solid line represents the instantaneous dividing streamline ($\hat{u}/U_\infty = 0$).	145
4.22	Corner vortex at the left-sidewall. See Fig. 4.2d for reference.	146
4.23	DMD modes on the ramp (a) Eigenspectrum (b) Mode amplitudes. Red markers indicate dominant modes obtained from SPDMD.	147
4.24	Contours of \hat{u}/U_∞ describing the low-frequency breathing of the sidewall separated zones. Red and white solid lines indicate the instantaneous and mean contour levels of $\hat{u}/U_\infty = 0.5$. Solid and dashed black lines highlight instantaneous contour levels of $\hat{w}/U_\infty = -0.1$ and 0.1 respectively.	148
4.25	Contours of \hat{u}/U_∞ describing the low-mid frequency motion the sidewall separated zones. Red and white solid lines indicate the instantaneous and mean contour levels of $\hat{u}/U_\infty = 0.5$. Solid and dashed black lines highlight instantaneous contour levels of $\hat{w}/U_\infty = -0.08$ and 0.08 respectively.	150
4.26	Contours of \hat{u}/U_∞ describing the mid-frequency dynamics of the sidewall separated zones.	151
4.27	DMD modes on the ramp (a) Eigenspectrum (b) Mode amplitudes. Red markers indicate dominant modes obtained from SPDMD.	152
4.28	Contours of \hat{p}/p_∞ depicting the low-frequency motion of the compression-ramp shock and the reattachment shock-system. Red and black solid lines represent the mean and instantaneous contour levels of $\hat{p}/p_\infty = 0.2$ and 0.4 respectively. .	153
4.29	Contours of \hat{p}/p_∞ depicting the low-mid frequency motion of the compression-ramp shock and the reattachment shock-system. Red and black solid lines represent the mean and instantaneous contour levels of $\hat{p}/p_\infty = 0.2$ and 0.4 respectively.	155

4.30	Contours of \widehat{p}/p_∞ depicting the mid-frequency vortex shedding. Black solid lines represent the mean contour level of $c_{f_x} = 0$	156
5.1	Actuator details. (a) Wall-normal profile (b) Body-force distribution.	160
5.2	Comparison of shear-layer growth rates between unforced (—) and forced (—) cases in SU2 for (a) Momentum thickness (b) Vorticity thickness.	162
5.3	Surface quantities of (a) Wall-pressure (b) Skin-friction coefficient with (—) and without (—) forcing in SU2. Mean and RMS values are highlighted by dashed and solid lines, respectively.	163
5.4	Comparison of mean velocity profiles in the shear-layer at (a) $x/D = 0.5$ (b) $x/D = 1.5$ (c) $x/D = 2.5$ (d) $x/D = 3.5$, with (—) and without (—) forcing in SU2.	164
5.5	Comparison of normalized profiles of mean-squared streamwise momentum fluctuations (—) and RMS of shear-stress component (—) in the shear-layer (a) $x/D = 0.5$ (b) $x/D = 1.5$ (c) $x/D = 2.5$, with (—) and without (—) forcing in SU2.	165
5.6	Comparison of wall-pressure spectra for the SU2 and HOPS run at (a) $x/D = 1.07$ (b) $x/D = 2.44$ (c) $x/D = 3.81$	166
5.7	Contours of pre-multiplied wall-pressure spectra corresponding to the SU2 run for (a) Baseline case (b) High-frequency forcing.	167
5.8	Comparison of pressure spectra between SU2 (without forcing) (—), SU2 (with forcing) (—), and HOPS (with forcing) (—) at (a) SH-1 (b) SH-2 (c) SH-3 (d) RZ-1 (e) RZ-2.	169
5.9	Contours of pre-multiplied pressure spectra corresponding to the SU2 run for the frequency components: (a) $St = 1.6$ (b) $St = 0.8$ (c) $St = 3.2$. The mean reattachment location at $x_R/D = 4.69$ is marked for reference. The actuator location at $(x/D, y/D) = (0.1, 0)$ is highlighted using a black marker.	171
5.10	Spectra of (a) reattachment shock motion and (b) separation bubble breathing in pre-multiplied coordinates for the baseline (—) and forcing (—) cases using the SU2 code.	173
5.11	Phase-averaged contours of pressure fluctuations corresponding to the SU2 run. Arrows in part (d) indicate the approximate path of disturbances in the recirculation zone.	174
5.12	Coherence of reattachment shock oscillations with (a) pressure fluctuations in the recirculation zone at RZ-1 (—) and RZ-2 (—) (b) wall-normal velocity fluctuations in the shear-layer at SH-1 (—), SH-2 (—), and SH-3 (—) (c) breathing motion of the recirculation zone, using the SU2 code.	176

5.13 (a) Pressure spectrum in the freestream at $(x/D, y/D) \approx (0.71, 0.21)$ (b) Coherence of pressure fluctuations in the freestream with reattachment shock motion, using the SU2 code. 177

LIST OF SYMBOLS

D	Step height (m)
$G(f)$	Power spectral density ((sig. units) ² /Hz)
L_c	Cavity length (m)
L_{sep}	Separation length (m)
L_i	Intermittent length (m)
M	Mach number
M_c	Convective Mach number
R	Correlation magnitude
S_{xx}	Auto-spectral density ((sig. units) ² /Hz)
S_{xy}	Cross-spectral density ((sig. units) ² /Hz)
St	Strouhal number
T	Temperature (K)
X, Y, Z	Cartesian coordinates non-dimensionalized by δ_o
c_{f_x}	Streamwise component of skin-friction coefficient
c_v	Specific heat at constant volume (Jkg ⁻¹ K ⁻¹)
e	Specific internal energy (J/kg)
f	Frequency (Hz)
f_s	Sampling Frequency (Hz)
i, j, k	Grid indices in x , y , and z directions
p	Pressure (Pa)
t	Elapsed time (s)
u	Streamwise velocity component (m/s)
v	Wall-normal velocity component (m/s)
w	Spanwise velocity component (m/s)
x, y, z	Cartesian coordinate system (m)
δ^*	Boundary layer displacement thickness (m)
δ_o	Incoming boundary layer thickness (m)
ν	Kinematic viscosity (kg m ⁻¹ s ⁻¹)

ρ	Density (kg/m ³)
κ	Turbulence Kinetic Energy (J/kg)
σ	RMS value of a signal (sig. units)
τ	Time-delay (s)
γ_{xy}^2	Coherence magnitude

Superscripts:

\prime	Fluctuating quantities
-	Mean quantities
\sim	Instantaneous quantities
+	Inner coordinates
*	Complex conjugate
$\hat{}$	Reconstructed mode from DMD

Subscripts:

∞	Freestream quantities
w	Wall quantities
R	Quantities at the mean reattachment location

ABBREVIATIONS

DDES	Delayed Detached-Eddy Simulations
FFT	Fast Fourier Transform
HOPS	Higher Order Plasma Solver
ILES	Implicit Large-Eddy Simulations
LES	Large-Eddy Simulations
PIV	Particle Image Velocimetry
POD	Proper Orthogonal Decomposition
DMD	Dynamic Mode Decomposition
RMS	Root Mean-Squared
RANS	Reynolds-Averaged Navier-Stokes
SA	Spalart-Allmaras
SVD	Singular Value Decomposition
SWTBLI	Shock-Wave/Turbulent Boundary-Layer Interactions

ABSTRACT

Shock-wave/turbulent boundary-layer interactions (SWTBLIs) are characterized by low-frequency unsteadiness, amplified aerothermal loads, and a complex three-dimensional flowfield. Presence of a broad range of length and time-scales associated with compressible turbulence generates additional gasdynamic features that interact with different parts of the flowfield via feedback mechanisms. Determining the physics of such flows is of practical importance as they occur frequently in different components of a supersonic/hypersonic aircraft such as inlets operating in both on- and off-design conditions, exhaust nozzles, and control surfaces. SWTBLIs can cause massive flow separation which may trigger unstart by choking the flow in an inlet. On control surfaces, fatigue loading caused by low-frequency shock unsteadiness, coupled with high skin-friction and heat transfer at the surface, can result in failure of the structure.

The objective of this study is twofold. The first aspect involves examining the causes of unsteadiness in SWTBLIs associated with two geometries – a backward facing step flow reattaching on to a ramp, and a highly confined duct flow. Signal processing and statistical techniques are performed on the results obtained from Delayed Detached-Eddy Simulations (DDES) and Implicit Large-Eddy Simulations (ILES). Dynamic Mode Decomposition (DMD) is used as a complement to this analysis, by obtaining a low-dimensional approximation of the flowfield and associating a discrete frequency value to individual modes.

In case of the backward facing step, Fourier analysis of wall-pressure data brought out several energy dominant frequency bands such as separation bubble breathing, oscillations of the reattachment shock, shear-layer flapping, and shedding of vortices from the recirculation zone. The spectra of reattachment shock motion suggested a broadband nature of the oscillations, wherein separation bubble breathing affected the low-frequency motion and shear-layer flapping, and vortex shedding correlated well at higher frequencies. A similar exercise was carried out on the highly confined duct flow which featured separation on the floor and sidewalls. In addition to the low-frequency shock motions, the entire interaction exhibited a cohesive back-and-forth in the streamwise direction as well as a left-right motion

along the span. Mode reconstruction using DMD was used in this case to recover complex secondary flows induced by the presence of sidewalls.

For the final aspect of this study, a flow-control actuator was computationally modeled as a sinusoidally varying body-force function. Effects of high-frequency forcing at $F^+ = 1.6$ on the flowfield corresponding to a backward facing step flow reattaching on to a ramp were examined. Conditionally averaged profile of streamwise velocity fluctuations, based on reattachment shock position, was used for the formulation of spatial distribution of the actuator. The forcing did not change the mean and RMS profiles significantly, but affected the unsteadiness of the interaction significantly. The effects of forcing were localized to the recirculation zone and did not affect the evolution of the shear-layer. The acoustic disturbances propagating through the freestream and recirculation zone drove the motion of the reattachment shock, and did not alter the low-frequency dynamics of the interaction.

1. INTRODUCTION

1.1 General Overview of Shock-Wave/Turbulent Boundary-Layer Interactions

Shock-wave/turbulent boundary-layer interactions (SWTBLIs) are ubiquitous in high-speed flows. They are characterized by large-scale separation, low-frequency unsteadiness, and amplified aerothermal loads in addition to a complex three-dimensional flowfield [1]–[3]. Such interactions occur commonly on both external and internal aircraft components such as inlets, control surfaces, and overexpanded exhaust nozzles. Extensive studies carried out on this phenomena have effectively highlighted the low-frequency unsteadiness of shock-motion by examining the spectral nature of fluctuating quantities [4]–[8], using reduced order modeling [9]–[12], or via linear stability analysis [11], [13], [14].

A typical SWTBLI strong enough to cause separation can be described in terms of the following components: incoming turbulent boundary layer, separation shock, recirculation bubble, free shear layer, and reattachment shock. These individual components represent have varying degrees of contribution to its overall unsteadiness. The low-frequency shock motion, typically of time-scale two orders of magnitude lower than the turbulence in the incoming boundary layer, is especially of practical interest in the aerospace community. In high-speed vehicles, this phenomenon can cause severe fatigue loading, ultimately resulting in failure of the structure. The corresponding design implications for high-speed vehicles are elaborated by Zuchowski [15]. Therefore, determining its causes can aid in designing efficient flow control techniques to inhibit some, if not all of its adverse effects.

Before discussing the causes of unsteadiness in SWTBLI, the models of amplifier, oscillator, and weakly-damped global mode are briefly introduced here. Huerre and Monkewitz [16] classified different types of flows into these categories based on the qualitative nature of their dynamical behaviour. The spatial evolution of boundary layers is sensitive to the characteristics of external excitations and therefore behave as frequency-selective amplifiers. These types of flows are typically convectively unstable. On the other hand, flows which are absolutely unstable (such bluff-body wakes) exhibit inherent instabilities that grow temporally and therefore behave as oscillators. These types of flows are self-sustaining and do not require any external perturbations. Finally, some flows can be classified into a third category of

marginally globally stable flows wherein the global modes are weakly damped in time. These three categories can be used to model separation unsteadiness in a SWTBLI [17]. This type of flow could be called a resonator because it responds very strongly to disturbances that match the marginally stable global mode. Owing to the complexity of a SWTBLI, a specific combination of the three categories may be required to account for multiple phenomena [18].

We continue the discussion on the causes of SWTBLI unsteadiness by first reviewing upstream effects. Plotkin [19] proposed a simple model in which the shock motion was driven by velocity fluctuations in the turbulent boundary layer with a linear restoring mechanism. The spectra derived from his analytical model agreed well with experimental data. Poggie et al. [18] validated this model with the spectra of separation shock motion obtained from experimental data and their LES calculations across a broad range of Mach numbers. Ganapathisubramani et al. [20] confirmed the presence of superstructures in the logarithmic region of the turbulent boundary layer with a streamwise length as long as 40δ , where δ corresponds to the boundary-layer thickness. In their subsequent work [21], these large-scale structures were found to affect the low-frequency unsteadiness of the separation shock based on the frequency scale $U_\infty/40\delta$, as well as using correlation measurements. Such flows are therefore sensitive to external perturbations and are potentially receptive to forcing in the vicinity of the global-mode frequency.

Beresh et al. [8] also confirmed this observation by carrying out conditional averages of upstream velocity profiles based on the instantaneous separation shock location. A downstream shock movement was associated with positive velocity fluctuations causing a “fuller” boundary layer profile, while negative velocity fluctuations were found to correlate well with an upstream shock movement. The shock motion exhibited selective response to the velocity fluctuations in the boundary layer, i.e. low and high-frequency aspects of the shock motion were responsive to velocity fluctuations of similar time-scales. These observations were consistent with the results of implicit LES simulations of a SWTBLI on a 24 deg. compression ramp carried out by Porter and Poggie [22] at Mach 2.25. Poggie [6] then used the conditionally averaged perturbation profile as the wall-normal profile for designing a streamwise body-force for flow control scheme. On incorporating this body-force in the ILES simulations, and driving at the $St = 0.03$ characteristic frequency, it was observed that the separation

shock and bubble were locked-in with the forcing frequency and the power spectral densities of wall-pressure fluctuations in the separated region displayed a low-frequency peak that scaled with the amplitude of forcing. These results support the amplifier model of a SWTBLI, wherein certain disturbances in the incoming flow are selectively amplified by the shock-separation bubble system.

Dupont et al. [23], [24] identified low-frequency motion in the interaction zone of an impinging SWTBLI with a similar time-scale as of the reflected shock motion. Based on the coherence and phase plots between wall-pressure measurements in the vicinity of the shock and downstream, these motions showed a quasi-linear dependence and were out of phase with respect to each other. Additionally, they also observed large-scale vertical flapping motions of the separated region, which correlated well with the reflected shock movements. Piponniau et al. [25] formulated a model to describe the low-frequency unsteadiness of the interaction. Using conditional averages, they showed that the reflected shock motion was affected by the variation in the size of the bubble. This variation was caused by the shedding of vortical structures from the bubble and entrainment of fluid by the mixing layer. Their experimental findings did not indicate any significant upstream effects. Wu and Martin [4] also observed downstream effects to play a dominant role in the low-frequency shock motion, and proposed a model entailing a feedback loop between the separation bubble, separated shear-layer, and the shock system.

Thomas et al. [5] investigated a weak SWTBLI generated by a compression ramp inclined at 6, 9, and 12 deg at Mach 1.5. It was noted that, irrespective of the strength of the interaction, upstream events did not play a role in modulating the shock motion. The latter was instead found to be affected by the motion of the separation bubble. Pirozzoli and Grasso [26] performed a DNS study on an impinging SWTBLI at Mach 2.25. They concluded that the unsteadiness of the separation bubble as well as the flapping motion of the reflected shock is a result of the upstream propagation of acoustic waves, generated by the interaction of coherent structures with the incident shock. Based on this model, they proposed an acoustic resonance mechanism in the interaction region, which is subsequently responsible for the large-scale low-frequency unsteadiness. This agrees with the oscillator model of a SWTBLI, in which any disturbances generated in the interaction are amplified through positive feed-

back, leading to self-excited oscillations. Poggie [6] argues that models based on upstream mechanism (amplifier, convective instability) and downstream mechanisms (oscillator, absolute instability) can be reconciled if in many cases the separation bubble is subject to a weakly-damped global mode. In that case, both amplifier and oscillator characteristics may be present.

These results are used as a foundation to perform data analysis and interpret the results associated with the two flowfields considered in this study: a compressible reattaching shear-layer and a compression ramp flow with sidewalls. These flowfields were chosen to investigate certain phenomena in SWTBLI that have not received significant investigation efforts in previous studies. The first case is used to study the unsteadiness of reattachment shock motion in a SWTBLI. The literature review mentioned in the previous paragraphs address the causes of unsteadiness of the separation shock motion, wherein the motion of reattachment was not the subject matter in most of these studies.

This study discusses the characteristics of SWTBLI corresponding to two flowfields – compressible reattaching shear-layers and compression ramp flow with sidewalls. Reattaching shear-layers occur in practical applications such as engine exhaust reattaching onto a surface, cavity flameholders, or an open bay for store release in an aircraft [27], [28]. Confined SWTBLIs are usually featured in high-speed engine inlets and wind tunnels, and nozzles operating at off-design conditions. In both the cases, the Reynolds number of the flow is $\sim \mathcal{O}(10^6)$ and the flowfield is characterized by regions of massive separation. Additionally, both upstream and downstream events elaborated in the previous paragraphs are present in the flowfield. Existing literature on both experimental and computational studies of cases similar to these two flowfields is expanded on in the upcoming sections.

1.2 Compressible Reattaching Shear-Layers

We start by reviewing literature on reattaching flows. Most of the studies referred to examine subsonic flows unless otherwise mentioned. This flowfield consists of a separated shear layer that is generated at the edge of a step, and flows downstream over a large recirculation zone in the cavity region, followed by reattaching on to a ramp. In the supersonic flow case,

a reattachment shock is generated to align the flow along the ramp surface. This flowfield comprises of almost all of the features found in a conventional SWTBLI – a separated shear layer, large recirculation zone, a reattachment shock, and a redeveloping flow downstream of the interaction. The only features absent in this flow are a separation shock and a moving separation zone (separation location fixed), which instead is replaced by a weak expansion fan at the step edge. The absence of a separation shock and separation motion enables one to focus solely on the dynamics of the reattachment shock as well as the recirculation zone. Therefore identifying the concomitant spectral characteristics could be helpful in analyzing results from interactions associated with other geometries. Also, Dupont et al. [29] showed that the shear-layer formed post separation follows the properties of a canonical mixing layer. The values of mean turbulent stress, spreading rate, and entrainment velocity follow the classical laws for turbulent transport in compressible shear-layers.

The adverse effects of the low-frequency unsteadiness mentioned previously are reproduced in this specific flowfield. Experiments on compressible reattaching shear-layers were carried out by Settles et al. [30] and Hayakawa et al. [31], in which measurements of mean and turbulent statistics were obtained. An experiment investigating the unsteadiness of this flowfield was carried out by Poggie and Smits [7] in which artificial disturbances were introduced in the boundary layer upstream of the step edge, which highlighted the role of upstream events. Increased intensity of pressure fluctuations and amplitude of shock-motion, as well as a distinct shift towards lower frequencies in the power spectra of pressure fluctuations at reattachment, were observed. The spectra for the baseline and control case scaled well with the vorticity thickness and RMS of pressure fluctuations in the shear layer.

Common unsteady features shared by both compressible and incompressible reattaching flows include shear-layer flapping and shedding of vortices from the recirculating zone. These events were also observed in the SWTBLI studies mentioned previously. Considerable research has been devoted to studying these phenomena in subsonic reattaching flows on backward and forward-facing steps. One of the promising hypothesis for the cause of flapping motion was propounded by Eaton and Johnston [32], [33] who carried out an experiment on a backward-facing step in a low-speed flow. They observed a flapping motion which possessed a long time-scale and led to broad movements in the instantaneous reat-

tachment point. The authors attributed the flapping motion to an instantaneous imbalance between shear-layer entrainment from the recirculating zone and re-injection of fluid near the reattachment point. In the experiment conducted by Spazzini et al. [34] on a backward-facing step, cyclical expansion and contraction of the separation bubble was observed. The frequency of this motion was comparable to the flapping frequency of the entire separated region. Additionally, formation and shedding of vortices occurred at a higher frequency. Scarano et al. [35] found vortices of varying size based on PIV measurements of a backward-facing step flow. The time-scale was directly proportional to the diameter of the vortical structure. Ma and Schröder [36] carried out SVD and POD analysis of a backward-facing step flow at a Reynolds number of 2×10^4 . They noticed a change in the recirculating region caused by feedback from the flapping motion.

Apart from the backward-facing step geometry, subsonic flow reattachment was also studied on a blunt flat plate and forward-facing step. Kiya and Sasaki [37] focused on the unsteadiness of the turbulent separation bubble formed along the sides of a blunt flat plate. Using statistical techniques, they deduced the length scale and the convection velocity of large-scale vortical structures, as well as their shedding frequency. The breathing motion of the separation bubble was accompanied by shear-layer flapping, and large accumulation of vorticity in the separation bubble led to shedding of vortices. In an extension of their work [38], they observed large-scale vortices with a hairpin geometry, with each end rotating in the opposite direction while simultaneously lifting fluid between them. They also constructed a mathematical model for unsteady flow at reattachment based on two governing factors: high-frequency vortex shedding and large-scale, low-frequency unsteadiness of the interaction.

In the case of a forward-facing step flow, Largeau and Moriniere [39] obtained wall pressure measurements and found evidence of shear-layer flapping and organized structures in the separation bubble using space-time correlations. The flowfield consisted of three regions: a separation bubble at the step front, a recirculation bubble at the upper edge of the step front, and a reattachment point downstream. Camussi et al. [40] performed a similar experiment and investigated wall pressure statistics over a forward-facing step. Their results agreed with Largeau and Moriniere [39]. Pearson et al. [41] showed the dependence of growth

and decay cycle of the separation bubble on elongated structures in the upstream flow using conditional averaging.

Organized vortical structures are also present in the shear-layer. Based on the experiments of Brown and Roshko [42], the mixing layer consists of large coherent spanwise rollers generated due to the Kelvin-Helmholtz instability. These structures grow in size by entraining fluid, or by the process of amalgamation of two smaller structures. Bernal and Roshko [43] state that the secondary streamwise vortices originate from an internal instability of the primary vortices. These streamwise vortices loop back and forth around the spanwise rollers and occur in counter-rotating pairs. Dimotakis and Brown [44] carried out similar experiments at higher Reynolds numbers up to 3×10^6 . Although the flow dynamics were different, the braid like structures observed in the experiments of Brown and Roshko [42] persisted at these Reynolds numbers.

Samimy et al. [45] investigated the effects of compressibility on structures in the mixing layer with moderate to high convective Mach numbers. At higher convective Mach numbers, the structures were highly three-dimensional with good spatial, but poor temporal organization. Based on the space-time correlations, the structures resembled a horse-shoe type vortex with its head on the low-speed side of the mixing layer, and inclined in both x - y and x - z planes. Poggie and Smits [27] observed coherent structures in a high-speed mixing layer with a convective Mach number of 1.1 using two-point correlations. The angle of these structures varied between 40–50 deg and streamwise elongation was observed downstream. Similar inclined structures were also found by Helm et al. [46] in a shear-layer associated with a Mach 3 SWTBLI on a compression ramp. Hu et al. [47], [48] investigated the mechanisms of unsteadiness of a SWTBLI over a backward facing step flow. They observed low-frequency motions associated with a breathing motion of the separation system and interaction between the shock wave and separated shear-layer. Interactions between shedding of vortices from the shear-layer and reattachment occurred at mid-frequencies. Additionally, Görtler like vortices caused by centrifugal instability originating from the shear-layer curvature were correlated well with the low-frequency dynamics of the interaction.

1.3 Compression Ramp Flow with Sidewalls

The second flowfield investigated in this study is a compression ramp flow with sidewalls. Most of the previous studies carried out on SWTBLI's associated with a compression ramp used a quasi two-dimensional approximation by incorporating aerodynamic fences or taking measurements along the centerline of the wind tunnel in experiments; or using periodicity on the side boundaries in numerical calculations. With recent advances in computational power, it has become feasible to incorporate the effect of sidewalls in SWTBLI calculations. Sidewalls introduce additional no-slip conditions which, when combined with the adverse pressure gradient of the shock, result in additional separated regions. These separated regions have a significant effect on the structure of centerline separation and eliminate the 2D nature of the interaction.

The highly non-uniform surface flow pattern of such flowfields was determined in the experimental studies on effects of sidewalls on reflected SWTBLI's, carried out by Reda and Murphy [49], [50]. Burton and Babinsky [51] studied the coupling between the corner and centerline separation in a Mach 1.5 normal SWTBLI by modifying the former using either vanes or suction. They found that the corner separation alters the structure of the λ -shock foot, which in turn affects the main separation bubble. Additionally, compression waves from the sidewall separation smeared the adverse pressure gradient at the corner. Bruce et al. [52] conducted a similar experiment at Mach 1.4 and 1.5 where they quantified the importance of effective aspect ratio δ^*/w (displacement thickness relative to width) on the onset of three-dimensional effects on quasi-2D interactions. In a similar study carried out by Xiang and Babinsky [53], the influence of corner separation on the tunnel centerline was illustrated by estimating the position of the corner shock crossing point. This location was found by extrapolating the compression waves along a straight line. When the crossing point lies downstream of the interaction, the interaction is unaffected by the sidewalls and retains its quasi-two-dimensional nature. The main separation increases as the crossing point moves inside the interaction in the upstream direction. The separation extent decreases when the crossing point falls upstream.

Eagle and Driscoll [54] carried out detailed velocity and vorticity measurements using PIV in a rectangular channel flow at Mach 2.75. The surface streamline pattern on the sidewalls and the centerline region indicated certain similarities with Type-1 and Type-2 separation respectively, as described by Tobak and Peake [55]. Funderburk and Narayanaswamy [56] performed experiments on a 12 deg compression corner at Mach 2.5. Both the primary and corner SWTBLI were investigated by surface streakline flow visualization and wall static pressure measurements. The pressure spectra in the intermittent region of the primary interaction was broadband in nature with a peak at $St = f_{L_{sep}}/U_\infty \approx 0.01$, consistent with the canonical 2D version. On the other hand, the spectrum corresponding to the intermittent region of the corner interaction was biased towards higher frequencies and displayed a peak at $St \approx 0.05$. Cross-coherence measurements indicated that pressure fluctuations in the incoming boundary layer drive the unsteadiness of corner SWTBLI, while the primary SWTBLI was more responsive to disturbances originating downstream. Morajkar et al. [57] analyzed a SWTBLI in a low-aspect-ratio duct using stereoscopic-PIV measurements in a Mach 2.75 flow. The swept interactions on the sidewalls and the incident interaction on the bottom wall were coupled via a complex three-dimensional vortical flowfield. Using the method of triple decomposition, three systems of vortices were identified: the corner vortex pair, swept-shock vortex on the sidewall, and a horseshoe-like vortex associated with the bottom wall interaction.

Wang et al. [58] carried out LES calculations on a reflected SWTBLI at Mach 2.7, including the effect of sidewalls in the domain. They tested the effect of tunnel aspect ratio (w/h) — where h is the tunnel height — and the sidewall boundary layer thickness on the interaction characteristics. The flowfield was highly three-dimensional for smaller aspect ratios and displayed spanwise uniformity at higher values. A swept SWTBLI, quasi-conical in nature, was formed on the sidewalls and distorted the main shock. The main shock was weakened at locations close to the shock foot and strengthened away from it. They also constructed a model based on the effective aspect ratio to estimate the complexity of the flowfield. Bermej- Moreno et al. [59] carried out wall-modeled large-eddy simulations (WMLES) of a flowfield characterized by multiple oblique SWTBLIs at Mach 2, in the presence of sidewalls. They considered three increasing strengths of the incident shock. The effect of confinement on the

mean flowfield resulted in the presence of a singular shock intersection (presence of a Mach stem between the incident and separation shock) in the first SWTBLI, as compared to a regular shock intersection in case of the spanwise-periodic simulation. Spectral analysis of wall-pressure fluctuations highlighted low-frequency content in the vicinity of the separation shocks. The low-frequency motions associated with different interactions in the flowfield were coupled by a non-linear mechanism.

Lushner and Sandham [60] carried out a numerical investigation of a three-dimensional laminar shock-wave boundary-layer interaction (SBLI) at Mach 2. Critical point analysis close to the wall revealed streamline patterns that resembled an owl-face pattern of the first kind, as introduced by Perry and Hornung [61]. A swept conical SBLI present between the shock generator and sidewalls was responsible for the strengthening of the interaction downstream. Presence of high-speed streaks downstream of the interactions near the centerline and in the corner suggested streak instability as a possible transition mechanism in a confined SBLI. Rabey et al. [62] used results from large-eddy simulations and high-frequency pressure measurements from experiments to examine the off-centerline behaviour in a SWTBLI with sidewall effects. They observed asymmetry about the spanwise centre with peak unsteadiness occurring off-centre. Using wall-pressure measurements, they were not able to find significant correlation between separations at the corner and centre. Garnier [63] carried out Stimulated Detached-Eddy Simulations (SDES) of an oblique SWTBLI, who also found strongest wall-pressure fluctuations present in the corner flows. He was not able to correlate the unsteadiness of the corner separations with that of the main separation.

Bisek [64] investigated sidewall interaction on a 24deg compression ramp with a large spanwise extent at Mach 2.25. In addition to the highly three-dimensional shock front, he observed a separation vortex at each sidewall junction upstream of the ramp. Both the ramp induced separation shock and leading foot of the λ -shock structure on the sidewall exhibited the characteristic low-frequency oscillations, but interestingly, the vortex induced separation bubble was nearly stationary. Poggie and Porter [65] extended this work by decreasing the spanwise extent to explore the effect of a very small (near choking) domain width parameter δ/w on the flow structure. Large scale symmetric and asymmetric motions were determined using conditional averaging. The curvilinear variation of centerline separation length

scale with the domain width parameter δ/w was verified. The onset of three-dimensional behaviour is dictated by the confinement ratio, δ^*/w where δ^* is the boundary layer displacement thickness in the center of the tunnel and w is the tunnel width [52]. Depending on the confinement ratio, the dynamics of the centerline and corner separations can be either independent or coupled. Additionally, the low-frequency shock motion observed in quasi two-dimensional cases was not affected by the presence of sidewalls.

1.4 High-Frequency Forcing of Shear-Layers

Linear stability analyses of mixing layers have provided a great deal of insight into their response to various excitation frequencies, which have in turn provided insights into their basic mechanisms such as vortex roll-up, vortex pairing, dynamics of large-scale structures. This has prompted many exploratory studies on different flow-control applications. A detailed review article documenting the effects of periodic perturbations in the shear-layer is provided by Ho and Huerre [66]. As a final aspect of this thesis, a brief study on the effects of high-frequency forcing on compressible reattaching shear-layers is carried out.

Some prior studies on perturbed shear-layers at high Reynolds numbers (and high convective Mach numbers) is reviewed. Samimy et al. [67] provide a comprehensive review on the usage Localized Arc Filament Plasma Actuators (LAFPAs) to excite natural instabilities in the shear-layer. The experiments were carried out on a exhaust jet from an nozzle for $Re \sim \mathcal{O}(10^6)$. The evolution of large-scale structures and as a consequence, the acoustic farfield, were dramatically altered by the introduction of thermal and acoustic perturbations. The shear-layer was found to be most receptive close to its inception, i.e. at the nozzle exit. Additionally, forcing at frequency representing the preferred mode of a jet led to significant lower levels of noise [68]. Dandois et al. [69] performed Direct Numerical Simulations (DNS) and Large-Eddy Simulations of synthetic jet forcing applied on a separated flow for a low- and high-frequency case. In case of low-frequency forcing, they observed reduced separation length caused primarily due to increased entrainment by the separated shear-layer.

Wiltse and Glezer [70] explored the effect of direct excitation of small scales in free shear flow, which lie within the dissipation regime of turbulence cascade. They observed enhanced

energy transfer from large scales to small scales, leading to increase in dissipation and rate of decay of turbulent kinetic energy. Vukasinovic et al. [71] carried out a similar study to investigate the effects of high-frequency actuation on the evolution of large- and small-scale motions in a subsonic turbulent shear-layer, using synthetic jets. Varying the vorticity flux introduced in the shear-layer led to changes in its growth and entrainment rates. The spectral plots showed broadband increase in the high-frequency regime accompanied by decrease in energy within the large-scale structures. Stanek et al. [72], [73] have demonstrated the effectiveness of high-frequency forcing in acoustic suppression of Rossiter modes in a cavity flow. The strategies for flow-control of high Reynolds number flow over open cavities were reviewed by Rowley and Williams [74].

1.5 Thesis Summary

This thesis consists of five additional chapters, the details of which are provided below:

1. **Chapter 2:** This chapter begins by examining the limitations of performing high-fidelity CFD computations of a high Reynolds number flow, in the context of multi-scale nature of turbulence. Concepts of turbulence modeling — Delayed-Detached Eddy Simulations (DDES) and Implicit Large Eddy Simulations (ILES) — used in this study to overcome these limitations are discussed briefly. The details of numerical schemes, grid spacings and time-steps, and locations of data extraction are specified. The chapter concludes by presenting the techniques used for data analysis.
2. **Chapter 3:** In this chapter, the flowfield unsteadiness corresponding to a compressible shear-layer reattaching on to a ramp is discussed in detail. Wall-pressure spectra and correlations are used to delineate different time- and length-scales, respectively. The effect of events in the shear-layer and recirculation zone on the reattachment shock motion is evaluated by calculating the estimates of correlation, coherence, and conditional averages. Additionally, a comparative study between the DDES and ILES approach is performed to discuss the efficacy of each approach in resolving the unsteadiness of the flowfield.

3. **Chapter 4:** A pattern similar to the previous chapter is followed here. This flow-field is particularly characterized by massive separation and presence of complicated gas-dynamics structures. The dominant time-scales in the flowfield are extracted using spectral analysis, with emphasis on the low-frequency shock motion. Estimates of correlation and coherence are then used to explore the causes of unsteady shock motion. Finally, Dynamic Mode Decomposition is used to recover complicated secondary motions using the process of mode reconstruction.
4. **Chapter 5:** Effects of high-frequency forcing on compressible reattaching shear-layer are elaborated in this chapter. Comparison of both frequency and wavenumber spectra corresponding to the forced case with those of the baseline case are carried out. Changes in the reattachment shock motion as well as other mid- to high-frequency events are investigated.
5. **Chapter 6:** This chapter presents the conclusions of this study.

2. METHODOLOGY

This chapter presents the details of numerical modeling employed in the study of SWTBLI associated with compressible reattaching shear-layers and a highly confined compression-ramp flow. Initially, the challenges in accurately resolving the physics of high-Reynolds number flows are discussed briefly. In this context, the methods of hybrid RANS/LES and ILES which were used to perform high-fidelity simulations are introduced in Sec. 2.1 and 2.2, respectively. This is followed by elaborating the approach to data analysis of the simulation results.

Turbulence is inherently a multi-scale phenomenon, with eddy sizes ranging from the order of boundary-layer thickness (δ) down to the Kolmogorov length-scale (η .) According to the energy cascade model of Richardson [75], the turbulent kinetic energy is produced in the large-scales and is eventually dissipated in the smaller scales by the action of viscosity. For wall-bounded flows, the length-scale of these smaller eddies (for isotropic flows) was estimated by Kolmogorov [76] as $\eta = (\nu^3/\epsilon)^{1/4}$, where ν is the kinematic viscosity and ϵ is the dissipation rate of turbulent kinetic energy. The scale separation becomes a prominent factor in turbulence at high Reynolds numbers flows, and is quantified by the friction Reynolds number $Re_\tau = \delta u_\tau/\nu = \delta^+$, which is the ratio of boundary-layer thickness (representing eddies in the outer layer) and viscous length-scale (representing eddies in the dissipative range.) Additionally, the fraction of total turbulent kinetic energy within the large-scale structures increases with Reynolds number, indicating their importance in the transport of turbulence properties. Details on the nature of turbulence in high Reynolds number are documented in the reviews by Jiménez [77], Smits et al. [78], [79], and Marusic et al. [80].

For a Direct Numerical Simulations (DNS), Chapman [81] derived an estimate for the required number of grid points – $N \sim Re_{L_x}^{9/5}$, where L_x is the flat-plate length in the stream-wise direction. These estimates were then revised to $N \sim Re_{L_x}^{37/14}$ by Choi and Moin [82], who used updated correlations of skin-friction coefficient and displacement thickness in the derivation process, specifically for high Reynolds number boundary layer flow. As is evident from the Re scaling, a Reynolds number of $\mathcal{O}(10^6)$ requires a grid size of $\sim \mathcal{O}(10^{15})$ points. Since the problem size of this order of magnitude is not feasible for current supercomputers,

small-scales in a turbulent flow which generate bulk of the computational cost, are modeled under the assumption of local isotropy and sufficient scale separation at high Reynolds numbers. Although DNS runs of grid sizes over $\mathcal{O}(10^{10})$ cells are expensive, they are possible at present [83], and demonstrations at the $\mathcal{O}(10^{12})$ cell scale have been carried out [84], [85].

There are numerous modeling strategies used to determine effective turbulent eddy viscosity due to the contribution of unresolved scales, each with a different degree of fidelity in a hierarchical sense. The most popular approach is the Reynolds Averaged Navier-Stokes Equations (RANS), supplemented with either a one-equation or a two-equation turbulence model to calculate the turbulent eddy viscosity (More complex models, with an equation for each component of the Reynolds stress tensor such as the SSG model [86], LRR model [87], and Wilcox Stress- ω model [88], are also available.) In this approach, all the turbulent scales are modeled, thus making it extremely adaptable for industrial applications. This study deals with two different modeling approaches: Delayed Detached-Eddy Simulations (DDES) and Implicit Large-Eddy Simulation (ILES), both of which lie on a significantly higher level in the trade of computational cost vs. resolution in turbulence modeling.

2.1 Delayed Detached-Eddy Simulations

The versatility of RANS turbulence models is limited to the applications that its empirical constants were tuned for. Outside of their respective domains of application — especially in case of unsteady separated flows — these models break down and typically lead to non-physical results and/or estimates that lie outside the bounds of their respective epistemic uncertainties. Recent advances in computational power have made wall-resolved LES possible for low to moderate Reynolds numbers and wall-modeled LES feasible at high Reynolds numbers.

Conventional hybrid RANS/LES models capitalize on the advantages of both RANS and LES methods, wherein the model switches between the two modes depending on whether the flow is either attached or separated and whether the grid is sufficiently resolved. This approach was designed primarily to circumvent the high computational cost associated with separated flows at high Reynolds number. The original formulation of DES by Spalart

involved setting a length-scale (\tilde{d}) to determine if the model functions in the RANS mode or LES mode. Within the RANS mode, the eddy viscosity ($\tilde{\nu}$) is calculated by the corresponding turbulent transport equations, whereas in the LES mode, the eddy viscosity is determined by a sub-grid scale (SGS) model. The length-scale \tilde{d} , which acts as a switch between the two modes, is a function of wall distance (d) and grid spacings (Δx , Δy , and Δz .) In the Spalart-Allmaras (S-A) turbulence model, the eddy viscosity scales with the deformation rate (S) and d : $\nu \propto Sd^2$, when the production and destruction terms are balanced. Similarly in the Smagorinsky Sub-Grid-Scale (SGS) model, the SGS eddy viscosity scales with S and the grid spacing: $\nu_{SGS} \propto S\Delta^2$, where $\Delta = \max(\Delta x, \Delta y, \Delta z)$ is the chosen measure of grid spacing [89]. Since the eddy viscosity scales differently in the RANS mode than in the LES mode, the DES length-scale \tilde{d} is responsible for controlling the same and is defined by

$$\tilde{d} = \min(d, C_{DES}\Delta). \quad (2.1)$$

wherein the DES model switches to the RANS mode when $d \ll \Delta$ and to the LES mode when $d \gg \Delta$.

Unlike the zonal DES approach, where \tilde{d} is set by the user, the concept elaborated in the previous paragraph is categorized as the “seamless” approach, which entails setting \tilde{d} based on the grid and/or solution without user intervention [90]. The seamless approach can be more robust and can be applied to complex flowfields with relative ease. In case of ambiguous grids wherein the wall-parallel grid spacings (Δx , Δz) are sufficiently small to trigger the LES branch of the model, but are not fine enough to resolve the LES content, a phenomenon called Modeled Stress Depletion (MSD) [91] can occur. Modeled Stress Depletion can lead to premature separation (also known as grid-induced separation) due to under-prediction of the Reynolds stresses by the SGS eddy viscosity, and occurs when the boundary layer thickness is a significant percentage of some macro length-scale such as the step height or airfoil chord (such as in the vicinity of flow separation.)

The issue of MSD can be circumvented by correctly identifying the boundary-layer region, in order to treat it purely as RANS and prevent the switch to LES. Several proposed alternatives to the original formulation of DES and their shortcomings are discussed by Spalart

et al. [91] and are not reiterated here. A common feature shared amongst these alternatives is their lack of ability to adapt to grids corresponding to complex geometries, thereby generating suspect solutions. In order to overcome the dependency of DES length-scale on the grid, Spalart et al. [91] formulated a modified DES length-scale that also depends on the local eddy viscosity. Additionally, blending functions – akin to the shielding functions used by Menter and Kuntz – are used to preserve the RANS mode within the boundary layer. In case of the S-A based DDES model, a parameter r_d incorporates the local eddy viscosity and is defined as,

$$r_d = \frac{\nu_t + \nu}{\sqrt{U_{i,j}U_{i,j}}\kappa^2 d^2} \quad (2.2)$$

where r_d is a modified version of the parameter r in the original S-A turbulence model ($r = \nu/S\kappa^2 d^2$.) In the above equation, ν, ν_t are the molecular and turbulent kinematic eddy viscosity respectively, $U_{i,j}$ is the velocity gradient, κ is the Kármán constant, and d is the distance to the wall. The shielding function f_d is defined as,

$$f_d = 1 - \tanh(8r_d)^3. \quad (2.3)$$

For $r_d \ll 1$ (away from the wall and lower ν_t), f_d equals 1 and the LES mode is activated. On the other hand when $r_d \gg 1$ close to the wall, f_d switches to zero and the RANS mode is activated. Finally, the modified DES length-scale that enters the turbulence model is given by,

$$\tilde{d} = d - f_d \max(0, d - C_{DES}\Delta) \quad (2.4)$$

where C_{DES} is a model constant which is calibrated by examining the behaviour at small scales in homogeneous turbulence. Therefore close to wall, the length-scale $\tilde{d} = d$ as $d < C_{DES}\Delta$, activating the RANS mode with the eddy-viscosity determined by the S-A model (see Sec. 2.3.2.) Away from the wall, $\tilde{d} = C_{DES}\Delta$ as $d > C_{DES}\Delta$, the LES mode is triggered with the Smagorinsky SGS model (see Sec. 2.3.3) used to determine the eddy-viscosity from the unresolved scales. Additional details on the common issues encountered in DES calculations are elaborated by Spalart [92]. As the computationally intensive turbu-

lence is modeled by RANS, the grid requirements for DDES scale as $\sim Re_{L_x}^{0.9}$ [93] (roughly proportional to Re_τ [94].)

2.2 Implicit Large-Eddy Simulations

Large Eddy Simulations (LES) of high Reynolds number flows are contingent upon the accuracy of the sub-grid scale (SGS) model to model the near wall turbulence. An SGS model prone to errors may lead to issues like insufficient dissipation of turbulent kinetic energy, resolution of the energy cascade from larger scales to smaller scales, and incorrect prediction of sub-grid stresses, which result in erroneous values of skin-friction and wall heat transfer. Increasing complexity in SGS modelling may address some of these issues but are inevitably more computationally intensive.

Implicit Large Eddy Simulations (ILES) on the other hand, do not use an explicit SGS model to treat the unresolved scales. Instead, the energy at high wavenumbers is treated implicitly by the inherent dissipative nature of the numerical scheme. Numerical approximations of partial differential equations (PDEs) generate truncation terms, which have the same order of magnitude as the SGS terms in LES [95]. Since this approach does not rely on the formulation of an explicit SGS model, it is computationally efficient and easy to implement. This method is particularly valuable in the case where the numerical scheme is stabilized by an explicitly applied filter, which can be precisely tailored to obtain desired spectral properties and overall dissipation [96].

The first formulation of this approach was done by Boris et al. [97], who termed it as Monotone ILES (MILES.) A non-oscillatory finite volume (NFV) scheme is used to discretize the Navier-Stokes equations. The numerical schemes that fall in this class display properties of numerical stability, monotonicity, efficient shock capturing, and suppression of numerical oscillations. Grinstein et al. [98] use the Modified Equation Analysis (MEA) approach to assess the stability and accuracy of NFV based ILES methods and examine the effects of different NFV schemes. They concluded that the leading truncation-error terms are instrumental in determining the dissipation properties provided by a particular NFV scheme.

ILES has been shown to reproduce the 4/5 law of Kolmogorov by Margolin et al. [99] who used MPDATA — an NFV algorithm — to simulate decaying turbulence, wherein the energy-dissipation characteristics depended on the order of accuracy of the NFV scheme which implicitly provides the SGS model. Simulation of the Taylor-Green Vortex by Drikakis et al. [100] using ILES captured the processes vortex stretching, instability, and production of small-scale eddies, which are typically involved in boundary layer transition to turbulence. Fuerby et al. [101] used MILES for a variety of compressible turbulent shear flow cases such as, supersonic flat-plate boundary layers, compression ramp SWTBLI, and supersonic base flows. They obtained reasonable agreement of surface properties (like skin-friction coefficient) as well as first and second order moments with DNS and experimental data.

Visbal et al. [102] implemented compact finite differences instead of an upwind biased finite volume discretization for spatial derivatives. Compact finite differences approach the resolution of spectral methods with increasing order of accuracy. Unlike MILES, wherein the dissipation at small scales is implicitly provided by the dissipative nature of the numerical scheme, this approach applies an explicit high-order low-pass filter to the conserved variables at every time-step. This filter is specifically selected to damp out the under-resolved high-frequency content in the flowfield.

Discretization of spatial derivatives using high-order compact finite differences are elaborated in the work by Lele [103]. Some of the previous efforts on formulating Padé type compact differencing schemes were carried out by Orszag and Israeli [104] and Hirsh [105]. For a particular flow variable f , its spatial derivative is determined by an approximate generalization of the Padé-type scheme of the form:

$$\beta f_{i-2} + \alpha f_{i-1} + f_i + \alpha f_{i+1} + \beta f_{i+2} = c \left(\frac{f_{i+3} - f_{i-3}}{6h} \right) + b \left(\frac{f_{i+2} - f_{i-2}}{4h} \right) + a \left(\frac{f_{i+1} - f_{i-1}}{2h} \right) \quad (2.5)$$

where the f_i denotes the spatial derivative at node i and $h = \mathbf{x}_{i+1} - \mathbf{x}_i$ is the mesh spacing between two consecutive nodes. The relationship between coefficients a , b , c , α , and β can be obtained by matching the Taylor series coefficients of various orders of accuracy, in order to obtain the desired order of accuracy. This scheme is convenient to implement on a non-

uniform, curvilinear, and stretched meshes by incorporating coordinate transformations in the governing equations, using appropriate Jacobians. As $\alpha, \beta \rightarrow 0$, the family of equations in Eq. (2.5) describes the class of commonly used central difference schemes. For the sixth order compact difference scheme used in this study, the coefficients are: $a = 14/9$, $b = 1/9$, $c = 0$, $\alpha = 1/3$, and $\beta = 0$. Similar coefficients for both compact finite difference and central difference scheme are derived in Refs. [103], [106].

Lele [103] used Fourier wave number analysis of the discretization scheme in Eq. (2.5) to derive a relationship between the wavenumber (k) and the modified wavenumber (\hat{k}), as shown in Eq. (2.6),

$$\hat{k} = \frac{a \sin(k) + (b/2) \sin(2k) + (c/3) \sin(3k)}{2\beta \cos(2k) + 2\alpha \cos k + 1}. \quad (2.6)$$

Using the coefficients corresponding to compact and central difference scheme of various orders of accuracy, a plot of the relationship between k and \hat{k} is illustrated in Fig. 2.1. The exact solution, $k = \hat{k}$ is also included in the figure as a black solid line.

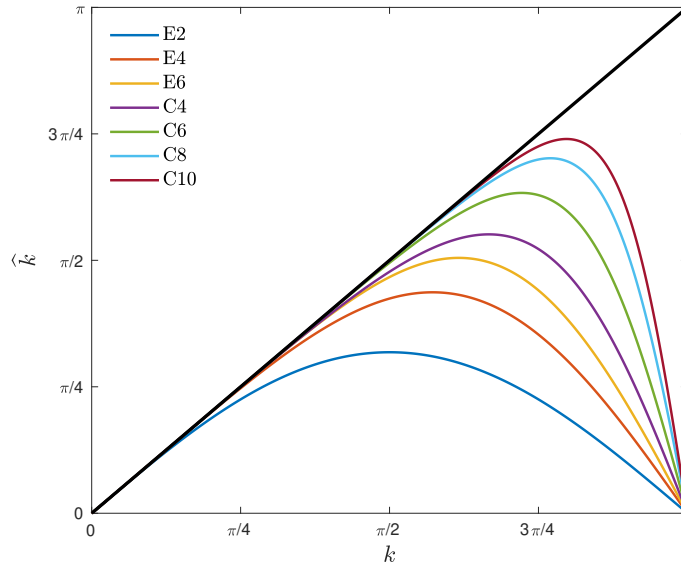


Figure 2.1. Fourier wave number analysis of central and compact discretization schemes. Black solid line represents the exact solution, $\hat{k} = k$.

In the legend nomenclature within this figure, the first letter stands for the type of discretization – “E” for explicit central differences and “C” for compact differences, while the number represents the order of accuracy of that particular scheme. As is evident from the figure, discretization schemes with higher order of accuracy match the exact solution for a wider domain of wavenumbers. Lower order compact difference schemes are still more accurate than the higher order explicit central difference schemes. Dispersion error at high wavenumbers is present in all the cases. For any given compact difference scheme of order N , the stencil on the RHS of Eq. (2.5) consists of $2N + 1$ points. Therefore the sixth-order compact difference scheme used in this study offers a reasonable compromise between the resolution capability and incurred computational cost. A tighter stencil also facilitates an efficient parallel implementation of the scheme.

2.3 Governing Equations

2.3.1 Compressible Navier-Stokes Equations

The compressible, three-dimensional Navier-Stokes equations under the assumption of calorically perfect gas shown in Eq. (2.7) are used in this study.

$$\begin{aligned} \frac{\partial \rho}{\partial t} + \frac{\partial}{\partial x_j}(\rho u_j) &= 0 \\ \frac{\partial}{\partial t}(\rho u_i) + \frac{\partial}{\partial x_j}(\rho u_i u_j) &= -\frac{\partial p}{\partial x_i} + \frac{\partial}{\partial x_j}(\tau_{ji}) + f_i \quad i, j \in \{1, 2, 3\} \\ \frac{\partial E}{\partial t} + \frac{\partial}{\partial x_j}[(E + p)u_j] &= \frac{\partial}{\partial x_j} \left(k \frac{\partial T}{\partial x_j} \right) + \frac{\partial}{\partial x_k}(\tau_{jk} u_j) + f_k u_k \end{aligned} \quad (2.7)$$

where $(x_1, x_2, x_3) = (x, y, z)$ represent streamwise, wall-normal, and spanwise direction and f_i indicates an applied body-force. Under the assumption of a calorically perfect gas, the total energy (E) is calculated as,

$$E = \frac{p}{\gamma - 1} + \frac{1}{2} \rho u_i u_i, \quad (2.8)$$

and using the ideal gas equation of state, the temperature is defined as,

$$T = \frac{P}{\rho R} \quad (2.9)$$

where R is the gas constant for air. The shear stress tensor (τ_{ij}) and the turbulent heat flux (\vec{q}_T) are shown in Eqs. (2.10) and (2.11), respectively:

$$\tau_{ji} = \mu_{tot}^1 \left(\frac{\partial u_i}{\partial x_j} + \frac{\partial u_j}{\partial x_i} - \frac{2}{3} \delta_{ji} \frac{\partial u_k}{\partial x_k} \right); \quad \mu_{tot}^1 = \mu_{dyn} + \mu_{tur} \quad (2.10)$$

$$\vec{q}_T = \frac{\mu_{tot}^2 c_p}{Pr} \nabla T; \quad \mu_{tot}^2 = \frac{\mu_{dyn}}{Pr_d} + \frac{\mu_{tur}}{Pr_t} \quad (2.11)$$

where μ_{tot}^1 , μ_{tot}^2 represent the effective dynamic viscosity and thermal conductivity and Pr_d , Pr_t are the dynamic and turbulent Prandtl numbers, respectively. The molecular viscosity follows the Sutherland's law in Eq. (2.12),

$$\mu = \mu_o \left(\frac{T}{T_o} \right)^{3/2} \left(\frac{T_o + S}{T + S} \right) \quad (2.12)$$

where $\mu_o = 1.716 \times 10^{-5}$ kg/ms, $T_o = 273.15$ K, and $S = 110.4$ K. The turbulent viscosity μ_t is determined from a suitable turbulence model. For DDES computations, the turbulent viscosity contribution from the unresolved scales is determined via a combination of the one-equation S-A turbulence model (close to the wall) and the Smagorinsky SGS model (away from the wall.) Their formulation is described in Sec. 2.3.2 and 2.3.3, respectively. In case of ILES computations, no explicit SGS model is used and instead, the physics of unresolved scales is handled by the elimination of unresolved scales by a sharp, low-pass filter function.

2.3.2 S-A turbulence model

In a RANS approach, the unknown mean Reynolds stresses ($\overline{u_i u_j}$) are modeled using the Boussinesq hypothesis,

$$-\overline{u'_i u'_j} = 2\nu_t S_{ij} - \frac{2}{3} k \delta_{ij}, \quad S_{ij} = \frac{1}{2} \left(\frac{\partial \bar{u}_i}{\partial x_j} + \frac{\partial \bar{u}_j}{\partial x_i} \right), \quad k = \frac{1}{2} \overline{u'_k u'_k} \quad (2.13)$$

where $\bar{\phi}$ denotes the Reynolds time-average of ϕ , ϕ' denotes the fluctuating component of ϕ , S_{ij} is the mean strain-rate, k is the mean turbulent kinetic energy, and ν_t is the turbulent eddy viscosity. The S-A turbulence model [107] computes the turbulent eddy viscosity as follows:

$$\nu_t = \mu_t/\rho = \hat{\nu}f_{v1}, \quad f_{v1} = \frac{\chi^3}{\chi^2 + c_{v1}^3}, \quad \chi = \frac{\hat{\nu}}{\nu}, \quad \nu = \frac{\mu}{\rho} \quad (2.14)$$

where ν is the molecular kinematic viscosity and the variable $\hat{\nu}$ is obtained by solving a transport equation,

$$\frac{D\hat{\nu}}{Dt} = c_{b1}\hat{S}\hat{\nu} - c_{w1}f_{w1}\left(\frac{\hat{\nu}}{d}\right)^2 + \frac{1}{\sigma}\frac{\partial}{\partial x_k}\left[(\nu + \hat{\nu})\frac{\partial\hat{\nu}}{\partial x_k}\right] + \frac{c_{b2}}{\sigma}\frac{\partial\hat{\nu}}{\partial x_k}\frac{\partial\hat{\nu}}{\partial x_k}. \quad (2.15)$$

The production term \hat{S} and other auxiliary relations are shown below,

$$\hat{S} = S + \frac{\hat{\nu}}{\kappa^2 d^2}f_{v2}, \quad f_{v2} = 1 - \frac{\chi}{1 + \chi f_{v1}}, \quad f_{v1} = \frac{\chi^3}{\chi^2 + c_{v1}^3}, \quad f_w = g\left[\frac{1 + C_{w3}^6}{g^6 + C_{w3}^6}\right]^{1/6} \quad (2.16)$$

where $S = |\bar{\omega}|$, $g = r + c_{w2}(r^6 - r)$, and $r = \hat{\nu}/\hat{S}\kappa^2 d^2$. The model coefficients required for closure are given by,

$$\begin{aligned} c_{b1} &= 0.1355, & c_{b2} &= 0.622, & c_{v1} &= 7.1, & \sigma &= \frac{2}{3}, \\ c_{w1} &= \frac{c_{b1}}{\kappa^2} + \frac{1 + c_{b2}}{\sigma}, & c_{w2} &= 0.3, & c_{w3} &= 2, & \kappa &= 0.41. \end{aligned} \quad (2.17)$$

In the SU2 code [108], the variable $\hat{\nu}$ is set to zero at the wall, implying the absence of significant turbulent eddies near the wall. A fraction of laminar viscosity is imposed in the far-field.

2.3.3 Smagorinsky Sub-Grid Scale Model

Within the LES mode in a DDES calculation, the unresolved sub-grid shear-stress tensor can be decomposed in a isotropic and a deviatoric component, $\tau_{ji}^{sgs} = \tau_{ji}^{iso} + \tau_{ji}^{dev}$. The isotropic and deviatoric components of the shear-stress tensor are defined as,

$$\begin{aligned}\tau_{ji}^{iso} &= \frac{1}{3}\tau_{kk}^{sgs} \\ \tau_{ji}^{dev} &= \tau_{ji} - \frac{1}{3}\tau_{kk}^{sgs}.\end{aligned}\tag{2.18}$$

The Smagorinsky SGS model [109] defines the deviatoric sub-grid shear-stress as,

$$\begin{aligned}\tau_{ji}^{dev} &= -2\nu_t\tilde{S}_{ji}, \quad \tilde{S}_{ji} = \frac{1}{2}\left[\frac{\partial\tilde{u}_i}{\partial x_j} + \frac{\partial\tilde{u}_j}{\partial x_i}\right] \\ \nu_t &= (C_s\Delta)^2|\tilde{S}|, \quad l = C_{DES}\Delta, \quad q = l|\tilde{S}|\end{aligned}\tag{2.19}$$

where $\tilde{S} = \sqrt{2\tilde{S}_{ji}\tilde{S}_{ji}}$, C_s is the Smagorinsky constant, and $\tilde{\cdot}$ denotes quantities filtered implicitly by the imposed grid spacing. The implicit filtering approach leads to a solution that is sensitive to any variations in grid spacings, which in turn affects the statistics of resolved turbulence [110].

2.3.4 Padé-type Non-Dispersive Spatial Filters

As mentioned in Sec. 2.2, the ILES approach depends on the inherent dissipation of the numerical scheme to act as a suitable SGS model. Compact differences are used in a portion of the present project to calculate the spatial derivatives due to their “spectral-like” resolution characteristics. Since the compact differencing approximation presented in Sec. 2.2 is typically of central difference form with an even order of accuracy, the leading order truncation error is of the dispersive type, i.e. there is no dissipation built-in the scheme [103]. Hence it is necessary to introduce external dissipation in the flowfield to counteract the accumulation of dispersion error at high wavenumbers [111].

The Padé-type non-dispersive spatial filters act as low-pass filters and are used to selectively damp out the high frequency content in the solution, specifically the under-resolved scales. For a conserved variable ϕ , the filtered variable $\hat{\phi}$ is given as,

$$\alpha_f \hat{\phi}_{i-1} + \hat{\phi}_i + \alpha_f \hat{\phi}_{i+1} = \sum_{m=0}^N \frac{a_m}{2} (\phi_{i+m} + \phi_{i-m}) \quad (2.20)$$

where N is the order of accuracy of the filter and a_m are the filter coefficients. The filtering of conserved variables is carried out at every time-step (or after every sub-iteration) along each direction, and entails solving a tridiagonal set of equations (for $\alpha_f \neq 0$.) A filter with an order of accuracy N would generate a stencil consisting of $2N+1$ points on the RHS. This formulation is analogous to the compact differencing stencil elaborated in Sec. 2.2. The free parameter α_f determines the degree of dissipation introduced by the filter. The primary constraint of α_f is that $|\alpha_f| \leq 0.5$ for proper behaviour of the filter [112]. Higher values α_f correspond to a less dissipative filter. As in the approach used in compact differencing, the filter coefficients are determined by matching terms in the Taylor series. These coefficients are documented in Ref. [106].

The filter transfer function following a Fourier analysis is shown in Eq. (2.21),

$$SF(k) = \frac{\hat{b}_n}{b_n} = \frac{\sum_{m=0}^N a_m \cos(mk)}{1 + 2\alpha_f \cos(k)} \quad (2.21)$$

where b_n and \hat{b}_n are the Fourier coefficients for the original and filtered functions, respectively. Following the low-ordered centered (LOC) approach by Gaitonde and Visbal [113], the filter order is gradually reduced as one approaches a boundary, in order to compensate for the reduced available stencil size. In this study, the filter order is gradually reduced from eighth order (in the interior) to second order (at one point off the boundary.) No filtering is carried out at the boundary point. This filter template can be represented as F8-F6-F4-F2-F0, where ‘‘F’’ stands for filter and the following number represents its order.

In this study, the value of $\alpha_f = 0.4$ at the interior points where an eighth order filter is applied. For filters of lower orders (F2, F4, and F6), the value of α_f is increased to 0.49. Using a value of the coefficient closer to 0.5 increases the sharpness of the filter, partially

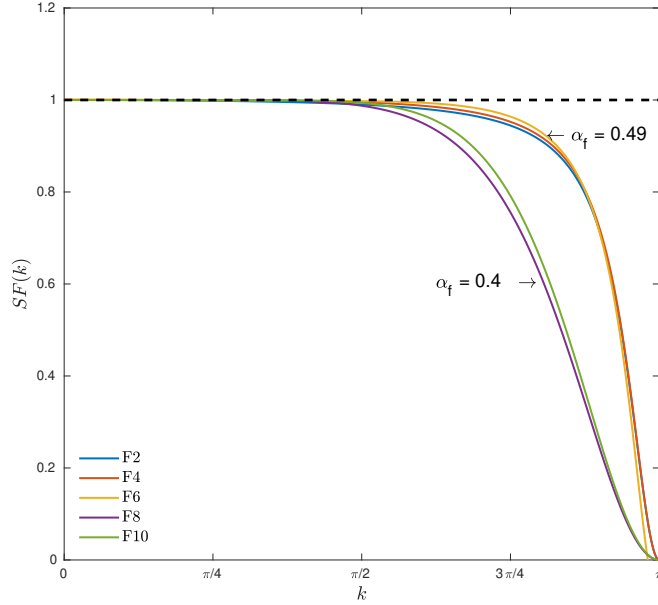


Figure 2.2. Filter transfer function. Black dashed line represents no filtering of the variables.

compensating for the reduced order of the filter. Note that at $\alpha_f = 0.5$, Eq. (2.21) reduces to an identity and no filtering is carried out. Using these values and Eq. (2.21), the resulting filter gain function is shown in Fig. 2.2.

According to the trends observed in this figure, there is a negligible effect on amplitude for the range of wavenumbers, $k \leq \pi/2$. Increasing the filter order from F8 to F10 preserves a slightly wider band of wavenumbers at a higher computational cost. Therefore, this observation justifies the usage of an eighth order filter for the interior points. Also for the consistency of the numerical formulation, the filter order needs to be the compact difference order plus two. Hence a combination of C6+F8 is used in this study.

In case of lower order filters, the dissipation at high wavenumbers is significantly reduced due to a higher value of α_f . In case of a shock wave, the filter template switches to F8-F6-F4-F2-F0-F0-F0-F0-F2-F4-F6-F8, wherein the shock point is located at the center of the template. At locations where the filter is switched off, the discretization scheme switches from compact differencing to an upwind biased scheme with an appropriate limiter to prevent spurious oscillations. Upwind biased schemes introduce the necessary dissipation required for

numerical stability in the vicinity of shocks. The shock detector uses a simple Jameson-type pressure switch. It is always off for $M < 1.05$ and always on for $M > 2.43$. These threshold Mach numbers are based on standard practice which aim for the shock detector to turn off for localized subsonic flows, but simultaneously capture the shock crisply in the supersonic freestream.

2.4 Computational Setup

This report presents the results from statistical analysis carried out on two flowfields: the compressible reattaching shear-layer (Case 1) and compression ramp flow with sidewalls (Case 2.) For each case, details of the grid spacings, flow conditions, numerical method, and data sampling are provided. Both of these cases represent a specific type of SWTBLI; Case 1 describes a SWTBLI that occurs in reattaching flows and Case 2 examines the effects of confinement on a quasi two-dimensional SWTBLI.

2.4.1 Case 1: Compressible Reattaching Shear-Layer

Most of the results presented for the first case were obtained from data analysis of DDES calculations carried out using the NASA OVERFLOW code by Leger, Bisek, and Poggie [28], on the geometry shown in Fig. 2.3 (this computation was made possible by a grant of computer hours from a DoD HPCMP Frontier Project and DoD Supercomputing Resource Center.) Two additional runs on the same geometry were carried out by the author via DDES calculations in SU2 and ILES calculations in HOPS (Higher Order Plasma Solver), an in-house code. These three runs are listed in Table 2.1. The grids used for each code were slightly different. The SU2 calculations were run in-part by Deshpande on the Stampede2 cluster of Texas Advanced Computing Center (TACC), under an XSEDE grant. The remaining calculations were carried out by Poggie on AFRL's Mustang and Narwahl HPC systems.

The SU2 code was originally developed by the Aerospace Design Lab (ADL) at Stanford University and is currently under active development by many international collaborators [114]. SU2 is an open-source unstructured finite volume solver implemented with

Table 2.1. List of calculations for Case 1.

Code	Run by
SU2	Deshpande and Poggie
HOPS	Poggie
OVERFLOW	Leger, Bisek, and Poggie [28]

object-oriented class architecture in C++ and high level Python scripts. The SU2 suite consists of several modules which are C++ executables, each designed for a specific task. The recent version of SU2 (SU2 v.7.0.2 - Blackbird) has both LES and DDES capability [108].

HOPS was originally developed for multi-fluid plasma calculations, but is also capable of single fluid gas dynamics [83]. The new, overset grid version of the code is called Wabash. This code is written in modern Fortran, and employs the MPI and OpenMP libraries. The computational approach employs multi-level parallelism. The computational domain is decomposed into blocks, each of which is handled by one MPI rank. Each block, in turn, is handled by several OpenMP threads which divide the work of outer loops. Inner loops are designed to be vectorizable by most modern compilers. Input and output are handled using derived data types and calls to MPI-IO.

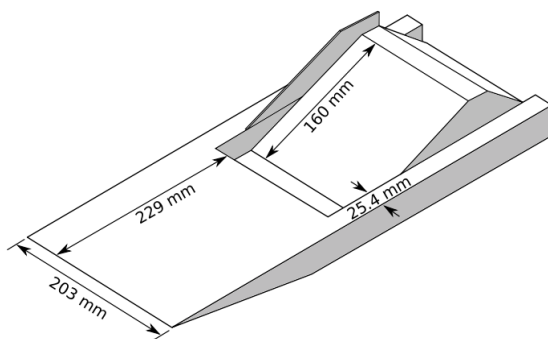


Figure 2.3. Geometry used in experiments [28].

This geometry shown in Fig. 2.3 was based on the model used for experiments conducted at Princeton University [7], [30], [31] in the 1980s and 1990s in the 8 in by 8 in, Mach 3, high Reynolds number wind tunnel. It consisted of a backward-facing step with a height of 25.4 mm, followed by a cavity region about 61.9 mm long. Downstream of the cavity, a ramp

inclined at 20 deg and extending 160 mm was present. For the calculations, OVERFLOW 2.2K, an overset grid computational fluid dynamics solver developed by NASA was used with a hybrid RANS/LES approach and the S-A turbulence model. The freestream conditions were chosen to correspond to the reported experimental values. Their respective values are shown in Table 2.2, where δ_o is the boundary layer thickness on the step close to separation. As mentioned previously, the DDES approach allows the numerical solution to be carried out at the true experimental Reynolds number, which is quite high.

Table 2.2. Flow conditions for Case 1.

Parameter	Value
u_∞	572 m/s
ρ_∞	0.77 kg/m ³
T_∞	95 K
T_w	266 K
$\rho_\infty u_\infty / \mu_\infty$	$67 \times 10^6 \text{ m}^{-1}$
M_∞	2.92
M_c	1.1
δ_o	3 mm

For the calculations in OVERFLOW, the x - y plane was divided into three regions. The first region lied upstream of the backward-facing step, the second region consisted of the cavity and redeveloping zone, with the third region lying directly on top of it. Following grid generation, the first, second, and third region consisted of 191×129 , 1669×161 , and 1669×129 points, respectively. This plane was extruded in the spanwise z -direction and discretized uniformly with 321 points. Overall, the problem size composed of $\approx 1.6 \times 10^8$ grid points. In terms of wall units, the grid size corresponds to $\Delta x^+ \approx 25$, $\Delta z^+ \approx 22.5$ and $\Delta y_w^+ \leq 1$ throughout the domain. These quantities were calculated using the conventional inner variable scaling: $\Delta x_i^+ = \Delta x_i u_\tau / \nu_w$, where $u_\tau = \sqrt{\tau_w / \rho_w}$ is the friction velocity; ν_w , τ_w , and ρ_w are the kinematic viscosity, shear-stress, and density at the wall respectively. Streamwise clustering was done in the regions characterized by high gradients.

For the calculations using SU2 and HOPS, the grid dimensions of the x - y plane are consistent with that used in OVERFLOW (1701×289 cells.) Therefore the Δx^+ value is ≈ 25 , with $\Delta y_w^+ \leq 1$ everywhere. The spanwise extent of the domain is truncated to 30 mm to

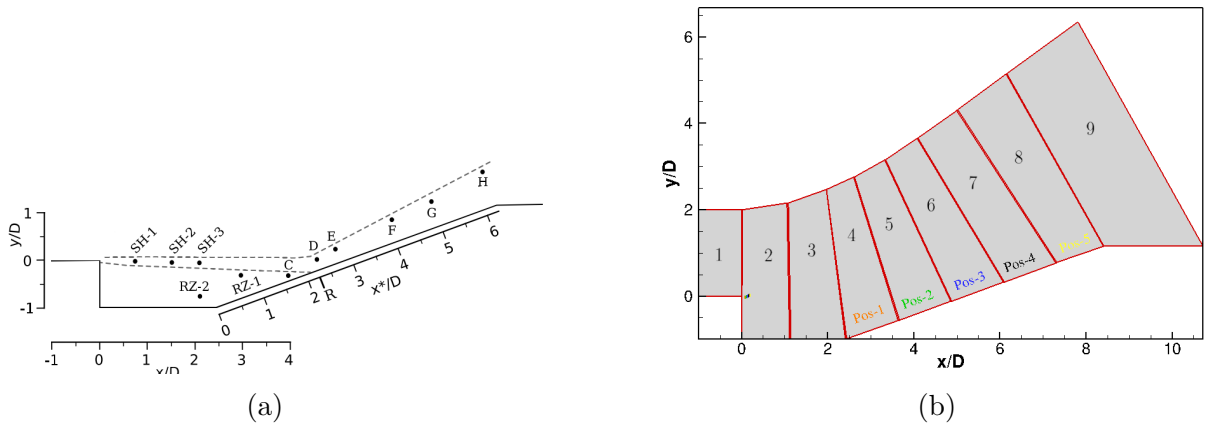


Figure 2.4. Extracted data locations (Case 1.) (a) Sampling stations [28] (Reprinted with permission from the author) (b) Division of grid on the centerplane.

reduce the computational cost. This value is equivalent to three times of the boundary layer thickness at mean reattachment ($\delta_R = 10$ mm) measured in the experiments [30], [31]. The domain width for these calculations should be sufficient to achieve spanwise decorrelation in the shear-layer, but not necessarily in the recirculation zone. The span was discretized using 181 points and 501 points for grids corresponding to SU2 and HOPS, respectively. The corresponding Δz^+ values are ≈ 23.6 and 8.5, respectively. The grid spacings for the DDES runs follow the criteria specified for LES mesh sizing by Georgiadis et al [115] and Spalart [107]. According to the criteria for DNS grids in Ref. [115], the $\Delta x^+ \approx 25$ value used for ILES runs is slightly higher than the upper limit of $\Delta x^+ = 20$. But the Δx^+ value lies within the recommended bounds. The resulting grid sizes consisted of ≈ 90 million grid points in case of SU2 and 246.3 million grid points in case of HOPS. The grid details for all the three runs are summarized in Table 2.3.

Table 2.3. Grid details for Case 1.

Case	Grid points ($N_x \times N_y \times N_z$)	Domain Width	Grid spacings ($\Delta x^+, \Delta z^+$)	Total points
SU2	$1669 \times 289 \times 181$	0.03 m	25, 23.6	90×10^6
HOPS	$1669 \times 289 \times 501$	0.03 m	25, 8.5	246.3×10^6
OVERFLOW	$1669 \times 289 \times 321$	0.0508 m	25, 22.5	160×10^6

For the DDES calculations in OVERFLOW, a boundary layer profile computed from a two-dimensional RANS computation was imposed at the inlet. The momentum thickness was matched with the corresponding experimental value. No-slip isothermal condition was set on the walls and flow properties were extrapolated on the upper surface and the outlet. Sponge layers at the domain exit and the top boundary prevented spurious wave reflections. A converged steady state RANS solution was used as the initial condition for DDES calculations. The improved Harten, Lax, van Leer, and Einfeldt (HLLE++) upwind scheme was used with successive symmetric overrelaxation (SSOR) [116], [117]. Third-order spatial accuracy achieved with Monotone Upstream Centered Schemes for Conservation Laws (MUSCL) approach [118]. The S-A turbulence model was implemented and the time-stepping was carried out with second-order accuracy. Based on a time-resolution study, a time-step of $\Delta t = 0.25 \mu\text{s}$ with three sub-iterations was chosen. The calculations in OVERFLOW were run for a physical time of 0.5 s, or a total of 2×10^6 iterations.

The DDES calculations in SU2 were set up in a similar manner, with the exception that the Jameson-Schmidt-Turkel scheme [119] was used to discretize the spatial derivatives, with second-order spatial accuracy. The addition of a blend of second-order and fourth-order artificial dissipation ensured monotonicity in the vicinity of shocks. The shear-layer adapted SGS model suggested by Shur et al. [120] was used to alleviate the difficulty encountered by DES methods in capturing the initial region of mixing layer development. They proposed a new sub-grid length-scale called the Shear-Layer Adapted (SLA) scale that takes into account the anisotropy of grid cells in the vicinity of shear-layer inception. A dual time-stepping strategy [121], [122] with 20 sub-iterations was used to achieve second-order accuracy in time, with a time-step similar to the one used for OVERFLOW calculations ($\Delta t = 0.25 \mu\text{s}$.) Based on the time-resolution study carried out by Leger et al. [28], a physical run-time of 0.05 s was sufficient to achieve convergence in a statistical sense. The available computational resources allowed for a physical run-time of ≈ 0.042 s (169596 iterations) for DDES calculations in SU2, which is close to the target value of 0.05 s.

For the ILES calculations in HOPS, the boundary layer profile corresponding to a two-dimensional RANS calculation is imposed at the inlet, and turbulence was allowed to evolve naturally until the separation point. The spatial derivatives were computed using a sixth-

order compact difference scheme described in Sec. 2.2. The scheme was dropped to fifth- and fourth-order towards the boundaries. In the vicinity of a shock, the discretization switches to a second-order Roe scheme with the continuous limiter of Anderson et al. [118] defined as,

$$s = \frac{2\Delta_+\Delta_- + \epsilon}{\Delta_+^2 + \Delta_-^2 + \epsilon} \quad (2.22)$$

where $\Delta_+ = f_{i+1} - f_i$, $\Delta_- = f_i - f_{i-1}$, f_i is a conserved variable, and $\epsilon = 10^{-12}$ is an arbitrary small value to prevent singularities. In order to introduce dissipation at small scales, a Padé-type, non-dispersive filter elaborated in Sec. 2.3.4, with the shock capturing scheme of Visbal and Gaitonde [96] was used. A second-order implicit Euler scheme was used for time integration with quasi-Newton sub-iterations. Additional details are provided in Ref. [123]. The calculations in HOPS were run for a physical time of ≈ 5 ms (2880600 iterations.)

Table 2.4. Time-stepping details for Case 1.

Case	Run-time	Time-step	Sampling rate(s)
SU2	0.042 s	0.25×10^{-6} s	4 MHz
HOPS	0.005 s	1.72×10^{-9} s	572 MHz 2.86 MHz
OVERFLOW	0.5 s	0.25×10^{-6} s	4 MHz 0.4 MHz

The numbers in the table denote the number of iterations between consecutive samples data. The highest sampling rate for SU2 and OVERFLOW is $f_s = 4$ MHz. The undersampled rate for the OVERFLOW run is $f_s = 400$ kHz. In case of HOPS, the highest sampling rate and the undersampled rates are $f_s = 572$ MHz and 2.86 MHz, respectively. A table summarizing the time-step, sampling rate (both the higher and lower values), and the physical run-time is shown in Table 2.4. The details of locations of data extraction for all the cases are summarized in Table 2.6.

2.4.2 Case 2: Compression Ramp Flow With Sidewalls

The results for Case 2 were obtained from data analysis of ILES calculations carried out by Poggie and Porter [65], using the HOPS code (this computation was made possible by the DoE INCITE program at the Argonne Leadership Computing Facility; additional calculations and postprocessing were carried out at the AFRL DoD Supercomputing Resource Center.) The compressible Navier-Stokes equations were solved under the assumption of thermally and calorically perfect gas.

Table 2.5. Flow conditions for Case 2.

Parameter	Value
U_∞	588 m/s
M_∞	2.25
T_∞	170 K
T_w	323 K
p_∞	2.383×10^4 Pa
δ_0	6.096×10^{-4} m

A second-order implicit Euler scheme was used for time integration with quasi-Newton sub-iterations. A sixth-order compact differencing scheme described briefly in Sec. 2.2 was used for spatial discretization of internal points, which was dropped to fifth- and fourth-order for points nearest to the boundaries. A Padé-type, non-dispersive filter was used to ensure numerical stability (see Sec. 2.3.4.) A shock capturing routine based on the approach of Visbal and Gaitonde [96] was implemented, which is elaborated in that same section. For cells in the vicinity of the shock, a third-order upwind Roe scheme with a continuous limiter of Anderson et al. [118] shown in Eq. (2.22) was used. The spatial discretization switches back to the original compact scheme away from the shock. Additional details of the numerical schemes are presented in Refs. [65], [83]. No sub-grid turbulence model was implemented, but instead any unresolved scales were eliminated by the filter. More information about the details of the discretization schemes used in the HOPS code can be found in the papers by Poggie et al. [17], [83].

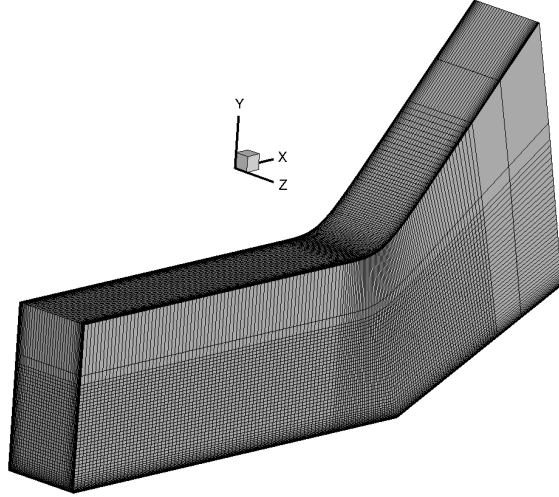


Figure 2.5. Computational grid; every 32nd point shown for clarity.

The computational mesh is shown in Fig 2.5. Its streamwise extent is $X = x/\delta_o = 130$, where δ_o is the boundary layer thickness at $X = 80$. The ramp begins at $X = 100$ and is inclined at 24 deg. The spanwise width of the domain is $Z = z/\delta_o = 20$. The grid consisted of $4711 \times 1420 \times 1401$ points in the x , y , and z directions respectively, totalling approximately to 9.4×10^9 cells. The corresponding grid spacing in wall units is $\Delta x^+ = 7.9$, $\Delta y^+ = 0.51$, and $\Delta z^+ = 0.51$. The grid was gradually stretched away from the floor and sidewalls towards the top boundary and center of the domain. At the inlet, a boundary-layer profile corresponding to the laminar-flow similarity solution for Mach 2.25 flow was imposed. The flow properties were extrapolated at the end and top of the domain.

Transition to turbulence was achieved by means of an artificial body-force implemented on the floor (at $X = 2.5, Y = 0$) and sidewalls (at $X = 2.5, Z = 0, 20$). On the floor, the trip was uniform along the span and was set to zero close to the corners. The body-force consisted of both streamwise and wall-normal components. It was oriented in the upstream direction, with a larger magnitude than the wall-normal component. The body-force on the sidewalls was composed of streamwise and spanwise components, oriented in the upstream direction. The spanwise component was reversed on the sidewall at $Z = 20$.

The mathematical expressions for implementation of the artificial trip model can be found in Ref. [65].

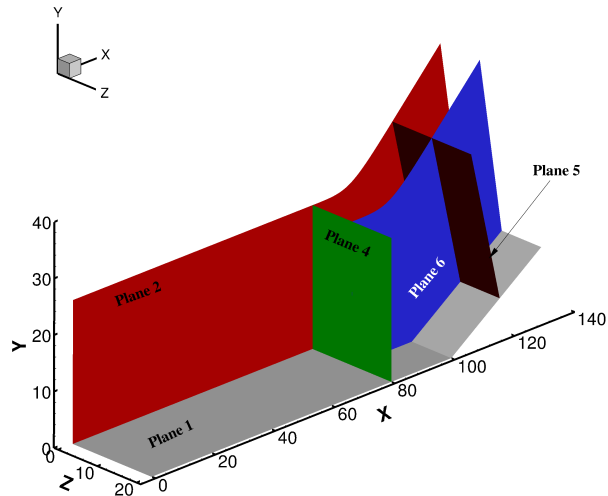


Figure 2.6. Sampled planes (near surface omitted).

The calculations were run for 2.39×10^5 iterations with a non-dimensional time step of $U_\infty t / \delta_0 = 5 \times 10^{-3}$. This corresponds to an overall simulation time of $U_\infty t / \delta_0 = 1195$. The calculation was initially run for about two flow-through times to establish a statistically steady state. The flow data were then saved for about seven flow-through times. The data were extracted at six different planes (see Fig. 2.6): the three no-slip walls (Planes 1–3), the $X = 80$ plane (Plane 4), the ramp-normal plane at $X \approx 116$ (Plane 5), and the portion of the centerplane ($Z = 10$) downstream of $X = 80$ (Plane 6). These planes were saved every 200 iterations which corresponds to a sampling frequency of $f_s \approx 965$ kHz. The total duration of the data set corresponds to about 5.3 cycles of the low-frequency shock motion and breathing of the separation bubble ($St \approx 0.03$) and about 50–60 cycles of the shear layer flapping and low-mid oscillations of the separation bubble ($St \approx 0.1$) and Kelvin-Helmholtz vortex shedding ($St \approx 0.5$.) The authors acknowledge that the integration time limits the analysis of the low-frequency events, but assert that those in the mid-frequency range are time-resolved.

2.5 Data Analysis

2.5.1 Statistical Methods

Statistical estimates of space-time correlations and two-point correlations were used to analyze the data. Their respective expressions are given in Eq. (2.23) and (2.24) respectively.

$$R_{\alpha\beta}(x, y, \tau) = \frac{\overline{\alpha(x, y, t)\beta(x + r_x, y + r_y, t + \tau)}}{\sigma_\alpha\sigma_\beta} \quad (2.23)$$

$$R_{\alpha\beta}(x, y) = \frac{\overline{\alpha(x, y, t)\beta(x + r_x, y + r_y, t)}}{\sigma_\alpha\sigma_\beta} \quad (2.24)$$

In the above equations, $R_{\alpha\beta}$ is the estimate of correlation magnitude between two time histories $\alpha(t)$ and $\beta(t)$, with an RMS value of σ_α and σ_β respectively. Conditional averages of flow properties based on a reference quantity were also carried out. The data were segregated into bins, each representing a physically meaningful event. For a given number of samples \mathcal{N} , the conditional average of a flow quantity Φ was calculated using Eq. (2.25).

$$\langle \Phi \rangle = \frac{1}{\mathcal{N}} \sum_{i=1}^{\mathcal{N}} \Phi_i(\mathbf{x}) \quad (2.25)$$

Spectral characteristics of turbulence were examined by calculating the power spectral density. The auto-spectral and cross-spectral densities were calculated using Eqs. (2.26a) and (2.26b) shown below [124].

$$S_{\alpha\alpha}(f) = \int_{-\infty}^{\infty} R_{\alpha\alpha}(\tau) e^{-i2\pi f\tau} d\tau \quad (2.26a)$$

$$S_{\alpha\beta}(f) = \int_{-\infty}^{\infty} R_{\alpha\beta}(\tau) e^{-i2\pi f\tau} d\tau \quad (2.26b)$$

To determine the degree of linear correlation at a given frequency between the signals $\alpha(t)$ and $\beta(t)$, the coherence magnitude ($\gamma_{\alpha\beta}^2$) between the two was calculated using Eq. (2.27),

$$\gamma_{\alpha\beta}^2(f) = \frac{S_{\alpha\beta}(f)S_{\alpha\beta}^*(f)}{S_{\alpha\alpha}(f)S_{\beta\beta}(f)} \quad (2.27)$$

where $S_{\alpha\alpha}, S_{\beta\beta}$ are the auto-spectral densities of the signals $\alpha(t)$ and $\beta(t)$, and $S_{\alpha\beta}, S_{\alpha\beta}^*$ are the respective cross-spectral densities with the superscript $*$ denoting a complex conjugate. The statistical estimates mentioned above, with the exception of conditional averages in Eq. (2.25), were calculated using the process of segment averaging. The individual samples were extracted by using a Hanning window to create an ensemble. The spectral density estimates were calculated using Welch’s method with 50% overlap between each segment. The segment lengths were long enough to resolve the lowest frequency f_l and were an integer multiple of $2^k, k \in \mathcal{I}$ for efficient execution of the FFT algorithm. Depending on the sampling frequency, the window segment size $N_w = \max(f_s/f_l, 2^k)$.

Filtering of signals was carried using the Butterworth filter in MATLAB. For Case 1, the mean reattachment location was calculated using a metric called reverse flow intermittency (γ .) This metric measures the amount of time the flow is travelling upstream, as a fraction of total time. The location at which $\gamma \approx 0.5$ is typically considered to be where the flow reattaches. This is especially useful when the instantaneous flowfield is characterized by multiple zones of separation. Case 2 is characterized by an open separation bubble at the centerline wherein the fluid does not recirculate upstream as observed in conventional 2D interactions. Hence the mean reattachment location in this case was determined by monitoring the sign of the skin-friction coefficient.

2.5.2 Dynamic Mode Decomposition

In addition to statistical analysis, Dynamic Mode Decomposition (DMD) [125], [126] is used to analyze the flowfields corresponding to both the cases. DMD is a process which finds the best linear operator that acts as a map between two flowfields at different instances in time. The eigenvalues and eigenvectors of this linear operator are used to compute the DMD modes. The resulting modes obtained from this technique occur as complex conjugates. Each mode is associated with a discrete value of frequency, which occurs as the imaginary part of the eigenvalue. This technique has been successfully used, for example, to analyze the unsteadiness in SBLIs by Grilli et al. [10], Nichols et al. [11], Pirozzoli et al. [127], Pasquariello et al. [128], and Statnikov et al. [129].

In order to determine the modes that have a significant influence on the flowfield, the Sparisity-Promoting DMD (SPDMD) algorithm formulated by [130] is used. A brief description of the procedure is described in this section. The snapshots of data are arranged such that each column of the matrix corresponds to the flowfield at a particular instant in time, as shown below,

$$\begin{aligned} X &= [x(t_1) \quad x(t_2) \quad \cdots \quad x(t_m)] \in \mathcal{R}^{n \times m} \\ Y &= [x(t_2) \quad x(t_3) \quad \cdots \quad x(t_{m+1})] \in \mathcal{R}^{n \times m} \end{aligned} \quad (2.28)$$

where n and m are the number of data-points and snapshots, respectively. The relationship between flowfields at instants with a constant time displacement is approximated by a linear operator A as follows,

$$Y = AX \implies A = YX^+ \quad (2.29)$$

where X^+ denotes the Moore-Penrose pseudo-inverse of the matrix X . The DMD eigenvalues and modes are determined from the eigendecomposition of matrix A . A low-rank approximation for the matrix A is obtained by performing reduced SVD (Singular Value Decomposition) on X , i.e. $X = U\Sigma V^T$, where the superscript T denotes the transpose. This approximation is represented as follows,

$$\tilde{A} = U^T A U \quad (2.30)$$

which can be interpreted as the projection of A onto the implicit POD basis contained in U . Substituting $A = YX^+$ and $X^+ = V\Sigma^{-1}U^T$ in the above equation, the approximation for the linear operator reduces to,

$$\tilde{A} = U^T Y V \Sigma^{-1} \in \mathcal{R}^{r \times r} \quad (2.31)$$

where r is the rank of \tilde{A} . The i^{th} DMD mode $\psi_i \in \mathcal{C}^n$ following the eigendecomposition of \tilde{A} , i.e. $\tilde{A}\phi_i = \lambda_i\phi_i$ is calculated as,

$$\psi_i = U\phi_i \quad (2.32)$$

where $\phi_i \in \mathcal{C}^n$, λ_i are the i^{th} eigenvector and eigenvalue of \tilde{A} , respectively. The numerical snapshots $x(t) \equiv x_t$ can be expressed as a linear combination of DMD modes in the r -dimensional subspace as,

$$x_t \approx \psi_t = \sum_{i=1}^r \phi_i \lambda_i^t \alpha_i, \quad t = k\Delta t; \quad k \in \{0, 1, \dots, m-1\} \quad (2.33)$$

and in matrix form as,

$$X \approx \underbrace{\begin{bmatrix} \psi_0 & \psi_1 & \dots & \psi_r \end{bmatrix}}_{\Psi} = \underbrace{\begin{bmatrix} \phi_0 & \phi_1 & \dots & \phi_r \end{bmatrix}}_{\Phi} \underbrace{\begin{bmatrix} \alpha_1 & & & \\ & \alpha_2 & & \\ & & \ddots & \\ & & & \alpha_r \end{bmatrix}}_{D_\alpha} \underbrace{\begin{bmatrix} 1 & \lambda_1 & \dots & \lambda_1^m \\ 1 & \lambda_2 & \dots & \lambda_2^m \\ \vdots & \vdots & \ddots & \vdots \\ 1 & \lambda_r & \dots & \lambda_r^m \end{bmatrix}}_{V_{and}}. \quad (2.34)$$

In the equation above, D_α is a diagonal matrix of the modal amplitudes, which are indicative of the influence of a mode on the approximation of a flowfield as given by the expression in Eq. (2.33). The Vandermonde matrix V_{and} consists of r complex eigenvalues of \tilde{A} that determine the temporal evolution of the modes and encode their frequency and growth/decay rates. For each mode, they are obtained by examining the imaginary and real component of λ_j , where

$$\mu_j = \frac{1}{\Delta t} \log(\lambda_j), \quad j = 1, r \quad (2.35)$$

The unknown amplitudes α_i ; $i = 1, r$ are determined by solving the following optimization problem,

$$\underset{\alpha}{\text{minimize}} \quad \|X - \Phi D_\alpha V_{and}\|_F^2 \quad (2.36)$$

where $\|\cdot\|_F$ denotes the Frobenius norm and the resulting amplitudes $\alpha_{i,opt}$ optimally approximate the entire dataset. In order to determine the optimal subset of the DMD modes, the SPDMD algorithm entails solving a convex optimization problem by inducing sparsity

via a penalty term, which is the l_1 norm of the vector α_i . The corresponding expression is shown in the equation below,

$$\underset{\alpha}{\text{minimize}} \|X - \Phi D_\alpha V_{and}\|_F^2 + \gamma \sum_{i=1}^r |\alpha_i| \quad (2.37)$$

where γ is a positive regularization parameter. Larger values of γ encourage sparser solutions from Eq. (2.37), while for $\gamma = 0$, the conventional optimization problem in Eq. (2.36) is recovered.

The subset of dynamically significant modes extracted by the SPDMD algorithm was chosen such that it captured frequencies within all the three bands. For a particular mode, only the oscillatory part is reconstructed by following the process described in [11] and [128]. For a non-linear statistically stationary system, the growth rate tends to zero in the limit of infinitely many snapshots [127]. Therefore, the effect of the oscillatory part of a DMD mode on the mean flowfield can be determined using the expression shown in Eq. (2.38),

$$f(\mathbf{x}, t) = \bar{f}(\mathbf{x}) + a_f \text{Re} \left[\alpha_{i,opt} \widetilde{f}_i(\mathbf{x}) \exp(j\omega_i t) \right] \quad (2.38)$$

where $j = \sqrt{-1}$, a_f is a suitable amplification factor, $\bar{f}(\mathbf{x})$, $\widetilde{f}_i(\mathbf{x})$ represent the mean and the i^{th} spatial mode respectively, and ω_i is the associated frequency. The oscillatory modes mentioned previously appear in complex conjugate pairs. Hence the contribution of the complex conjugate portion of a particular oscillatory mode is incorporated in the amplification factor a_f . The reconstructed modes were evaluated at discrete time values: $t_k = k\pi/16$; $k = 0, 1, \dots, 31$.

Table 2.6. Locations of data extraction for Case 1.

Location	OVERFLOW	HOPS	SU2
Spanwise Lines			
SH1	1	1	N/A
SH2	1	1	N/A
SH3	1	1	N/A
RZ1	1	N/A	N/A
RZ2	1	N/A	N/A
Wall ($x/D = 1.07$)	N/A	1	N/A
Wall ($x/D = 2.44$)	N/A	1	N/A
Wall ($x/D = 3.81$)	N/A	1	N/A
Wall ($x/D = 5.19$)	N/A	1	N/A
Wall ($x/D = 8.35$)	N/A	1	N/A
C	1	1	N/A
D	1	1	N/A
E	1	1	N/A
F	1	N/A	N/A
G	1	N/A	N/A
H	1	N/A	N/A
Surface streamwise Lines			
Ramp + Cavity ($z/D = 0.29$)	N/A	1	N/A
Ramp + Cavity ($z/D = 0.59$)	N/A	1	N/A
Ramp + Cavity ($z/D = 0.89$)	N/A	1	N/A
Ramp ($z/D = -0.75$)	1	N/A	N/A
Ramp ($z/D = -0.5$)	1	N/A	N/A
Ramp ($z/D = -0.25$)	1	N/A	N/A
Ramp ($z/D = 0$)	1	N/A	N/A
Ramp ($z/D = 0.25$)	1	N/A	N/A
Ramp ($z/D = 0.5$)	1	N/A	N/A
Ramp ($z/D = 0.75$)	1	N/A	N/A
Planes			
Centerplane ($z/D = 0$)	10	200	1
Wall ($y/D = 0$)	N/A	200	1
Plane 1 ($x/D = 1.07$)	N/A	200	1
Plane 2 ($x/D = 2.44$)	N/A	200	1
Plane 3 ($x/D = 3.81$)	N/A	200	1
Plane 4 ($x/D = 5.19$)	N/A	200	1
Plane 5 ($x/D = 8.35$)	N/A	200	1

3. COMPRESSIBLE REATTACHING SHEAR-LAYER

In this chapter, the physics associated with a compressible reattaching shear-layer is discussed. Three different runs listed in Table 2.1 were used to perform time-resolved calculations of this flowfield. Initially, the mean and statistical quantities obtained from DDES calculations in OVERFLOW and SU2, as well as ILES calculations using HOPS are compared. This is followed by spectral analysis in the frequency and wavenumber domain, which highlights events corresponding to different time-scales and quantifies the various length-scales in the flowfield. Comparison of spectra obtained from the three runs are also shown at select locations. Finally, causality amongst these events is established using statistical estimates of correlations and coherence. Time-resolved data from DDES calculations in OVERFLOW is used for this purpose. The results of data analysis of the OVERFLOW case carried out previously by Deshpande and Poggie [131] are reproduced from [131], with permission from AIP publishing.

3.1 Flowfield structure

This section characterizes the compressible mixing layer that is formed downstream of the backward facing step. The contours of mean density are shown in Fig. 3.1. The density is non-dimensionalized by its freestream value. The mean reattachment location ($x_R/D \approx 4.69$) is highlighted by a red dashed line. The axes are scaled by the step height and the mean streamlines are included in this figure.

The flow separates at the edge of the backward-facing step resulting in a free shear-layer that turns downwards before reattaching on the ramp. The recirculation zone is characterized by a large vortex, and a smaller corner vortex is present close to the bottom of the step. The flow is aligned along the ramp surface through a reattachment shock. Notice that the reattachment shock foot is highly smeared, and composed of multiple compression waves. At the end of the ramp, the flow accelerates via an expansion fan.

The resolved Reynolds stresses are plotted in Fig. 3.2. In this figure, $\langle \rangle$ denotes the RMS of a particular quantity. Only the R_{33} component of the normal stress is shown in Fig. 3.2a, as the other two Reynolds normal stress components are qualitatively similar, but

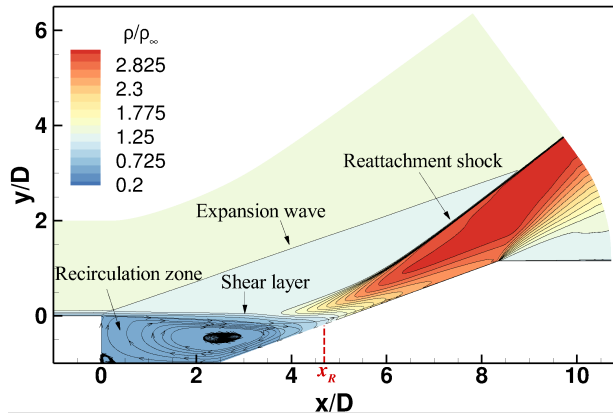


Figure 3.1. Mean density field (from OVERFLOW.) The mean reattachment location is marked at $x_R/D = 4.69$ for reference.

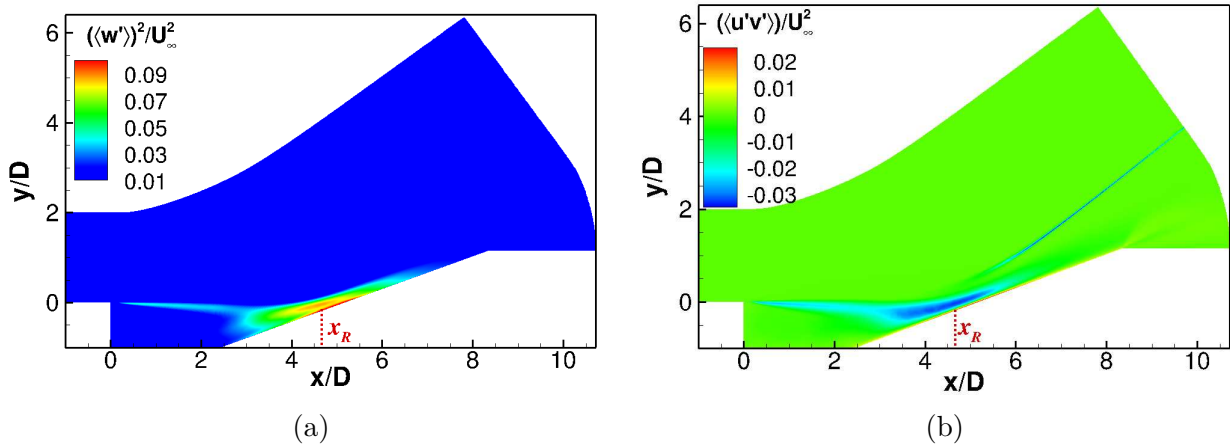


Figure 3.2. Resolved Reynolds stresses (from OVERFLOW.) (a) $R_{33} = \langle w' \rangle^2$ component (b) $R_{12} = \langle u'v' \rangle$ component. The mean reattachment location is marked at $x_R/D = 4.69$ for reference.

lower in magnitude. The peak magnitude occurs in the vicinity of the mean reattachment location for both the stress components. Their magnitudes start to increase prior to the mean reattachment location, and continue with this trend downstream. A similar observation was noted in the experiments of Hayakawa et al. [31] who attributed this behaviour to the mean dilation rate after examining the turbulent kinetic energy equation. The shear-stress component (R_{12}) shown in Fig. 3.2b has a large magnitude in the neighborhood of the mean reattachment location, which includes some part of the recirculation zone. Lower values are

observed in the remaining portion of the cavity, as well as farther downstream on the ramp in the redeveloping zone.

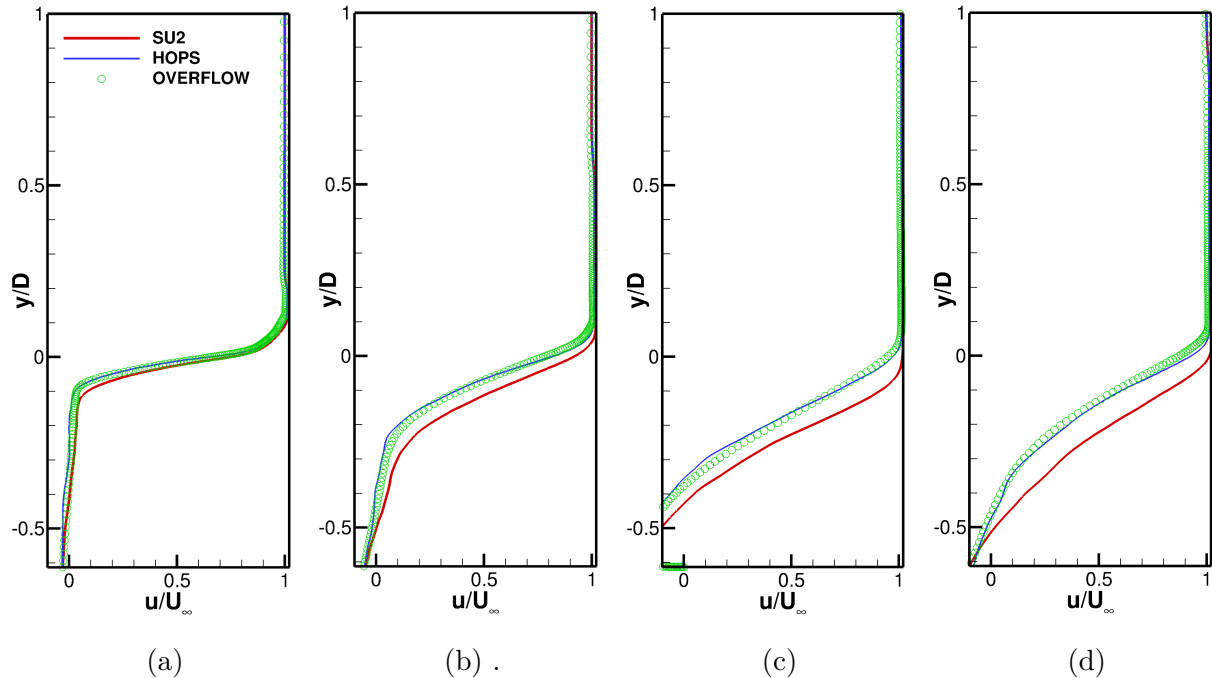


Figure 3.3. Comparison of mean velocity profiles in the shear-layer at (a) $x/D = 0.5$ (b) $x/D = 1.5$ (c) $x/D = 2.5$ (d) $x/D = 3.5$.

Figure 3.3 compares the non-dimensional streamwise velocity profiles obtained from the three runs at various streamwise locations in the shear-layer. Overall the profiles show reasonable agreement with each other. In all the cases, the velocity gradient: $\partial u/\partial y$ becomes less steep, indicating increased turbulence production downstream caused by the entrainment of external flow by the mixing layer. The velocity profile corresponding to the SU2 runs deviates from its counterparts progressively downstream. This may be a result of the difference in the numerical method or the turbulence model between SU2 and OVERFLOW, which leads to different predictions of the shear-layer spreading rate - $d\theta/dx$, where θ is the shear-layer momentum thickness.

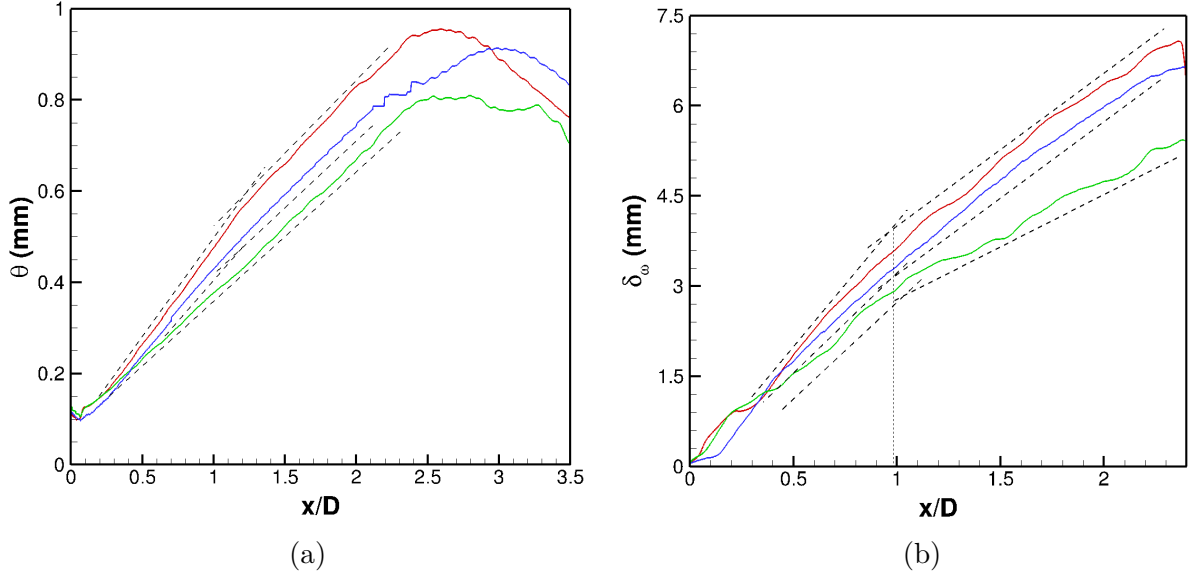


Figure 3.4. Comparison of shear-layer growth rates between SU2 (—), OVERFLOW (—), and HOPS (—) for (a) Momentum thickness (b) Vorticity thickness.

The evolution of shear-layer momentum and vorticity thickness is shown in Fig. 3.4 for all the three cases. The expressions used to calculate the momentum and vorticity thickness are shown in Eq. (3.1) [132],

$$\theta = \int_{-\infty}^{\infty} \frac{\rho}{\rho_1} U^* [1 - U^*] dy \quad (3.1)$$

$$\delta_w = \frac{U_1 - U_2}{(\partial U / \partial y)_{max}}$$

where $U^*(y) = (U(y) - U_2)/(U_1 + U_2)$, U_1, U_2 and ρ_1, ρ_2 are the freestream velocity and density values of the high-speed and low-speed side of the mixing layer, respectively. The growth rates for DDES calculations in SU2 and OVERFLOW are higher than those for the ILES calculation. All the plots follow a similar trend i.e., initial linear growth signifying merging of spanwise vortices followed by the non-linear regime where growth rate saturates and small-scale breakdown occurs. The difference in the growth rates may be a result of difference in the dissipation of the numerical method, the nature of boundary layer before separation, or some combination of both. Also, HOPS is using an ILES model, whereas SU2 and OVERFLOW include a sub-grid scale model (or may be still in RANS mode.) Bell

and Mehta [133] observed higher growth rates for tripped boundary layer as compared to untripped boundary layers. Also, it is worth mentioning that the growth rates determined from Fig. 3.4 are much larger than those of a classical mixing layer generated by a splitter plate. The increased turbulence in the recirculation zone is responsible for this behaviour [69], [134].

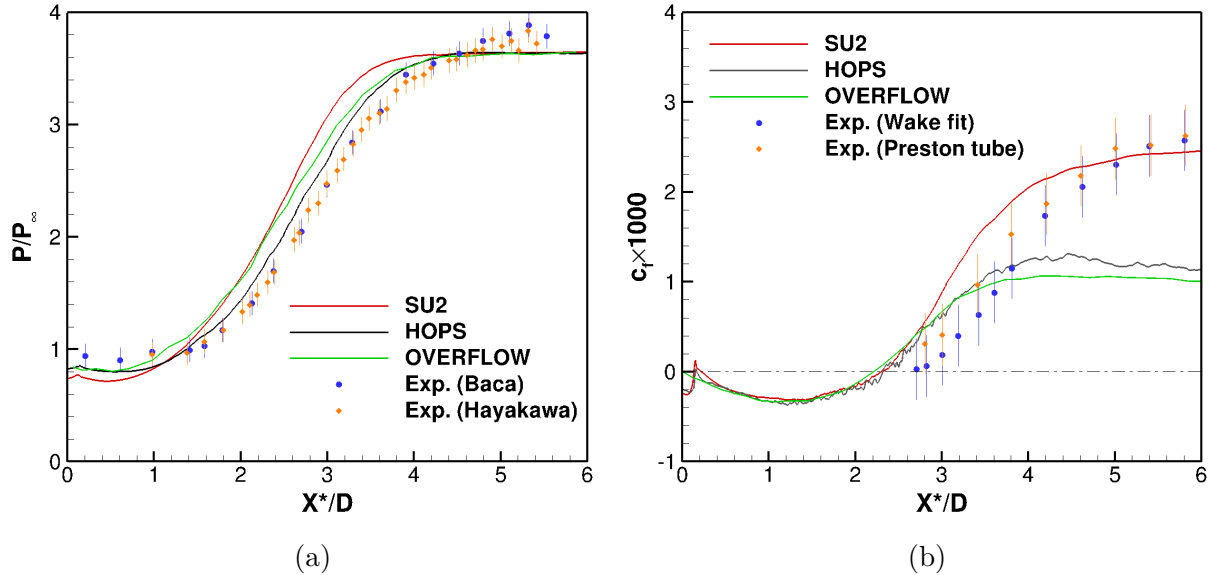


Figure 3.5. Surface quantities of (a) Wall-pressure (b) Skin-friction coefficient.

The comparison of wall-pressure and skin-friction coefficient plots between the computational results and experiments is shown in Figs 3.5a and 3.5b respectively. Error bars with an experimental uncertainty of 5% for wall-pressure for and 10% skin-friction coefficient are included in the plots. The data are plotted along the ramp surface, starting from the cavity-ramp junction (see Fig. 2.4a.) In case of wall-pressure, the computational plots agree well with experimental results. The plots corresponding to the DDES runs in SU2 and OVERFLOW show a slightly larger deviation from the experiments as compared to the ILES runs in HOPS. The plots for skin-friction coefficient corresponding to the computational results lie on top of each other prior to reattachment. Downstream of reattachment, the plots corresponding to HOPS and OVERFLOW relax to a lower value skin-friction coefficient in the recovery region. On the other hand, the plot associated with SU2 follows the trend of experimental data and shows better agreement. The difference in the skin-friction distribution

between the SU2 and HOPS case can be attributed to the approach used in sub-grid scale modeling. Similar difference between the SU2 and OVERFLOW case is most likely caused due to higher domain width and wall-spacing (Δy_w^+) on the ramp for the OVERFLOW case.

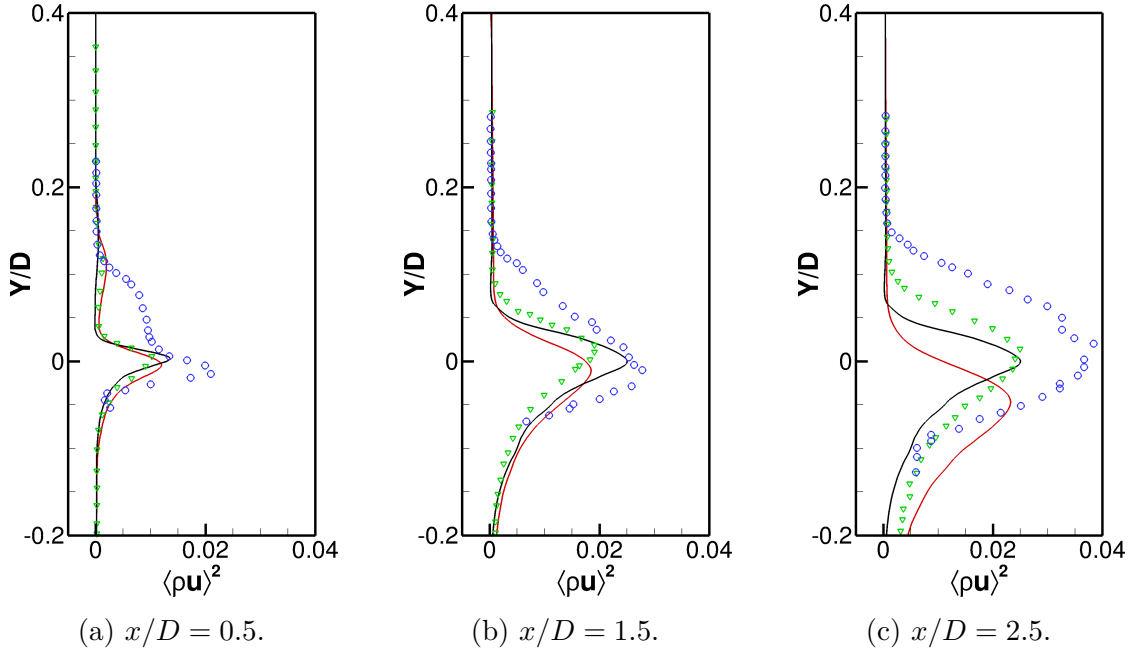


Figure 3.6. Comparison of normalized mean-squared streamwise momentum fluctuations in the shear-layer between SU2 (—), HOPS (—), OVERFLOW (∇), and experimental data (\circ) [31].

Figure 3.6 shows the comparison of mean-squared streamwise momentum fluctuations ($\langle (\rho u)' \rangle^2$), normalized by the reference streamwise momentum flux ($\rho_\infty U_\infty^2$) in the shear-layer, between computations and experimental data. The computational results display significant deviation from the experimental results at all the streamwise locations. Close to the shear-layer origin at $x/D = 0.5$, the wall-normal location of the peaks are relatively closer, though the peak values in the computations are under-predicted. Farther downstream at $x/D = 1.5$ and $x/D = 2.5$, the predicted computational peak values along with their respective wall-normal locations are different for each case. Overall, the results from OVERFLOW show better agreement with results from HOPS, as compared to the results from SU2. This may be due to the fact that OVERFLOW computations used an upwind method of high-order of accuracy (3^{rd} order) as compared to SU2, wherein the convective fluxes were discretized

using the JST scheme, which is 2^{nd} order accurate. Additionally, differences in the domain width and grid spacings (see Sec. 2.4.1) could also contribute to this result.

Figure 3.7 shows the flowfield at a specific instant in time for the all the three cases. The structures in the shear-layer and the recirculation zone are highlighted using a constant value of Q-criterion. These iso-surfaces are colored using the magnitude of non-dimensional streamwise velocity. An x - y plane at $z/D = -1$ is colored with the contours of the quantity $\vec{u} \cdot \nabla p$. This quantity is effective in highlighting regions in which a strong pressure gradient is aligned with the flow direction. An iso-surface of this quantity is used to show the reattachment shock. All the flowfields are qualitatively similar as with the structure of the shear-layer immediately downstream of the step and towards the reattachment location.

Based on the work carried out by Lasheras and Choi [135], we suggest that the mixing layer, via the Kelvin-Helmholtz instability, distributes the vorticity in the incoming boundary layer between regions of high and low vorticity. The regions of strong vorticity correspond to the spanwise coherent vortices, with residual vorticity concentrated in the braids connecting these structures. The strain field between the spanwise rollers, coupled with vortex stretching along its principal axes leads to the amplification of streamwise vorticity in the braids. As a consequence, these braids loop over the spanwise rollers, and are characterized by a counter-rotating pair of vortices.

A similar interpretation can be applied to Figs. 3.7a–3.7c. Immediately downstream of the separation point, spanwise coherent vortices are observed which persist for a short distance. Non-linear interaction between the streamwise braids and the spanwise vortices causes breakdown to yield fine scale turbulence. Note that in DDES, there is no resolved turbulence until after this breakdown. Farther downstream, structures resembling hairpin vortices are observed. It seems that many such instances of hairpin vortices are stacked together in the streamwise direction, forming superstructures akin to the ones commonly observed in the logarithmic region of the boundary layer. This observation is consistent with studies of Samimy et al. [45] and Dimotakis and Brown [44]. The reattachment shock, highlighted as a white surface, is highly corrugated along the span. On the x - y plane at $z/D = -1$, shocklets emanating from the eddies in the shear-layer can be observed. The convective Mach number for this flow is $M_c = 1.1$ (see Table 2.2), which indicates that the

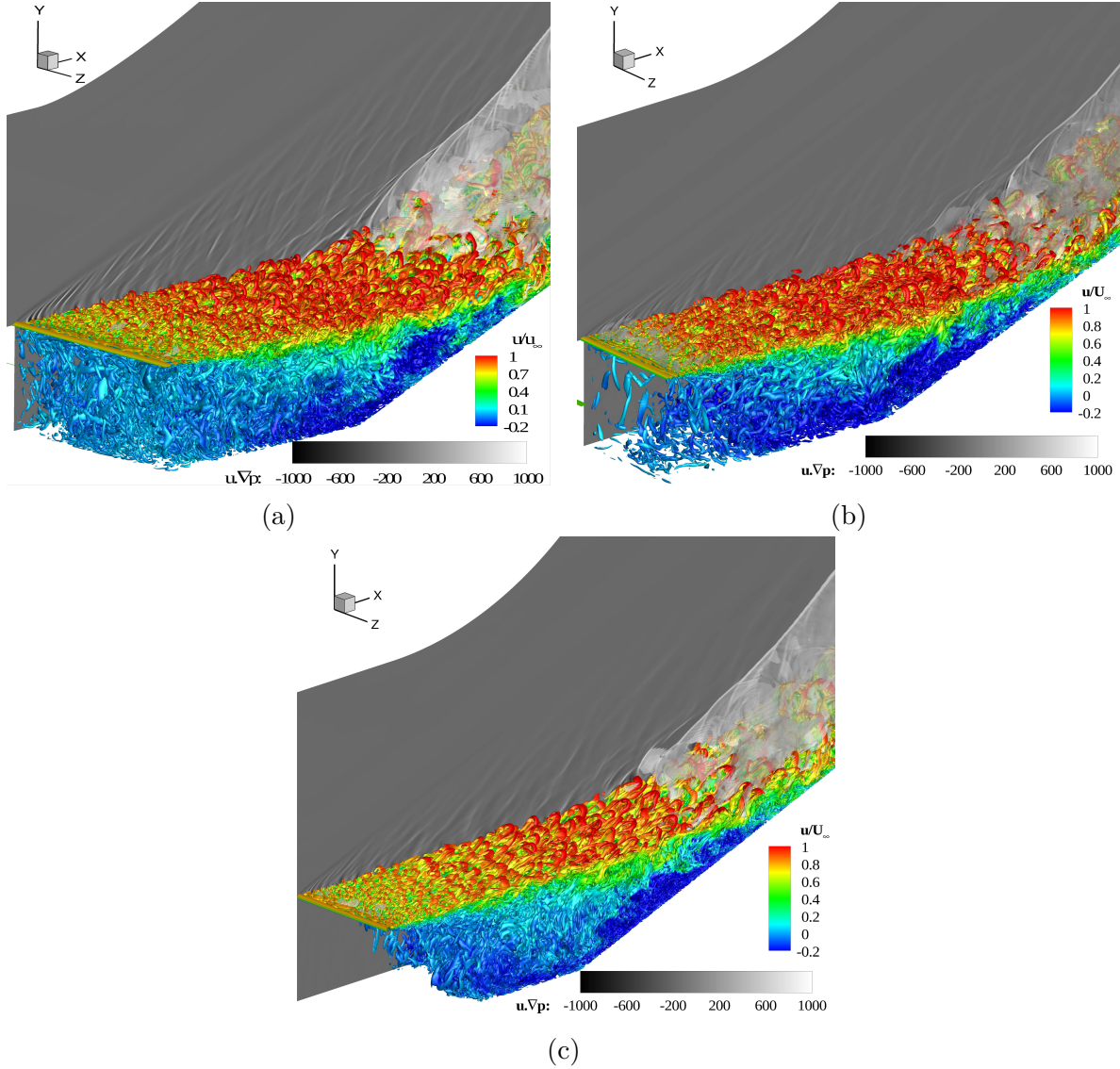


Figure 3.7. Snapshots of instantaneous flowfields for (a) OVERFLOW case (b) SU2 case (c) HOPS case.

convection velocity of large-scale structures is supersonic, leading to the observed shocklets. They have also been observed experimentally in planar laser scattering data (eg., Figs. 3 and 4 of Poggie and Smits [7]). These shocklets form a complex wave pattern which extends up to the boundary demarcated by the expansion wave at the step edge. These shocklets form a complex wave pattern which extends up to the boundary demarcated by the expansion wave at the step edge.

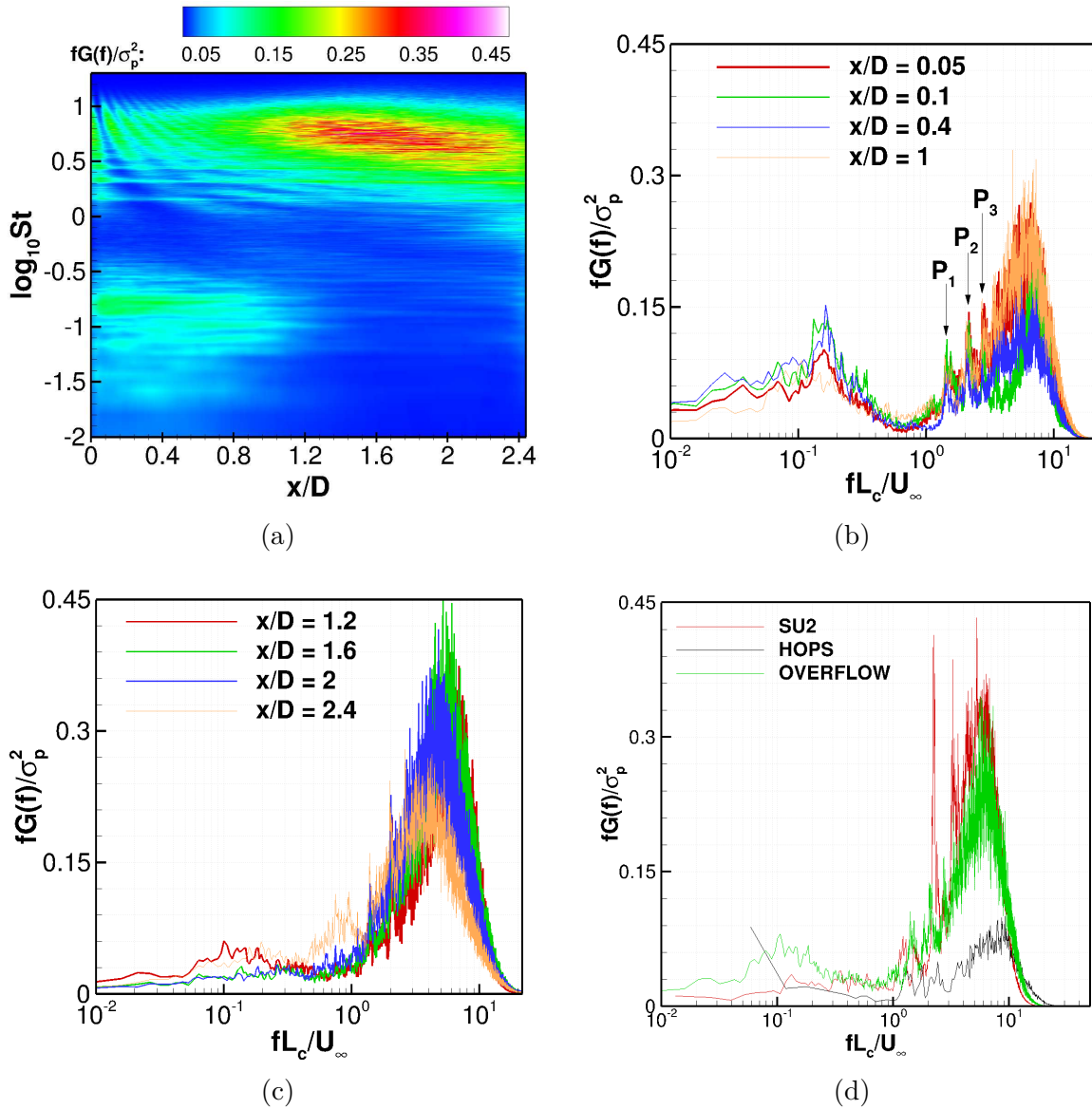
3.2 Unsteadiness of the interaction

This section elaborates the dominant time-scales in the interaction, primarily through the highly time-resolved data obtained from OVERFLOW calculations. Comparison of spectra among the OVERFLOW, SU2, and HOPS cases are shown at select locations in the domain. Before discussing the spectral characteristics, an attempt to justify the choice of length scale to non-dimensionalize frequency is made. Note that in Fig. 3.8b, all the spectra have two local maxima in nature. These results agree qualitatively with the plots obtained in the study on incompressible turbulent separation bubbles carried out by Kiya and Sasaki [37], [38] as well as Hillier and Cherry [136]. The peak at lower frequency is a signature of shear-layer flapping, whereas the peak at higher frequency represents the turbulent eddies. The second peak consists of multiple sub-peaks which may correspond to Rossiter modes. From previous studies, the flapping frequency when non-dimensionalized by reattachment length and freestream velocity, lay in the range $0.12 < fx_R/U_\infty < 0.16$. In order to be consistent with previous studies, the cavity length $L_c = 0.0619$ m was chosen as the length scale, which resulted in a Strouhal number ($St = fL_c/U_\infty$) of $St \approx 0.16$. Based on this formulation, the energy associated with flapping is concentrated at frequencies $St \leq 1$. Henceforth, the spectra are non-dimensionalized using the cavity length L_c and freestream velocity U_∞ unless mentioned otherwise.

We start with the cavity region. The corresponding data were obtained from the centerplanes sampled at $f_s = 400$ kHz. The spectra are plotted in the pre-multiplied semi-log form. The two-dimensional contour plot for the streamwise variation of pre-multiplied energy density is shown in Fig. 3.8a. In the region between $0 < x/D \leq 1.2$, there are two energy-dominant frequency bands, $0.1 \leq St \leq 0.2$ and $1.25 \leq St \leq 10$. As mentioned previously, the first band is representative of shear-layer flapping, whereas energy corresponding to turbulent eddies is present in the second band. Additionally, the cavity region seems to be characterized by events of frequency scale which are an order of magnitude lower than the first band ($0.02 \leq St \leq 0.1$). This is suggested by the relatively lower magnitude of energy present in that range. Based on previous studies on SWTBLI [4], [5], [25] frequencies

in this range most likely represent separation bubble breathing. A more detailed analysis is presented in Sec. 3.4.

A detailed view of the spectral plots at streamwise locations lying in the range $0 < x/D \leq 1.2$ is shown in Fig. 3.8b. All the plots consist of two peaks. The magnitude of the peak at lower frequency increases initially from $x/D = 0.05$ to $x/D = 0.1$, and decreases monotonically downstream of $x/D = 0.1$. Another feature that was not apparent from the contour plot is the presence of discrete local peaks within the second peak at the higher frequency. They are labeled as P_1 , P_2 , and P_3 in Fig. 3.8b. These local peaks may



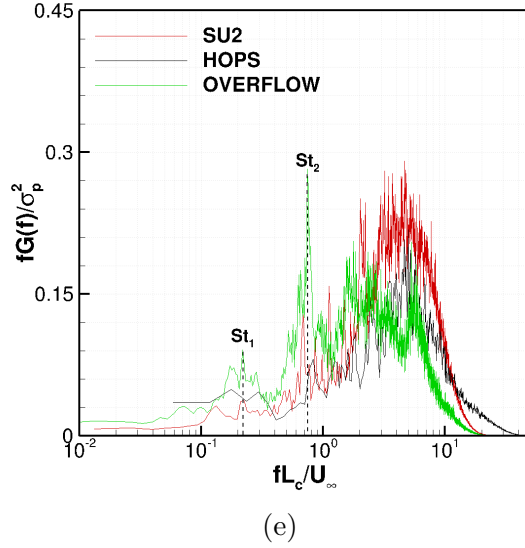


Figure 3.8. Pre-multiplied wall pressure spectra in the cavity region for the OVERFLOW case in parts (a)–(c). (a) Contour plot (b) Spectral plots in the first half of the cavity; the local peaks that may correspond to Rossiter modes are labeled as P_1 , P_2 , and P_3 (c) Spectral plots in the second half of the cavity (d) Comparison of spectra at $x/D \approx 1.07$ (e) Comparison of spectra at $x/D \approx 2.44$. For reference, the ramp starts at $x_R/D = 2.44$ and mean reattachment occurs at $x_R/D = 4.69$.

correspond to Rossiter modes [137]. A more rigorous analysis to establish this point is carried out. Rossiter developed an analytical expression to predict the resonant modes generated by flow-induced cavity oscillations in subsonic and transonic flows. This model is based on the coupling between vortex shedding at shear-layer impingement and acoustic modes in the cavity, creating a feedback loop. Heller and Bliss [138] used a modified expression in case of high-speed flows, which is shown in Eq. (3.2). The length and velocity scales in this case are L_c and U_∞ respectively.

$$St_m = \frac{f_m L_c}{U_\infty} = \frac{m - \alpha}{M_\infty / \sqrt{1 + M_\infty^2 (\gamma - 1)/2} + 1/k_v} \quad (3.2)$$

In the above equation, m is an integer representing a specific resonant mode, α , k_v are empirical constants, γ is the ratio of specific heats, and M_∞ is the freestream Mach number. In the plot at $x/D = 0.05$, there are four local peaks at $St \approx 1.50, 2.16, 2.75$, and 3.58 respectively. Based on the aspect ratio of the cavity ($L_c/D \approx 2.44 > 1$), shallow cavity behaviour

can be expected in which longitudinal standing waves may be present [139]. Assuming that these frequencies represent the resonant modes, the empirical constants calculated using Eq. (3.2) with $St_1 = 1.50$ and $St_2 = 2.16$ are $\alpha = -1.27$, $k_v = -3.82$. The frequencies of resonant modes at $m = 3$ and $m = 4$ corresponding to these empirical constants turn out to be $St_3 \approx 2.82$ and $St_4 \approx 3.48$. These values are reasonably close to the frequencies corresponding to the third and fourth local peak in the spectra at $x/D = 0.05$. A slight discrepancy occurs on account of the assumption of a purely rectangular cavity in the original theory, which is not the case in this study. The purpose of this analysis was to verify the possibility of feedback mechanism in the recirculating zone. The details of the complex acoustic wave-structure in the cavity is not discussed in this study.

Downstream of $x/D \approx 0.05$, the peaks at higher resonant modes ($m = 3, 4$) are smeared out, while the peaks at lower modes ($m = 1, 2$) persist up to $x/D \approx 1.2$. The energy associated with shear-layer flapping decreases substantially downstream of $x/D = 1.2$ as seen in Fig. 3.8c. The energy at higher frequencies increases concurrently from $x/D = 1.2$ to $x/D = 1.6$. A distinct shift of the spectra towards lower frequencies is observed downstream of $x/D = 1.6$, accompanied by reduction of the peak at higher frequencies. At $x/D = 2.4$ (close to the ramp-cavity junction), a smaller peak occurs at $St \approx 0.85$ which may correspond to the shedding of vortical structures from the recirculation zone. A similar observation was noted by Kiya and Sasaki [37] who observed that the shedding frequency was six times the shear-layer flapping frequency.

Comparison of wall-pressure spectra between the three computational cases in the cavity region is shown in Figs. 3.8d and 3.8e, respectively. The spectrum corresponding to the HOPS run was obtained by averaging over three windows with segment size of $N_w = 2^{20}$ samples, resulting in a frequency resolution of $\Delta St \approx 0.06$. The spectra corresponding to the SU2 and OVERFLOW runs were obtained by averaging over 8 and 37 windows respectively, with same segment sizes of $N_w = 2^{15}$ ($\Delta St \approx 0.013$) and $N_w = 2^{13}$ samples ($\Delta St \approx 0.0053$.) At $x/D \approx 1.07$, the wall-pressure spectra corresponding to the DDES runs in SU2 and OVERFLOW agree well for $St \geq 1$. The peaks corresponding to the Rossiter modes are more pronounced for the SU2 case. The peak corresponding to the flapping frequency for the SU2 case is not as prominent as the one in the OVERFLOW case, owing to a smaller

total run-time. The wall-pressure spectrum corresponding to the HOPS case indicates less energy in high-frequency domain. This is most likely caused due to a shorter run-time. Also, the normalization of the spectra by variance of the signal could result in lower amplitudes.

Figure 3.8e compares the spectra at $x/D \approx 2.44$, which lies at the ramp-cavity junction. The overall disagreement between the spectra persists at this location. The spectrum corresponding to the OVERFLOW run resolves more peaks in the high-frequency range ($St \leq 1$) as compared to the other two cases. The spectra corresponding to both SU2 and OVERFLOW seem to capture the peaks (highlighted as St_1 and St_2 in the figure), wherein the lower peak represents the flapping frequency and higher peak is indicative of passage of large-scale structures. The spectrum corresponding to the HOPS run fails to capture these details accurately. Again, this can be attributed to insufficient run-time.

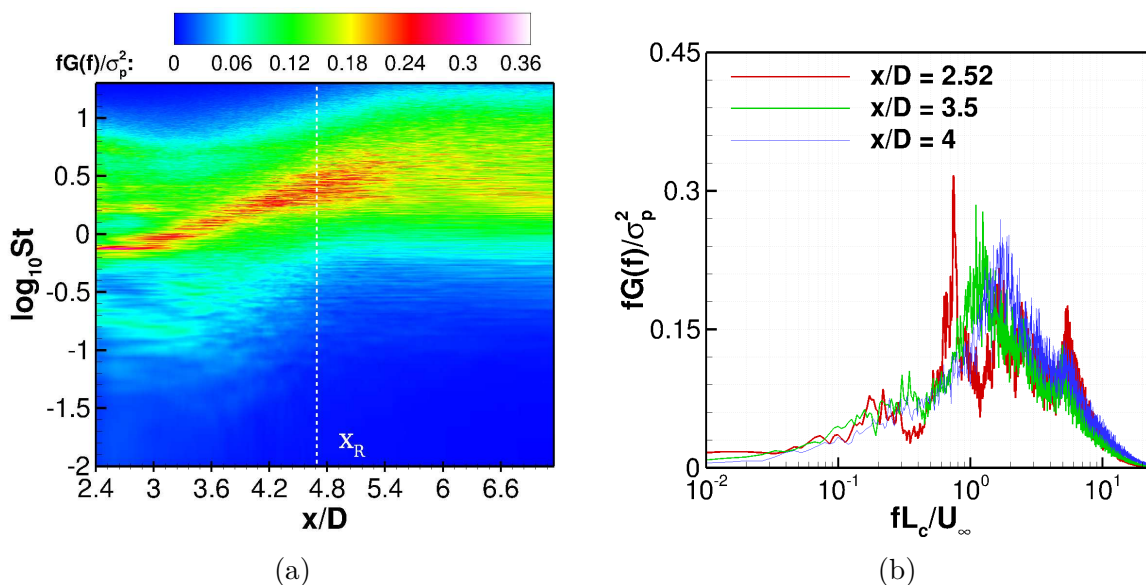
A similar exercise was carried out to examine the spectral characteristics on the ramp. Wall pressure fluctuations on the ramp surface sampled at a higher frequency ($f_s = 4$ MHz) were used for this purpose. For both the SU2 and HOPS cases, the window segment sizes (and corresponding the frequency resolutions) are consistent with the ones used to calculate the spectra shown in Figs. 3.8d and 3.8e. For the OVERFLOW case, the window segment size was increased to 2^{16} segments (averaging over 45 windows) resulting in a frequency resolution of $\Delta St \approx 0.006$. The contour plot of premultiplied spectra is shown in Fig 3.9a. In this figure, the logarithm of Strouhal number is plotted on the y -axis and non-dimensional streamwise coordinate is shown on the x -axis, with contours of the quantity $fG(f)/\sigma_p^2$. The resulting spectrum was averaged across seven spanwise locations. The mean reattachment location is indicated by a white dashed line.

The energy-dominant frequency scales over the entire ramp extent lie in the range $0.63 \leq St \leq 7.94$. At the ramp-cavity junction ($x/D = 2.41$), a significant amount of energy is also present in the band $0.1 \leq St \leq 0.31$. This region persists up to $x/D = 3.5$. In contrast to the cavity region, low-frequencies of the order $St \approx \mathcal{O}(10^{-2})$ are not dominant in this region of the flow. Most of the energy is present at frequencies $St > 0.1$. (Nonetheless, some low-frequency content is detectable.) This observation is consistent with the spectra in a SWTBLI associated with a compression ramp or an impinging SWTBLI [141], [142]. The

energy dominant low-frequencies are present only a short distance in the separation bubble, downstream of the separation line.

A detailed view of the evolution of spectra, upstream of the mean reattachment line is shown in Fig. 3.9b. Shortly downstream of the ramp-cavity junction at $x/D = 2.52$, the spectra exhibit multiple peaks. The peak at lowermost frequency is present at $St \approx 0.15$, which is close to the shear-layer flapping frequency. The peak with the highest magnitude occurs at $St \approx 0.75$, which corresponds to the vortex-shedding frequency. This frequency is approximately five times of the flapping frequency. The peaks lying above $St > 1$ ($St \approx 1.66, 2.46, 5.45$) may represent eddies of different length scales, with higher frequencies corresponding to a smaller eddy size. At $x/D = 3.5$, almost all the peaks above $St > 1$ disperse and instead, a single peak at $St \approx 1.12$ is observed.

Additionally, a peak at $St \approx 5.45$ originally present at $x/D = 2.52$ now occurs at a slightly lower frequency ($St \approx 4.97$) at this location, but with a decreased magnitude. Close to the mean reattachment ($x/D = 4$) and downstream (see Fig. 3.9c), this peak diminishes resulting in a broadband spectrum, which gradually shifts towards higher frequencies in the redeveloping region. The spectrum at $x/D = 5.21$ shows good agreement with the corresponding experimental result of Shen et al. [140]. The experimental spectrum rolls off prematurely at higher frequencies because the measured signals were band-pass filtered



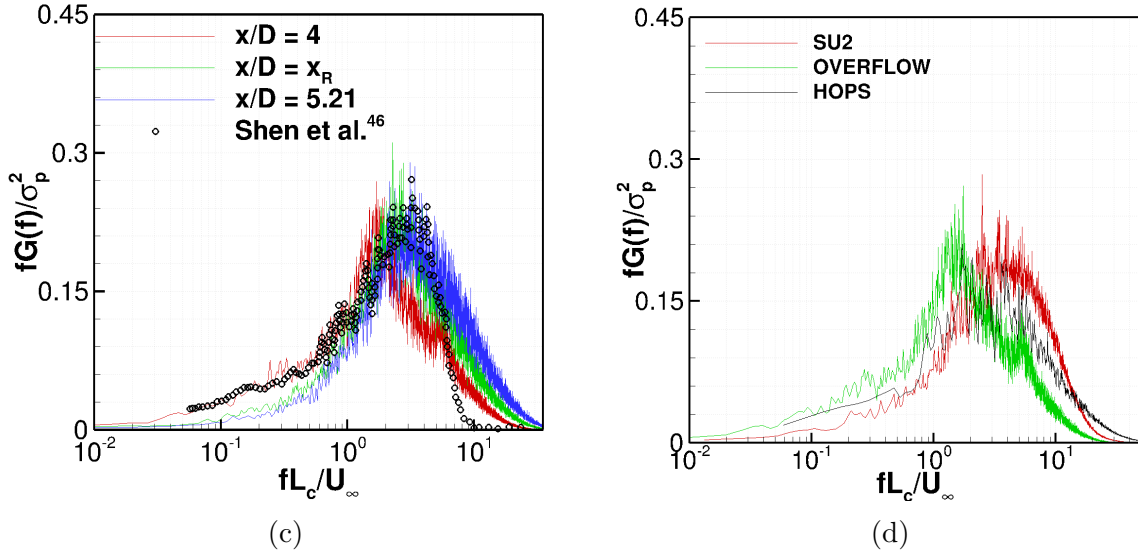


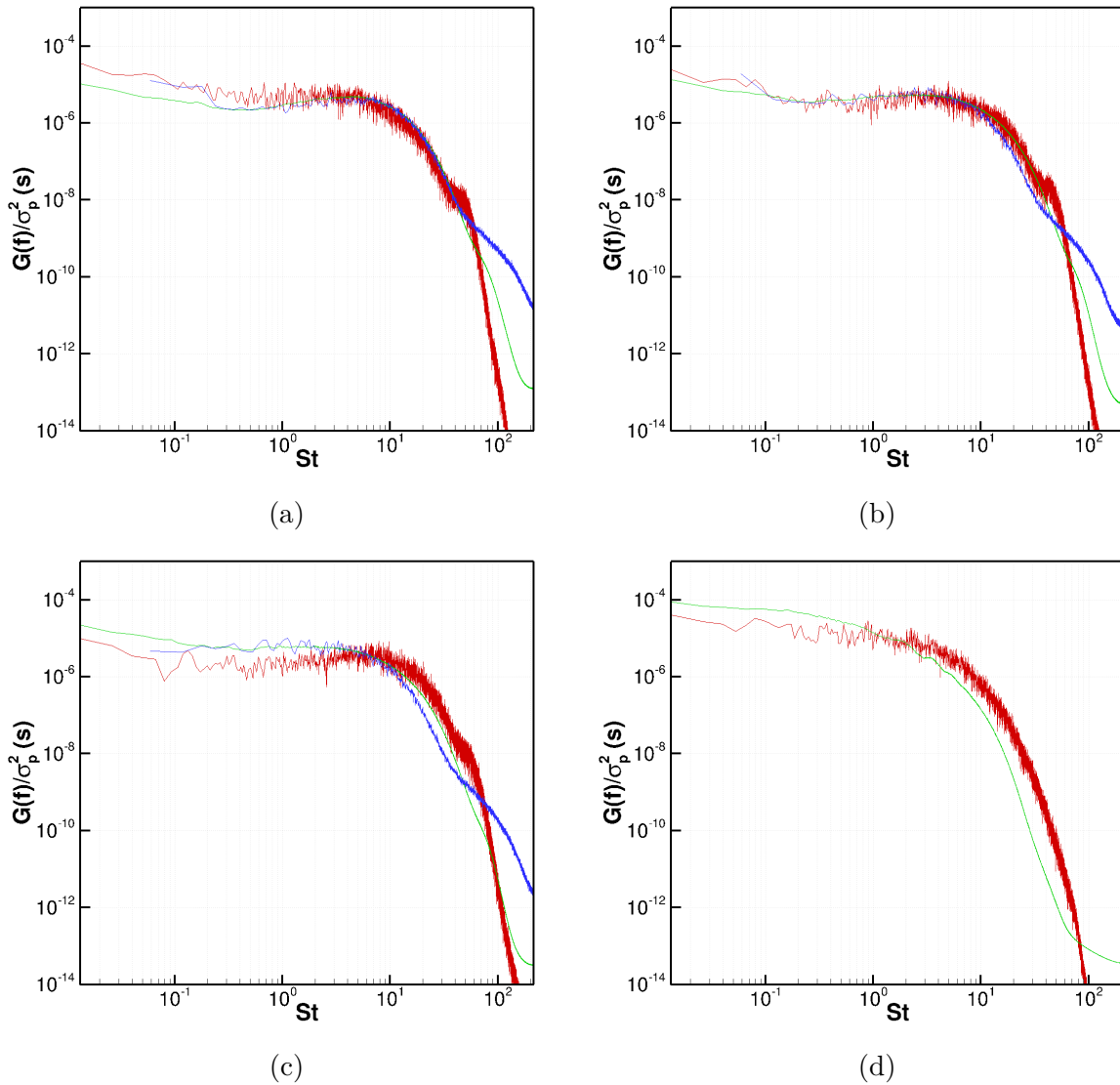
Figure 3.9. Premultiplied wall pressure spectra on the ramp for the OVERFLOW case in parts (a)–(c). (a) Contour plot (b) Spectral plots upstream of mean-reattachment (c) Spectral plots downstream of mean-reattachment (d) Comparison of spectra at $x/D \approx 3.81$. The ramp starts at $x_R/D = 2.44$ and the mean reattachment location is marked at $x_R/D = 4.69$ for reference. Symbols indicate experimental results of Shen et al. [140] at $x/D = 5.21$.

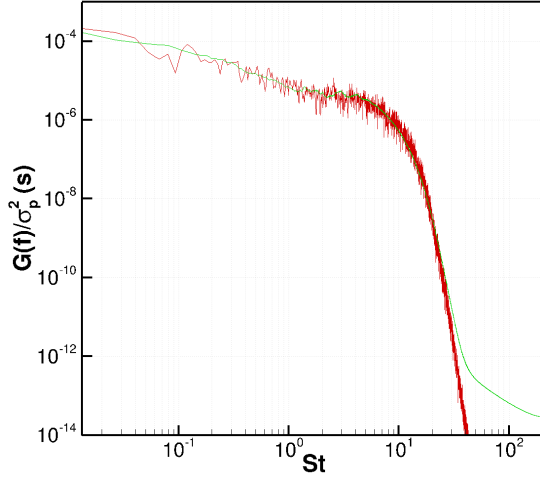
between 50 Hz and 80 kHz ($5.4 \times 10^{-3} \leq St \leq 8.66$). Figure 3.9d compares the spectra between the three runs at $x/D \approx 3.81$, which lies upstream of mean reattachment. The spectra corresponding to the HOPS and SU2 runs were averaged over the span. As with the comparison of wall-pressure spectra in the cavity region (shown in Figs. 3.8d and 3.8e), the peak amplitudes differ for each case. The spectra corresponding to HOPS and SU2 runs show reasonable agreement, but both differ from the spectrum corresponding to the OVERFLOW run. Although such disagreements were also observed by Weston et al. [143], [144], the observations noted from the comparison of wall-pressure spectra underscore the sensitivity of surface quantities on the total run-time and the SGS modelling approach.

Based on the results in this section, the flowfield seems to be characterized by large-scale structures present both in the shear-layer and recirculation zone. Evidence of shear-layer flapping was obtained from the two maxima present in the spectral plot close to the step. Based on the pressure spectra on the ramp, the effect of flapping persists up to the mean reattachment location. Also, the same spectral plot indicated a low-frequency band with

$St \approx \mathcal{O}(10^{-2})$. The rest of this chapter will focus on studying these aspects individually, as well as investigating their effect on the unsteadiness of the reattachment shock, and at the mean reattachment location.

Finally, the pressure spectra at locations within the shear-layer (SH-1, SH-2, and SH-3) and the recirculation zone (RZ-1 and RZ-2) for the three runs are compared in Fig. 3.10 (see Fig. 2.4a for details of these locations.) The spectra are plotted in log-log coordinates with the Strouhal number plotted on the x -axis and the normalized power spectral density plotted on the y -axis. The window segment sizes for all the three cases are similar to the ones used in Fig. 3.9d.





(e)

Figure 3.10. Comparison of Pressure spectra between SU2 (—), OVERFLOW (—), and HOPS (—) at (a) SH-1 (b) SH-2 (c) SH-3 (d) RZ-1 (e) RZ-2.

The number of segments corresponding to the OVERFLOW case are much larger due to the associated higher sampling frequency (see Table 2.6.) The smoothness of the spectra corresponding to the HOPS and OVERFLOW run relative to the SU2 run can be attributed to the additional spanwise averaging. Unlike the wall-pressure spectra shown in Figs. 3.8 and 3.9, good agreement amongst the spectra is obtained here. Slight mismatch at lower frequencies is present at SH-1 (in Fig. 3.10a), SH-3 (in Fig. 3.10c), and RZ-1 (in Fig. 3.10d.) But the overall roll-off to higher frequencies is captured well in all the cases. The observations suggest sufficient run-time for the SU2 case. On the other hand, the HOPS case needs a longer run-time to sufficiently resolve the frequencies lying in $St \leq 0.06$ using additional samples of data. Figures 3.10d and 3.10e do not plot the spectrum corresponding to the HOPS case as the data was not sampled at those locations (see Table 2.6.)

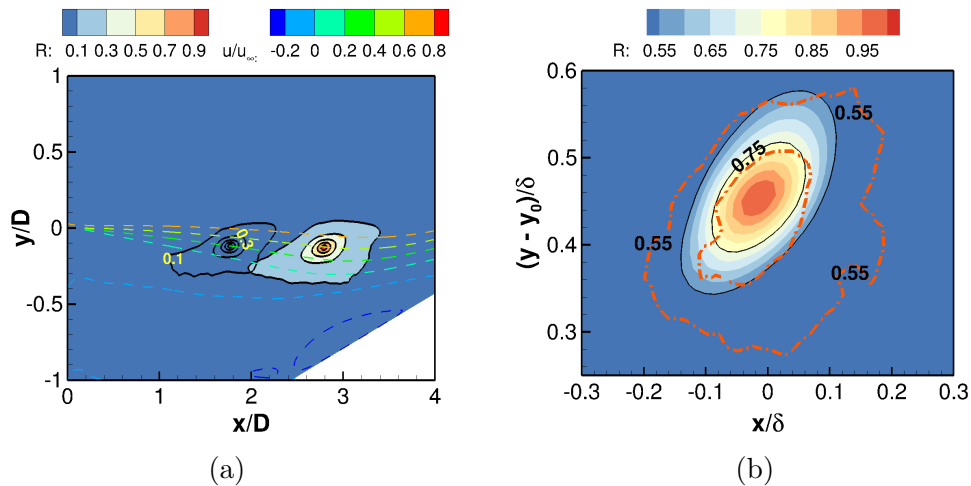
3.3 Large-scale structures

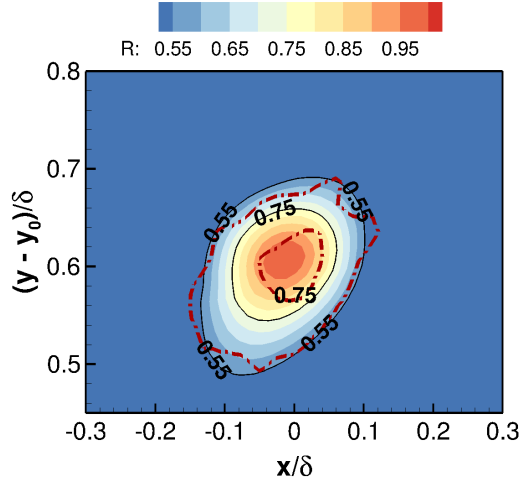
To investigate the presence of organized structures, two-point correlations corresponding to the OVERFLOW case (using the expression in Eq. (2.24)) are carried out for locations lying within the shear-layer. Time-series of streamwise velocity fluctuations are used for

this purpose. In the data presented in Fig. 3.7, the large-scale structures were observed at locations in the vicinity of the reattachment shock. Hence Sub-planes 1 to 5 (see Fig. 2.4b) were used to extract the signals, with the flow reattachment occurring in the latter. The reference points used to calculate the correlations were $(x/D, y/D)_{ref} = (1.77, -0.12)$ in Sub-plane 3 (Case I), and $(x/D, y/D)_{ref} = (2.76, -0.12)$ in Sub-plane 4 (Case II). The streamwise location of the reference points correspond to the midpoint of the sub-planes, and their respective wall-normal locations lie close to the shear-layer center. The correlation plots for the OVERFLOW case, obtained for two cases corresponding to the two reference points mentioned earlier are shown in Fig. 3.11a.

The contours of correlation for Case I are shown as solid black lines over the flooded contours of Case II. The contour levels for both the cases are similar. The first two levels ($R = 0.1$, $R = 0.3$) are labeled for Case I. The contours of non-dimensional mean u -velocity are used to highlight the shear-layer and recirculation zone. For both cases, the plots are roughly elliptical in shape and are slightly inclined within the shear-layer. A representative length scale of large-scale structures corresponding to the contour value of $R = 0.1$ was calculated. The average length scale for structures in Sub-plane 3 is approximately $10\delta_o$, where $\delta_o = 3$ mm is the boundary layer thickness in the vicinity of separation. It increases to $12\delta_o$ downstream in Sub-plane 4.

Correlations of density fluctuations with reference points $(x/D, y/D)_{ref} = (2.66, -0.012)$ and $(x/D, y/D)_{ref} = (2.66, 0.055)$ are shown in Figs. 3.11b and 3.11c, respectively. The





(c)

Figure 3.11. Two-point correlations for the OVERFLOW case on the centerplane ($z/D = 0$) using (a) Streamwise velocity fluctuations (u); colored dashed lines are contours of non-dimensional mean u -velocity. (b) Density fluctuations $(x/D, y/D)_{ref} = (2.66, -0.012)$. (c) Density fluctuations $(x/D, y/D)_{ref} = (2.66, 0.055)$. Dashed lines indicate experimental correlations obtained by Poggie and Smits [145]; y_0 is the height of zero mean velocity line and δ is the thickness of the undisturbed shear-layer at $x/D = 2.79$.

vertical axis shows the wall-normal distance from the zero mean velocity line ($y_0/D = 0.8$) at $x/D = 2.79$, and the horizontal axis plots the distance from the abscissa of the reference point. Both of these quantities are normalized by the undisturbed shear-layer thickness ($\delta/D = 0.42$) at $x/D = 2.79$. Experimental correlations obtained by Poggie and Smits [145] are included in the same figures as dashed lines. The data were obtained via planar laser scattering, and are representative of the density of scattering particles. The experimental planar laser scattering procedure records the intensity of light scattered from particles of condensate in the flow, which was then used to obtain correlations shown in Figs. 3.11b and 3.11c. Only the contour levels $R = 0.55$ and $R = 0.75$ are shown, with the latter used to calculate the length scale in experiments. Overall, the shape of experimental and computational correlations show good agreement. Scattering intensity is roughly proportional to gas density, except in regions of the flow where the temperature is high enough to vaporize the condensate [146]. Since the correlations of the computational

data are not carried out using exactly the same variable, the contour levels for computational and experimental results do not match exactly.

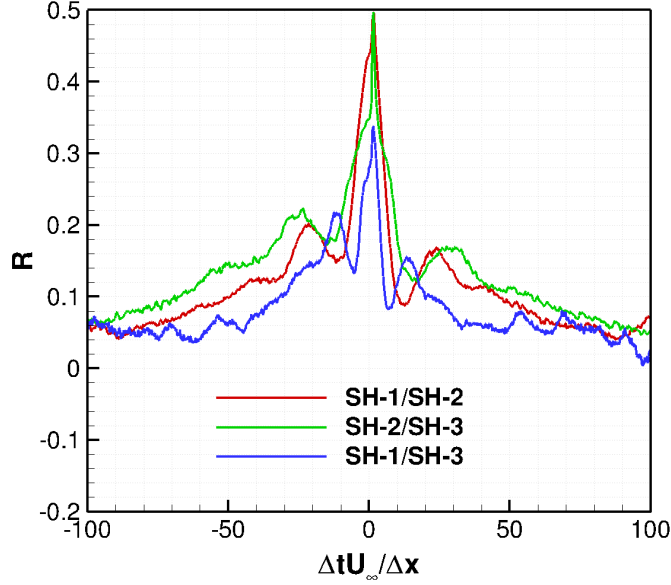


Figure 3.12. Space-time correlation of streamwise velocity fluctuations in the shear-layer for the OVERFLOW case.

Space-time correlation of streamwise velocity fluctuations for the OVERFLOW case were used to calculate the convection velocities of these structures. In the shear-layer, correlations between SH-1, SH-2, and SH-3 (see Fig. 2.4b) are plotted in Fig 3.12. The time-delay is non-dimensionalized by the distance between the location of two signals ($\Delta\mathbf{x} = \sqrt{(x - x_{ref})^2 + (y - y_{ref})^2}$) and the freestream velocity U_∞ . The reciprocal of the optimum time-delay results in the non-dimensional convection velocity ($\Delta\mathbf{x}/(\Delta t U_\infty) = U_c/U_\infty$). The signals were spanwise averaged to reduce statistical noise. The correlation plots in Fig. 3.12 show of a peak at approximately the same non-dimensional time-delay. A positive value of time-delay indicates that the event occurred first at an upstream location. The average value of the convection velocity calculated from the these plots is about $U_c \approx 0.61U_\infty$. The local mean velocity increases from $\approx 0.25U_\infty$ at SH-1 to $\approx 0.4U_\infty$ at SH-3. The smaller peaks on either side of the primary peak could be a manifestation of longer time-scale motions originating upstream/downstream of the reference point ($St \approx \mathcal{O}(10)^{-2}$) or through shear-layer flapping ($St \approx 0.12-0.16$).

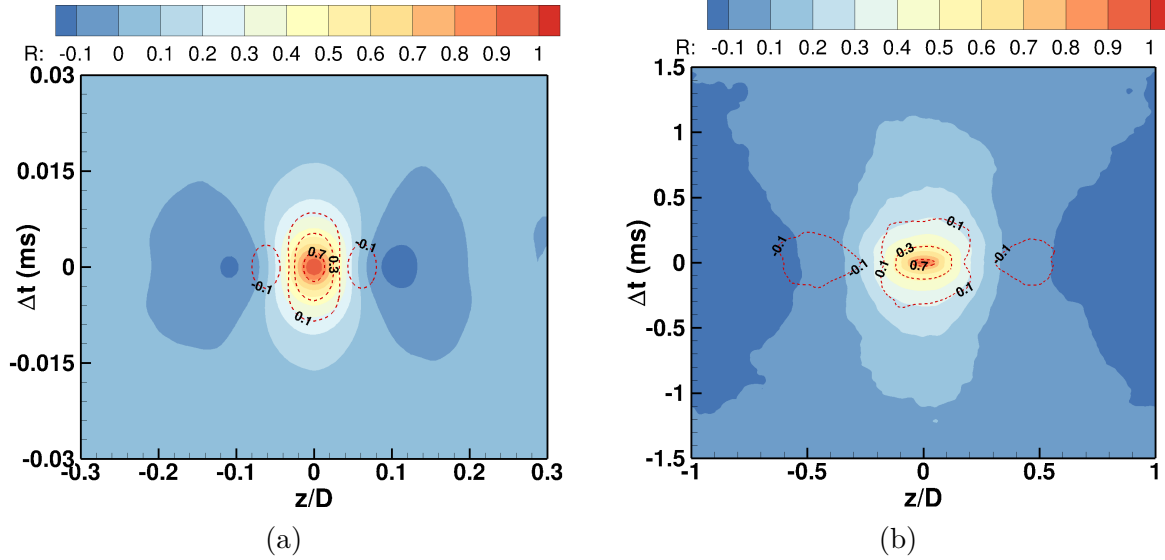


Figure 3.13. Spanwise space-time correlations for the OVERFLOW case of (a) streamwise velocity fluctuations between SH-1 (dashed red lines) and SH-3 (flooded contours) (b) RZ-1 (dashed red lines) and RZ-2 (flooded contours).

Contours of spanwise space-time correlations for the OVERFLOW case using pressure fluctuations in the shear-layer are shown in Fig. 3.13a. The reference point for these correlations lay midway on the spanwise line. The flooded contours correspond to SH-3, whereas the dashed red lines represent SH-1. The contour labels for the latter are included in the figure. The time-delay is shown in milliseconds. The contours consist of a large region of positive correlation in an elliptical shape, and smaller regions of negative correlation. These correlation plots point towards a hairpin vortex packet [147] which induces velocity fluctuations in the flow direction between the legs, and in the opposite direction on its either side. As one progresses downstream from SH-1 to SH-3, both the spanwise length scale and time-scale increase, corresponding to the growth of the mixing layer. The rise in the spanwise length scale is higher. This region of the flow is characteristic of the presence of hairpin vortices wherein the velocity induced between its legs is along the same direction and in the opposite direction on either sides [147].

The wavenumber spectra of spanwise velocity fluctuations ($E_{33}(k_z)$) within the shear-layer are shown in Fig. 3.14 in log-log coordinates. The dimensional wavenumber is plotted on the x -axis and the power spectral density is shown on the y -axis. The arrow in the figure

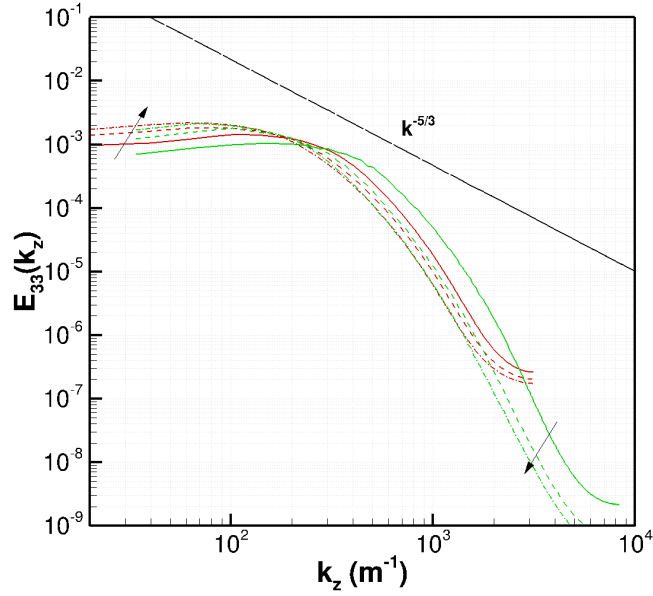


Figure 3.14. Comparison of spanwise wavenumber spectra of (a) streamwise velocity fluctuations between OVERFLOW (—) and HOPS (—) at SH-1 (—), SH-2 (---), and SH-3 (-·-). Arrow indicates the downstream direction.

points the direction while moving downstream from SH-1 to SH-3. For all the locations in the shear-layer, the wavenumber spectra corresponding to the OVERFLOW run indicates higher energy content residing within lower wavenumbers (large-scale structures.) These spectra also show signs of energy saturation as one approaches the Nyquist wavenumber. The spectra corresponding to the HOPS run resolve a wider range of wavenumbers. On traversing downstream from SH-1 to SH-3, the energy content amongst the large-scale structures increases, which is accompanied by decrease in the energy content amongst the small-scale structures. A similar trend was observed by Pirozzoli et al. [148] in the wavenumber spectra of streamwise velocity fluctuations, obtained from DNS calculations of a spatially evolving compressible mixing layer. Unlike the spanwise velocity spectra shown in that study, the spectra in this case do not follow the Kolmogorov’s inertial range scale of $-5/3$, presumably on account of strong anisotropy in the turbulent field caused by the high Reynolds number of the flow or streamwise shear-layer development.

Similar to Fig. 3.13, spanwise correlations of wall pressure fluctuations were carried out in the recirculation zone. The resulting plots are shown in Fig. 3.13b, wherein the same

unit is used for time-delay. The dashed red lines correspond to RZ-1 and the flooded contours correspond to RZ-2. Both the length and time scales increase substantially at RZ-2, which lies well within the cavity region unlike RZ-1, which lies relatively close to the shear-layer. Compared to the correlation plots in the shear-layer, larger spanwise length scales and time-scales are observed in the recirculation zone. Between RZ-1 and RZ-2, the time-scale increases substantially. The spanwise length scale at RZ-1, corresponding to the $R = 0.75$ contour level, is $l_z \approx 2.2$ mm. This agrees with the length scale derived from the same contour level of the correlation plot in Fig. 10 of [145].

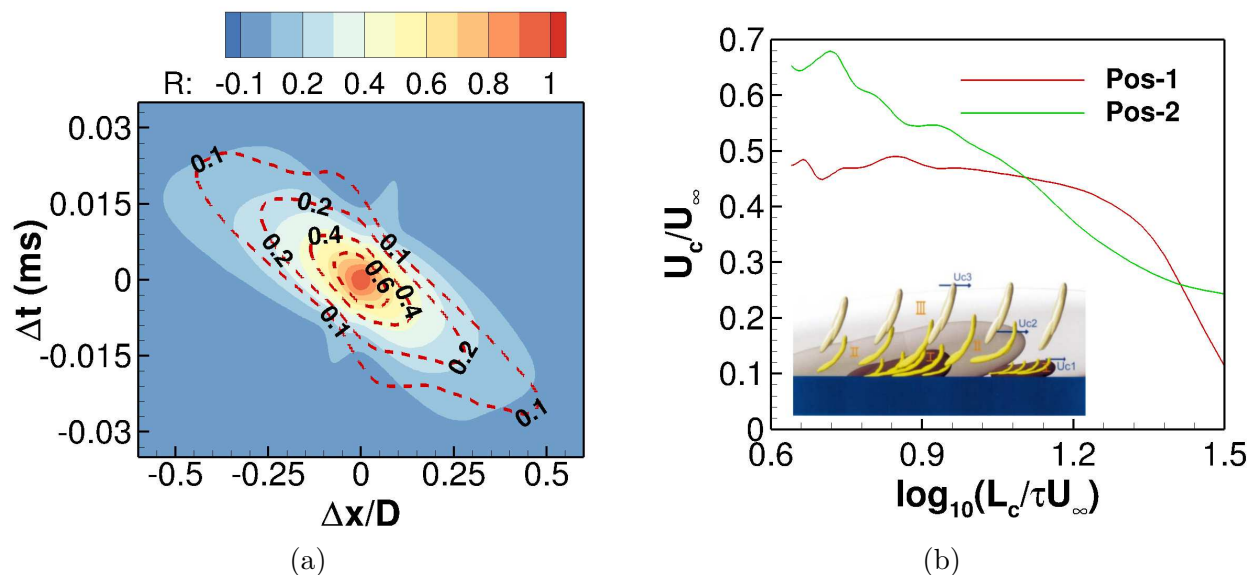


Figure 3.15. (a) Space-time correlations of wall pressure fluctuations for the OVERFLOW on the ramp at Pos-1 (flooded contours) and Pos-2 (dashed red lines). (b) Convection velocities on the ramp. (Bottom-left) Nested hairpin model [147] (Reproduced with permission from J. Fluid Mech. (2000), 422, pp.1-54. Copyright 2000 Cambridge University Press).

Using wall pressure fluctuations on the ramp, space-time correlations were carried out for the OVERFLOW case using data sampled at $f_s = 4$ MHz. The reference signal was extracted at the midpoint of each spanwise segment at Pos-1 and Pos-2 on the ramp surface, followed by spanwise averaging of the signals across the seven spanwise locations. Recall that Pos-1 and Pos-2 are streamwise lines on the ramp surface, placed at seven equidistant spanwise locations (see Fig. 2.4b.) The resulting correlations are shown in Fig. 3.15a. In

this figure, the time-delay in milliseconds is plotted on the y -axis and the distance from the reference point ($\Delta x/D = (x_{ref} - x)/D$) is shown on the x -axis. The flooded contours and the red dashed lines correspond to the correlations at Pos-1 and Pos-2 respectively. Selected contour levels are shown for the latter. The streamwise length scale is $l_x/D \approx 0.63$. In both the cases, the length scale was calculated using the $R = 0.1$ contour level. The nature of the correlation plot does not change significantly at Pos-2.

Bernardini and Pirozzoli [149] investigated effects of compressibility on the characteristics of wall pressure field in case of supersonic adiabatic turbulent boundary layers. From the space-time correlations, they determined convection velocity corresponding to each discrete value of time-delay. Duan et al. [150] followed a similar methodology to calculate the speed of propagation of pressure fluctuations in a hypersonic boundary layer at Mach 6. This concept was also adapted in the current work. Figure 3.15b illustrates the resulting plot, which highlights the scale dependence of convection velocity. The reciprocal of time-delay (τ), non-dimensionalized by the cavity length (L_c) and freestream velocity (U_∞), is shown on the x -axis. The non-dimensional convection velocity (U_c/U_∞) is plotted on the y -axis.

Low-frequency events on the ramp have a higher non-dimensional convection velocity, with latter decreasing rapidly at higher frequencies. This trend is consistent with the observation of Bernardini and Pirozzoli [149] in which convection velocities increased with time-delay. This led to the conclusion that large-scale structures move faster and are located farther away from the wall as compared to the smaller eddies, which applies here as well. At the beginning of the ramp, the convection velocity of large-scale structures lies in the range $0.48U_\infty \leq U_c \leq 0.5U_\infty$. This result is consistent with the previous studies of Largeau and Morinere [39], Camussi et al [40], and Kiya and Sasaki [37]. Downstream at Pos-2, this range increases to $0.62U_\infty \leq U_c \leq 0.68U_\infty$.

A physical picture associated with this analysis is best illustrated by the nested hairpin model, proposed by Adrian et al. [147]. The model schematic is shown in the bottom left corner of Fig. 3.15b. In this schematic, zones I, II, and III consist of packets of eddies with convection velocities, U_{c1} , U_{c2} , and U_{c3} respectively. The convection velocity increases as one progresses from zone I to zone III, i.e. away from the wall. The features of this model that may pertain to this flowfield are reiterated here. Groupings of individual hairpin vortices

called packets, move together with a specific convection velocity. Smaller packets are formed most recently and propagate with a lower convection velocity than the larger, older packets. They co-exist within packets of larger hairpin vortices, which may be overtaken by the latter, causing a constantly changing flow pattern.

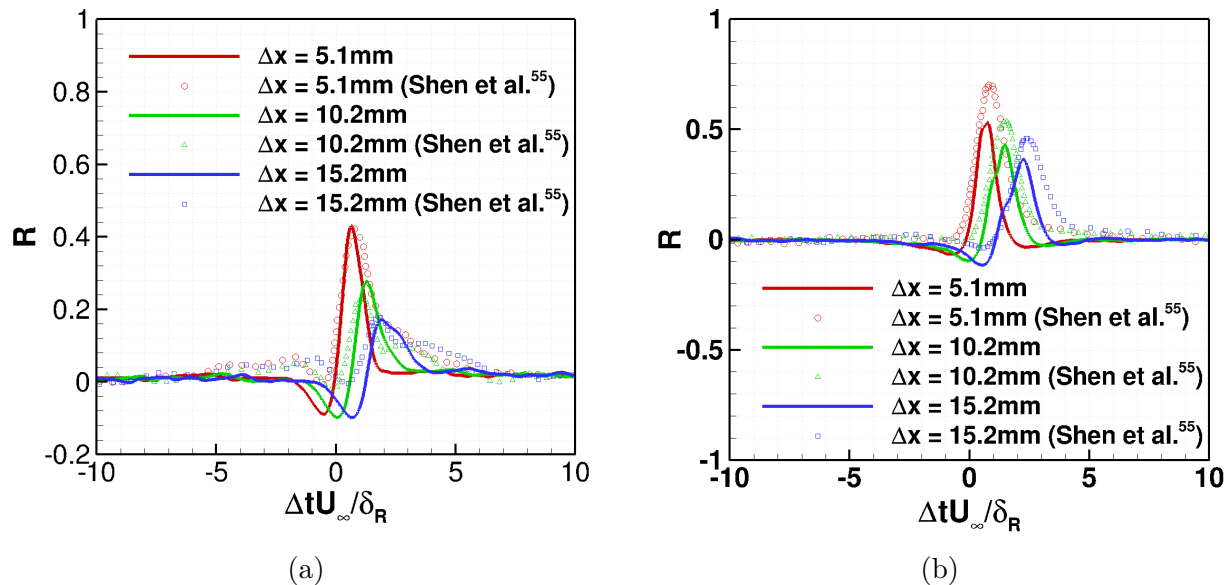


Figure 3.16. Space-time correlations of wall pressure fluctuations on the ramp for the OVERFLOW case at (a) $(x/D, y/D)_{ref} = (4.83, -0.13)$ (b) $(x/D, y/D)_{ref} = (6.24, 0.38)$; δ_R is the experimentally measured boundary layer thickness at the mean reattachment location. Symbols indicate experimental results of Shen et al. [140].

Figure 3.16 shows additional space-time correlations of wall pressure fluctuations on the ramp for the OVERFLOW case. The reference point for the plot in Fig. 3.16a, $(x/D, y/D)_{ref} = (4.83, -0.13)$, lies close to the mean reattachment location. In case of the plot in Fig. 3.16b, the reference point, $(x/D, y/D)_{ref} = (6.24, 0.38)$, lies farther downstream in the redeveloping boundary layer. Correlations obtained from the experiments of Shen et al. [140] with high-frequency wall-pressure transducers are included in the figures. They were carried out for three longitudinal distances from the reference points mentioned above; the same approach was used in this study. The time-delay on the horizontal axis is non-dimensionalized by the freestream velocity and experimental value of boundary layer thickness at the mean reattachment location, $\delta_R = 10$ mm.

Overall, the correlation curves show good agreement with the experimental results. In case of Fig. 3.16a, the peaks in the correlation plot align well with the experimental data. Slight disagreements are observed away from the peaks. The magnitude of peaks in Fig. 3.16b are lower than the experiments, but the values of corresponding optimal time-delays are almost equal. The mismatch in the peak magnitude can be attributed to the difference in the averaging process — instantaneously averaged over the transducer surface in experiments vs. averaged over the span after calculating the correlation in this study — and uncorrelated high frequency components in case of correlations carried out using computational results. According to Shen et al. [140] higher peak correlation magnitude farther downstream of reattachment (in Fig. 3.16b) is indicative of wall pressure field that quickly relaxes towards an equilibrium turbulent boundary layer.

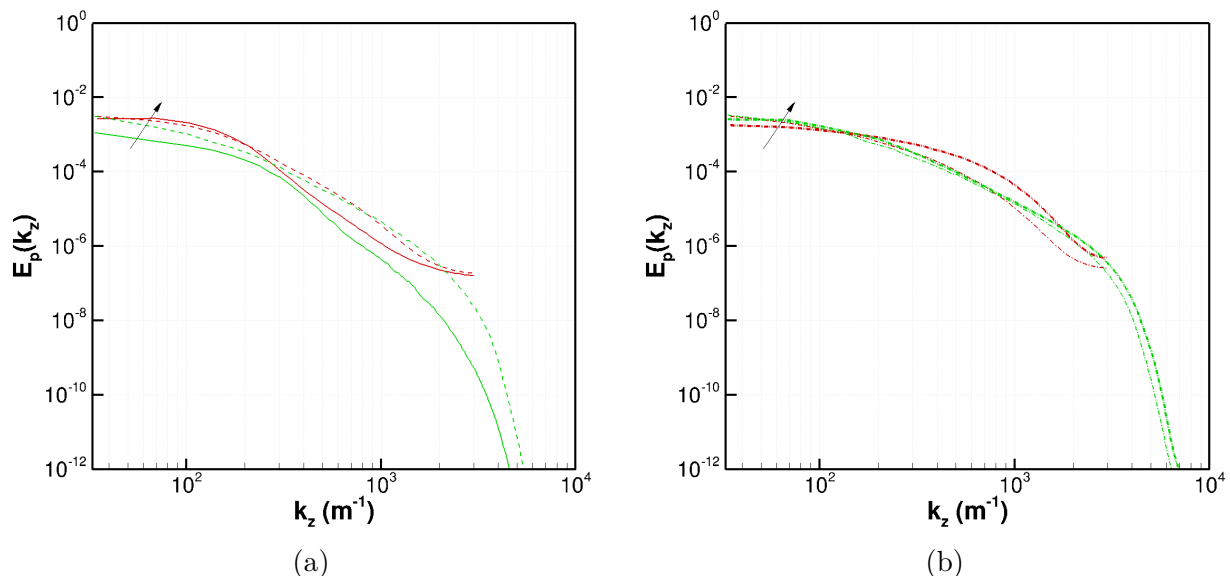


Figure 3.17. Comparison of spanwise wavenumber spectra ($E_p(k_3)$) of wall-pressure fluctuations between SU2 (—) and HOPS (—) at (a) $x/D = 1.07$ (—) and $x/D = 2.44$ (---) (b) $x/D = 3.81$ (-·-) and $x/D = 5.18$ (-·-·). Arrow indicates the downstream direction.

Figure 3.17 characterizes the spanwise length-scales in the cavity (see Fig. 3.17a) and on the ramp (see Fig. 3.17b) at various streamwise locations in log-log coordinates. The dimensional wavenumber is shown on the x -axis with power spectral density plotted on the y -axis. The results from DDES calculations in SU2 are compared with the ILES calcula-

tions from HOPS. In the latter, the width of the domain was discretized using 501 points, thereby resulting in a higher Nyquist wavenumber as compared to the former, wherein the width of the domain was discretized using 181 points. The wavenumber spectra for the SU2 results at all the streamwise show saturation of energy at higher wavenumbers, caused as a result of poor-resolution of small-scale structures. In the cavity region at $x/D = 1.07$, the wavenumber spectra for SU2 suggests more energy residing within the large-scale structures as compared to HOPS. This trend is consistent with that in Fig. 3.17, which compared spanwise wavenumber spectra of streamwise velocity fluctuations in the shear-layer, between the OVERFLOW (DDES) run and HOPS (ILES) run. The spectra show good agreement farther downstream at $x/D = 2.44$, in the initial portion of the inertial subrange. Slight disagreement still persists in the low wavenumber regime.

The spectra on the ramp at $x/D = 3.81$ (in Fig. 3.17b) show reduced energy content amongst the large-scale structures with increased energy content amongst the mid- to high-wavenumbers. At this streamwise location, the spectra for both the cases show good agreement across the entire wavenumber domain. At $x/D = 5.18$ which lies downstream of the mean reattachment location, compared to the spectrum corresponding to the ILES run, the spectrum corresponding to the DDES run shows significantly higher energy content in the inertial subrange. This is most likely caused due to poor resolution of high-wavenumbers, resulting in insufficient dissipation. The HOPS spectra at both the streamwise locations are similar and display a characteristic slope in the inertial range, which indicates gradual return to locally isotropic behavior. On the other hand, the variation in the SU2 spectra prior to and post reattachment suggests that DDES is error-prone in capturing the statistics of redeveloping flows.

3.4 Shear-layer flapping, separation-bubble breathing, and reattachment shock motion

This section elaborates on the events corresponding to energy dominant frequencies observed in the premultiplied pressure spectra in Figs. 3.8a and 3.9a. We start with shear-layer flapping. This phenomenon can be viewed as a vertical motion of the shear-layer causing wall-normal velocity perturbations (v) about the mean. Therefore evidence of such motion

can be obtained by correlating wall-normal velocity fluctuations with other relevant quantities. To investigate the effect of flapping on the recirculation zone, correlations of pressure fluctuations at RZ-2 and wall-normal velocity in the shear-layer (SH-1 to SH-3) were carried out for the OVERFLOW case, with the results plotted in Fig. 3.18. The time-delay is non-dimensionalized by the distance between the reference points and freestream velocity. In the same figure, a contour plot of non-dimensional local speed of sound (a_{loc}/U_∞) is included on the top-left corner.

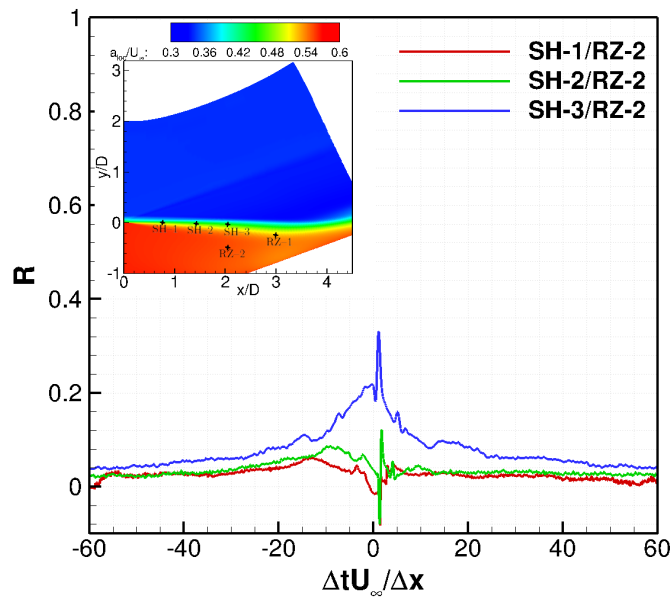


Figure 3.18. Space-time correlations of p and v for the OVERFLOW case. (Top-left) Contour plot of local speed of sound.

The extrema occur at positive time delays, indicating that the event occurred first in the shear-layer. The correlation plot for SH-3/RZ-2 shows a broad peak with the highest correlation magnitude. The curve drops slowly towards zero at large time-delay, probably on account of large-time scales associated with the combined effect of flapping motion and separation bubble breathing. The magnitude of peak correlation drops sharply in case of SH-2/RZ-2, with the appearance of a valley. A similar trend occurs for SH-1/RZ-2, where the wall-normal velocity fluctuations are negatively correlated with pressure fluctuations in the recirculating zone.

The physical nature of these correlations can be interpreted as follows. During the flapping motion, an upward movement of the shear-layer causes a positive wall-normal velocity fluctuation ($v > 0$) and vice-versa for a downward movement. At SH-3, the optimal time-delay is very close to zero. The effect of flapping is almost instantaneous at RZ-2 as it shares the same streamwise location with SH-3. The velocity scales associated with the optimal time delays in case of SH-2 and SH-1 are $U_c/U_\infty = 0.56$ and $U_c/U_\infty = 0.68$ respectively. In case of SH-2, the local speed of sound a_{loc} lies within the range $0.54U_\infty < a_{loc} < 0.6U_\infty$ (see top-left in Fig. 3.18). Therefore the flapping motion at SH-2 may affect the local pressure at RZ-2 via acoustic disturbances. In case of SH-1, a different mechanism may be responsible for the same, as the corresponding velocity scale lies outside this range. Similar correlations with pressure at RZ-1 did not indicate any significant effect of flapping at that location. Hence the corresponding plots are not included for brevity.

From the spectral plot in Fig. 3.8a, the peak corresponding to shear-layer flapping was obtained by examining wall pressure fluctuations close to the step. This result indicates a possible causality between the wall pressure fluctuations and the velocity fluctuations in the shear-layer. In order to verify this hypothesis, two-point correlations of these quantities at the same streamwise station were calculated for the OVERFLOW case. The resulting contour plot is shown in Fig. 3.19.

The contours are shown on the centerplane up to the location of mean reattachment, i.e. Sub-planes 1 to 5. The contours of non-dimensional density shown as dashed lines are superimposed on the correlation contours. High absolute values of correlation are observed in the region close to the step ($0 \leq x/D \leq 1$) and on the ramp ($3.4 \leq x/D \leq 4.8$). At the separation point, alternating regions of positive and negative correlations occur on account of oscillations of the expansion fan at the separation point, caused by the flapping motion. Within the recirculation zone, a positive correlation suggests that an upward motion of the shear-layer ($v > 0$) is associated with a higher instantaneous pressure ($p > 0$) at the same streamwise location, and vice-versa. The streamwise extent of this region ($0 \leq x/D \leq 1$) is consistent with the domain wherein spectral energy corresponding to shear-layer flapping is dominant (see Fig. 3.8a). The ramp surface is characterized with regions of negative

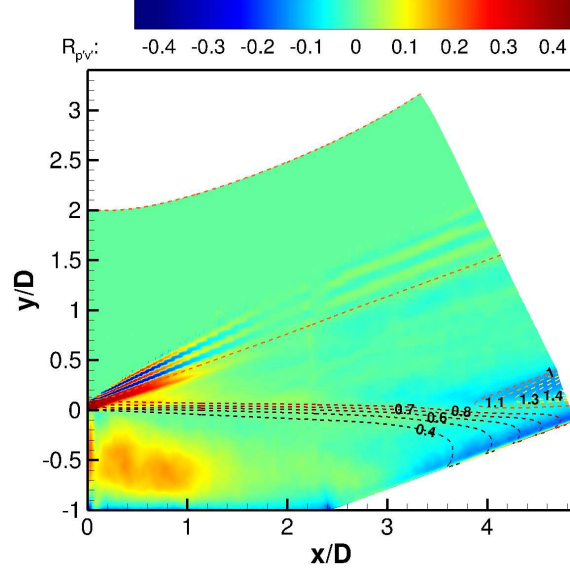


Figure 3.19. Two-point correlations of p_w at a given streamwise station x/D and v in the shear-layer at the same station for the OVERFLOW case. Colored dashed lines are contours of non-dimensional mean density.

correlation values. Physically, they may be representative of large-scale turbulent structures on the ramp.

In the spectra of Fig. 3.8a, energy corresponding to the flapping motion is observed to be concentrated at $St \leq 1$. Based on this threshold, the centerplane data were low-pass filtered to highlight the flapping motion. Four frames from the reconstructed movie are shown in Fig. 3.20. The contours of non-dimensional u -velocity are plotted on the centerplane. Three contour levels are specifically highlighted: $u/U_\infty = 0.7$, $u/U_\infty = 0.15$, and $u/U_\infty = -0.1$ to illustrate the breathing and flapping motions. These three contour levels will be referred to as C1, C2, and C3 respectively. The black solid lines represent the instantaneous contour levels and the red dashed lines are the respective time-mean values. The location of mean reattachment is also shown for reference.

Figure 3.20a shows the recirculation zone and the shear-layer approximately at their time-mean location. In Fig. 3.20b, the recirculating zone enveloped by C3 shrinks in size with respect to the mean, thereby depicting the contraction phase of the breathing motion. At the same instant in the shear-layer, C2 moves below its mean value while the position of

C1 remains relatively unchanged. After the contraction phase, the separation bubble and the shear-layer revert back to their respective time-mean locations in Fig. 3.20c. Figure 3.20d illustrates the expansion phase of the breathing motion wherein the bubble expands in size. This is accompanied by an upward movement of C2. Similar to the contraction phase, the position of C1 does not change significantly.

To investigate the breathing motion highlighted by the results presented in Fig. 3.20, the mass history of the separation zone was examined. At any given instant, the separation bubble is characterized by pockets of positive and negative u -velocity, instead of a homogeneous region of upstream flowing fluid. A few causes that result in the variation of the mass of the separation bubble include vortex shedding, reinjection of fluid, and entrainment

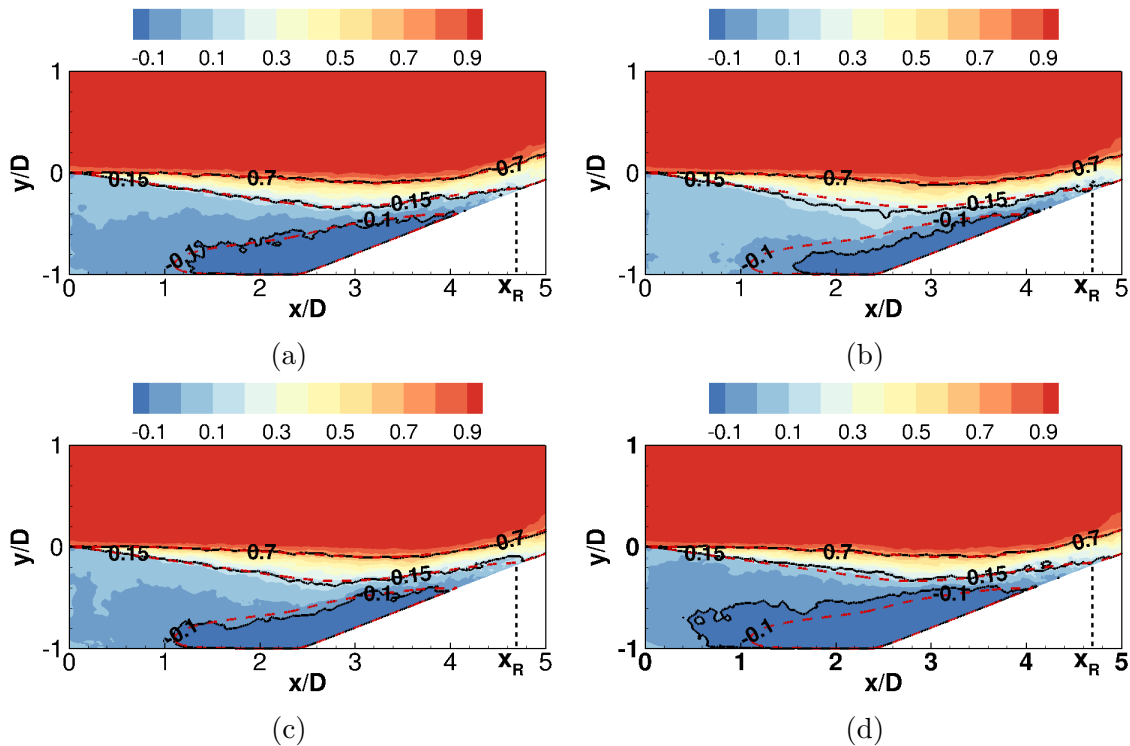


Figure 3.20. Contours of u/U_∞ describing the shear-layer flapping motion and separation bubble breathing cycle for the OVERFLOW case. (a) Mean location/Equilibrium. (b) Downward movement/Bubble contraction. (c) Mean location/Equilibrium. (d) Upward movement/Bubble expansion. Dashed line indicates the mean reattachment location.

of fluid by shear-layer to support its growth rate. Accounting for these factors, the mass of the separation bubble at any given instant can be calculated as:

$$m(t) = \iiint_{\mathcal{V}} \rho(\mathbf{x}, t) f(\mathbf{x}, t) dx dy dz \quad (3.3)$$

where m is the instantaneous mass, \mathcal{V} is the control volume, and ρ is the instantaneous density. The centerplane data (with $f_s = 400$ kHz) were used for this purpose, assuming unit length in the spanwise direction. The integration was carried out numerically using the trapezoidal rule. To exclude regions of downstream flow from the calculations, the following weighting function was used for numerical integration:

$$f(\mathbf{x}, t) = \begin{cases} 1 & u(\mathbf{x}, t) < 0 \\ 0 & u(\mathbf{x}, t) \geq 0 \end{cases} \quad (3.4)$$

where u is the instantaneous streamwise velocity. The resulting time history was Fourier transformed to calculate the spectra of the mass of the separation bubble, shown in Fig. 3.21 for the DDES runs in SU2 and OVERFLOW. The spectrum corresponding to the ILES run in HOPS is not included as the samples of centerplane data were not recorded for long enough time to achieve sufficient low-frequency resolution. The spectra are shown in pre-multiplied semi-logarithmic form with the magnitude normalized by the variance of the signal. The Strouhal number is plotted on the x -axis. The spectra from the SU2 and OVERFLOW runs show good agreement and peak at approximately the same Strouhal number, $St \approx 0.02$. Note that the data used to compute the SU2 spectrum were sampled at a higher frequency. The energy corresponding to separation bubble breathing is seen to be concentrated in the frequency band $0.01 \leq St \leq 0.05$. This range lies within the low-frequency range indicated by spectra of wall pressure in the cavity region (see Fig. 3.8a). This phenomenon may also be responsible for the large time-scales observed in the spanwise correlation plot corresponding to RZ-1 (see Fig. 3.13b).

The movement of instantaneous reattachment location due to shear-layer flapping and separation bubble breathing is also evident in Fig. 3.20. This phenomenon can be inferred

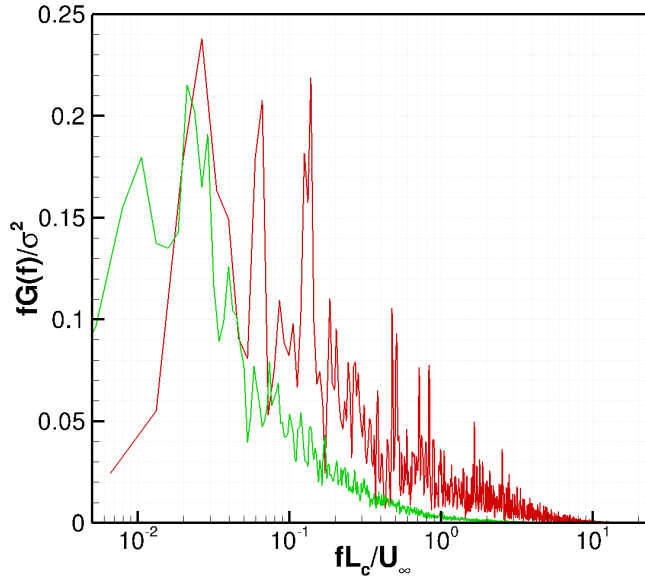


Figure 3.21. Spectrum of separation bubble mass for SU2 (—) and OVERFLOW (—).

by tracking the movement of C2, where C2 is the contour level of $u/U_\infty = 0.15$. At the mean position, C2 approximately ends at the mean reattachment location (indicated by the black dashed line). During the contraction phase, C2 shows a downward movement leading to a slight decrease in the separation extent and upstream movement of the instantaneous reattachment point. During the expansion phase, C2 moves above its mean position, resulting in an increased separation extent and downstream movement of the instantaneous reattachment point. The low-frequency motions associated with separation bubble breathing and shear-layer flapping are aperiodic and asymmetric. This observation is consistent with previous studies carried out on low-frequency unsteadiness in SWTBLI's [25], [141]. Additional analysis on this phenomena is carried out in the next section.

In this study, it was difficult to determine the reattachment shock position history using wall-pressure data. Unlike a compression ramp or an incident SWTBLI, the reattachment shock foot was composed of multiple compression waves and weak shocks (see Fig. 3.1). Therefore conventional pressure threshold methods were not effective in determining the shock location history. To overcome this limitation, the shock position was obtained at a certain height in the freestream. It was assumed that the low-frequency shock motion at

the wall and away from it is similar in nature. Priebe and Martín [141] determined the shock indicator signal using pressure fluctuations in the freestream. Based on its phase with respect to the location of separation, they concluded that shock in the freestream and the separation point at the wall move almost synchronously.

Agostini et al. [142], [151] also determined the shock location history at an elevation in order to perform statistics. They used the location of maximum pressure gradient normal to the shock as an indicator to determine its instantaneous streamwise location. Pirozzoli and Bernardini [152] used a modified Ducros sensor in their DNS calculations for shock capturing, which compares the local dilation with the vorticity magnitude and a large-scale velocity gradient. A combination of these two methods was used in this study. At a specific instant, the location of maximum pressure gradient normal to the ramp surface was determined. The value of the Ducros sensor corresponding to that location was then chosen as the threshold for detecting a shock. Using this approach, the spectra of shock position is shown in Fig. 3.22.

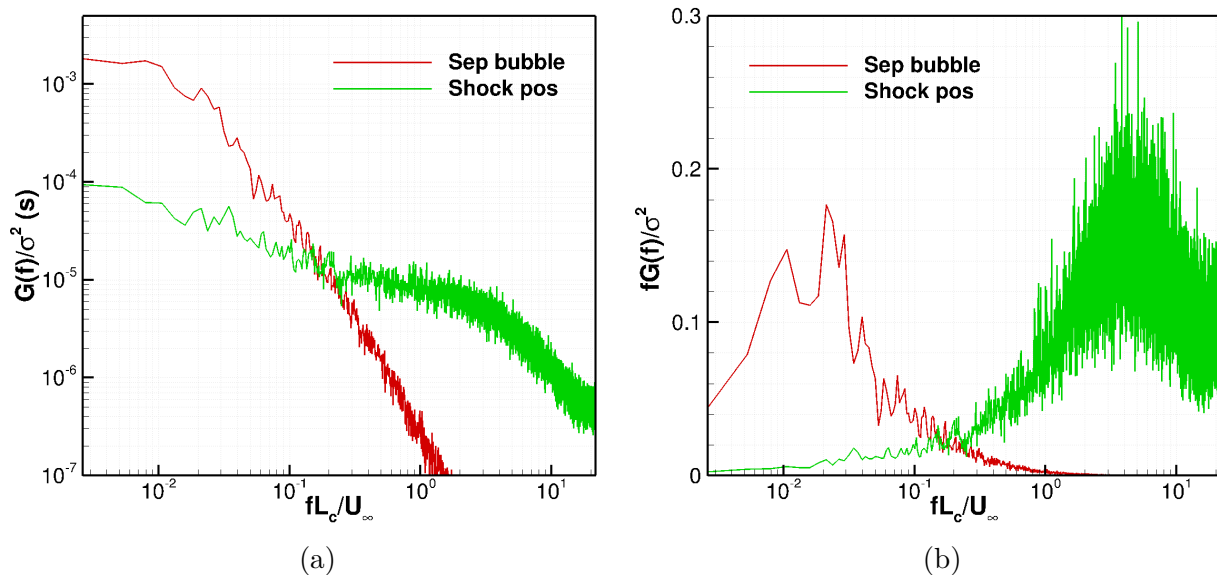


Figure 3.22. Spectra of shock location and separation bubble mass for the OVERFLOW case in (a) log-log coordinates (b) semilog coordinates.

The spectrum of shock location is compared with the spectrum of mass-history of the separation bubble (calculated using Eq. (3.3)) in log-log coordinates and semilog coordinates in Figs. 3.22a and 3.22b, respectively. The Strouhal number is shown on the x -axis. In

Fig. 3.22a, the spectrum of separation bubble mass has a steeper roll-off as compared to the spectrum of shock position. This may be a result of the averaging and low-pass filtering process inherent in integration. From the spectrum of shock motion, it is evident that the low-frequency band ($\mathcal{O}(10^{-2}) \leq St \leq \mathcal{O}(10^{-1})$) is dominant in energy. But the relative magnitudes in this band are higher for the separation bubble mass spectrum than for the shock position spectrum. Also note that at higher frequencies ($St \geq 0.18$), the spectrum of shock position has more energy than that of separation bubble mass. This suggests that the reattachment shock motion comprises both low-frequency $St \approx \mathcal{O}(10^{-2})$ and mid-frequency $St \approx \mathcal{O}(10^{-1})$ motion. Based on the spectra shown in premultiplied coordinates in Fig. 3.22b, energy content in the low-frequency regime of the spectrum of shock position is significantly lower than the same in the spectrum of mass-history of the separation bubble. This suggests dominant mid-frequency motion of the reattachment shock.

3.5 Unsteadiness of the reattachment shock

This section attempts to relate the unsteady shock motion with shear-layer flapping and separation bubble breathing by examining coherence between the respective signals. Only data from the DDES runs in OVERFLOW are used here, owing to the need for a long physical run time to fully capture the low-frequency shock motion. The time history of shock location used for the spectral calculation presented in Fig. 3.22 was used as the reference signal. Note that the results in this section are derived from the centerplane data (with $f_s = 400$ kHz). We start with shear-layer flapping, and assume that the wall-normal velocity of the shear-layer is representative of this phenomenon. The signals are extracted at locations in the shear-layer that correspond to the coordinates of spanwise lines shown in Fig. 2.4b. The resulting coherence plot is shown in Fig. 3.23a.

The Strouhal number is shown on the x -axis on a logarithmic scale, and the magnitude of coherence (γ_{xy}^2) is plotted on the y -axis. The upper limit of the x -axis is maintained at $St = 1$ in order to focus on the events of interest in the low-frequency range ($St \approx \mathcal{O}(10^{-2})$) and the mid-frequency range ($\mathcal{O}(10^{-1})$). Given the low coherence and statistical uncertainty evident in the data, conclusions must be drawn with some caution. Nonetheless, a coherent

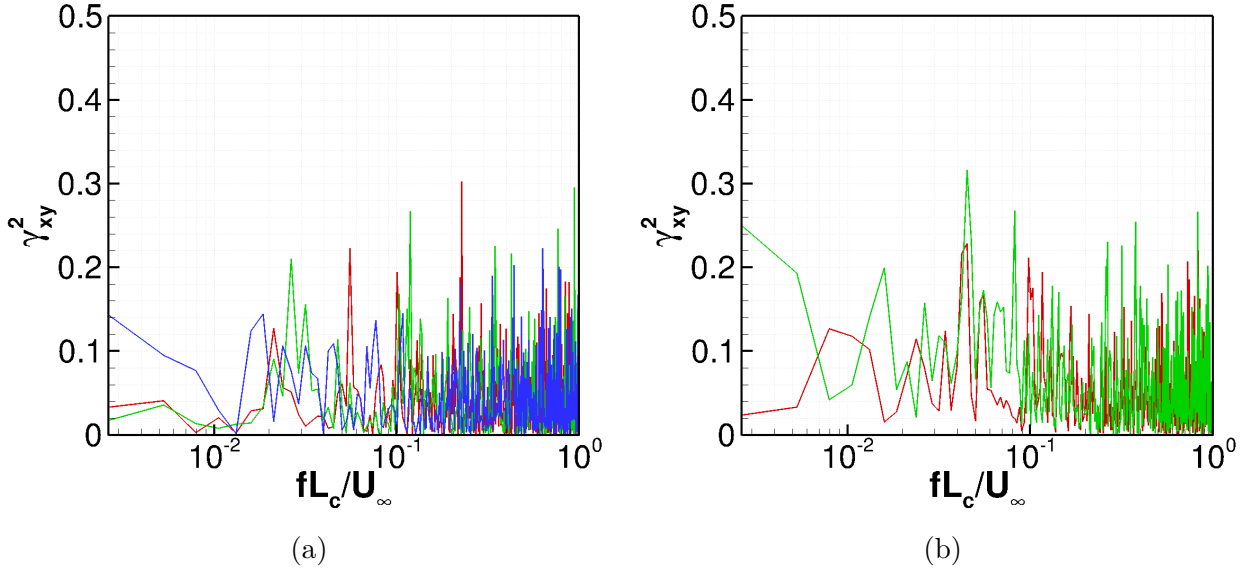


Figure 3.23. Coherence of shock position relative to (a) SH-1 (—), SH-2 (—), and SH-3 (—) (b) RZ-1 (—) and RZ-2 (—) for the OVERFLOW case.

behaviour is believed to lie within a random background signal. In case of SH-1, two local peaks are observed in the low-frequency range at $St \approx 0.02$ and 0.05 respectively, which correspond to the energy-dominant frequencies in the spectra of separation bubble breathing (see Fig. 3.21). In the mid-frequency range ($St \approx \mathcal{O}(10^{-1})$), the peaks occur at $St \approx 0.1$ and $St \approx 0.22$. A similar trend in the case of low-frequency range is observed at SH-2, where the contribution of separation bubble breathing is evident. The mid-frequency range seems to be broadband in nature; relative contributions from large-scale structures and shear-layer flapping cannot distinguished. This broadband behaviour extends to the low-frequency range at SH-3.

Figure 3.23b plots the coherence between pressure fluctuations in the recirculation zone and the shock-position. At RZ-1, which lies close to the shear-layer, a distinct peak at $St \approx 0.045$ is observed in the low-frequency range. The mid-frequency range is composed of broadband frequencies, analogous to SH-2 and SH-3. At RZ-2, apart from a peak at $St \approx 0.045$, additional peaks occur in the low-frequency range. Hence it seems that almost all of the energy-dominant frequencies in the spectra of separation bubble breathing contribute towards the low-frequency motion of the reattachment shock.

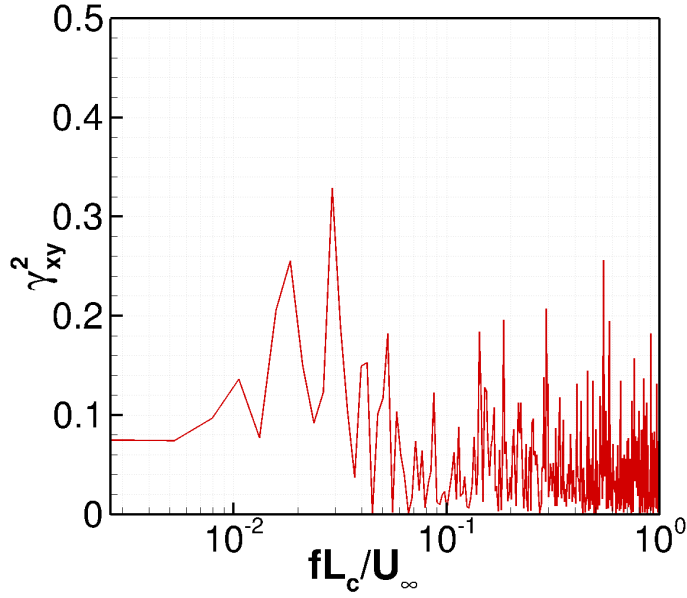


Figure 3.24. Coherence of shock position with the mass history of separation bubble for the OVERFLOW case.

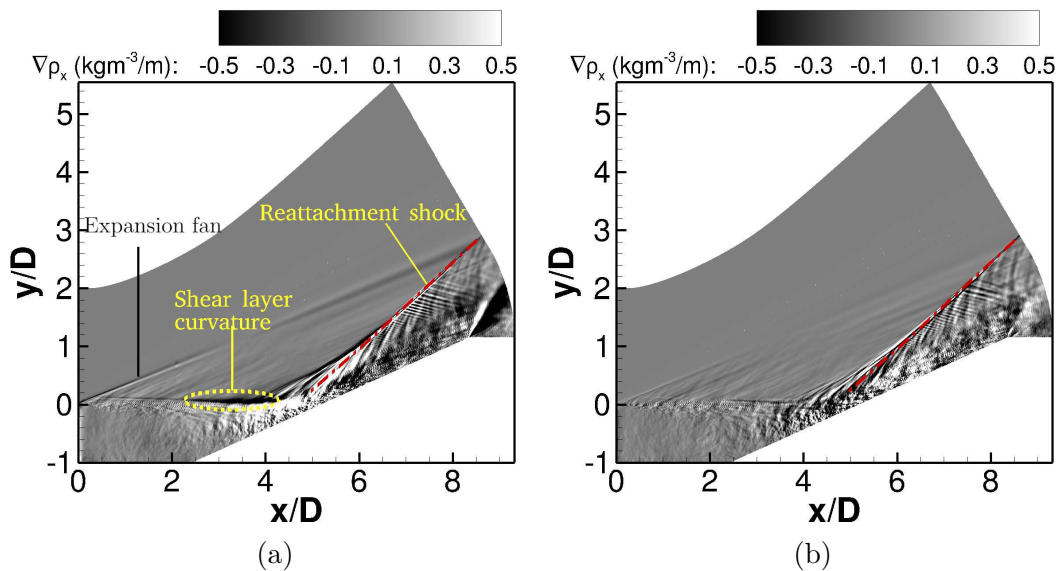
With Fig. 3.24 the effect of separation bubble breathing on reattachment shock motion is investigated. The mass history of separation bubble derived in Sec. 3.4 was used for this purpose. In this figure, the coherence plot shows multiple peaks in the low-frequency range (although some of these may reflect statistical uncertainty). The highest peak occurs at $St \approx 0.03$, with the second highest peak at $St \approx 0.02$. Similar to the coherence plots in Fig. 3.23, these frequencies belong to the set of energy dominant frequencies of separation bubble breathing. Peaks in the mid-frequency range are also noted, but higher magnitudes of the peaks at lower frequencies indicate a stronger effect of events in this range time-scales.

Figure 3.25 shows conditionally averaged streamwise component of the density gradient ($\partial\rho/\partial x$), based on the instantaneous mass of the separation bubble \tilde{m}_{sep} . The corresponding time history was divided into four bins, with each bin containing about 50 000 samples. The first bin was composed of samples wherein the instantaneous mass was less than the mean (\bar{m}_{sep}) (bubble contraction phase). Both the second and third bin contained samples in which the bubble was in the equilibrium phase. Hence the conditional mean for only the second bin is shown. In the final bin, instantaneous mass of the separation bubble was higher than the mean (bubble expansion phase). Specific features such as reattachment shock, expansion

fan, and shear-layer curvature, which undergo a distinct change during the breathing cycle are labeled in Fig. 3.25a.

Consider the flow condition shown in Fig. 3.25a as the reference state. The expansion fan can be identified as a region of negative density gradient close to the step. The shear-layer curvature close to the ramp surface shows slight concavity as it curves downwards during the bubble contraction phase. This concavity results in local expansion of the flow, which is implied by the negative density gradient in the region marked by a dotted circle. The flow compression occurs farther downstream via multiple compression waves, which coalesce in the freestream to form the reattachment shock. The latter can be identified as a thin region of positive density gradient.

In Fig. 3.25b as the bubble expands towards equilibrium, a noticeable change is observed in the shear-layer curvature and the region of negative density gradient dissipates gradually. The reattachment shock begins to move upstream from its location in the reference state. In Fig. 3.25c the bubble is seen to have completely expanded, while the shear-layer curvature shows a distinct convexity, i.e. it curves upwards. Note the change of sign of the gradient relative to the dotted oval region of Fig. 3.25a. This causes local compression of the flow, leading to a positive density gradient in that region. In this phase the flow compression occurs upstream, which may likely cause an upstream movement of the reattachment shock.



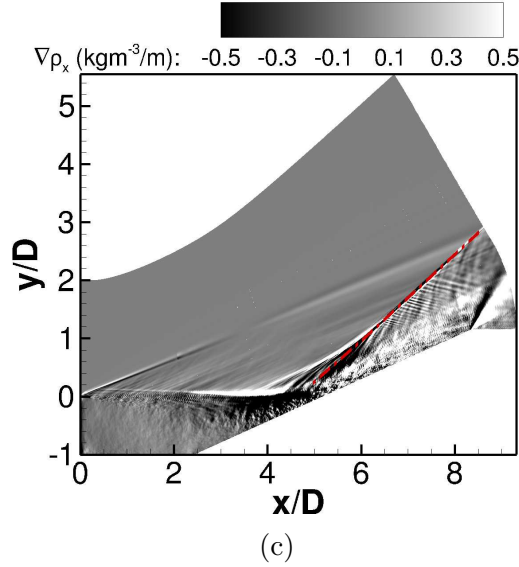


Figure 3.25. Conditionally averaged streamwise component of the density gradient on the centerplane ($z/D = 0$) for the OVERFLOW case, based on instantaneous mass of the separation bubble. (a) Bubble contraction phase. (b) Equilibrium phase. (c) Bubble expansion phase.

A negative density gradient close to reattachment indicates influx of fluid in the recirculation zone.

3.6 Unsteadiness at the mean reattachment location

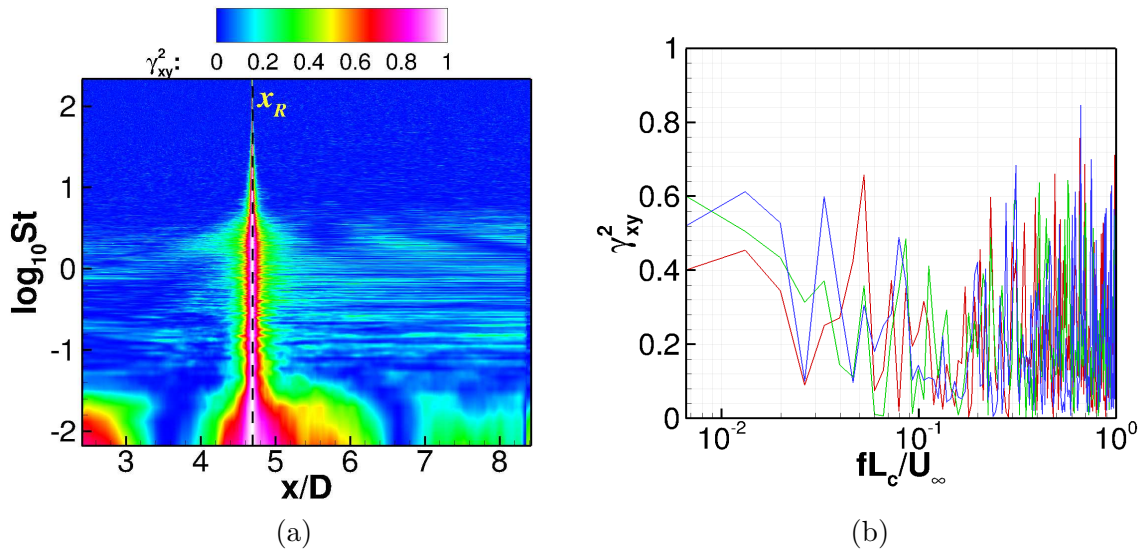
The previous section discussed the effect of upstream events — namely large-scale structures, shear-layer flapping, and separation bubble breathing — on the reattachment shock motion. A similar exercise on the unsteadiness of the instantaneous reattachment location/shock system (IRSS) is carried out in this section by examining coherence between various physical quantities. Similar to Sec. 3.5, only data from the DDES runs in OVERFLOW is used here. Data extracted at the higher sampling frequency ($f_s = 4$ MHz) are used for the analysis, thereby providing a higher frequency resolution.

For the purpose of signal analysis, it is assumed that IRSS moves as a single unit about the mean reattachment location. When this system moves downstream of the mean, $x_R(t)$ falls upstream of the reattachment shock foot and within the recirculating zone, causing wall pressure fluctuations at the mean reattachment, $p_{x_R} < 0$. Similarly when it moves

upstream of the mean, $x_R(t)$ falls downstream of the reattachment shock foot and outside the recirculating zone, causing $p_{x_R} > 0$.

Figure 3.26 plots the coherence of pressure fluctuations on the ramp surface and recirculation zone (RZ-1, RZ-2), as well as wall-normal velocity fluctuations in the shear-layer (SH-1, SH-2, and SH-3) with the wall pressure fluctuations at the mean reattachment for the OVERFLOW case. Figure 3.26a shows the 2D contour plot of coherence between wall pressure fluctuations on the ramp at a specific streamwise location with p_{x_R} . The logarithm of the Strouhal number is plotted on the vertical axis with non-dimensional streamwise location on the horizontal axis. The mean reattachment location is highlighted by a black dashed line. High values of coherence are observed at low-frequencies, specifically in the range $0.01 \leq St \leq 0.03$. As mentioned previously, this frequency band corresponds to separation bubble breathing which seems to have a strong relationship with the motion of IRSS, and affects the same via pressure perturbations. This is also consistent with the coherence plot shown in Fig. 3.24. This region of high coherence extends from $x/D \approx 2.41$ to $x/D \approx 3.4$.

Downstream of $x/D = 3.4$, the coherence for this specific band plummets to low values. This region of low coherence was also observed by Agostini et al. [151] in an impinging SWT-BLI. The magnitude of coherence increases in the vicinity of the mean reattachment location $x/D \approx 4.2$. This region of high coherence persists for a significant distance downstream of



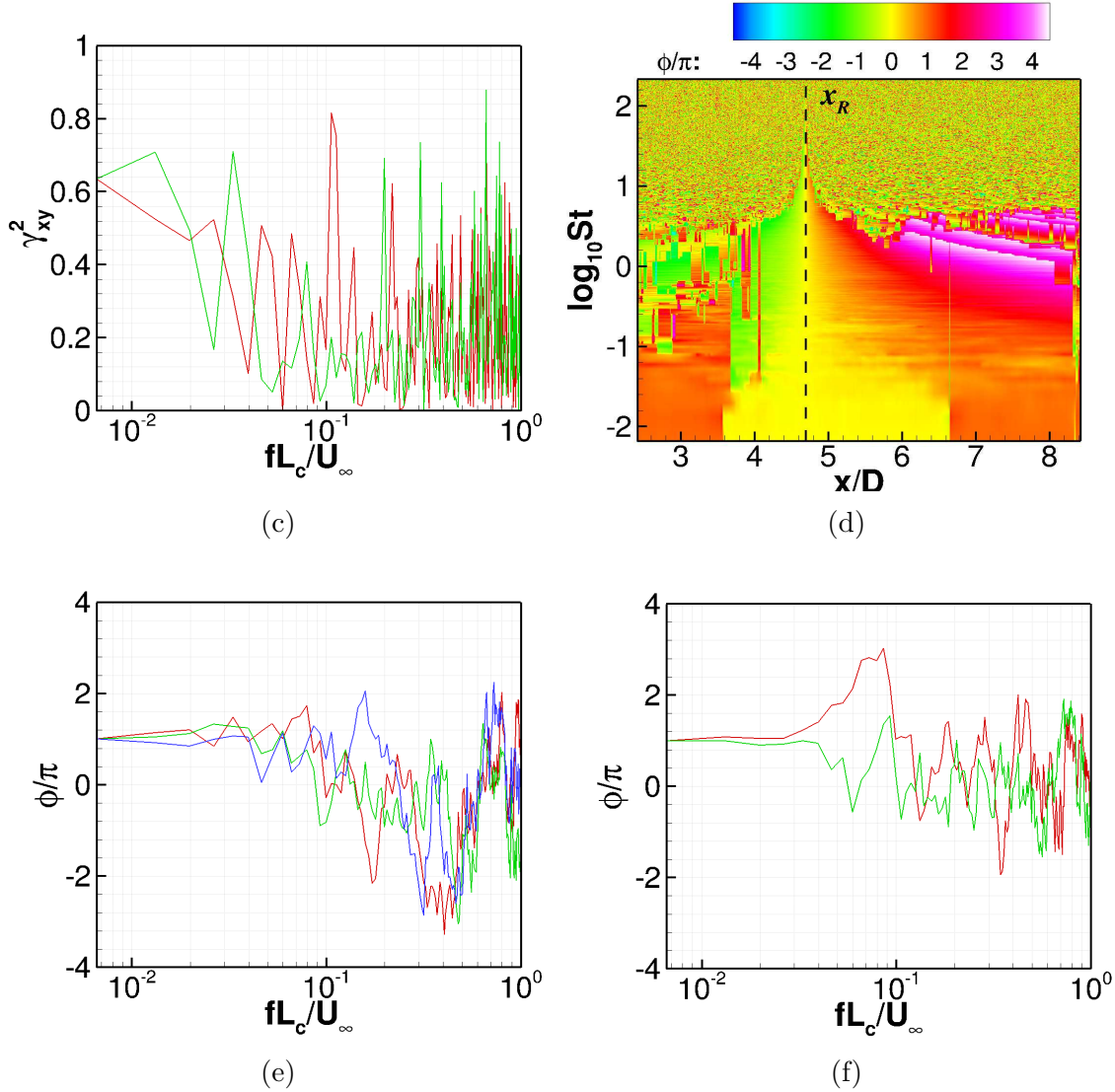


Figure 3.26. Plots of coherence of wall pressure fluctuations at mean reattachment for the OVERFLOW case with (a) wall pressure fluctuations on the ramp, (b) Wall-normal velocity fluctuations in the shear-layer, and (c) Pressure fluctuations in the recirculation zone. Phase plots of wall pressure fluctuations at mean reattachment with (d) wall pressure fluctuations on the ramp, (e) Wall-normal velocity fluctuations in the shear-layer, and (f) Pressure fluctuations in the recirculation zone. In parts (b) and (e) SH-1 (—), SH-2 (—), and SH-3 (—). In parts (c) and (f) RZ-1 (—) and RZ-2 (—).

reattachment, extending up to $x/D \approx 6.6$. The physical phenomena associated with this region is most likely a combined effect of low-frequency motion of the IRSS and large-scale structures shed from the separation bubble. Farther downstream on the ramp, a brief region

of low coherence is encountered before it increases again towards the end. This specific region of high coherence may be a result of the unsteadiness associated with the expansion fan present at the ramp exit (see Fig. 3.1). Structures lying in the frequency range $0.2 \leq St \leq 1$ have a localized effect on the movement of IRSS.

The corresponding phase plot is shown in Fig. 3.26d. The phase is scaled by π rad. Focusing on the low-frequencies, an interesting trend is observed. In the vicinity of the ramp-cavity junction ($2.41 \leq x/D \leq 3.4$), the pressure fluctuations are approximately 180 deg out of phase ($\phi = \pi$) with those at the mean-reattachment for lower frequencies. At $x/D \approx 3.5$, the non-dimensional phase magnitude switches to zero from one, and persists up to $x/D \approx 6.7$. This trend agrees with the results of Agostini et al. [151] Downstream of $x/D \approx 6.7$, the pressure fluctuations on the ramp and at mean reattachment are 180 deg out of phase. No definitive phase relationship is observed for higher frequencies.

3.7 Summary

This chapter has described the unsteadiness involved in a compressible shear-layer reattaching on to a ramp by means of statistical analysis. Data from three cases — DDES calculations carried out by Leger et al. [28] using OVERFLOW, SU2 and ILES calculations using HOPS — was used to investigate the effects of sub-grid scale modeling approach. The DDES calculations in OVERFLOW were highly resolved in time. The mean quantities corresponding to the three cases showed good agreement. Significant differences in the mean-squared profiles of fluctuating quantities within the shear-layer were observed. The instantaneous flowfields were consistent across all the cases and resolved the flow structures (such as hairpin-like vortices) in the shear-layer. The pressure spectra in the resolved region showed reasonable agreement, but deviated significantly on the surface. Time-resolved data from DDES calculations in OVERFLOW was used for any forthcoming analysis.

Premultiplied wall-pressure spectra highlighted events such as low-frequency separation bubble breathing, shear-layer flapping, shedding of vortical structures from the recirculation zone. The spatially evolving large-scale structures in the shear-layer were characterized by space-time correlations and the spanwise wavenumber spectra. The spectrum of

reattachment shock motion and separation bubble breathing indicated dominant mid- and low-frequency motion, respectively. Based on the coherence plots and conditional averaged density gradient, separation bubble breathing contributed to the secondary low-frequency motion of the reattachment shock. Shear-layer flapping and upstream turbulence drove its dominant mid-frequency motion. The unsteadiness of reattachment was strongly affected by the motion of the recirculation zone and large-scale structures in its vicinity. The flapping motion of the shear-layer had a weak effect on the same.

4. COMPRESSION RAMP FLOW WITH SIDEWALLS

This chapter elaborates on the flowfield corresponding to a compression ramp flow, in the presence of no-slip sidewalls. The computations were carried out by Poggie and Porter [22], [65] and data analysis of the results was performed by Deshpande. In addition to a brief discussion on the mean and instantaneous flowfields, a critical point analysis is presented to characterize the secondary flows induced by the presence of sidewalls. This is followed by a detailed discussion on the flowfield unsteadiness by examining the wall-pressure spectra. Unlike the previous chapter, a different approach in visualizing the spectra is used here, wherein the contours of premultiplied spectral energy density is shown for a single frequency component. The frequency components are chosen based on the dominant bands of unsteadiness commonly observed in SWTBLI. A similar approach is used while examining the coherence estimates. This chapter concludes with a detailed modal analysis of this flowfield using Sparsity Promoting Dynamic Mode Decomposition (SPDMD.) The results of data analysis carried out previously by Deshpande and Poggie [153], [154] are reiterated in this chapter. The results of statistical analysis in [153] are reproduced here with permission from APS publishing.

4.1 Flowfield structure

In this section, the features of mean and instantaneous flowfield are discussed. This is followed by a spectral analysis of wall-pressure fluctuations. Figure 4.1a shows the mean non-dimensional wall-pressure on the floor and left sidewall. The limiting streamlines (shown as black solid lines) and mean zero skin-friction contours ($c_{f_x} = 0$, shown as white solid lines) are included in the figure.

The mean flowfield on the floor shown in Fig. 4.1b is approximately symmetric about the spanwise center. The shock front, characterized by an abrupt pressure rise, is highly curved due to the influence of sidewalls. Based on the $c_{f_x} = 0$ contour, the flow separation at the corners occurs earlier than at the centerline. This occurs because the net momentum of the flow is lower due to the presence of two no-slip boundaries, making it more susceptible to the adverse pressure gradient imposed by the shock front. Across the span, the

separation extent decreases away from the sidewalls, before increasing again close to the midspan. The compression waves generated due to sidewall separation regions modify the three-dimensional shock structure, thereby moderating the pressure gradient which lowers the separation extent [51], [52], [155].

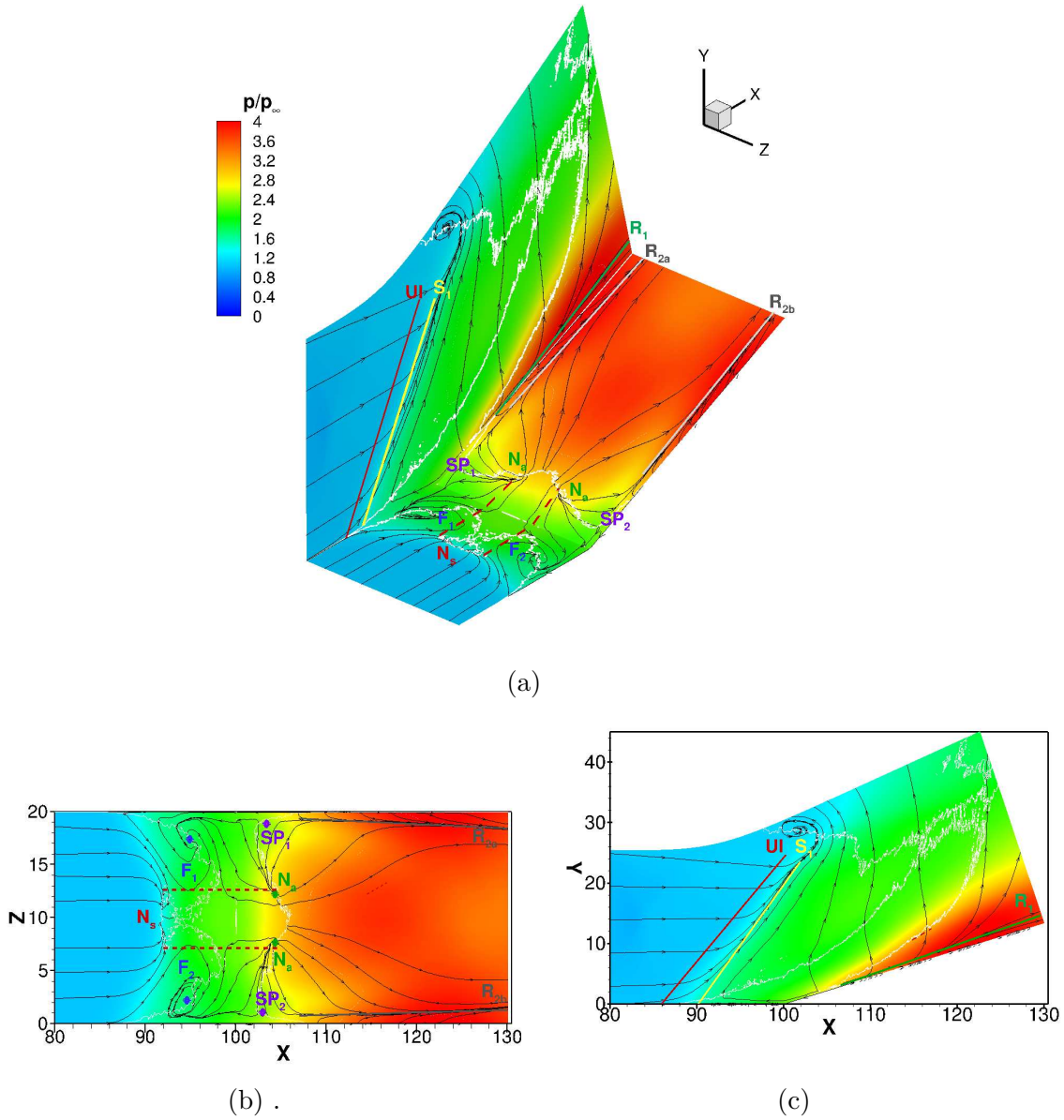


Figure 4.1. Contours of mean wall-pressure (a) Three-dimensional view (b) Projection on the ramp surface (Plane 1) (c) Projection on the left-sidewall (Plane 2). The ramp corner lies at $X = 100$.

Critical points deduced from the limiting streamlines are also highlighted in order to gain insight on the nature of separation and attachment of primary and corner flows. Shortly upstream of the separated zones between the midspan and sidewalls, the flow rolls up into two foci: F_1 and F_2 . Based on previous studies [52], [54], [156], these foci are expected to be the source of tornado vortices, lifting up fluid from the wall. The separation and reattachment in the vicinity of the centerline are characterized by a combination of nodes and saddle points (see Fig. 5(f) in Ref. [157]). These regions are marked by red dashed lines and are indicative of two-dimensional separation and reattachment [157]. A separation node N_s and two attachment nodes N_a are included for clarity. Additionally, two saddle points: SP_1 and SP_2 are present close to the left and right sidewall respectively. Two reattachment lines: R_{2a} and R_{2b} are a signature of corner vortices reattaching on to the ramp.

The mean flow features on the left sidewall in Fig. 4.1c are reminiscent of a swept SWTBLI caused by the compression ramp shock [158]. Surface flow features such as the upstream influence line UI , separation line S_1 , and reattachment line R_1 are noted in the figure. The incoming flow on the left sidewall begins to turn at UI and separates at S_1 . The flow downstream of S_1 is believed to turn into a separation vortex and follow a helical trajectory. As a result an open type of separation exists, wherein the flow does not recirculate upstream, as in a two-dimensional separation. Note that the separation extent grows downstream, as indicated by the $c_{f_x} = 0$ contour. The flow reattaches along the reattachment line R_1 . This region is characterized by amplified aerothermal loads.

Figure 4.2 shows the mean density contours on the centerplane ($Z = 10$), streamwise plane at $X = 80$, and ramp-normal plane at $X \approx 116$. On the centerplane in Fig. 4.2b, a flow analogous to a classical two-dimensional interaction is present wherein the compression ramp shock splits into a λ -shock foot due to viscous effects. Within the separated zone, the focus point F suggests the presence of a horseshoe vortex. Combined with the results of the critical point analysis associated with Fig. 4.1, this interaction is judged to resemble an owl-face pattern of the second kind, as described by Perry and Chong [159] (see Fig. 22 in that reference). Although the centerline region resembles a quasi-two-dimensional SWTBLI, the flow does not recirculate upstream, but is swept away from the midspan by the horseshoe vortex originating at the focus point F . In Fig. 4.2c, a pair of corner vortices are observed

on the streamwise plane, upstream of the interaction. This feature was also present in the work of Bermejo-Moreno et al. [59], Wang and Sandham [58], Eagle and Driscoll [54], and Morajkar et al. [57].

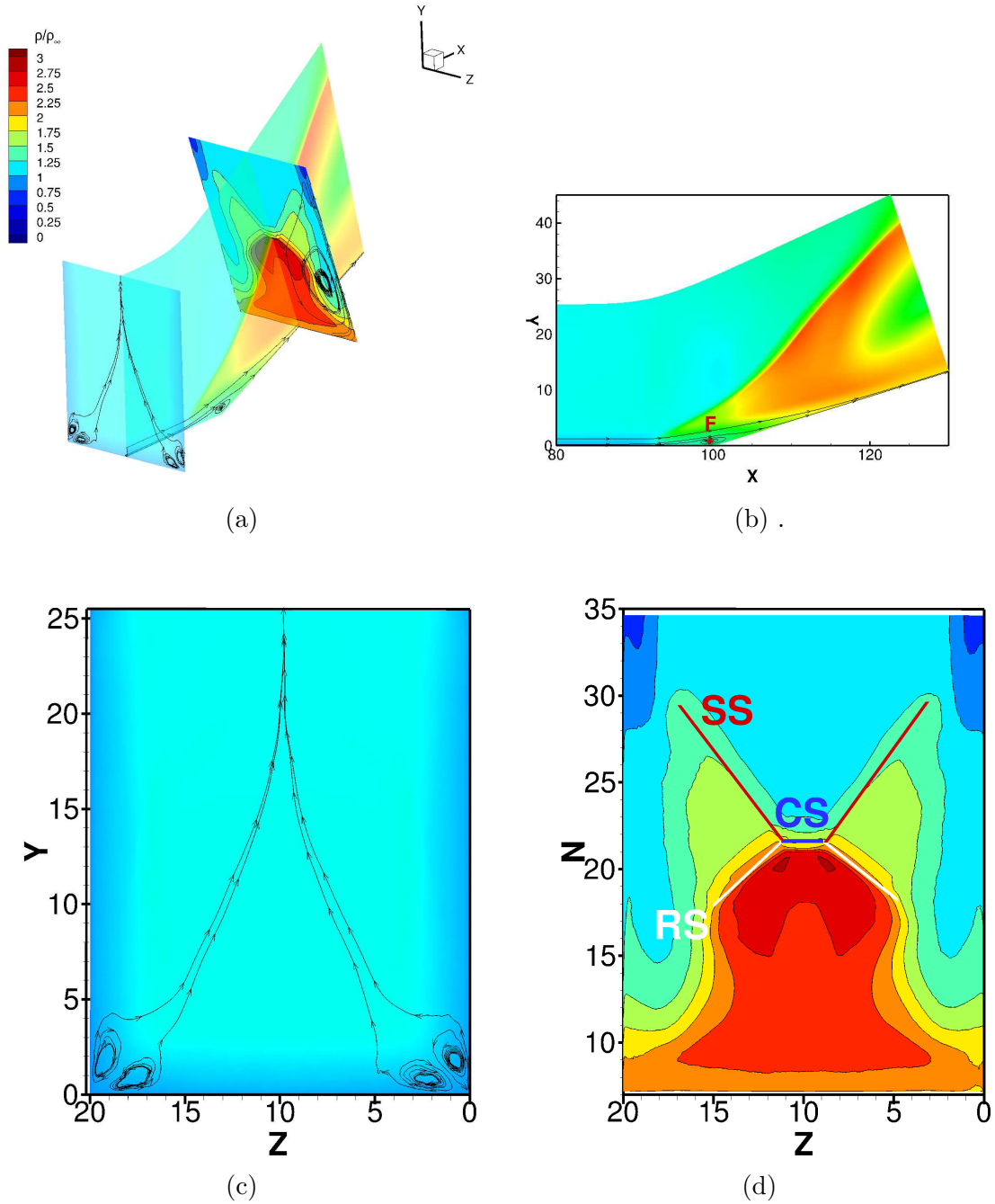


Figure 4.2. Contours of mean density. (a) Three-dimensional view (b) Projection on the centerplane at $Z = 10$ (Plane 6) (c) Projection on the streamwise plane at $X = 80$ (Plane 4) (d) Projection on the ramp-normal plane (Plane 5).

On the ramp-normal plane in Fig. 4.2d, specific features of the swept interaction described earlier can be visualized. Note that the direction normal to the ramp surface, labelled as $N = n/\delta_o$, is shown on the vertical axis. The compression ramp shock labelled as CS (shown as a solid blue line) bifurcates into λ -shock feet on both the sidewalls on account of the influence of sidewall boundary layers. The corresponding separation and reattachment shocks are labelled as SS and RS respectively as solid red and white lines. (From the perspective of the sidewall, the flow is analogous to a fin interaction, with the freestream coming in opposite the N -axis.) The streamlines close to the right sidewall highlight the separation vortex present downstream of the primary separation line S_1 (see Fig. 4.1). This region extends from the foot of the separation shock and ends slightly above the ramp surface, downstream of the reattachment shock.

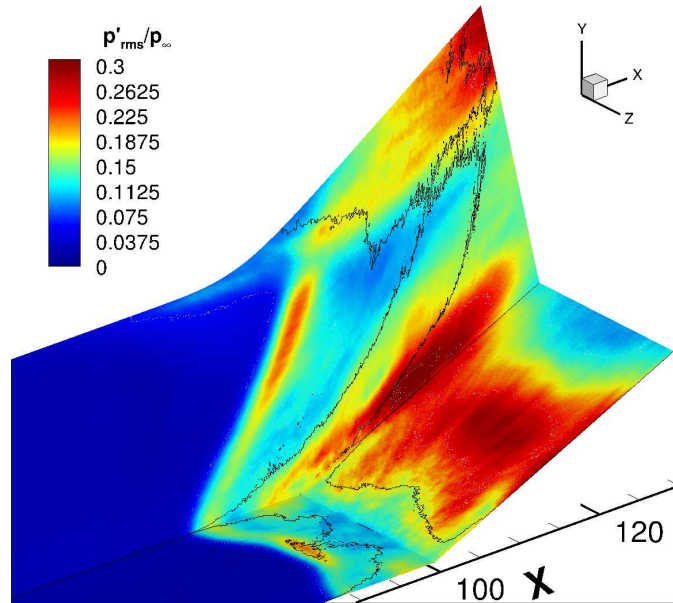


Figure 4.3. Contours of RMS pressure. Black solid lines represent the $c_{fx} = 0$ contour level.

As mentioned previously, the separation on the sidewalls is of the open type wherein the entrapped fluid follows a helical path downstream instead of recirculating upstream. Notice the drastically reduced spanwise extent of the compression ramp shock (highlighted using a solid red line) caused due to the growing separation extent on the sidewall. Following the outermost streamline over the separation vortex, the flow is compressed through the λ -shock foot. Downstream of the reattachment shock, it accelerates across the local expansion fan curving downwards and reattaching at R_1 as an impinging jet. Such flows fall under the category of Edney Type-IV interaction wherein the reattachment location is characterized by high aerothermal loads [160]. The vortex system observed in this figure — a pair of corner vortices upstream of the interaction, a horseshoe vortex originating at the focus point F , and the swept sidewall vortices — is consistent with the results of Eagle and Driscoll [54] and Morajkar et al. [57].

The variation of RMS of pressure fluctuations on the floor and left sidewall are shown in Fig. 4.3. The contour of mean $c_{fx} = 0$ is shown as a black solid line on both the surfaces. The RMS pressure shows a steep rise across the shock front from its undisturbed value. The amplification of this quantity is higher across the primary interaction as compared to the corner interactions. This occurs most likely on account of reduced shock strength away from the centerline, which in turn is caused by the smearing effect of corner interactions mentioned previously. Within the separated zone on the floor, the RMS pressure fluctuations decrease in magnitude before increasing dramatically downstream of reattachment on the ramp. The peak value occurs approximately at $X = 117$. Farther downstream, the fluctuations gradually decrease and approach the undisturbed level towards the end of the domain. A similar pattern is observed on the left sidewall, with peak values lying along the reattachment line R_1 (see Fig. 4.1).

Figure 4.4 shows the instantaneous snapshot of the flowfield. In order to exclude the right sidewall for visualization purposes, the domain is truncated at $Z = 16$. Contours of density gradient magnitude ($|\nabla\rho|$) on four y - z planes highlight the evolution of the shock structure along the streamwise direction. Additionally, contour lines of the same quantity are shown on the centerplane ($Z = 0$) to visualize the centerline shock structure. The iso-surfaces of zero

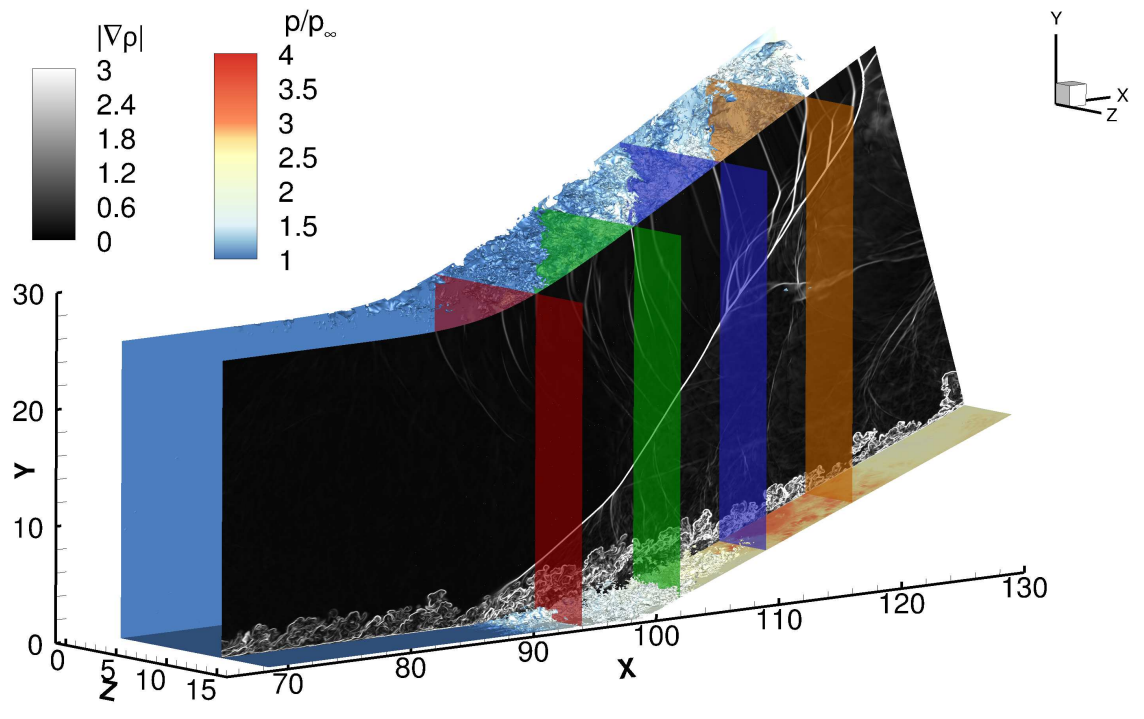
streamwise velocity ($u/U_\infty = 0$), colored by non-dimensional pressure (p/p_∞) distinguish the separated regions on the left sidewall and the floor.

The contour plot of $|\nabla\rho|$ on the streamwise plane at $X \approx 95$ is shown in Fig. 4.4(b). The contours consist of a distinct compression ramp shock, spanning almost the entire domain width. Close to both the sidewalls, the viscous effects cause it to bifurcate into a λ -shock structure. On the planes lying at $X \approx 103$ and $X \approx 110$ in Figs. 4.4(c) and (d) respectively, the spanwise extent of the compression ramp shock gradually decreases on account of increasing separation extent on the sidewalls.

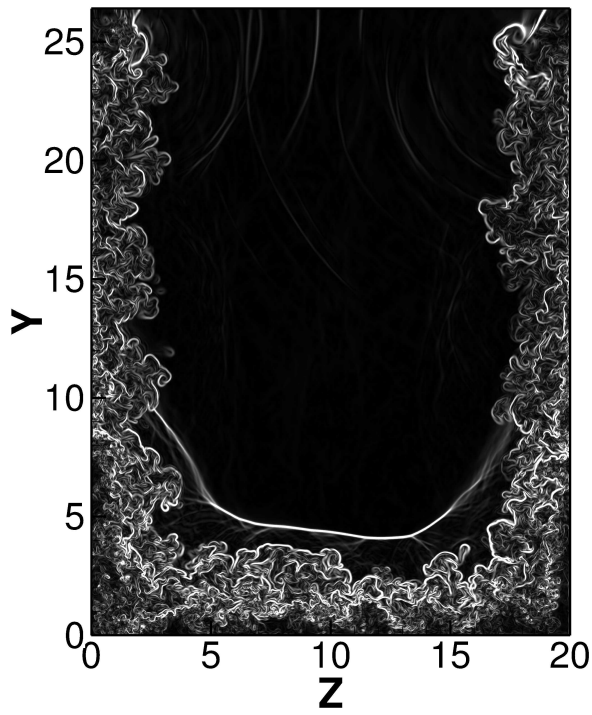
This phenomenon also pushes the λ -shock structures closer to each other and towards the center of the domain. The strength of the reattachment shock — within the λ -shock foot — is higher than the separation shock, which is smeared closer to the left sidewall. Also notice the slip-surfaces emanating from the triple-points. At $X \approx 117$ in Fig. 4.4(e), the two λ -shock structures intersect, leading to reflected shock waves downstream. This event is most likely responsible for the regions of high RMS pressure values on the floor in the range $110 \leq X \leq 120$, downstream of reattachment (see Fig. 4.3).

The iso-surfaces of $u/U_\infty = 0$ indicate earlier separation at the sidewalls, consistent with the mean flowfield shown in Fig. 4.1. On the centerplane, the shock structure resembles that of a quasi-two-dimensional interaction. The separation shock is distinct and higher in strength compared to the reattachment shock, which is relatively smeared. Compression waves emanating from the eddies within the separated shear-layer as well as the redeveloping boundary layer coalesce to form shocklets. The compression ramp shock seems to split into multiple shock waves downstream of the intersection location of sidewall λ -shock structures ($X \geq 110$) and towards the top boundary. Regions lying above the compression ramp shock are populated by unsteady waves.

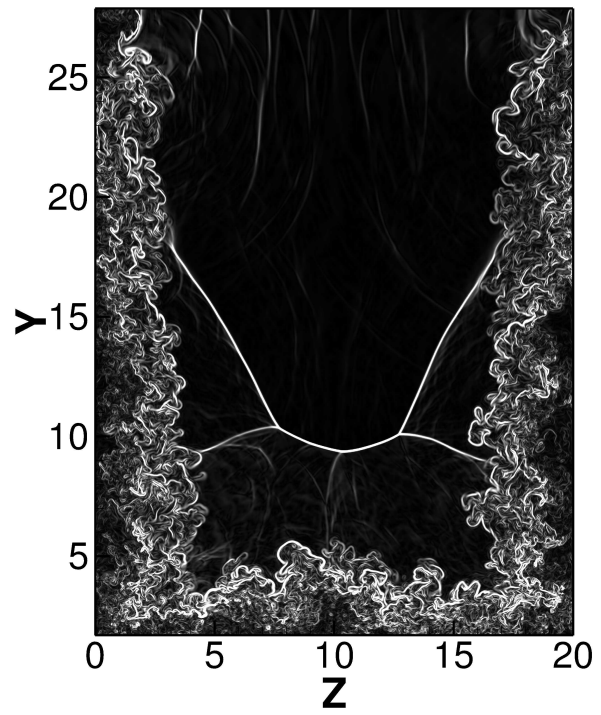
The downstream evolution of the shock structure is shown in Fig. 4.5 using contours of density gradient magnitude. The contours are plotted on four x - z planes at different wall-normal coordinates as shown Fig. 4.5a, with the respective top views presented in Figs. 4.5b–4.5e. At the lowermost wall-normal location in Fig. 4.5b, the compression ramp shock spans a major portion of the domain width. Viscous effects at the sidewalls lead to bifurcation of the shock into a λ -shock foot. Notice the bending of the compression ramp



(a)



(b)



(c)

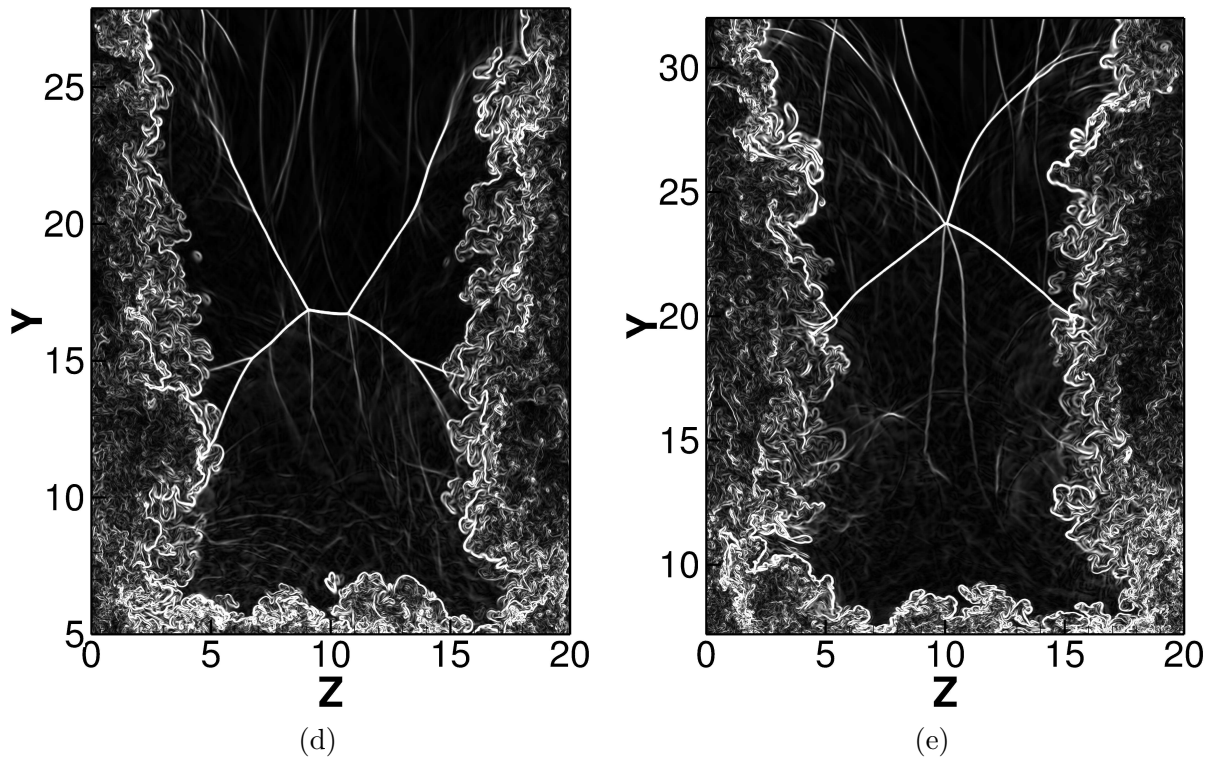
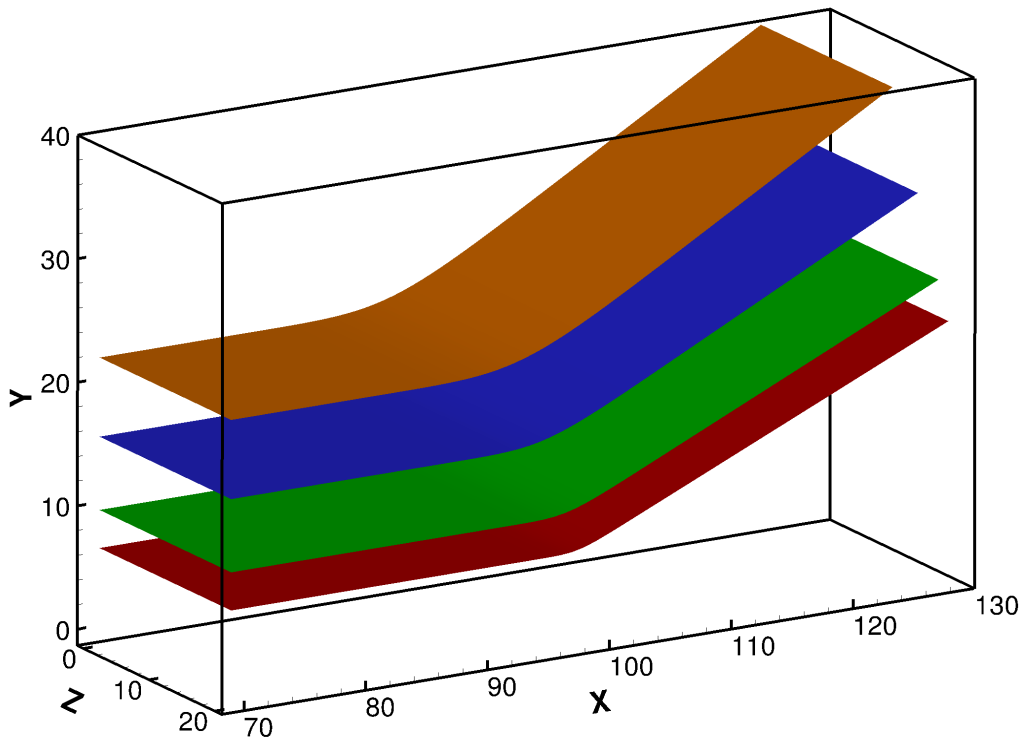


Figure 4.4. Instantaneous flowfield. (a) Iso-surfaces of $u = 0$ colored with the magnitude of non-dimensional pressure. Contours of density gradient magnitude are shown on the centerplane ($Z = 0$) and colored streamwise planes at (b) $X = 95$ (red) (c) $X = 103$ (green) (d) $X = 110$ (blue) (e) $X = 117$ (orange).

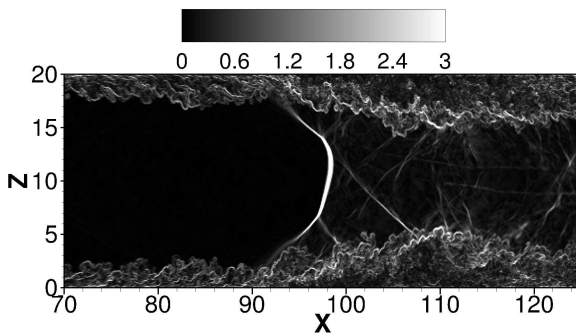
shock caused by sidewall effects. Wang and Sandham [58] and Bermejo-Moreno et al. [59] also observed a similar bending of the incident shock in their study of a reflecting SWTBLI with sidewalls. The latter attributed this to the presence of corner shocks and strong lateral motions. Flow separation on the sidewalls caused by the imposed adverse pressure gradient is also evident from the figure. In each of the subfigures, a complex wave pattern, mostly composed of compression waves emanating from the eddies in the boundary layer, is present in the core flow both upstream and downstream of the shock. These waves correspond to those apparent in the y - z sections in Fig. 4.5.

Figure 4.5c shows the shock structure on the plane $j = 750$. At this height, the spanwise extent of the compression ramp shock is reduced significantly, while strength of the λ -shock feet is higher. There are two sets of slip-lines originating from the triple-points. One is

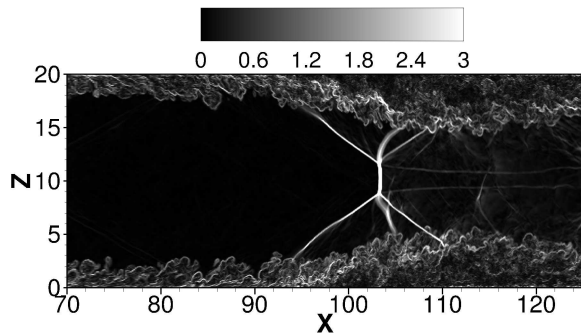
oriented towards the floor (see the plane at $X \approx 102$ in Fig. 4.4), and the other is aligned with the core flow. At $j = 1000$ in Fig. 4.5d, the λ -shock structures on the sidewall are on the verge of intersection. The resulting wave structure towards the domain exit (shown in Fig. 4.5e) resembles a bow-shock, with a clutter of compression waves lying immediately upstream.



(a)



(b)



(c)

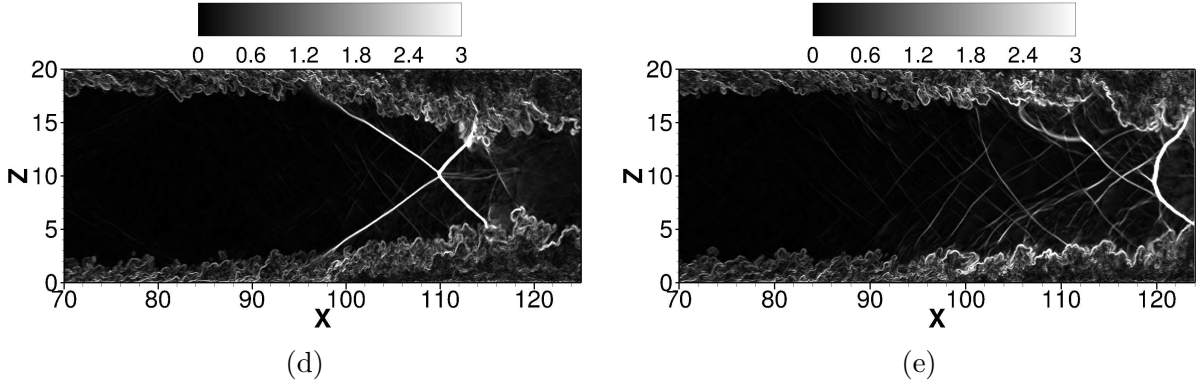
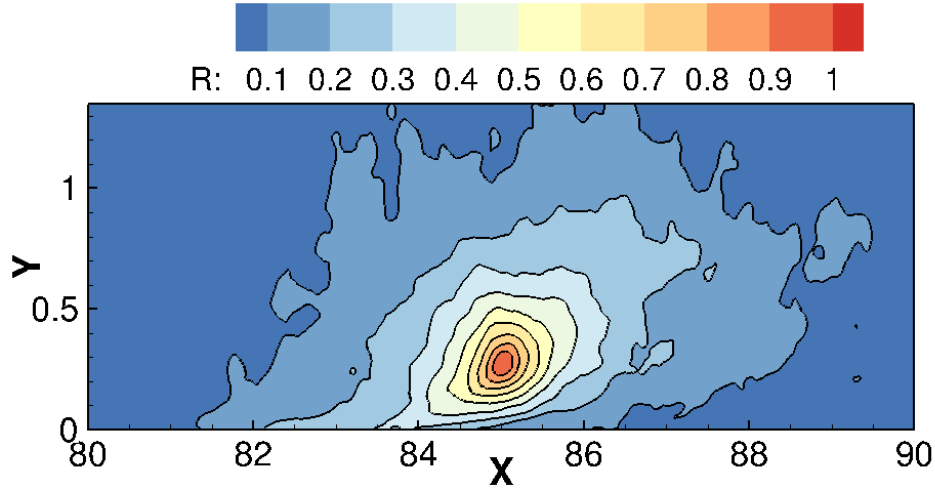


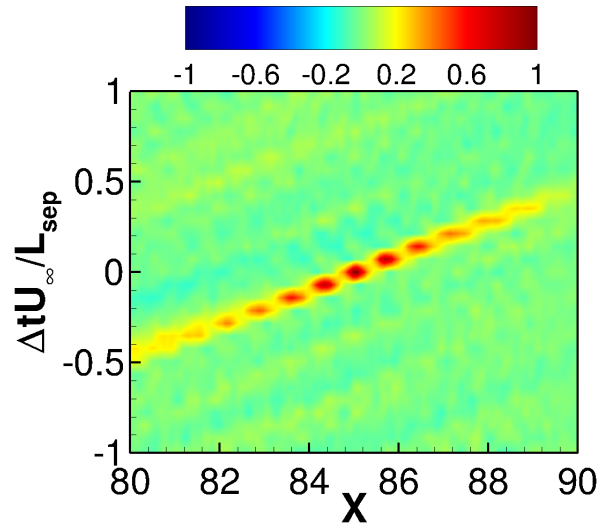
Figure 4.5. Contours of instantaneous density gradient magnitude ($|\nabla\rho|$) on inclined planes (at constant j -values) (a) Location of extracted planes in the domain (b) $j = 620$ (red) (c) $j = 750$ (green) (d) $j = 1000$ (blue) (e) $j = 1270$ (orange).

Figure 4.6 describes the length and time-scale of large-scale structures present in the upstream boundary layer. Two-point and space-time correlations of streamwise velocity fluctuations are used for this purpose. Superstructures in the logarithmic region of a turbulent boundary layer were observed in the experiments carried out by Ganapathisubramani et al. [21], [161], who later showed that the time-scales involved matched closely with that of the low-frequency shock oscillations. Beresh et al. [8], Porter and Poggie [17], and Pirozzoli and Grasso [162] arrived at similar conclusions. For the two-point correlations, the reference signal was extracted at $(X, Y) \approx (85.02, 0.28)$, which was correlated with streamwise velocity fluctuations within the boundary layer and upstream of the interaction.

The contours in Fig. 4.6a are elliptical in shape whose major axes are inclined with respect to the streamwise direction. This angle increases for contours associated with higher correlation magnitude. The nature of the contour plot agrees with the results of experiments of Ganapathisubramani et al. [21], [161]. Based on the $R = 0.5$ contour level, the streamwise length scale is $l_x \approx 1.29\delta_o$. This scale hardly matches the $100\delta_o$ scale found by Ganapathisubramani et al. [21], [161]. Space-time correlations of the same quantity were used to deduce the convection velocity of these structures. The reference point was same as the previous case, and the signal corresponding to that location was correlated with similar signals along the streamwise direction, while maintaining the wall-normal coordinate. The resulting plot



(a)



(b)

Figure 4.6. Characterization of large-scale structure by correlations of streamwise velocity fluctuations (a) Two-point correlations (b) Space-time correlations of streamwise velocity fluctuations.

is shown in Fig. 4.6b. Time delay scaled by the separation extent at the centerline (L_{sep}) and freestream velocity (U_∞) is plotted on the y -axis with the streamwise coordinates on the x -axis. The contour plot exhibits regions of high correlation magnitude along a straight line. The corresponding slope leads to a non-dimensional convection velocity of $U_c/U_\infty = 0.78$.

4.2 Unsteadiness of the flowfield

This section presents a map of unsteadiness in the flowfield by plotting wall-pressure spectra for individual frequency components. Based on previous studies [11], [14], [151], [162], a SWTBLI is typically characterized by mid-frequency motion of the bubble ($St \approx 0.1$) and high frequency Kelvin-Helmholtz shedding ($St \approx 0.5$), in addition to low-frequency shock motion and bubble breathing ($St \approx 0.03$). Grilli et al. [10] used DMD to analyze the unsteady modes in a SWTBLI. Using the first four dominant modes occurring at low-frequency, they were able to reproduce the pulsating motion of the separation bubble and low-frequency streamwise oscillations of the shock. The presence of similar events in this flowfield was investigated by examining the wall-pressure spectra. The spectra were calculated using Welch’s method with 50% overlap between each segment. Based on the net simulation time mentioned in Sec. 2.4.2, a total 908 samples of data at select planes in the domain were available. To estimate the power spectral density, an ensemble of two signals with 454 samples each was created. An additional sample obtained from the overlap process was used for averaging, in conjunction with the original two samples.

The contours of premultiplied spectral energy are plotted initially on the floor (Plane 1), left sidewall (Plane 2), and ramp-normal plane (Plane 5), followed by the centerplane (Plane 6). In the following figures, $fG(f)/\sigma_p^2$ is the premultiplied spectral energy, f is the frequency, $G(f)$ is the power spectral density, and σ_p^2 is the variance. Based on the window segment size, a frequency resolution of $\Delta St = \Delta f L_{sep}/U_\infty \approx 0.03$ was obtained. The contours are plotted for $St_1 = 0.03$, $St_4 = 0.12$, and $St_{18} = 0.54$, where $St_k = f_k L_{sep}/U_\infty = k f_s L_{sep}/N_w U_\infty$. The results for the first case are shown in Fig. 4.7. The domain size was reduced by calculating the spectra at every 10^{th} point in the streamwise direction and every 5^{th} point in the wall-normal and spanwise directions respectively. Mean limiting streamlines, as well as the $c_{f_x} = 0$ contours are superimposed on the floor and left sidewall. Contours of mean density (shown as white lines) are shown on the ramp-normal plane.

We start from the lowest frequency component in Fig. 4.7a. The spectral energy on the floor is higher along a narrow band present at the separation line. As we are dealing with the frequency component typically associated with shock oscillations, this region most likely

corresponds to its intermittent length. Similar regions were also observed by Rabey et al. [62]

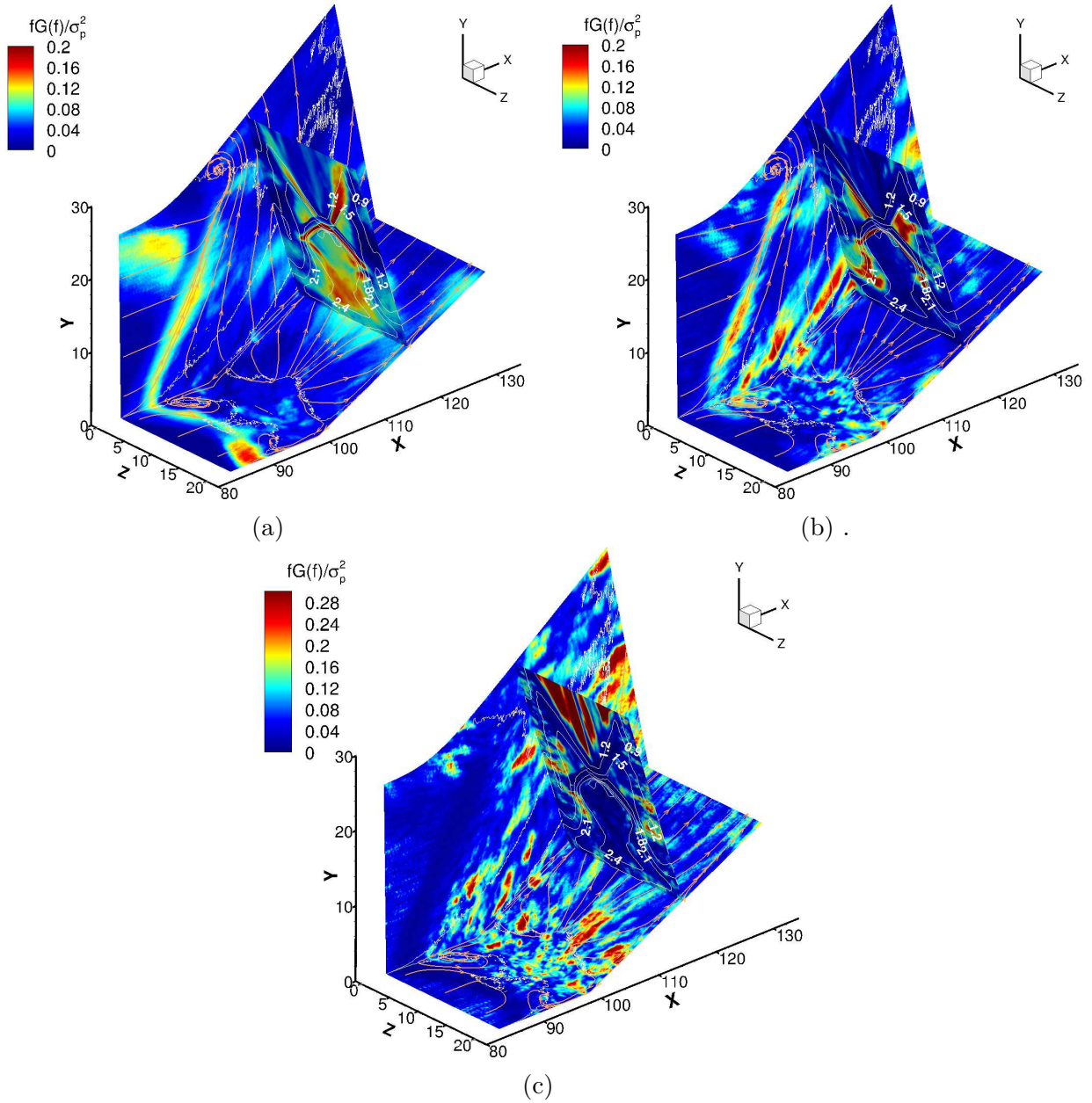


Figure 4.7. Premultiplied pressure spectra on the floor, left sidewall, and ramp-normal plane (a) $St = 0.03$ (b) $St = 0.12$ (c) $St = 0.54$. The $c_{fx} = 0$ contour is shown as a white solid line. Limiting streamlines in orange are included for reference. Mean density contours (white lines) are shown on the ramp-normal plane.

for the case of a reflecting SWTBLI. The contours are asymmetric across the centerline, with higher energy magnitude close to the right sidewall. We expect that such asymmetry would

disappear with averaging over long simulated times. The streamwise extent of this band varies along the span. It is higher close to the sidewalls and decreases progressively towards the centerline. This observation agrees with the results of Rabey et al. [62] which suggest a stronger prevalence of low-frequency content close to the sidewalls for cases with smaller aspect ratios. It is possible that the compression waves generated by the corner separations are locked in with the oscillations of the shock front, thereby resulting in larger regions with dominant low-frequency content.

Moderate magnitudes of spectral energy are observed in a localized region on the ramp ($110 \leq X \leq 125$), downstream of reattachment. This region is also characterized by high values of RMS pressure (see Fig. 4.3), which were a result of reflection of the λ -shock feet on the sidewalls. Hence the moderate to high values of spectral energy can be attributed to the low-frequency oscillations of the shock system post reflection. On the left sidewall, the intermittent length of the swept shock oscillations in the vicinity of the separation line S_1 is distinguished by high magnitudes of energy. The peak value occurs away from the wall at $Y \approx 15$ and decreases dramatically at higher wall-normal coordinates. Farther downstream on the left sidewall, the presence of lower magnitudes suggests that events at higher frequencies occur in these regions.

In the ramp-normal plane, λ -shock feet on both the sidewalls are composed of regions with high energy magnitudes. This observation suggests coherent streamwise oscillations of the entire shock system in the domain. Additionally, moderate magnitudes of energy are also present in the region between the λ -shock feet. This may be a result of a local compression wave system locked in with the oscillations of the shock system. Within the core flow region, the spectral energies increase progressively as the ramp surface is approached. This region consists of several gasdynamic features present in an Edney Type-IV interaction, namely slip surfaces, expansion fans, and impinging jets, and seem to possess similar unsteady characteristics.

Figure 4.7b illustrates the contours of premultiplied energy density associated with the mid-frequency component: $St = 0.12$. On the floor, features such as the narrow band of high spectral energy in the vicinity of separation, as well as a similar localized region present downstream of reattachment on the ramp surface are no longer visible. Instead, both the

sidewall junctures are interspersed with relatively smaller regions characterized by events of this time-scale. Based on their location, it is possible that these events are associated with the corner vortices. On the left sidewall, high magnitudes of spectral energy tracing the intermittent length of the λ -shock foot suggest a mid-frequency component, in addition to a low-frequency component.

Additionally, regions in the vicinity of the $c_{f_x} = 0$ contour as well as along the reattachment line R_1 are characterized by events at mid-frequencies. Physically these events may be representative of the vortex roll-up process, flapping of the separated shear-layer in the vicinity of separation, and unsteadiness of the impinging jet at R_1 . On the ramp-normal plane, regions close to the triple-points are highlighted by high magnitudes of spectral energy. These regions include the λ -shock feet as well as the compression fan system between their legs. Presence of high energy magnitudes over the separation vortex may be indicative of unsteadiness associated with the expansion fan, which typically occurs in the Edney Type-IV interaction.

The contours of premultiplied energy density for a high frequency component ($St_{18} = 0.54$) are shown in Fig. 4.7c. Notice that the bands of high energy magnitudes characterizing shock oscillations on both the floor and left sidewall are no longer present in this case. Instead, regions within the separated zone (delineated by the $c_{f_x} = 0$ contour) are representative of events at this frequency. These zones most likely correspond to the unsteadiness associated with small-scale turbulence. Also, bands of high magnitude of spectral energy are observed at locations in the vicinity of centerline reattachment. Based on the frequency component in consideration, these bands are most likely associated with vortex shedding from the separated shear-layer. A similar trend is observed on the left sidewall. On the ramp-normal plane, the λ -shock feet are no longer distinguished by high energy magnitudes. Following the pattern on the floor and left sidewall, such regions now occur within the separation vortex.

Figure 4.8 illustrates the premultiplied pressure spectra for individual frequency components (used in Fig. 4.7) on the centerplane. Spectral estimates were calculated by adapting the same procedure employed to determine the wall-pressure spectra in Fig. 4.7, with the same frequency resolution. The black solid and dashed lines represent the mean dividing

streamline ($u/U_\infty = 0$) and the sonic line, respectively. The dashed-dotted line in Fig. 4.8c highlights the incoming boundary layer. Starting from the lowermost frequency component ($St = 0.03$) in Fig. 4.8a, the entire extent of the compression ramp shock is characterized by high magnitudes of spectral energy, signifying its low-frequency streamwise oscillations. This region ends approximately at the sonic line. The spectral magnitude drops significantly within the centerline separation region. Regions of moderate energy magnitudes are also present above and below the compression ramp shock. Such regions may be caused by oscillations of certain features of the sidewall interaction, i.e. local compression waves above the shock and expansion fans, slip surfaces below the shock (see Figs. 4.4 and 4.5). Post reattachment, the spectral energy magnitude increases approximately in the range, $116 \leq X \leq 120$. This observation — consistent with the results in Fig. 4.7a — can be attributed to the reflection of sidewall λ -shock feet.

In case of the second frequency component ($St = 0.12$), the contours of premultiplied spectral density shown in Fig. 4.8b exhibit a significantly lower energy magnitude along the trace of the reflected shock foot. Farther away from the floor, high energy magnitudes persist along the remainder of the shock. Hence it seems that motion of the reflected shock foot is dominated by the low-frequency component, while motion of the shock away from the wall is characterized by both low and low-mid frequency components. The sidewall shock system follows a similar trend (see Fig. 4.7b). Contours of premultiplied energy density for the final frequency component ($St = 0.54$) are shown in Fig. 4.8c. In this case, the region within the centerline separation consists of events associated with this time-scale. The compression ramp shock is no longer highlighted by high energy magnitudes. Moderate magnitudes of energy are observed upstream of the interaction, aligned approximately along the Mach lines emanating from the incoming boundary layer. In both the figures, the region of high energy density is present approximately in the top-right corner of the centerplane may be related to the presence of the sponge layer (not included in the figure), and is physically not relevant for this analysis.

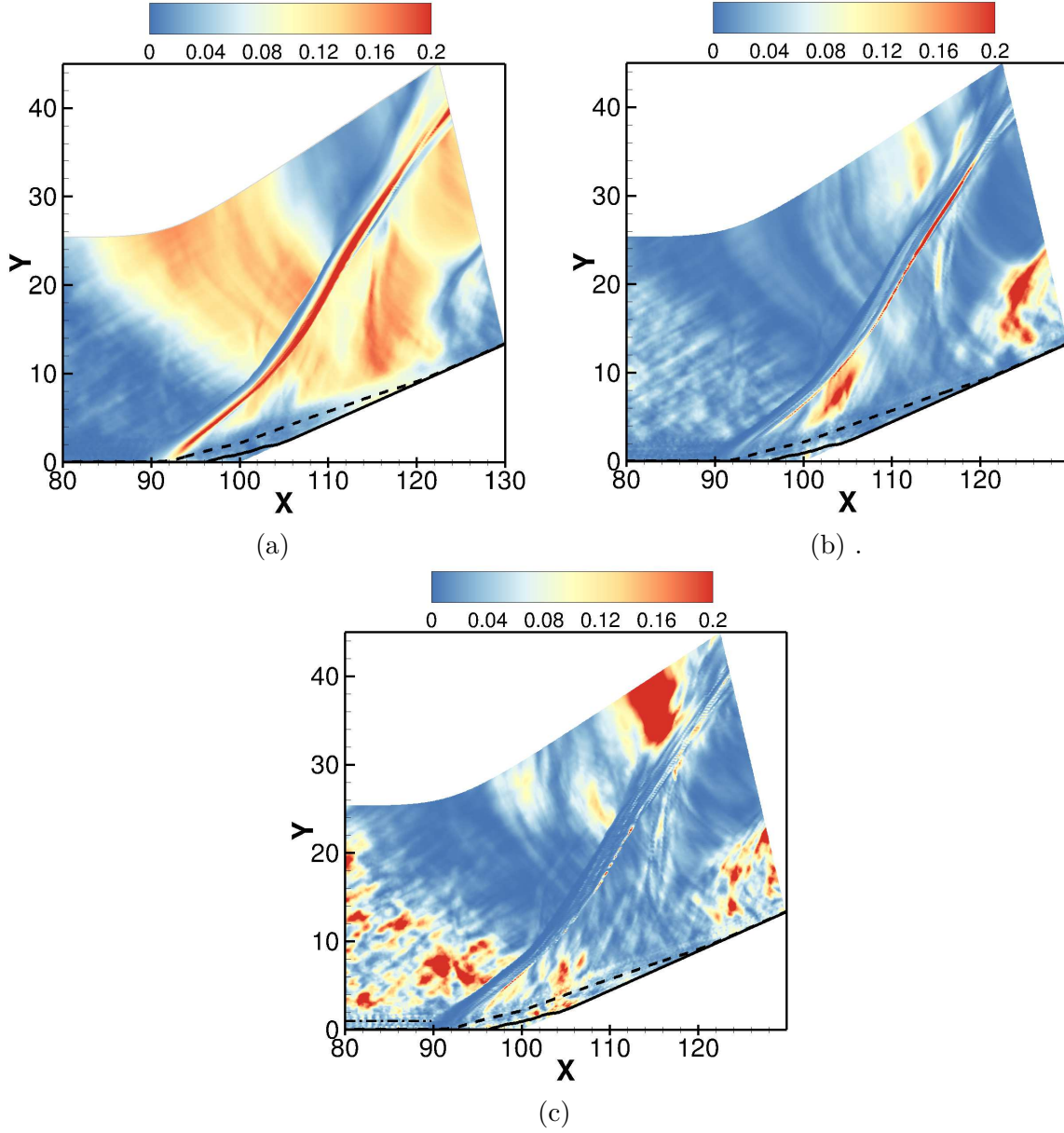


Figure 4.8. Contours of premultiplied pressure spectra ($fG(f)/\sigma_p^2$) on the centerplane ($Z = 10$) (a) $St = 0.03$ (b) $St = 0.12$ (c) $St = 0.54$. Solid and dashed black lines indicate the mean dividing streamline ($u/U_\infty = 0$) and the sonic line, respectively. The dashed-dotted line in part (c) highlights the boundary layer edge upstream of the interaction.

4.3 Unsteadiness of the shock front

This section discusses the spectral characteristics of oscillations of the compression ramp shock and the λ -shock feet on the sidewalls. Henceforth these two features will be collectively

referred to as the “shock front.” The time-histories of shock location are extracted at the centerline and the juncture at the left sidewall. A pressure based threshold method devised by Porter and Poggie [17] was used for this purpose. At every time-step, the instantaneous pressure (\tilde{p}) at the desired location was monitored. The shock location at a particular instant was assigned the streamwise value at which $\tilde{p} \geq p_\infty + 10\sigma_p$, where p_∞ is the freestream pressure and σ_p is the RMS of pressure fluctuations in an undisturbed boundary layer.

The spectral estimates were calculated using Welch’s method. In order to resolve frequencies lower than $St = 0.03$, no windowing was carried out, i.e. the segment size was $N_w = 908$. The corresponding lowermost frequency component is $St_1 = f_s L_{sep} / N_w U_\infty \approx 0.015$. In the case of the centerline shock history, to compensate for the lack of ensemble averaging, the spectra were instead averaged across the span in order to improve the signal to noise ratio. Based on the critical point analysis in Fig. 4.1b, the centerline interaction shows quasi-two-dimensional behaviour for $7.23 \leq Z \leq 12.63$ (marked by red dashed lines in the figure). The aforementioned spanwise averaging was carried out within this domain. In case of the left juncture, spanwise averaging was not possible as that region is characterized by strong three-dimensional effects. The resulting shock spectra are shown in Fig. 3.22.

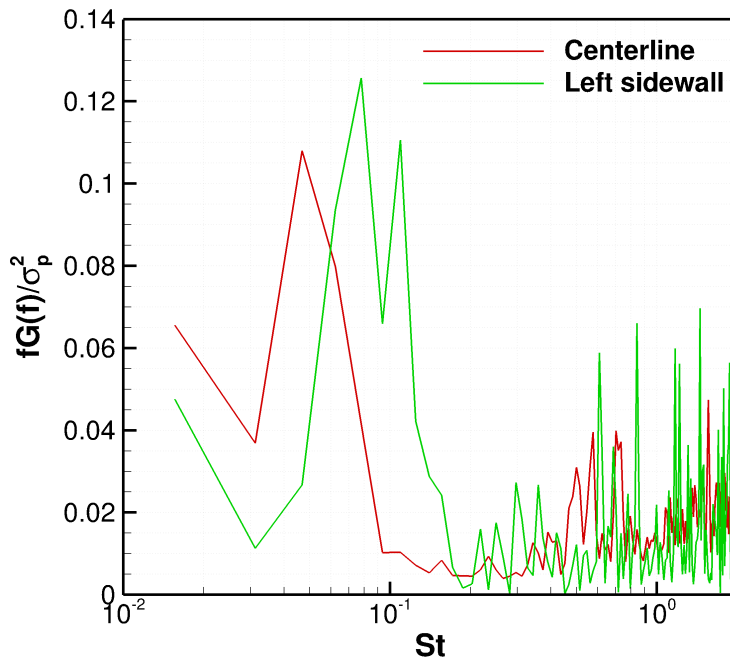


Figure 4.9. Spectra of shock oscillations.

The spectra are shown in premultiplied coordinates, with Strouhal number on the x -axis. In case of the centerline shock, a distinct peak is present $St \approx 0.04$, consistent with the observations in spectra shown in Fig. 4.7. A spectral plot characterizing shock motion at the left juncture shows a peak at a slightly higher frequency ($St \approx 0.08$), but is of the same order of magnitude. A second peak of almost similar magnitude occurs at $St \approx 0.11$, which might be caused by the presence of corner vortices or could be a statistical artifact. A similar trend was observed in the experiments of Funderburk and Narayanaswamy [56], who obtained a higher peak Strouhal number for the corner interaction – $St_L \approx 0.05$ as compared to the primary interaction – $St_L \approx 0.01$, where $St_L = fL_{sep}/U_\infty$. The spectrum for the centerline shock oscillations is slightly smoother at higher frequencies on account of spanwise averaging. Using these respective time-histories, the causes and effects of shock unsteadiness on the entire domain were investigated by calculating the coherence magnitude (see Eq. (2.27)) with pressure fluctuations.

The template used to present the results in Sec. 4.2 is reproduced here, wherein contours of coherence magnitude are shown for individual frequency components. The coherence magnitude was estimated by averaging over an ensemble of two segments, each consisting of 454 samples, resulting in a frequency resolution of $\Delta St = 0.03$. Figure 4.10 displays the contours of coherence on the floor, left sidewall, and ramp-normal plane, as well as on the centerplane. The time-history of centerline shock oscillations was used as the reference signal. Limiting streamlines on the floor and left sidewall are illustrated using solid black lines. On the centerplane, the black solid and dashed lines represent the mean dividing streamline ($u/U_\infty = 0$) and the sonic line, respectively; the mean separation ($x_S \approx 92$) and reattachment locations ($x_R \approx 112$) are also highlighted for reference. Contours of mean density (see Fig. 4.2) are shown on the ramp-normal plane. The corresponding contour labels are not included to reduce clutter. Since the low-frequency unsteadiness associated with shock oscillations is of primary interest, the coherence plots corresponding only to the first two frequency components, i.e. $St_1 = 0.03$ and $St_2 = 0.06$ are discussed. The coherence plots can be interpreted as follows: the red region represents high values coherence (strong linear relationship), the yellow-green region represents moderate values of coherence (weakly-

linear relationship), and the blue region is comprised of low coherence magnitudes (weak or non-linear relationship).

In case of the lowermost frequency component shown in Fig. 4.10a, a band of high coherence magnitude on the floor, lying approximately at $X = 90$ is indicative of the pressure fluctuations induced by the low-frequency shock motion. This band is slightly skewed in the upstream direction towards the left sidewall. Small patches of moderate to high coherence are observed within the centerline separation, suggesting an overall weakly-linear relationship of shock motion with the corresponding events. Similar regions are present downstream of reattachment. It is possible that they are associated with the unsteadiness of the centerline separation bubble, which in turn affect the shock motion via a feedback mechanism.

On the left sidewall, high to moderate coherence magnitudes present along the primary separation line are caused by the oscillations of λ -shock feet, which are coupled with those of the centerline shock. Any events downstream of the primary separation line seem to be uncorrelated with the centerline shock motion. On the ramp-normal plane, moderate coherence magnitudes are observed shortly downstream of the separation shock foot (of the λ -shock structure), which persist only for a short distance. The portion of the separation shock foot closer to the sidewalls is characterized by low coherence magnitudes. This suggests that the concomitant oscillations are not strongly coupled with the centerline shock motion, and may be caused by a different phenomenon. Regions close to the triple-points consisting of slip-surfaces, as well as on the upper boundary of the separation vortex are well correlated with the centerline shock motion.

On the centerplane in Fig. 4.10b, nearly the entire trace of the compression ramp shock is highlighted by high coherence magnitude. It decreases to low values towards the top-right corner of the domain. Additionally, high values of coherence below the compression ramp shock ($x_R \leq X \leq 125$) may be indicative of low-frequency oscillations of the shock front formed due to interaction between the sidewall λ -shock feet (see Fig. 4.4). Moderate values of coherence are present in the vicinity of the mean reattachment location, which is consistent with the results of Thomas et al. [5], Priebe and Martin [141], and Agostini et al. [151].

Figure 4.10c shows the trend of coherence for the frequency component $St = 0.06$. On the floor, the previously observed band of high coherence does not extend across the entire

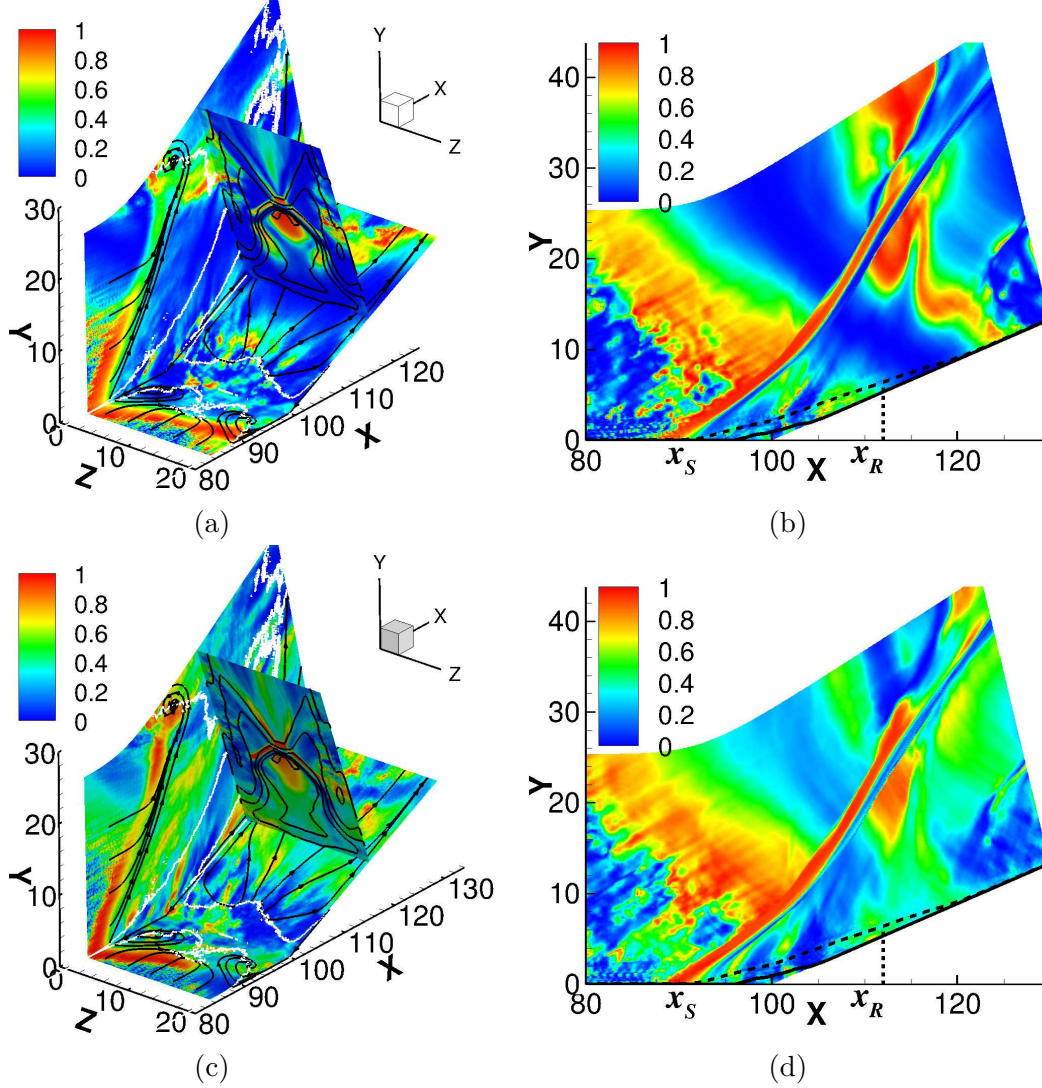


Figure 4.10. Coherence of centerline shock oscillations with pressure fluctuations for frequency component: (a,b) $St = 0.03$ (c,d) $St = 0.06$. In parts (a) and (c), the solid black and white lines on the floor and left sidewall represent the limiting streamlines and $c_{f_x} = 0$ contour, respectively. Solid black lines on the ramp-normal plane indicate the mean density contours. Solid and dashed black lines on the centerplane in parts (b) and (d) indicate the mean dividing streamline ($u/U_\infty = 0$) and the sonic line, respectively.

span. Instead, it begins from the left juncture and ends at $Z \approx 16$. Akin to the previous case, this region is skewed in the upstream direction towards the left sidewall, though the skew angle is comparatively higher. The coherence decreases to moderate magnitudes towards the right sidewall. Based on the limiting streamlines, the events at the foci F_1 and F_2 display a

weakly-linear relationship with the shock motion. Increased coherence magnitudes are also observed for events within the separated zone and downstream of reattachment.

On the left sidewall, coherence increases along the primary separation line as well as downstream of this location. A similar pattern is noted on the ramp-normal plane, with the exception that the motion of λ -shock feet are not well correlated with the centerline shock oscillations at this particular frequency. The coherence contours on the centerplane for this frequency component follow a similar pattern as that in the case of $St = 0.03$. A similar exercise was carried out with the left sidewall shock location history as the reference signal (not shown here for brevity). The coherence contours for the lowermost frequency components ($St = 0.03$ and 0.06) mostly followed the trend present in Fig. 4.10. Some notable differences were manifested as increased coherence magnitudes as well as a higher skew angle of the band of high coherence on the floor. Additionally, the coherence plots indicated that the left sidewall shock oscillations were in-phase with those of the centerline shock.

Based on these results, we make some inferences regarding the nature of oscillations of the shock front. Figure 4.10 highlighted a band of high coherence on the floor, skewed in the upstream direction at the left sidewall. This observation suggests that the portion of the shock front lying on the left of the centerplane ($Z = 10$) translates upstream. This upstream movement may be caused by the expansion of the sidewall separation region. Similar phenomenon can be expected to occur at the right sidewall, resulting in the alternate back and forth movement of the interaction. Porter and Poggie [65] used conditional averaging to observe similar large-scale asymmetric motion. In case of the lowermost frequency component ($St = 0.03$), the coherence magnitude along the separation shock foot (within the λ -shock structure) suggests a non-linear coupling with the centerline shock oscillations. On the other hand, the motion of the reattachment shock foot and slip surfaces are locked in with the centerline shock motion.

Figure 4.11 shows the space-time correlations of streamwise velocity fluctuations upstream of the interaction, with the centerline shock oscillations. The correlations estimates were calculated by averaging over an ensemble of two signals with 454 samples each. The signals are extracted along the wall-normal direction at $X \approx 85.02$. The contour plot in

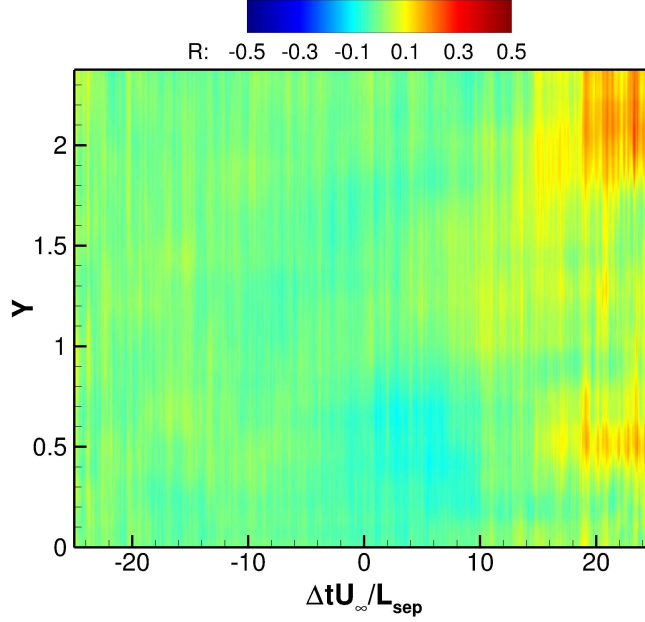


Figure 4.11. Upstream influence of large-scale structures on separation shock motion.

this figure shows variation of the correlation magnitude along the wall-normal direction, corresponding to various values of non-dimensional time delay. The edge of the boundary layer lies at $Y \approx 1.1$. In this figure, localized regions of high correlation magnitude are observed both within and outside the boundary layer edge. They occur at positive values time delay, which lie in the range $20 \leq \Delta t L_{sep} / U_{\infty} \leq 30$. Therefore any event occurs first in the upstream boundary layer, which then affects the shock motion. Additionally, positive correlations suggest that a downstream movement of the shock foot ($x_{shk} > 0$) is associated with a higher net momentum in the upstream boundary layer ($u > 0$), and vice-versa. This observation is consistent with the results of Ganapathisubramani et al. [161], Beresh et al. [8], and Porter and Poggie [17]. The Strouhal numbers corresponding to the optimal values of time delay ($St = 1/T$) lie approximately in the range $0.03 \leq St \leq 0.05$, which includes the dominant frequency of centerline shock oscillation (see Fig. 4.9). Localized region of high correlation magnitude outside the boundary layer edge may be representative of Mach waves locked-in with the shock oscillations.

4.4 Unsteadiness of the centerline separation bubble

In this section, we focus only on the centerline separation. The unsteadiness of separation bubble breathing is characterized in terms of its spectral content. Coherence magnitudes are used to determine the relationship with other events in the domain, which is analogous to the approach used in Sec. 4.3. We begin by estimating the spectra of separation bubble breathing using the procedure described in Eq. 3.3 in Sec. 3.4. Once the mass-history was obtained, the spectra were calculated using Welch’s method without segment averaging in order to resolve the lower frequencies. The resulting spectrum is shown in Fig. 4.12. The premultiplied spectral density is plotted on the vertical axis and the Strouhal number is shown on the horizontal axis in a logarithmic scale. The spectrum displays a peak at $St \approx 0.11$, with significant energy present in the lower frequencies. Previous studies on SWTBLI highlighted both the low-frequency breathing mode as well as the mid-frequency mode [4], [128]. The latter is typically the response of the separation bubble to shear-layer flapping or shedding of vortical structures.

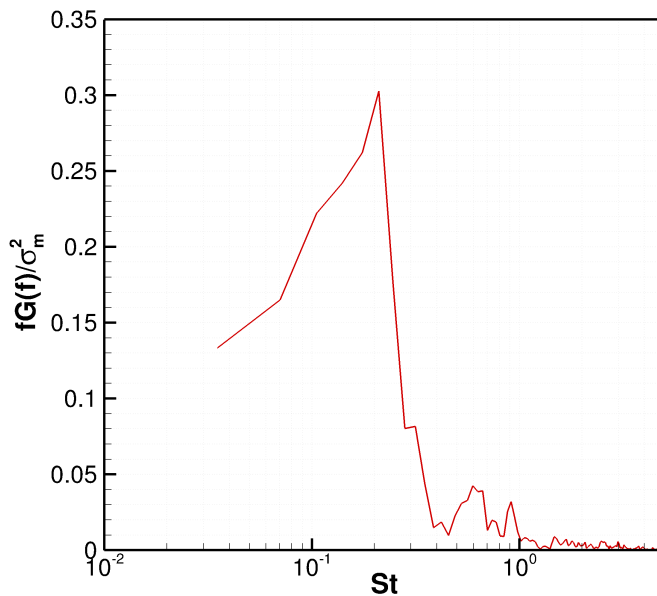


Figure 4.12. Spectra of centerline separation bubble unsteadiness.

The influence of separation bubble unsteadiness on the domain is examined by calculating coherence with the pressure fluctuations. The corresponding contours are shown for

individual frequency components. The coherence estimation technique was similar to the one used in Sec. 4.3, wherein the time-series was divided in two segments with 454 samples each. The corresponding frequency resolution is $\Delta St \approx 0.03$. In this case, the second frequency component: $St = 0.12$, lies close to the dominant frequency obtained from the spectrum in Fig. 4.12. The first frequency component is similar to the one used in Fig. 4.10. Limiting streamlines and the $c_{f_x} = 0$ contour are shown on the floor and left sidewall using solid black and white lines, respectively. The contours of mean density (shown in Fig. 4.2) on the ramp-normal plane as well as the locations of mean separation and reattachment are also included. The corresponding contour labels are not shown to reduce clutter.

Figure 4.13a shows the trend of coherence magnitude for the lowermost frequency component: $St = 0.03$. The separation bubble breathing shows a strong linear relationship with events inside the separated zone (indicated by the $c_{f_x} = 0$ contour) as expected. The coherence magnitude decreases along the span, both towards the left and right sidewall. It is significantly lower along the intermittent length of the shock oscillations (compare with Fig. 4.10a). On the left sidewall, moderate to high values of coherence (in green) are observed within and close to sidewall separation, based on the $c_{f_x} = 0$ contour. Therefore it seems that the breathing motion of sidewall separation zones — hypothesized in Sec 3.3 — are affected by the dynamics of centerline separation. On the ramp-normal plane, the λ -shock structure is characterized by low values of coherence. The region between the shock system and ramp surface is well correlated with the separation bubble motion. On the centerplane in Fig. 4.13b, the trace along the compression ramp shock is characterized by low-coherence magnitudes, suggesting a weak correlation between shock oscillations and breathing motion of the separation bubble at this particular frequency. On the other hand, high coherence magnitudes are present within the centerline separation.

In case of $St = 0.12$ shown in Fig. 4.13c, the coherence magnitude increases along the intermittent length, closely resembling the band of high coherence observed in Fig. 4.10. This result indicates the response of the centerline shock to bubble oscillations at the dominant frequency. Within the separated region on the floor, the coherence magnitude is comparatively lower for this component. Post reattachment, streaks of high coherence approximately aligned with the streamlines on the ramp surface are observed. These streaks are most likely

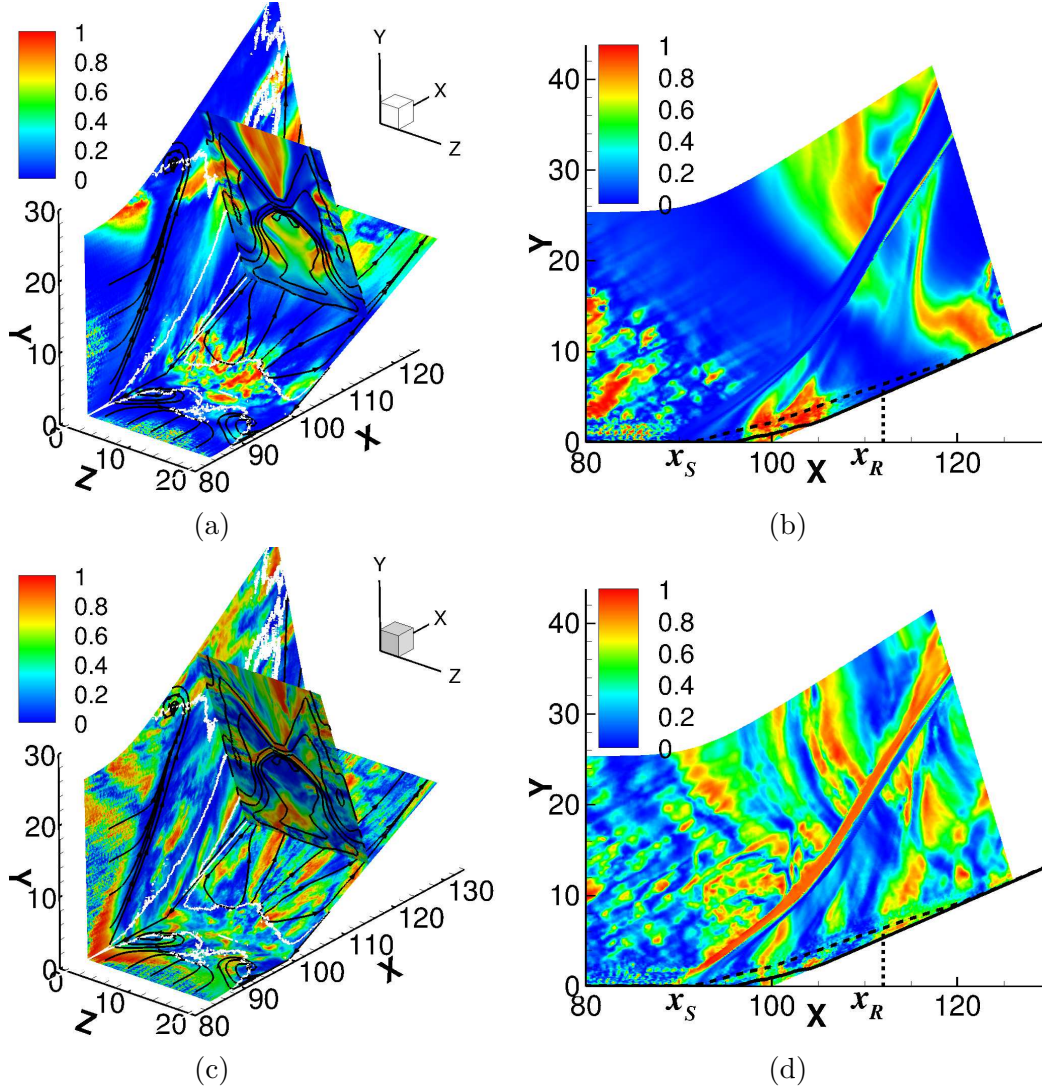


Figure 4.13. Coherence of oscillations of centerline separation bubble with pressure fluctuations for (a,b) $St = 0.03$ (c,d) $St = 0.12$. In parts (a) and (c), the solid black and white lines on the floor and left sidewall represent the limiting streamlines and $c_{fx} = 0$ contour, respectively. Solid black lines on the ramp-normal plane indicate the mean density contours. Solid and dashed black lines on the centerplane in parts (b) and (d) indicate the mean dividing streamline ($u/U_\infty = 0$) and the sonic line, respectively.

a manifestation vortical structures shed from the bubble. On the left sidewall, a small region along the trace of the sidewall shock foot oscillations, lying close to the floor, is distinguished by high values of coherence. The λ -shock structures on the ramp-normal plane are characterized by similar regions. Hence from these observations, it can be said that the bubble

oscillations at this frequency partly drive the motion of the shock front. On the centerplane in Fig. 4.13d, the motion of the compression ramp shock shows a strong linear relationship with the separation bubble breathing motion, suggesting that the latter drives the former at this frequency.

The coherence plot in Fig. 4.10 suggested an asymmetric back and forth motion of the interaction, most likely occurring at low-frequency. From Fig. 4.12, the frequencies corresponding to bubble breathing and shock motion are concentrated at frequencies $St \leq 0.21$. Hence to visualize the motion suggested by the coherence plots, a movie of low-pass filtered velocity field was made (this movie is available on our research group’s website.) A box filter with a cut-off frequency of $St = 0.21$ was used for this purpose. The movies clearly highlighted the spanwise motion of the interaction caused due to alternate breathing motions of the separation bubbles on the left and right sidewalls. Four clips from the movie are shown in Fig. 4.14.

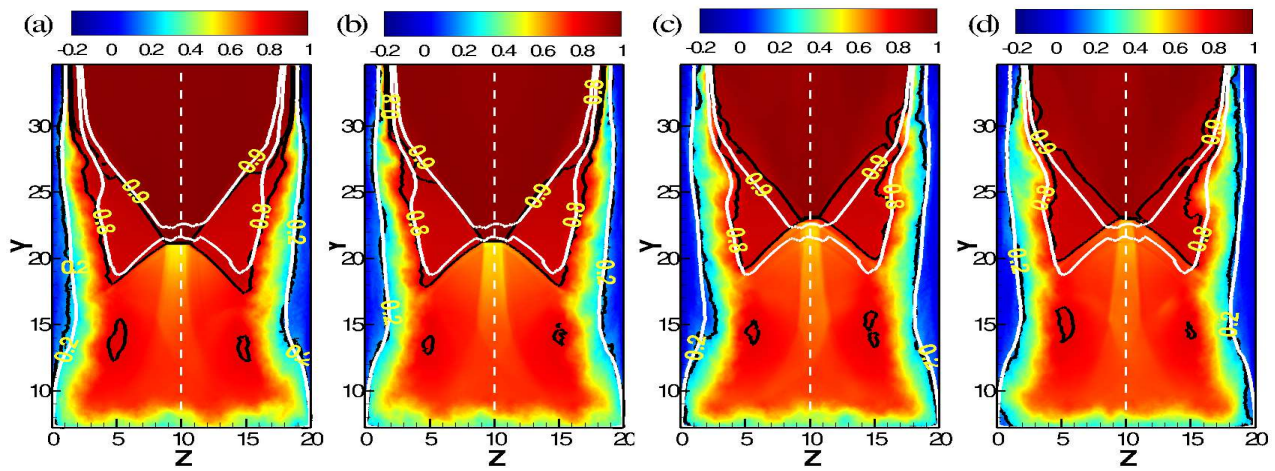


Figure 4.14. Contours of low-pass filtered streamwise velocity field (u/U_∞) on the ramp-normal plane at (a) $t \approx 145 \mu s$; larger right separation bubble (b) $t \approx 332 \mu s$; mean location/equilibrium (c) $t \approx 798 \mu s$; larger left separation bubble (d) $t \approx 871 \mu s$; mean location/equilibrium. Black and white solid lines indicate instantaneous and mean contour levels of: $u/U_\infty = 0.2, 0.8, \text{ and } 0.9$, respectively.

In this figure, the contours of instantaneous streamwise velocity are shown on the ramp-normal plane at $X \approx 116$. The instantaneous contour levels $u/U_\infty = 0.2$ (C1), 0.8 (C2), and 0.9 (C3) are highlighted using black solid lines, with the appropriate labels included.

In order to describe the bubble expansion and contraction process, the mean contours levels (shown as white solid lines) corresponding to the aforementioned values are also included. The spanwise center ($Z = 10$) is shown as a white dashed line.

The contour levels $u/U_\infty = 0.2$ is assumed to be the upper boundary of the sidewall separation bubbles. On the other hand, the contour levels $u/U_\infty = 0.8$ and 0.9 are considered to represent the separation and reattachment shock foot respectively. Figure 4.14(a) shows the expansion of the separation bubble on the right sidewall. Notice that the instantaneous contour level C1 lies above its mean counterpart. This expansion motion is associated with the dilation of the separation bubble on the left sidewall. Hence the interaction moves effectively towards the left and the resulting asymmetry is manifested across the dashed centerline. The instantaneous λ -shock structures lie below their respective mean locations. In Fig. 4.14(b), the separation bubbles on the sidewalls are approximately at their mean location.

Figure 4.14(c) shows the expansion process of the separation bubble on the left sidewall. The interaction moves effectively towards the right, while the separation bubble on the right sidewall contracts below the contour level C1. At this instant, the instantaneous λ -shock structures move above their respective mean locations, possibly as a result of downstream movement of the interaction. The interaction returns to the mean position again in Fig. 4.14(d). The movement of the λ -shock structures seems to be affected by the breathing motion of sidewall separated regions. Also another interesting feature observed in the movies is the presence of localized regions of non-dimensional velocity with magnitude ≥ 0.8 . These regions are present approximately in the range $10 \leq Y \leq 15$, at spanwise locations $Z \approx 5, 15$. Based on Fig. 4.1, these regions are most likely representative of tornado vortices emanating from the focus points F_1 and F_2 respectively (see Fig. 4.1).

To investigate the influence of events originating within the separation bubble in this interaction, space-time correlations of the mass history of the separation bubble and the shock position histories at the centerline and left sidewall juncture were carried out. Similar to Figs. 4.6b and 4.11, the time delay is non-dimensionalized by L_{sep} and U_∞ . Its reciprocal translates to the Strouhal number. The correlation plots are shown in Fig. 4.15.

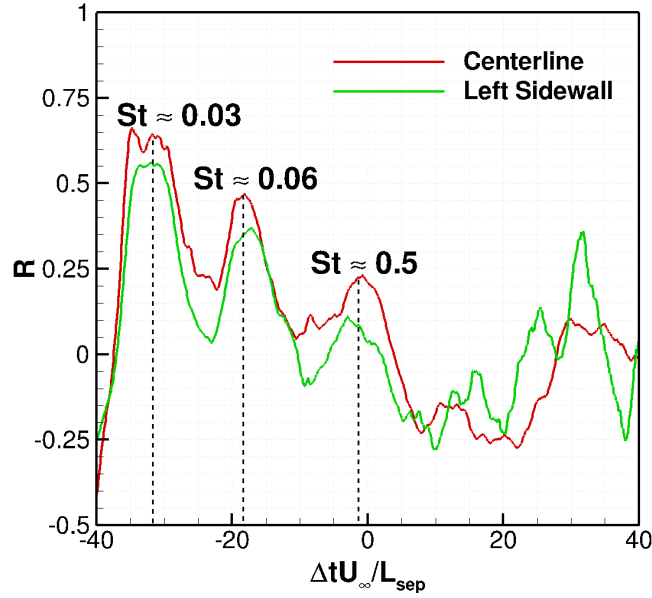


Figure 4.15. Space-time correlation of centerline shock oscillations and separation bubble breathing.

The correlation estimates were calculated without the process of segment averaging in order to resolve higher time-scales. The trend of the correlation curves is almost identical for both the shock location histories. Multiple peaks are observed at negative values of time delay ($\Delta t U_\infty / L_{sep} \approx -32, -18,$ and -2) indicating that an event in the time-history of separation bubble mass precedes a similar event in the time-history of shock motion. The corresponding Strouhal numbers are representative of low-frequency shock oscillations ($St \approx 0.03, 0.06$) and vortex shedding from the separated shear-layer ($St \approx 0.5$). A local peak occurs at a positive value ($\Delta t U_\infty / L_{sep} \approx 32, St \approx 0.03$) of time delay which suggests that certain shock motions trigger the motion of the separation bubble. These observations agree with the results of Dupont et al. [23], [24], Piponniau and Dussauge [25], and Wu and Martin [4].

4.5 Coupling between centerline, corner, and sidewall interactions

This section investigates the extent to which the dynamics of the centerline separation affects the corner and sidewall interactions. Previous studies on confined SWTBLI [62], [65]

have examined the spanwise variation of two-point correlations of wall-pressure fluctuations in the vicinity of the mean separation line. Rabey et al. [62] analyzed the flowfield associated with a reflecting SWTBLI with a confinement ratio $\delta/w = 0.069$. They observed that when the reference point was located at the centerline, the correlations diminished beyond 20% of the half-span. When the reference point was moved towards the sidewalls, the correlation magnitudes decreased beyond the foci. Based on these results, they concluded that the corner and centerline separations did not influence each other significantly.

Poggie and Porter [65] carried out a similar procedure in case of a compression ramp with a confinement ratio – $\delta/w = 0.12$. When the reference point was located at the centerline, high correlation magnitudes persisted up to the sidewall, indicating a relationship between the centerline and corner separations. This is caused by a higher confinement ratio, which translates to higher three dimensionality in the flowfield. On moving the reference point towards the sidewalls, the resulting correlation plot showed no indication of affecting the centerline separation. High correlation magnitudes were localized, thereby suggesting response local events such as asymmetric back-and-forth motion of the interaction or passing of corner vortices.

For the same case, space-time correlations of wall-pressure fluctuations are shown in Fig. 4.16. Segment averaging over an ensemble of two signals (with 454 samples each) was used to calculate the correlation estimates. The spanwise variation of correlations is examined at $X \approx 92$, which lies close to the mean separation line. Time delay plotted on the y -axis is scaled by U_∞ and L_{sep} . The spanwise coordinates are shown on the x -axis. Following the approach Rabey et al. [62], the contour levels lying in the range: $-0.2 < R < 0.2$ are suppressed to mitigate noise.

Figure 4.16a illustrates the correlations with the reference point located at the centerline. Using the threshold mentioned earlier, the extent of well correlated region is $L_z \approx 15$, covering 75% of the span. Starting from the left, the width of this well correlated region decreases across the span. Physically, it represents the time-scale of an event at a particular location. The Strouhal number(s) across the span range from $0.05 \leq St \leq 0.07$, indicating that the pressure fluctuations are caused by the low-frequency shock oscillations. In Fig. 4.16b when the reference point is moved towards the left sidewall ($Z \approx 1.5$), the length

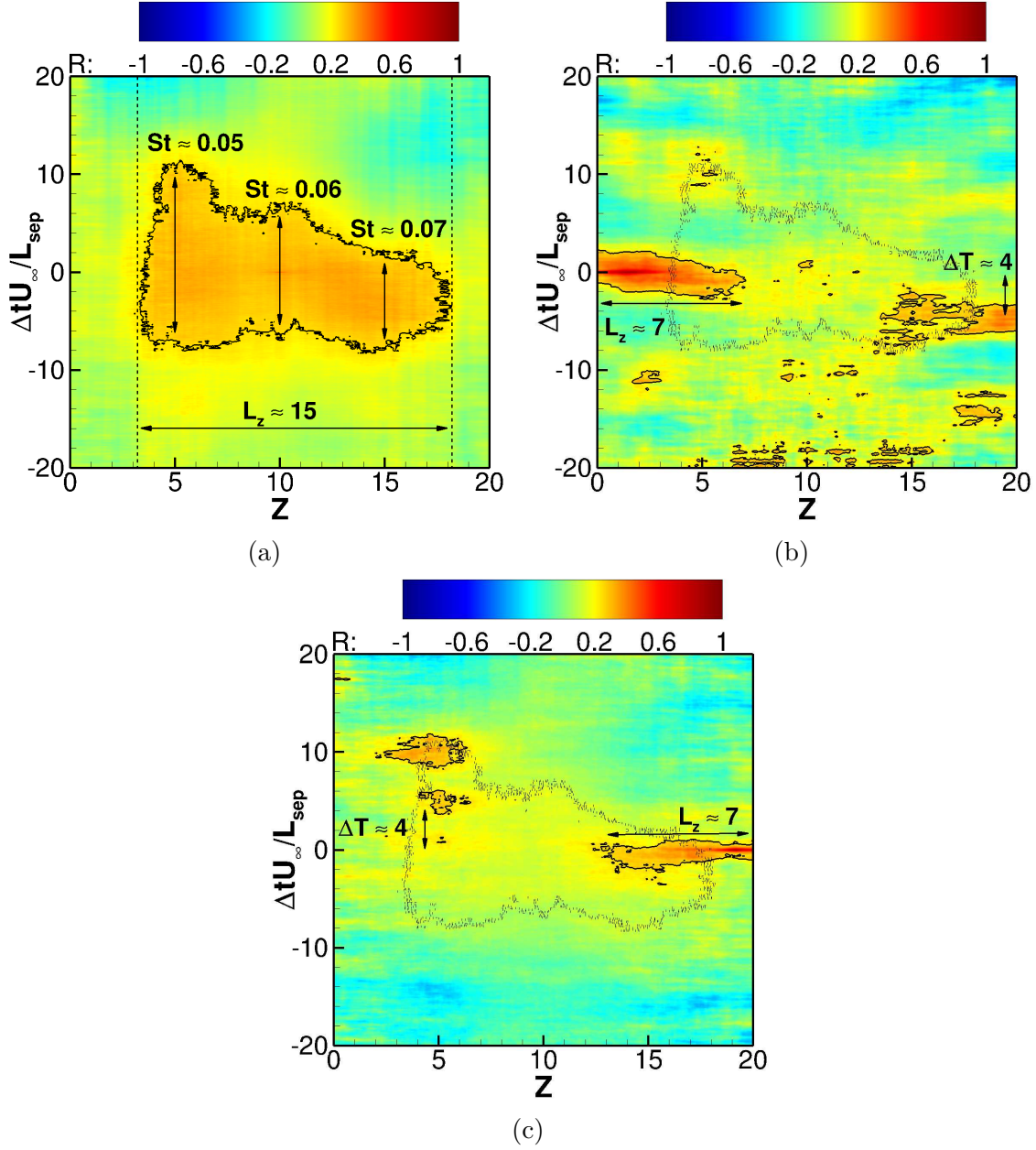


Figure 4.16. Space-time correlations with reference point at $X \approx 92$ and (a) at the centerline ($Z = 10$) (b) close to the left sidewall ($Z \approx 1.5$) (c) close to the right sidewall ($Z \approx 19.2$). Solid lines represent the $R = 0.25$ contour level. Dotted lines in (b) and (c) represent the $R = 0.25$ contour level in (a).

of the well correlated region (L_z) is ≈ 7 , thereby covering about 35% of the span. The corresponding region is roughly elliptical in shape. The Strouhal numbers calculated from the width lie in the range $0.25 \leq St \leq 0.33$. At the right sidewall ($Z \approx 20$), a similar well

correlated region occurs at a non-dimensional time delay $\Delta T \approx 4$. Since this region occurs at a negative value, the event at the left sidewall is preceded by a similar event at the right sidewall. Based on the Strouhal number ($St \approx 0.25$), these events most likely correspond to the alternate passing of the corner vortices.

The well correlated region delineated by the $R = 0.25$ contour level in Fig. 4.16a is also included in this figure. Notice that there is a significant overlap between the well correlated regions in Figs. 4.16a and 4.16b, suggesting that the dynamics of corner separation at the left sidewall extend well into the domain affected by the dynamics of centerline separation. This trend is repeated in Fig. 4.16c, wherein the reference point is located close to the right sidewall. The spanwise extent and shape of the well correlated region is same as the one in Fig. 4.16b, and similar events at the right sidewall occur at the same non-dimensional time delay $\Delta T \approx 4$.

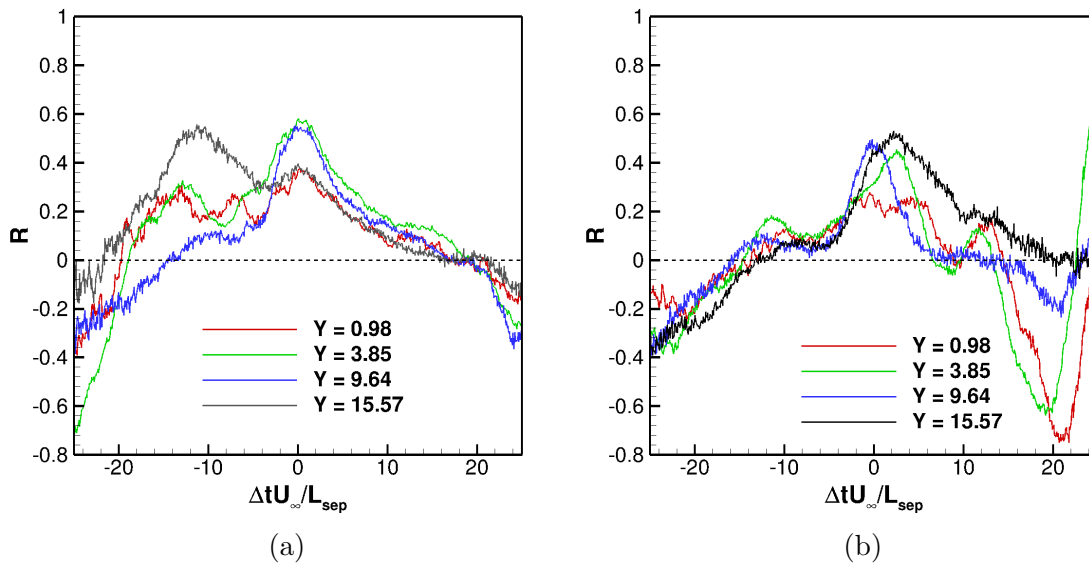


Figure 4.17. Space-time correlation between (a) pressure fluctuations on the centerline and left sidewall (b) pressure fluctuations on the left and right sidewall.

Figure 4.17 illustrates the plots of space-time correlations which determine the relationship between the centerline and sidewall interactions. For the plot shown in Fig. 4.17a, the reference signal was constructed using pressure fluctuations extracted on the floor at $(X, Z) = (90.2, 10)$. This signal is correlated with pressure fluctuations on the left sidewall

along various wall-normal locations, at the same streamwise station. In case of Fig. 4.17b, the reference signal was composed of pressure fluctuations at $(X, Y) = (90.2, 8.55)$. It was then correlated with pressure fluctuations on the right sidewall along various wall-normal locations at the same streamwise location. The correlations estimates were calculated by averaging over an ensemble of two signals with 454 samples each. The non-dimensional time delay used in the previous figure is plotted on the x -axis and the correlation magnitude is shown on the y -axis.

Figure 4.17a determines the relationship between interactions at the centerline and on the left sidewall. For all the cases, there exists a broad region of positive correlation, suggesting in-phase pressure fluctuations (p). At $Y = 0.98$, this region starts at $T \approx -19.8$. Since the time delay is negative, the event first occurs on the left sidewall and is most likely caused by an upstream movement of the corresponding λ -shock structure ($p > 0$). This event is correlated with a similar upstream movement of the centerline shock ($p > 0$) after $\Delta T \approx 19.8$, leading to a positive correlation. The peak at $T = 0$ suggests that the centerline shock and λ -shock structure on the left sidewall are at their most upstream location.

For positive time delays, the event first occurs at the centerline. Downstream movement of the centerline shock leads to the drop in correlation magnitude. At $T \approx 17$, the correlation plot switches signs as the centerline shock moves downstream of the reference station ($p < 0$), while the λ -shock structure is still upstream ($p > 0$). A valley is expected to occur either at the edge of the correlation plot ($T = 25$) or beyond it. This particular feature is representative of the centerline shock at its most downstream location. The elapsed time between when the centerline shock is at its most upstream location (at $T = 0$) and when it reaches its most downstream location ($T = 25$) translates to a Strouhal number of $St = 1/\Delta T = 0.04$. This value corresponds to the centerline shock oscillation frequency and is consistent with the spectrum in Fig. 4.9. In presence of a longer window segment that resolves higher values of time delay, the correlation plot can be expected to trend towards positive value as the λ -shock structure on the left sidewall would have moved downstream of the reference station ($p < 0$), while the centerline shock is still downstream of its mean but is translating upstream.

This trend persists at $Y = 3.85$, but changes slightly at $Y = 9.64$. For this case, upstream motion of the left sidewall λ -shock structure occurs later at $T = -13.67$ since at this height, it is farther away from the reference station (along the streamwise direction). Again, the plot peaks at $T = 0$. Interestingly, this upstream movement occurs earliest at $Y = 15.57$. A possible explanation for this can be attributed to an increased separation extent at higher heights, due to the nature of swept interactions. This in turn causes the separation shock foot (within the λ -shock structure) to reach the corresponding reference station earlier. Notice that for all wall-normal locations, the valley occurs at approximately the same value of positive time delay.

Figure 4.17b inspects the relationship between the interactions on the left and right sidewall. As mentioned previously, the reference signal for this case was extracted at $(X, Y) = (90.2, 8.55)$ on the left sidewall. At negative time delays, the event occurs first on the right sidewall. At $Y = 0.98$, it seems that the plot switches sign to negative values at some value of time delay < -25 . This instant can be interpreted as the λ -shock structure on the right sidewall moving downstream of its reference station ($p < 0$), while that on the left sidewall moving upstream ($p > 0$). The valley at $T \approx -20$ corresponds to the λ -shock structure on the right sidewall at its most downstream location and beginning its upstream motion. This confirms the asymmetric motion deduced from the coherence plots in Fig. 4.10. Poggie and Porter [65] carried out conditional averaging in their analysis of the same flowfield, which highlighted similar asymmetric motions. (See Figs. 16 and 17 in that reference.)

At $T = -13.75$, the right sidewall shock structure moves upstream of the reference station ($p > 0$). The resulting region of positive correlation peaks at $T = 0$ and extends up to $T = 14.28$. Note that at positive time delays, any particular event occurs first on the left sidewall. The latter may correspond to a downstream movement of the left sidewall shock structure ($p < 0$). A valley occurs at $T \approx 20$, after which the plot immediately switches back to positive values of correlation at $T = 24.45$, possibly caused by downstream movement of the right sidewall shock structure. At this instant, both the shock structures lie downstream of their respective reference stations. Considering the shock structure on the right sidewall, the elapsed time between its upstream (at $T = -13.75$) and downstream movement (at $T = 24.45$) is 38.2. This translates to a Strouhal number of ≈ 0.026 , which seems to be a

representative frequency scale of the asymmetric motion of sidewall interactions described earlier.

4.6 Dynamic Mode Decomposition

This section presents the dynamics of dominant modes obtained from the SPDMD process on five planes mentioned in Sec. 2.4.2: wall (Plane 1), sidewalls (Planes 2 and 3), ramp-normal plane (Plane 5), and centerplane (Plane 6). The primitive variables used to construct the data matrix are specified for each case. The results for each of these cases are elaborated in different subsections. The mean and instantaneous flowfields, as well as the details of spectral analysis are presented in Ref. [163], and hence only select results are included here in order to orient the reader. Typically, SBLI's are characterized by low-frequency oscillations of the shock and breathing of separation bubble, low-mid frequency flapping of the separated zone, and high-frequency vortex shedding. The dominant modes corresponding to representative frequencies from each of these bins are analyzed individually for each plane.

4.6.1 Centerplane

The flowfield in Figure 4.2b is analogous to a quasi-two dimensional SBLI, wherein the compression-ramp shock in the freestream bifurcates into a λ -shock foot close to the wall due to boundary layer separation. The separated zone that occurs between the two shock feet is of the “open” type, wherein the fluid is swept away from the mid-span instead of recirculating upstream as in the infinite span case. Figures 4.9 and 4.12 show the spectra of compression-ramp shock location history and mass history of the separation bubble, respectively in premultiplied coordinates. The former peaks in the low-frequency range at $St \approx 0.04$ and the latter peaks in the low-mid frequency range at $St \approx 0.12$.

For this case, the data matrix used to perform SPDMD was: $\{\rho, u, v\}^T$. Due to memory constraints, the domain size was reduced by skipping points in steps of 10 points in the streamwise direction and 5 points in the wall-normal direction, resulting in a total of $3 \times 238 \times 281$ data points. The eigenspectrum as well as the mode amplitudes are shown

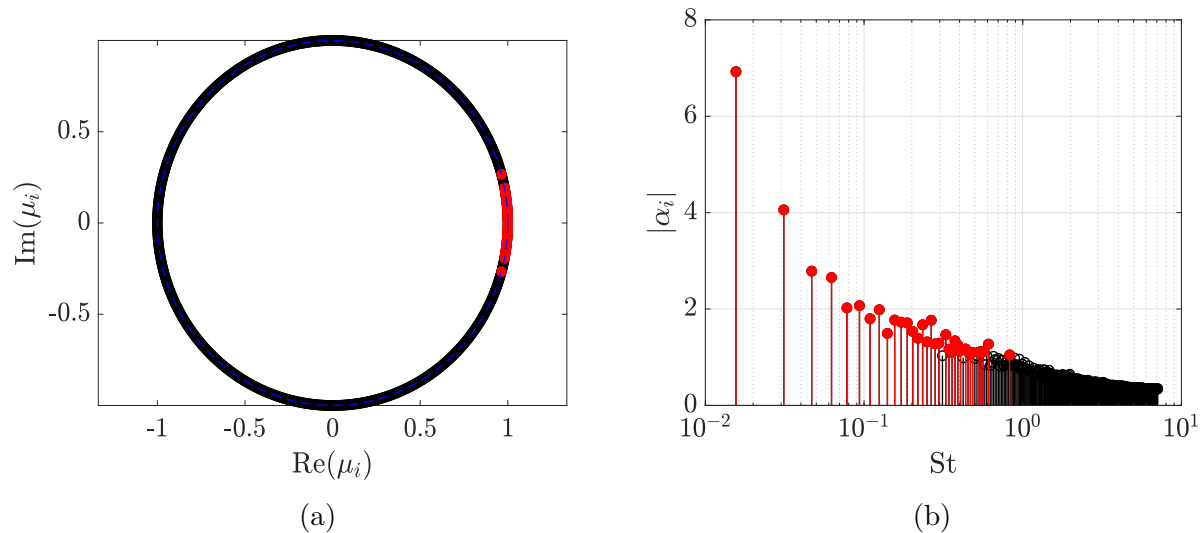


Figure 4.18. DMD modes on the centerplane (a) Eigenspectrum (b) Mode amplitudes. Red markers indicate dominant modes obtained from SPDMD.

in Fig. 4.18. In Fig. 4.18a, all the eigenvalues lie on the unit circle suggesting that the corresponding modes are neutral, i.e. neither damped nor amplified. Such a flow is receptive to forcing (via external disturbances or internal non-linear mechanisms) corresponding to the weakly damped global mode, thus displaying both amplifier and oscillator characteristics, as demonstrated by Poggie and Porter [6]. The optimal mode amplitudes are shown in Fig. 4.18b on the y -axis. The Strouhal number is shown on the x -axis in a log scale. The red markers in both these figures indicate the dynamically significant modes as determined from the SPDMD algorithm. The size of this subset is $N_z = 68$, with the maximum frequency of $St \approx 0.83$. The modal amplitudes decrease monotonically with increasing Strouhal numbers, with the dominant modes lying in the low and low-mid frequency range. Based on the spectra shown in Figs. 4.9 and 4.12 as well as the plot of mode amplitudes shown previously in Fig. 4.18b, choices of representative frequencies from the low and low-mid frequency bands are $St = 0.03$ and $St = 0.12$ respectively. In case of the mid-frequency band, a value of $St = 0.6$ was chosen due its relatively higher amplitude amongst other frequencies in the same band. These values are kept consistent in all the following subsections for simultaneous interpretation of results.

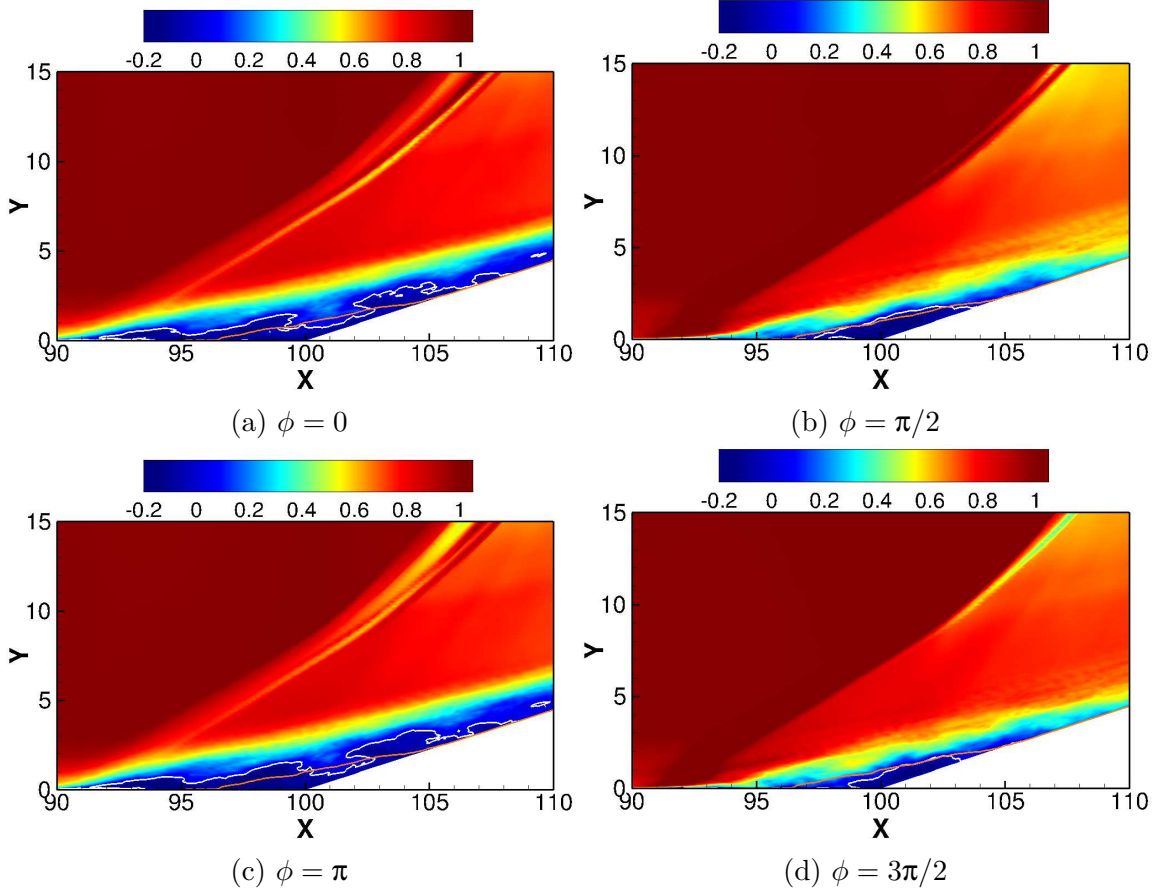


Figure 4.19. Contours of \hat{u}/U_∞ describing the low-frequency breathing of the separated zone and oscillations of the compression-ramp shock. Orange and white solid lines represent the mean and instantaneous mean dividing streamline ($\hat{u}/U_\infty = 0$).

Figure 4.19 shows four instances of the low-frequency mode at $St = 0.03$ for equidistant phase angles: $\phi = 0, \pi/2, \pi$, and $3\pi/2$ via the contours of \hat{u}/U_∞ . The superscript $\hat{\cdot}$ denotes a reconstructed mode. In this figure, boundary of the separated zone is differentiated using the dividing streamline ($\hat{u}/U_\infty = 0$). Mean and instantaneous locations of the same are highlighted using orange and white solid lines respectively. Starting from $\phi = 0$ in Fig. 4.19a, the overall extent of the instantaneous separated zone is larger than its mean counterpart, indicating the bubble expansion phase. The compression-ramp shock — which can be identified as a region of low values of \hat{u}/U_∞ — is at its most upstream location.

At $\phi = \pi/2$ in Fig. 4.19b, the boundary of the instantaneous separated zone lies approximately on the mean dividing streamline. Concurrently, the compression-ramp shock

translates in the downstream direction. Figure 4.19c shows the contour plot at $\phi = \pi$, wherein the instantaneous separated zone expands again, most likely following a contraction phase in $\pi/2 < \phi < \pi$. Notice that the compression-ramp shock translates upstream at this instant. The contraction phase of the breathing motion can be visualized in Fig. 4.19d at $\phi = 3\pi/4$, as indicated by shrinking of the instantaneous separated zone below its mean and downstream movement of the compression-ramp shock. This behaviour is consistent with the observations of Nichols et al. [11] and Pasquariello et al. [128] for the low-frequency mode. The dynamics of other DMD modes at low-frequencies exhibit similar breathing motion of the separated zone and streamwise oscillations of the shock.

The dynamics of the mode at low-mid frequency ($St = 0.12$) are shown in Fig. 4.20. Four instances of this mode are shown for phase angles $\phi = 0, \pi/2, \pi$, and $3\pi/2$. This frequency is typically associated with the flapping motion of the shear layer/separated zone. In order to highlight the same, mean and instantaneous contour levels of $\hat{u}/U_\infty \in [0.3, 0.6]$ which lie within the shear layer are used. For the purpose of analysis, the shear layer is divided into the aft portion, which lies upstream of the ramp corner (at $X = 100$) and the rear portion, which lies downstream of it.

In Fig. 4.20a at $\phi = 0$, the overall aft portion of the shear layer lies above its mean location while the rear portion lies below it. This seems to correlate with the size of the instantaneous separated zone and may represent the entrainment of low-momentum fluid into the aft portion of the shear layer. This is followed by a downward movement of the same at $\phi = \pi/2$ in Fig. 4.20b. At the same instant, the rear portion is at its lowermost position and begins its upward movement. Note the increased separation extent downstream of the ramp corner as compared to Fig. 4.20a. In Fig. 4.20c, the aft portion of the shear layer continues its downward movement. As the separation extent downstream of the ramp corner continues to increase, the rear portion of the shear layer moves upwards. This phase most likely represents the re-injection of fluid into the separated zone. The aft portion of the shear layer begins its upward movement at $\phi = 3\pi/2$ in Fig. 4.20d, while the rear portion starts moving below its mean position. Based on the description, this frequency does represent the flapping motion of the separated zone. A similar phenomenon was also observed by Stantikov et al. [129].

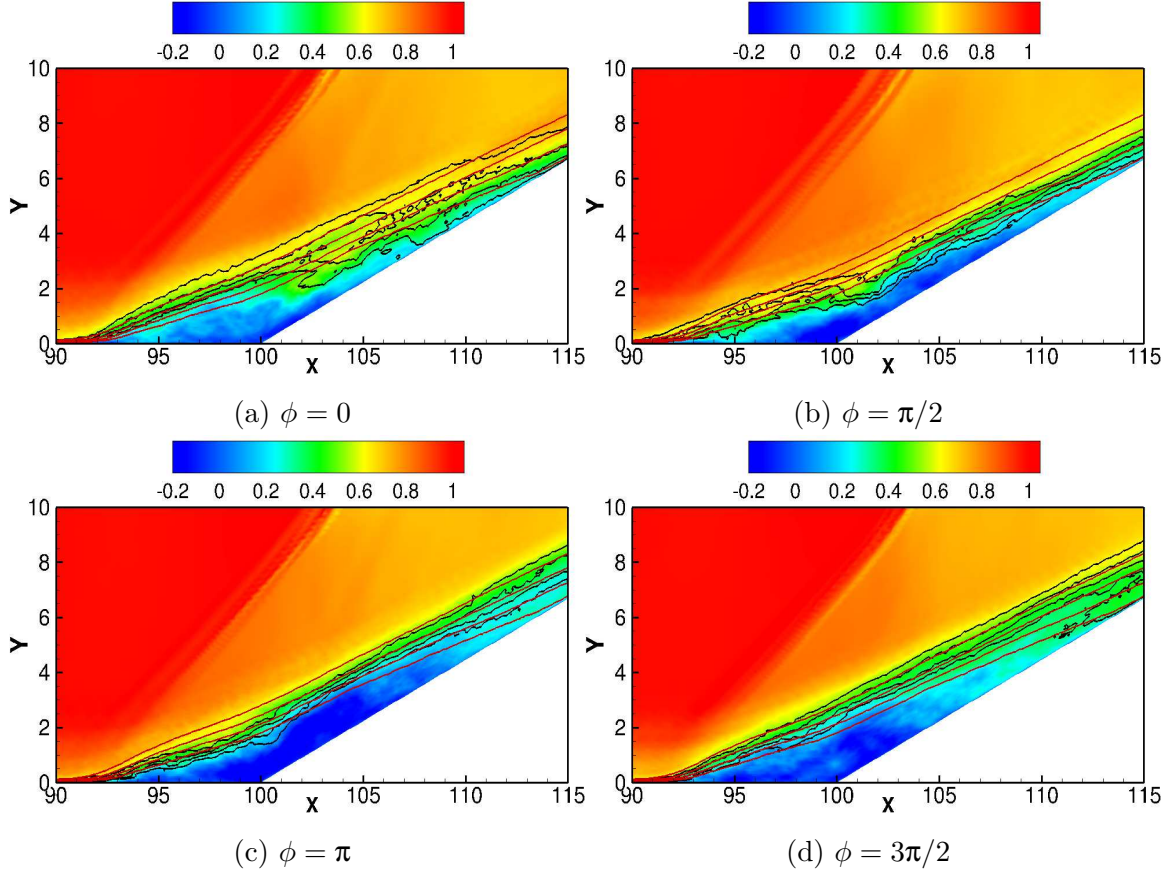


Figure 4.20. Contours of \hat{u}/U_∞ depicting the low-mid frequency flapping of the separated zone. Red and black solid lines represent the mean and instantaneous contour levels of $\hat{u}/U_\infty = 0.3, 0.4, 0.5,$ and 0.6 .

The flapping motion is asymmetric in nature and seems to conform to the hypothesis proposed by Eaton and Johnston [33], which attributes the same to an instantaneous imbalance between the re-injection of fluid in the separated zone and entrainment of fluid by the shear layer. Additionally in Fig. 4.12, the spectrum of the mass-history of the instantaneous separated zone peaks at $St \approx 0.12$. Since the flowfield is highly three-dimensional with an open separation (as indicated by the focus point F in Fig. 4.2b), spanwise transport of fluid away from the centerline may also contribute towards the observed flapping motion.

For the final frequency component, we study the dynamics associated with the mode corresponding to $St = 0.6$ in Fig. 4.21 by examining the contours of $\hat{\rho}/\rho_\infty$. This frequency typically represents vortex shedding from the separated zone. The mean is not added while reconstructing the mode in order to view the vortical structures as density perturbations.

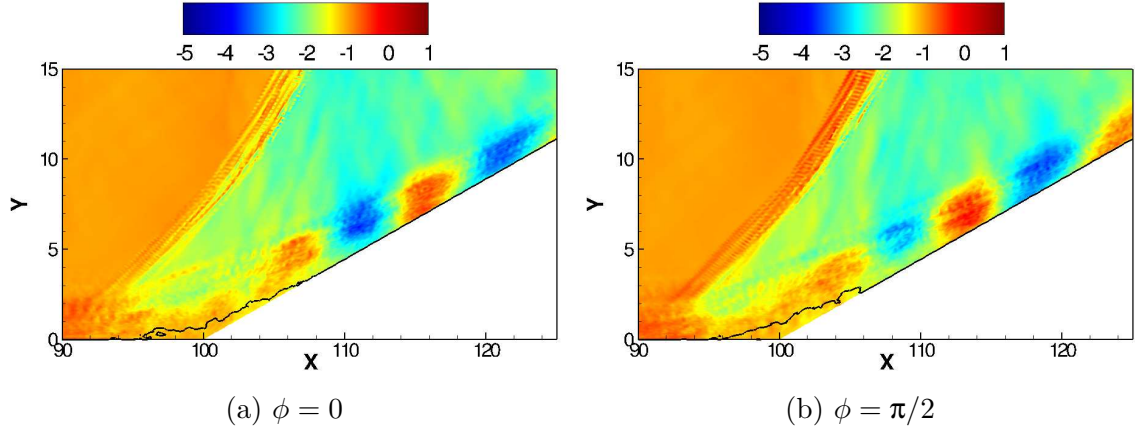


Figure 4.21. Contours of $\hat{\rho}/\rho_\infty$ showing the mid-frequency vortex shedding. The black solid line represents the instantaneous dividing streamline ($\hat{u}/U_\infty = 0$).

Only two phases: $\phi = 0, \pi$ of the reconstructed mode are shown. The instantaneous dividing streamline is shown as a black solid line in order to examine the effect of vortex shedding on the instantaneous reattachment location. Alternating regions of positive and negative density perturbations on the ramp are observed in the figure. In Fig. 4.21a at $\phi = 0$, a region of $\hat{\rho}/\rho_\infty > 0$ is present immediately downstream of reattachment. This is substituted by a region of $\hat{\rho}/\rho_\infty < 0$ at $\phi = \pi$ in Fig. 4.21b, suggesting the presence of a vortical structure. The separation extent is smaller as compared to the one in Fig. 4.21a. Therefore it seems that the instantaneous reattachment location moves upstream after the shedding process and downstream before it begins.

4.6.2 Ramp-normal plane

This section discusses the characteristics of DMD modes on the ramp-normal plane. We start by examining the mean density contours shown in Fig. 4.2d. The sidewalls are characterized by λ -shock structures generated by the bifurcation of the compression-ramp shock, labelled as *CS*. The separation and reattachment shock are labelled as *SS* and *RS* respectively. The right-sidewall separation vortex is highlighted via the streamlines. Farther downstream, the λ -shock structures undergo shock reflection, resulting in a complex wave pattern. From the spectral analysis carried out by Deshpande and Poggie [163], the λ -shock

structures undergo low-frequency oscillations at $St = 0.03$ (see Fig. 5 in that reference). Regions of high spectral energy density at $St = 0.12$ and $St = 0.6$ were present within the separation vortex. Figure 4.22 shows a magnified view of Fig. 4.2d, focused on the bottom-left corner. The corner vortex corresponding to the left-sidewall can be clearly observed. The mean flowfield is approximately symmetric across the centerline ($Z = 10$.)

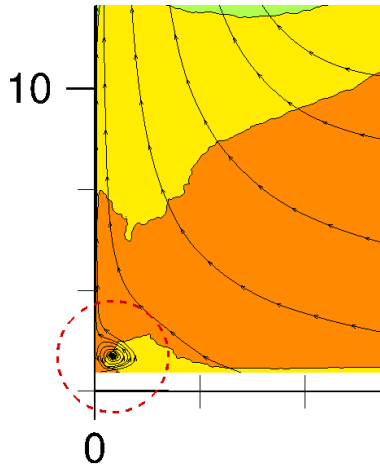


Figure 4.22. Corner vortex at the left-sidewall. See Fig. 4.2d for reference.

The data matrix for this case consisted of $\{\rho, u, w\}^T$. The domain size was reduced by selecting every fifth point in the wall-normal and spanwise directions, resulting in a total of $3 \times 281 \times 281$ data points. The size of the subset of dynamically significant modes is $N_z = 88$, and consists of the representative frequencies used in Sec. 4.6.1. The eigenspectrum as well as the plot of mode amplitudes are shown in Fig. 4.23. In Fig. 4.23a, all the eigenvalues lie on the unit circle indicating neutral modes. The spectrum of mode amplitudes shown in Fig. 4.23b is similar to the one for the centerplane case in Fig. 4.18b, wherein high amplitudes are biased towards lower frequencies.

Figure 4.24 shows the reconstructed low-frequency DMD mode of \hat{u}/U_∞ at three equally spaced phase angles: $\phi = \pi/2, \pi$, and $3\pi/2$. In order to demonstrate the breathing process, the contour value of $\hat{u}/U_\infty \approx 0.5$ is considered the boundary of the separated zone. The mean and instantaneous counterparts are highlighted using solid white and red lines respectively. Additionally, contour lines corresponding to $\hat{w}/U_\infty \approx -0.1, 0.1$ are highlighted using solid and dashed black lines, respectively. They are used to monitor the spanwise motion of

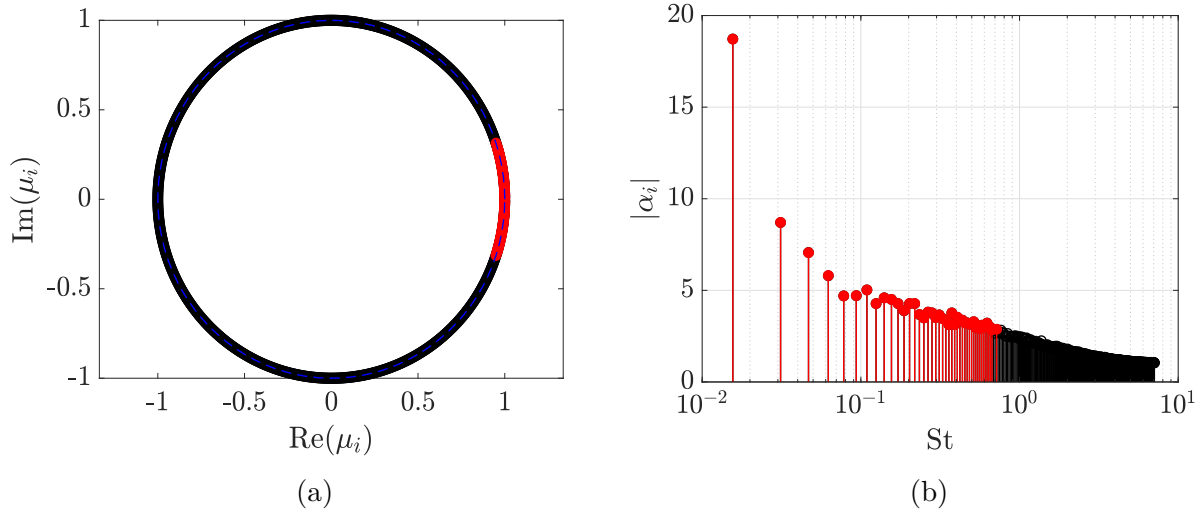


Figure 4.23. DMD modes on the ramp (a) Eigenspectrum (b) Mode amplitudes. Red markers indicate dominant modes obtained from SPDMD.

the separation and reattachment shock feet (within the λ -shock structure; see Fig. 4.2d) for varying phase angles. At each instant, the approximate direction that is followed by a particular shock foot is indicated by an arrow in the figure.

Both the separated zones lie approximately below their mean positions at $\phi = 0$ in Fig. 4.24a. Note that the reattachment shock-system (ensemble of shock structures post-reattachment) translates in the downstream direction at this instant, as evidenced by high magnitudes of \hat{u}/U_∞ along its trace. The separation shock feet move towards the wall while the reattachment shock feet move away and towards the mid-span. In Fig. 4.24b, the separated zones approach their respective mean locations at $\phi = \pi/2$ while the reattachment shock-system begins to move in the upstream direction. The angular span between the separation and reattachment shock feet increases in a forceps-like fashion due to trend reversal in spanwise velocities of the separation shock feet. At $\phi = \pi$ in Fig. 4.24c, expansion of the separated zones occurs simultaneously as the reattachment shock-system translates upstream. The reattachment shock feet now move towards the wall while the separation shock feet continue moving towards the centerline. From the snapshots in this figure, the breathing of the sidewall separated zone occurs in-phase (symmetrically). An expansion of the same is concurrent with the upstream translation of the reattachment shock-system and vice-versa.

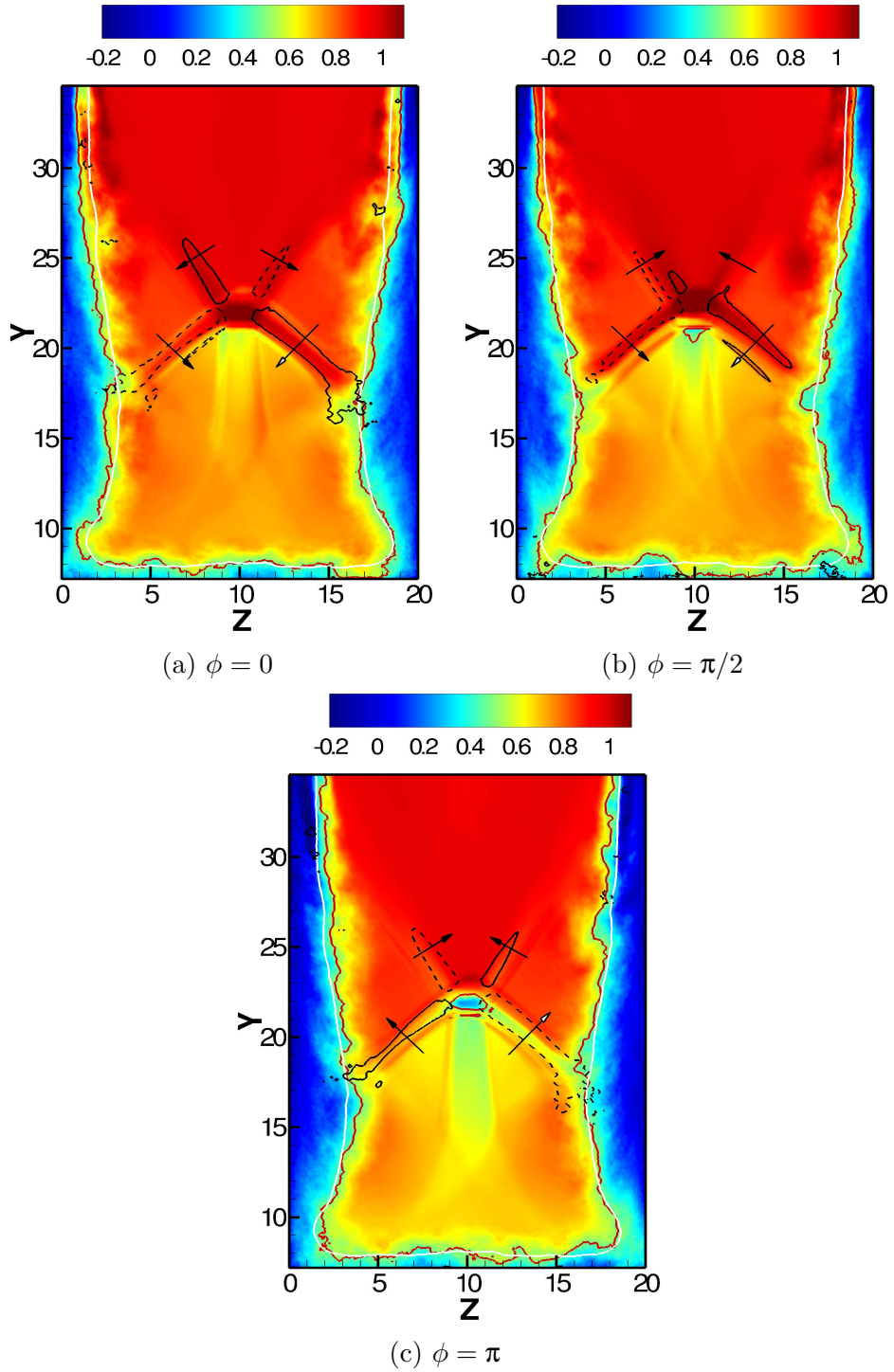


Figure 4.24. Contours of \hat{u}/U_∞ describing the low-frequency breathing of the sidewall separated zones. Red and white solid lines indicate the instantaneous and mean contour levels of $\hat{u}/U_\infty = 0.5$. Solid and dashed black lines highlight instantaneous contour levels of $\hat{w}/U_\infty = -0.1$ and 0.1 respectively.

Additionally, the spanwise movement of the individual λ -shock feet seem to be coupled with the low-frequency breathing motion.

Dynamics of the DMD mode at $St = 0.12$ are described in Figure 4.25 using the contours of \hat{u}/U_∞ . The template used in this figure is adapted from Fig. 4.24. In order to examine the spanwise motion of the reattachment shock-system at this frequency, contour levels corresponding to $\hat{w}/U_\infty = -0.08$ and 0.08 are highlighted using solid and dashed black lines respectively. Starting from $\phi = \pi/2$ in Fig. 4.25a, both the separated zones lie approximately on their mean locations. At $\phi = \pi$ in Fig. 4.25b, the separation size on the right-sidewall increases, while that on the left-sidewall contracts below its mean position. This causes an effective leftward movement of the core flow and the resulting asymmetry can be observed across the centerline. The angular span between the λ -shock feet on the left-sidewall decreases, while that on the right-sidewall increases. Figure 4.25c illustrates a similar phenomenon occurring at $\phi = 3\pi/2$ wherein the left-sidewall is characterized by a larger separated region while that on the right-sidewall decreases, resulting in the rightward movement of the core flow.

Contours of streamwise velocity perturbations \hat{u}/U_∞ shown in Fig. 4.26 are used to study the mode associated with the mid-frequency component, $St = 0.6$. The reconstructed mode does not include contribution from the mean flowfield. Two instances of this mode are shown for phase angles, $\phi = 0$ and $\phi = \pi$ in Figs. 4.26a and 4.26b, respectively. Based on these figures, the vortical structures on the floor move away from the centerline due a strong spanwise velocity component. They are then transported away from the wall, possibly by a combined influence of the sidewall separation vortex and the corner vortex (see Figs. 4.2d and 4.22). This process can be visualized by tracking the encircled structure, which moves towards the left-sidewall at $\phi = 0$ and is swept upwards at $\phi = \pi$ as indicated by arrows in the respective figures.

4.6.3 Wall and sidewalls

This section discusses the modes on the wall and sidewalls corresponding to representative frequencies used in the previous sections. The SPDMD algorithm was applied separately on

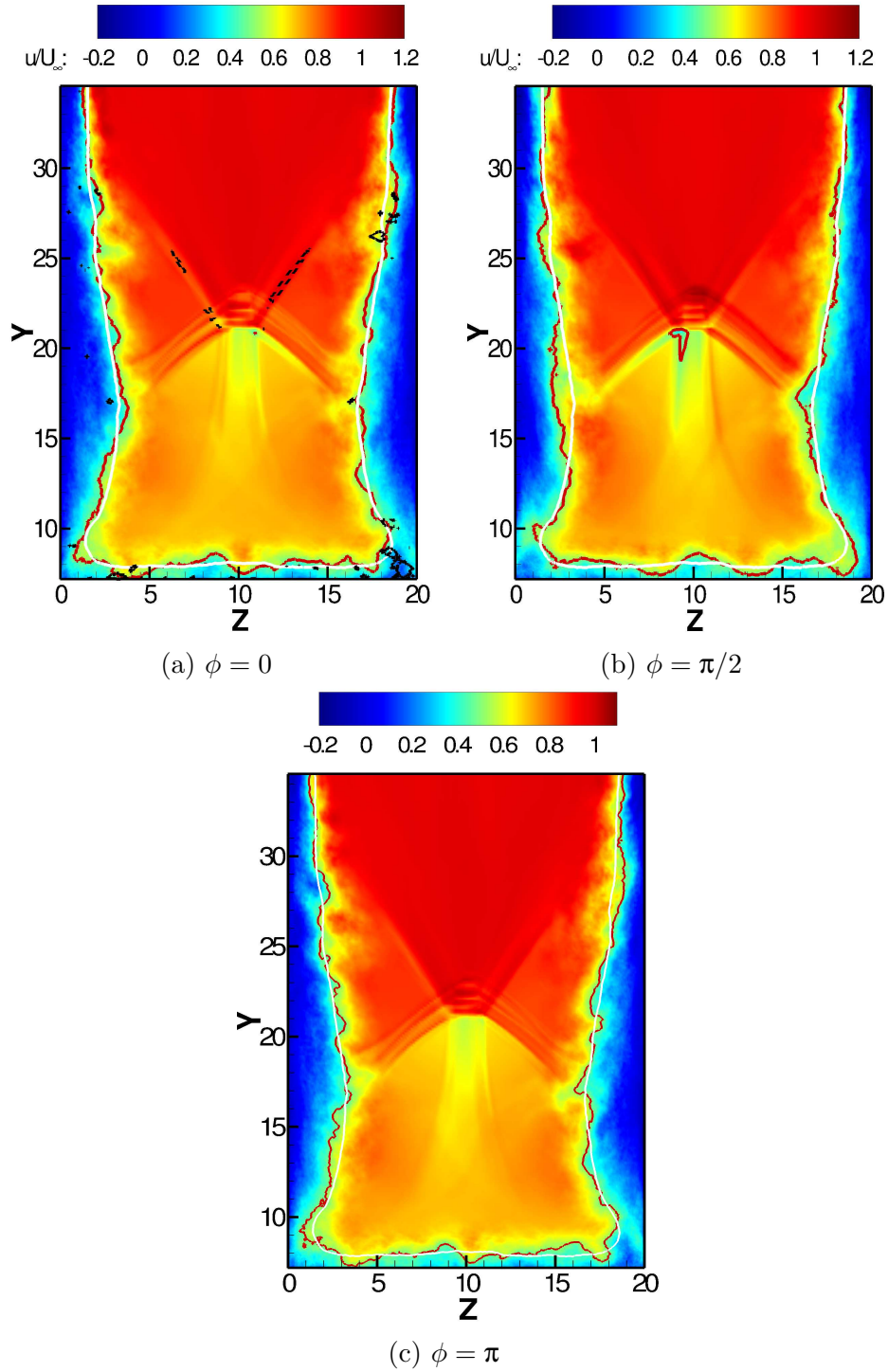


Figure 4.25. Contours of \hat{u}/U_∞ describing the low-mid frequency motion the sidewall separated zones. Red and white solid lines indicate the instantaneous and mean contour levels of $\hat{u}/U_\infty = 0.5$. Solid and dashed black lines highlight instantaneous contour levels of $\hat{w}/U_\infty = -0.08$ and 0.08 respectively.

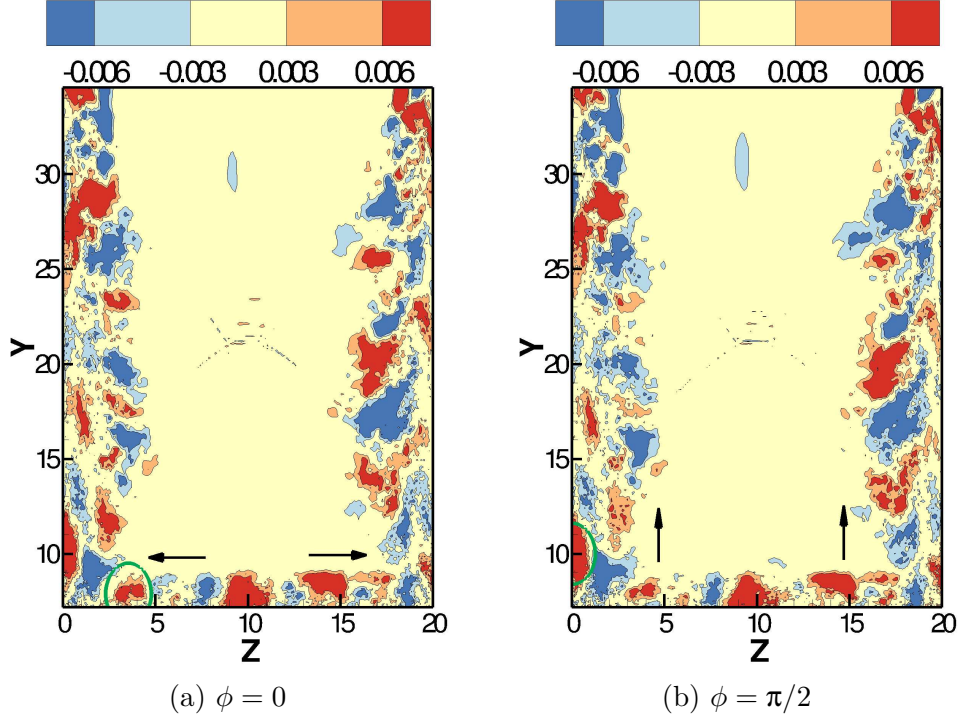


Figure 4.26. Contours of \hat{u}/U_∞ describing the mid-frequency dynamics of the sidewall separated zones.

the wall and each sidewall, using a data matrix consisting of only wall pressure fluctuations. The domain size was reduced by selecting every tenth point in the streamwise direction and every fifth point in the wall-normal and spanwise directions. Total data points on the wall and both the sidewalls were 238×281 and 281×281 respectively. The size of the subset of dynamically significant modes is $N_z = 76$ for all the cases. Since the plots of eigenspectrum and mode amplitudes obtained for all the cases were identical, they are only shown for the case of wall in Fig. 4.27. These plots share similar characteristics to those described in Figs. 4.18 and 4.23.

Figure 4.28 highlights the low-frequency motion of the compression-ramp shock as well as that of the reattachment shock-system formed downstream of mean reattachment at $St = 0.03$. The reconstructed modes are shown at four equidistant phase angles $\phi = 0, \pi/2, \pi,$ and $3\pi/2$. In this figure, the mean and instantaneous levels of $\hat{p}/p_\infty = 0.2$ and 0.4 are shown using red and black solid lines respectively. The former tracks the movement of

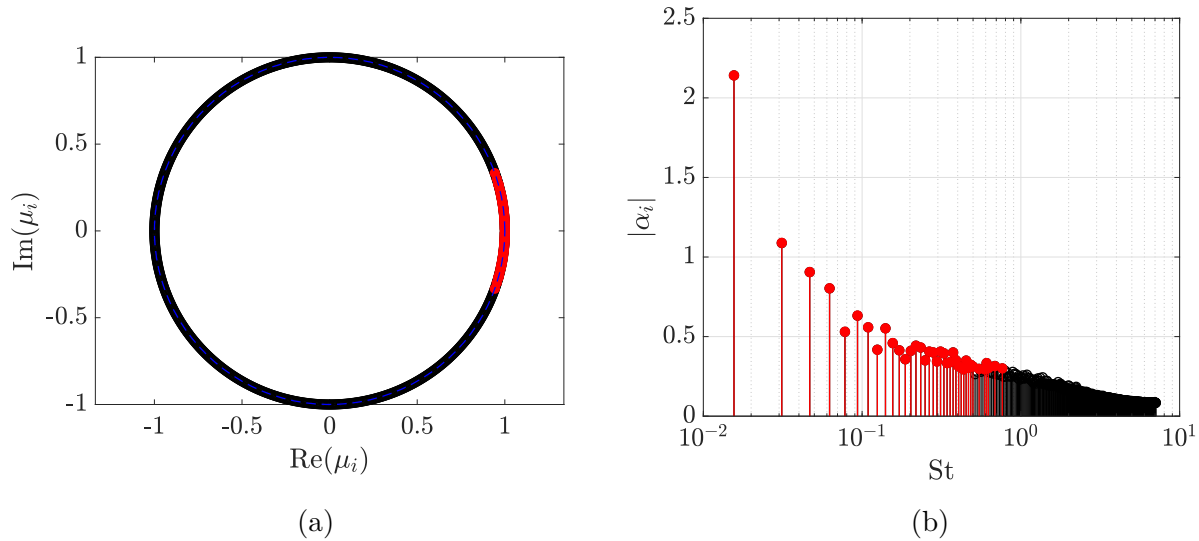


Figure 4.27. DMD modes on the ramp (a) Eigenspectrum (b) Mode amplitudes. Red markers indicate dominant modes obtained from SPDMD.

the compression-ramp shock and the latter monitors oscillations of the reattachment shock-system.

Figure 4.28 highlights the low-frequency motion of the compression-ramp shock as well as that of the reattachment shock-system formed downstream of mean reattachment at $St = 0.03$. The reconstructed modes are shown at four equidistant phase angles $\phi = 0, \pi/2, \pi,$ and $3\pi/2$. In this figure, the mean and instantaneous levels of $\hat{p}/p_\infty = 0.2$ and 0.4 are shown using red and black solid lines respectively. The former tracks the movement of the compression-ramp shock and the latter monitors oscillations of the reattachment shock-system.

Initially at $\phi = 0$ in Fig. 4.28a, the compression-ramp shock lies upstream of its mean location on the wall, while the reattachment shock-system lies downstream. Note the corrugated nature of the latter, wherein the extremities of the contour level (lying in the range $0 \leq Z \leq 5$ and $15 \leq Z \leq 20$) are displaced slightly downstream as compared to the contour level in the vicinity of the centerline. These extremities are most likely caused by the λ -shock structures on the sidewalls. On the left-sidewall, a portion of the compression-ramp shock close to the wall ($0 \leq Y \leq 10$) lies upstream of its mean while the rest of it lies approximately on its mean. The trace of the reattachment shock-system lies on its mean on the

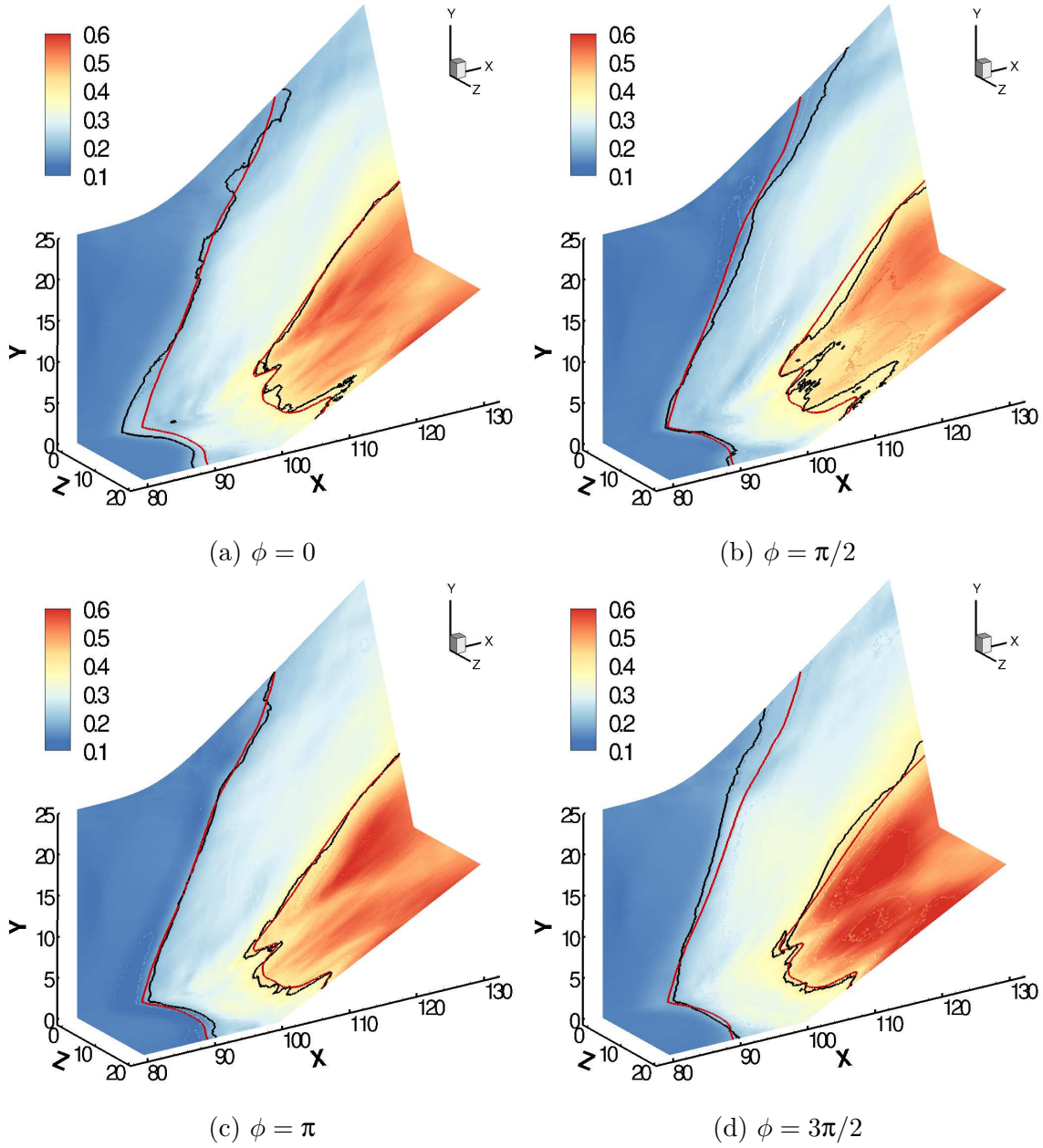


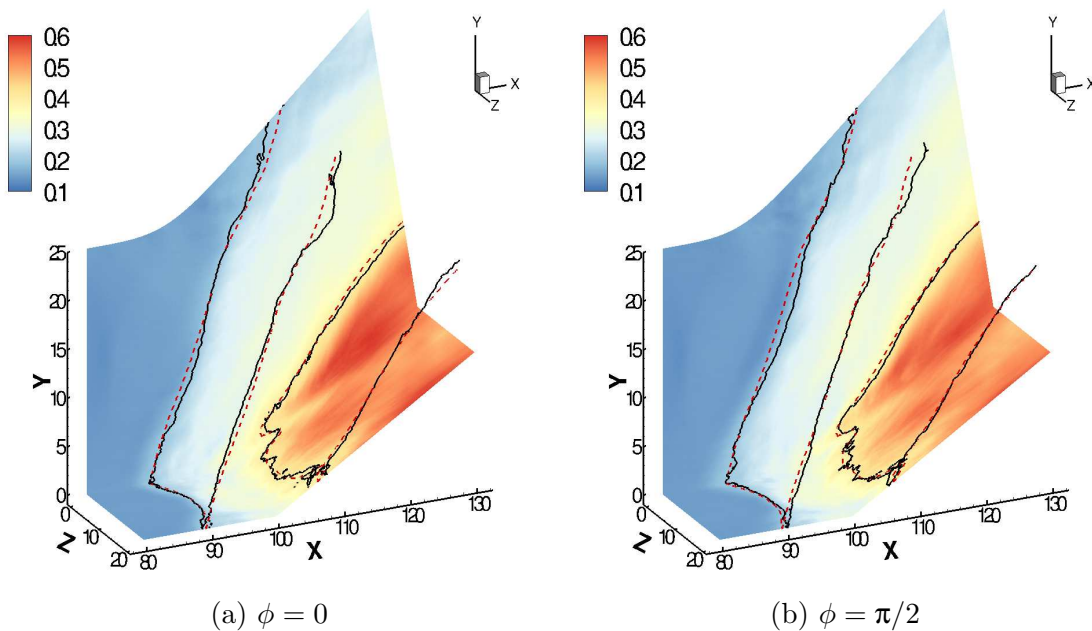
Figure 4.28. Contours of \hat{p}/p_∞ depicting the low-frequency motion of the compression-ramp shock and the reattachment shock-system. Red and black solid lines represent the mean and instantaneous contour levels of $\hat{p}/p_\infty = 0.2$ and 0.4 respectively.

left-sidewall. In Fig. 4.28b at $\phi = \pi/2$, both the compression-ramp shock and the reattachment shock-system translate downstream of their respective mean locations, which is then followed by an upstream movement of the latter at $\phi = \pi$ (see Fig. 4.28c.) At this phase,

the compression-ramp shock remains downstream of its mean which then moves upstream at $\phi = 3\pi/2$ in Fig. 4.28d. Based on these figures, there exists a finite time-delay between the oscillations of the compression-ramp shock and the reattachment shock-system. Also, note that the motion of parts of the compression-ramp shock lying above and below $Y \approx 10$ are not synchronous.

The motion of the interaction at $St = 0.12$ is shown in Fig. 4.29. The template used in the previous figure is reproduced here. The right-sidewall ($Z = 20$) is included as a translucent surface to visualize the motion described hereafter. For the upcoming analysis, we focus only on the motion of the compression-ramp shock.

At $\phi = 0$ in Fig. 4.29a, the compression-ramp shock on the left-sidewall lying in $Y \leq 15$ is downstream of its mean, while the rest of it is approximately upstream of it. An opposite trend is observed on the right-sidewall at this instant. In Fig. 4.29b at $\phi = \pi/2$, the lower portions of the compression-ramp shock on the left and right-sidewall ($Y \leq 5$) begin to move upstream and downstream of their respective mean locations. This is followed by their upper portions ($Y \geq 15$) moving in opposite directions at $\phi = \pi$ (see Fig. 4.29c), while the lower portions on the left and right-sidewall begin translating downstream and upstream of their mean locations.



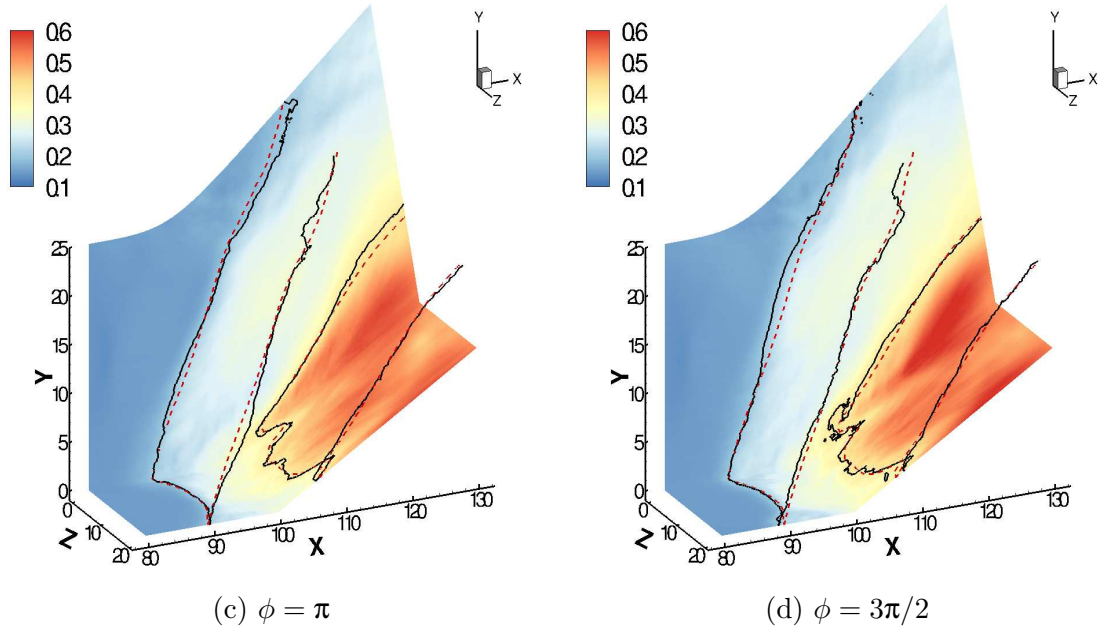


Figure 4.29. Contours of \hat{p}/p_∞ depicting the low-mid frequency motion of the compression-ramp shock and the reattachment shock-system. Red and black solid lines represent the mean and instantaneous contour levels of $\hat{p}/p_\infty = 0.2$ and 0.4 respectively.

The compression-ramp shock front at $\phi = 3\pi/2$ in Fig. 4.29d returns to its original location (corresponding to $\phi = 0$), and the cycle repeats. Based on this description, the low-mid frequency mode highlights a low-amplitude asymmetric streamwise motion of the interaction. This asymmetric motion of the interaction was observed by Poggie and Porter [65] on plotting conditionally averaged wall pressure (see Figs. 16 and 17 in that reference) as well as in the coherence plots by Deshpande and Poggie [163] (see Figs. 8 and 9 in that reference). One of the contributing factors for this phenomenon could be variation in the size of the sidewall separated zones, as described in Fig. 4.25 on the ramp-normal plane at this frequency.

Figure 4.30 illustrates the process of vortex shedding through contours of \hat{p}/p_∞ for the frequency component $St = 0.6$. The reconstructed mode does not include contribution from the mean flowfield, and two instances at $\phi = 0$ and $\phi = \pi$ are shown in Figs. 4.30a and 4.30b respectively. The mean contour level of $c_{f_x} = 0$ is included as a black solid line. From both the figures, the vortices on the wall and away from the centerline are swept towards the

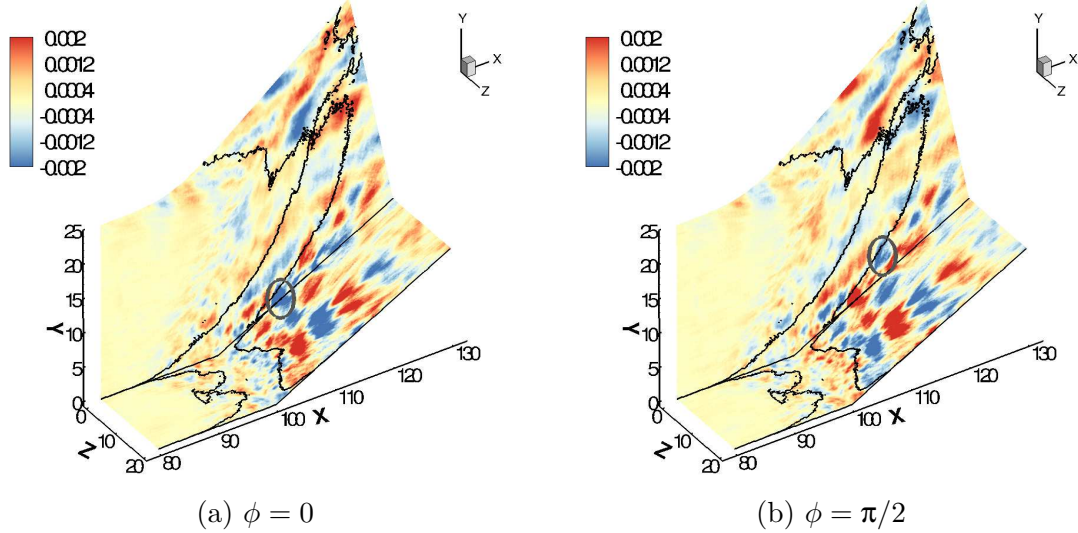


Figure 4.30. Contours of \hat{p}/p_∞ depicting the mid-frequency vortex shedding. Black solid lines represent the mean contour level of $c_{f_x} = 0$.

corners and into the corner vortex system present at the sidewall junctures (see Fig. 4.2). It seems that the sidewall vortex system transports the shed vortices from the wall to the left-sidewall, which then follow a helical trajectory of the open separation vortex. This process can be visualized by tracking the encircled region in the figure, which enters the corner vortex system associated with left-sidewall at $\phi = 0$, followed by the sidewall separation vortex at $\phi = \pi$. This observation is consistent with the behaviour of the mid-frequency mode in Sec. 4.6.2 (see Fig. 4.26). The vortices in the vicinity of the centerline follow the path of the core flow as shown in Fig. 4.21.

4.7 Summary

Data analysis of ILES computations on a highly confined compression ramp flow with sidewalls carried out by Poggie and Porter [17], [65] was elaborated in this chapter. The mean and instantaneous flowfields were used to elucidate the three-dimensionality of the interaction. Secondary flows within the interaction were characterized by Critical Point Analysis. Spectra of wall-pressure fluctuations highlighted events such as low-frequency separation shock motion, low-mid frequency breathing of the centerline separated zone, and mid-frequency vortex shedding. Individual spectrum plotted for the first two phenomena

showed peaks in the respective frequency regimes. Contours of coherence of pressure fluctuations in the domain suggested an asymmetric back-and-forth motion of the interaction. Space-time correlations of the same were used to quantify the degree of coupling between the centerline and corner separations. The complex secondary flows were recovered using modal reconstruction from the SPDMD algorithm.

5. HIGH-FREQUENCY FORCING OF SHEAR-LAYERS

This chapter characterizes the effects of introducing high-frequency perturbations in the flowfield described in Chapter 3. Initially, the formulation of the source term used to introduce periodic perturbations in the flowfield is elaborated. This is followed by a discussion on the effects of forcing on the mean and statistical quantities. Spectral analysis is performed to examine any new time-scales caused as a result of forcing. The effect of forcing was examined using ILES calculations in HOPS and DDES calculations in SU2. These calculations are being carried out by Deshpande and Poggie, and are currently in progress. This chapter presents a snapshot of work in progress.

5.1 Actuator Formulation

The method used for formulating the actuator model that was implemented as source terms in the momentum and energy equations (labelled as f_i in Eq. (2.7) in Sec. 2.3) is described in this section. Deshpande and Poggie [164] carried out conditional averaging of the fluctuating velocity field, based on the instantaneous location of the reattachment shock ($x_{shk}(t)$.) A time offset between two events: positive (negative) streamwise velocity fluctuations in the shear-layer followed by upstream (downstream) movement of the reattachment shock was incorporated while carrying out the conditional averages. This value was obtained from the optimum time-delay in the space-time correlations of streamwise velocity fluctuations ($u'(t)$) and $x_{shk}(t)$ (see Fig. 9(a) in Ref. [164].)

The flow-control approach is to take the form of disturbances identified through conditional averaging to precede separation bubble/reattachment shock motion, and impose them in the flow to attempt to modify such motion. Following the methodology used by Poggie [6], the actuator was modeled computationally as an artificial body-force actuator varying sinusoidally in time, with a Gaussian distribution in the streamwise direction. On implementing the expressions in Eqs. (5.1) and (5.2) in a CFD code, physically similar fluctuations can be

generated in the flowfield. The analytical expression of the actuator's wall-normal profile is given as,

$$g(y) = \begin{cases} \frac{\exp(-C_1^2 Y^2) \exp(A_1 C_1 Y)}{(y_r/2C_1)\sqrt{\pi}\exp(A_1^2/4) [1+\operatorname{erf}(\frac{A_1}{2})] - (y_r/2C_2)\sqrt{\pi}\exp(A_2^2/4) [1+\operatorname{erf}(\frac{A_2}{2})]} & Y > 0 \\ \frac{-\exp(-C_2^2 Y^2) \exp(-A_2 C_2 Y)}{(y_r/2C_1)\sqrt{\pi}\exp(A_1^2/4) [1+\operatorname{erf}(\frac{A_1}{2})] - (y_r/2C_2)\sqrt{\pi}\exp(A_2^2/4) [1+\operatorname{erf}(\frac{A_2}{2})]} & Y \leq 0 \end{cases}; \quad Y = \frac{y}{y_r} \quad (5.1)$$

where $y_r = D = 0.0254$ m, $A_1 = 1.6$, $A_2 = 1.7$, $C_1 = 400$, and $C_2 = 300$. In this study, the actuator was placed close to the step at $x_a/D = 0.1$. The expression for the body-force (N/m³) to be used in the momentum equations is shown in Eq. (5.2),

$$\begin{aligned} \Phi(x, y, t) &= \mathcal{A}f(x)g(y) \cos(2\pi f_0 t) \\ f(x) &= \frac{\exp(-X^2)}{\sqrt{\pi}x_r}; \quad X = \frac{x - x_a}{x_r} \end{aligned} \quad (5.2)$$

where Φ is the body-force, $x_r = 0.1D$ m, \mathcal{A} is the forcing amplitude (in N/m), f_0 is the forcing frequency (in Hz), and x_a is the streamwise location of the actuator. The functions $f(x)$ and $g(y)$ are normalized such that,

$$\int_{-\infty}^{\infty} f(x) dx = 1; \quad \int_{-\infty}^{\infty} g(y) dy = 1 \quad (5.3)$$

A comparison of the analytical velocity profile with the conditionally averaged velocity profile is shown in Fig. 5.1a. Although there is a slight disagreement in the vicinity of $y/y_r = 0$, the maxima/minima of the analytical profile agree well with the conditionally averaged profile. Figure 5.1b shows the contour plot of the body-force function evaluated from Eq. (5.2), where $\mathcal{A} = 1$.

The amplitude corresponding to the forcing term can be tuned by examining some previous studies [165], [166], which quantify the degree of forcing using the ratio of perturbation velocity to the freestream velocity (u'/U_∞) or the momentum coefficient, $C_\mu = \rho_a u_a^2 b / \rho_\infty U_\infty^2 L$,

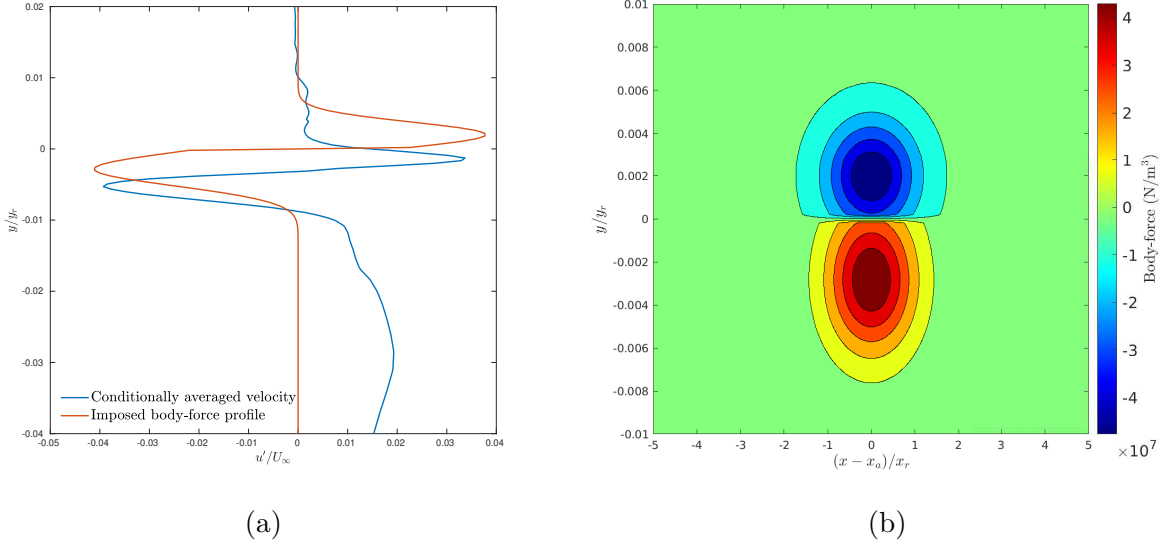


Figure 5.1. Actuator details. (a) Wall-normal profile (b) Body-force distribution.

where the subscript a stands for “actuator” and L is the choice of length-scale (which is cavity length (L_c) in this study.)

In the expression for momentum coefficient, the dynamic pressure term $\rho_a u_a^2$ is integrated across the wall-normal extent of the actuation region. Using this interpretation, the momentum coefficient can be defined as,

$$C_\mu = \frac{1}{\rho_\infty U_\infty^2 L_c} \int_{-\infty}^{\infty} \rho_a(y) u_a(y)^2 dy \quad (5.4)$$

Estimates of the momentum coefficient were obtained by performing Euler calculations with the actuator switched on, followed by extracting the momentum flux at the outlet. A two-dimensional square box with a length of $2D$ with a grid size of 2000×2000 points was used for the calculations. The actuator was placed at the center of the domain Table 5.1 below shows the values for u'_{max}/U_∞ and C_μ corresponding to different values of \mathcal{A} , which is dimensional. These values were obtained by carrying out Euler calculations with varying \mathcal{A} values. The momentum coefficient is integrated over the entire span of the source term, i.e $-0.01 \leq y/D \leq 0.01$ using Eq. (5.4). On the other hand, the ratio of u'_{max}/U_∞ is calculated to determine the relative influence of actuator velocity.

Table 5.1. Amplitude values.

\mathcal{A} (N/m)	C_μ	u'_{max}/U_∞
1	0.33×10^{-4}	0.06
2	1.35×10^{-3}	0.12
5	7.4×10^{-3}	0.25

Based on the review paper by Greenblatt and Wygnanski [165], the effective value of C_μ for reduced frequencies $F^+ = fL_c/U_\infty \sim \mathcal{O}(1)$ lie in the range: $0.01\% \leq C_\mu \leq 3\%$, where $C_\mu = (c_\mu, < c_\mu >)$ includes the contribution from both steady blowing and oscillatory blowing. The former is not as effective and requires higher values to obtain the desired effect. The latter was found to be more effective and typically requires lower values. For the reduced frequency value of $F^+ = 1.6$ used in this study, a value of $\mathcal{A} = 1.5$ N/m was chosen. Note that the definition of reduced frequency is equivalent to the Strouhal number used in this study.

The grid sizes, time-steps, and sampling rates used for the DDES calculations in SU2 and ILES calculations in HOPS are consistent with the ones used for calculations of the baseline (unforced) flowfield. They are listed in Tables 2.3 and 2.4 in Sec. 2.4.1. Additionally, the data were extracted at locations chosen for the baseline case (see Table 2.6 at the end of Chapter 2.) The SU2 calculations were carried out for a total run-time of ≈ 0.023 s (~ 93000 iterations and 343 actuator cycles) while the HOPS calculations were carried out for a total run-time of ≈ 0.002 s (~ 1165000 iterations and 30 actuator cycles.)

5.2 Flowfield Structure

This section investigates any changes in the mean and statistical quantities caused as a result of forcing. The baseline flow consists of a flow separating at the edge of a backward facing step over a recirculation zone in the cavity region. The separated shear-layer reattaches onto a ramp and is aligned along its surface through a reattachment shock. The mean flowfield highlighting these features is shown in Fig. 3.1.

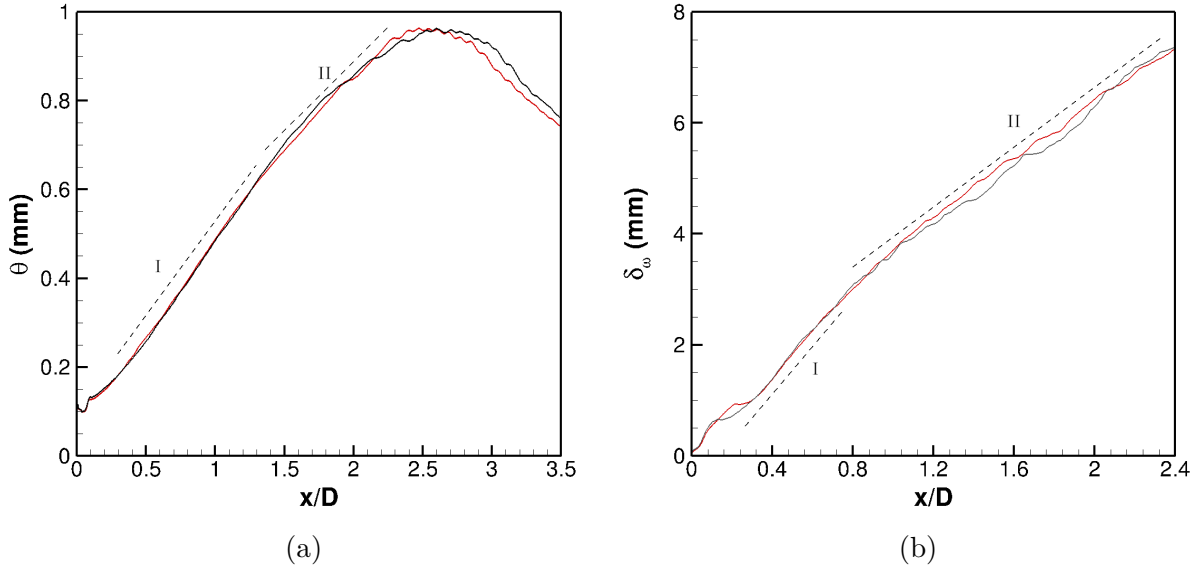


Figure 5.2. Comparison of shear-layer growth rates between unforced (—) and forced (—) cases in SU2 for (a) Momentum thickness (b) Vorticity thickness.

We start by comparing the growth rates of the forced case with the baseline case in Fig. 5.2. The momentum thickness curve in Fig. 5.2a for the forced case follows that for the baseline case until the saturation location. Subtle variations between the two curves are observed in region II, which may subside with additional samples. Similarly, the vorticity thickness curve for the forced case also follows the curve for the unforced case up to $x/D \approx 0.8$ (labelled as region I in Fig. 5.2b.) The growth rate for the forced case is slightly reduced as compared to the unforced case, downstream of $x/D \approx 0.8$ (in region II.) But the overall trend in growth rates with actuator forcing remains largely unchanged with respect to the baseline case.

Figure 5.3 highlights the effect of forcing on the mean (right y -axis) and RMS (represented by $\langle \rangle$ on the left y -axis) surface properties. In Fig. 5.3a, the forcing has almost no effect on both the mean and RMS wall-pressure distribution. The invariance of pressure rise across the reattachment shock with application of forcing suggests that the latter does not affect the mean shock strength significantly. As with the study of Poggie [6], the intent was to perturb the instantaneous flow without significantly distorting the mean flow. The mean reattachment location also does not change with the application forcing, as indicated by the

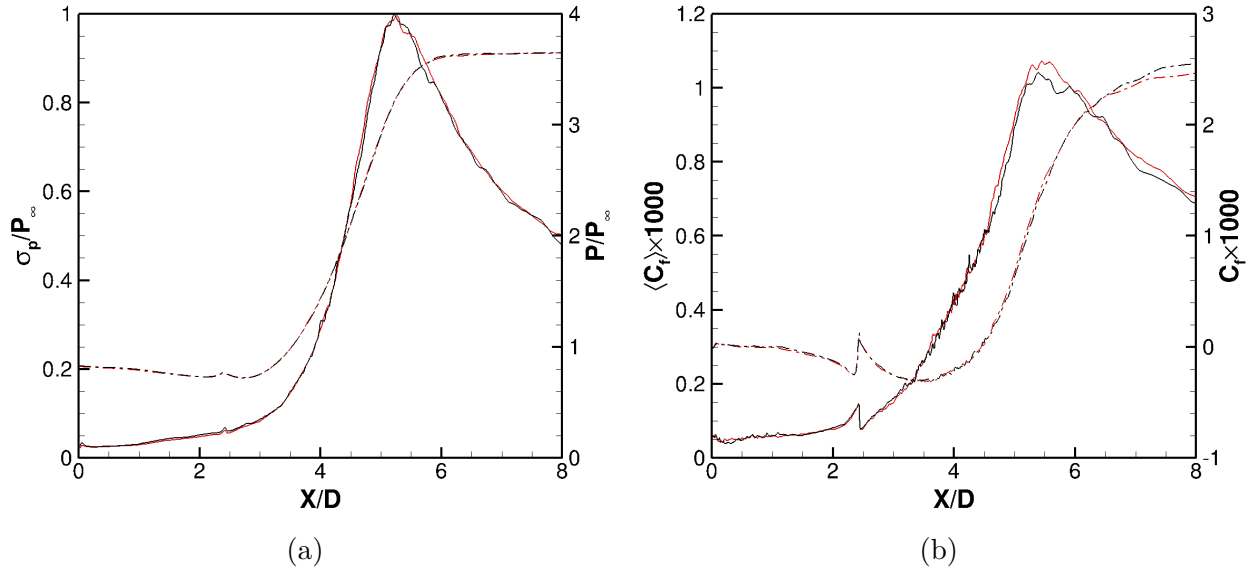


Figure 5.3. Surface quantities of (a) Wall-pressure (b) Skin-friction coefficient with (—) and without (---) forcing in SU2. Mean and RMS values are highlighted by dashed and solid lines, respectively.

mean skin-friction coefficient distribution in Fig. 5.3b. Some variation is observed in the redeveloping region wherein the mean skin-friction coefficient decreases to a slightly lower value with forcing towards the domain exit. On the other hand, the peak RMS value of skin-friction coefficient decreases slightly in the case of forcing.

The comparison of mean velocity profiles with and without forcing is shown in Fig. 5.4. The streamwise locations are consistent with those used in Fig. 3.3. Based on the trend observed in Figs. 5.4a to 5.4d, the forcing does not alter the mean velocity profile in the shear-layer significantly. Also, unlike observations in the study carried out by Dandois et al. [69], no additional inflection points are observed. Possible causes for this result are discussed in the next section.

Figure 5.5 examines the effect of forcing on the resolved Reynolds stresses in the shear-layer. In this figure, an RMS quantity is represented by $\langle \rangle$. Comparison of the normalized mean-squared streamwise momentum fluctuations and the shear-stress component of the stress tensor ($\overline{u'v'}$) is carried out. The normalization is carried out using freestream quantities, i.e. $(\rho_\infty U_\infty)^2$ and U_∞^2 in case of $\overline{(\rho u)'^2}$ and $\overline{u'v'}$, respectively. The figure has two x -

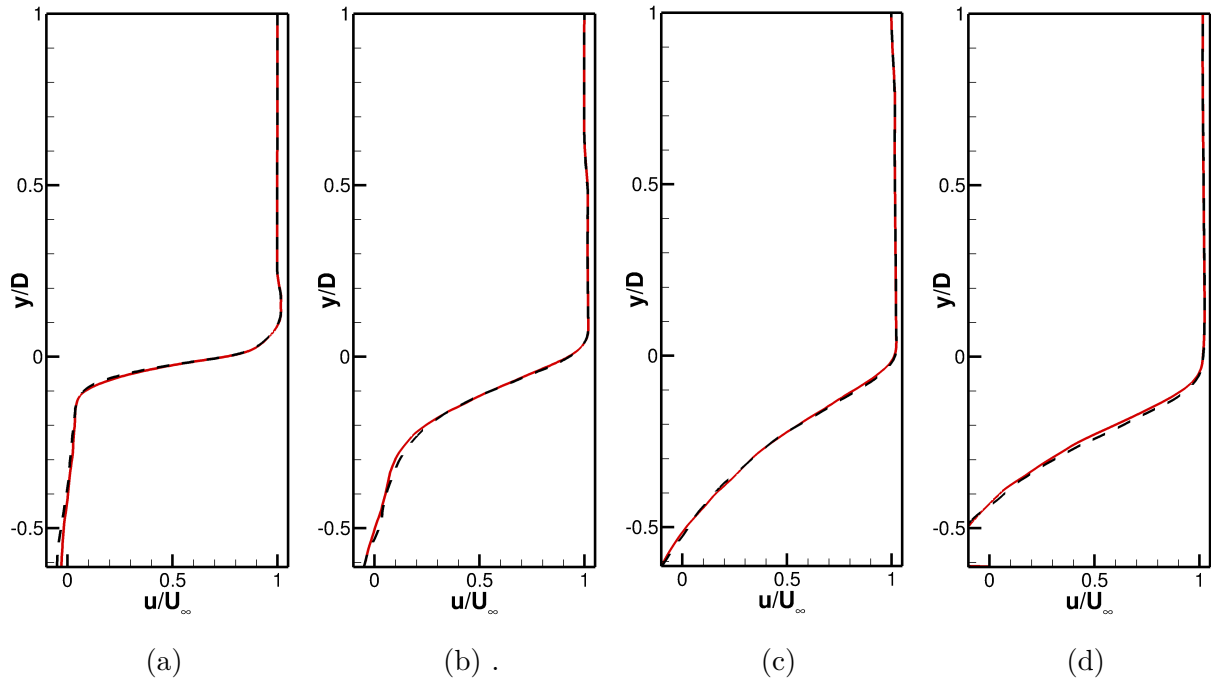


Figure 5.4. Comparison of mean velocity profiles in the shear-layer at (a) $x/D = 0.5$ (b) $x/D = 1.5$ (c) $x/D = 2.5$ (d) $x/D = 3.5$, with (—) and without (---) forcing in SU2.

and y -axes. For the streamwise momentum flux (plotted using solid lines), the x - and y -axis lie on the bottom and left side of the figure. For the shear-stress component (plotted using dashed lines), the x - and y -axis lie on the top and right side of the figure.

Application of forcing does not seem to affect the distribution of the mean-squared streamwise momentum fluctuations in the shear-layer at all the streamwise locations shown in the figure. On the other hand, subtle variations in the profile of the shear-stress component are observed at $x/D = 0.5$ in Fig. 5.5a. The maxima of the profile present within the shear-layer decreases slightly. At wall-normal locations away from the shear-layer, the profile does not show any notable change. On moving downstream to $x/D = 1.5$ and 2.5 in Figs. 5.5b and 5.5c, respectively, the magnitude of the shear-stress component is unaffected. This observation also suggests that actuator forcing does not alter the turbulent production ($\Pi = -\overline{u_i' u_j'} \partial \overline{u_i} / \partial x_j$) in the shear-layer.

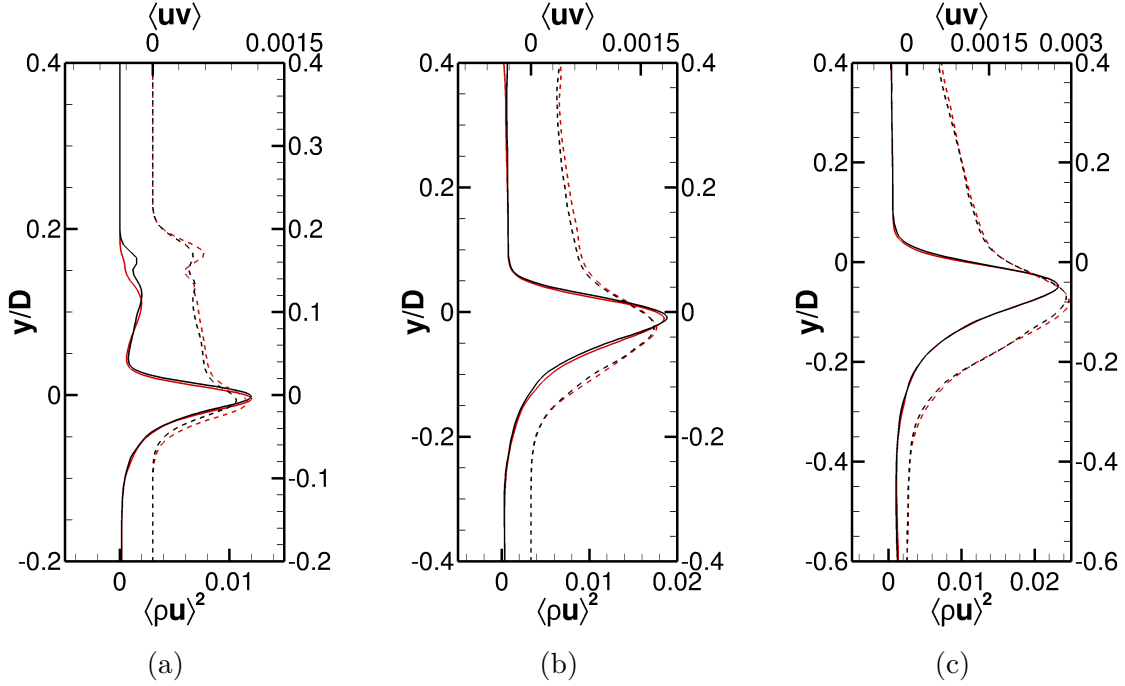


Figure 5.5. Comparison of normalized profiles of mean-squared streamwise momentum fluctuations (—) and RMS of shear-stress component (— —) in the shear-layer (a) $x/D = 0.5$ (b) $x/D = 1.5$ (c) $x/D = 2.5$, with (—) and without (— —) forcing in SU2.

5.3 Unsteadiness of the interaction

This section discusses the unsteadiness of the flowfield in the presence of forcing by examining the pressure spectra on the surface and within the shear-layer. The comparison of wall-pressure spectra at select streamwise locations corresponding to the SU2 and HOPS run is shown in Fig. 5.6. The spectra are shown in semi-logarithmic scale. Since the physical run-time is not long enough to resolve the lower frequencies, the nature of only low-mid and mid frequencies is studied here. The spectra for the SU2 and HOPS run were obtained by segment averaging with window sizes of $N_w = 32768$ (~ 4 windows) and $N_w = 524288$ (~ 4 windows), respectively, followed by averaging across the span. The resulting frequency resolutions are $\Delta St \approx 0.013$ and $\Delta St \approx 0.1$, respectively.

Figure 5.6a compares the wall-pressure spectra at $x/D = 1.07$, which lies close to the step within the cavity region. At this location, a sharp peak corresponding to the forcing frequency of $St_f = 1.6$ is clearly observed in the spectrum. An additional peak at a higher

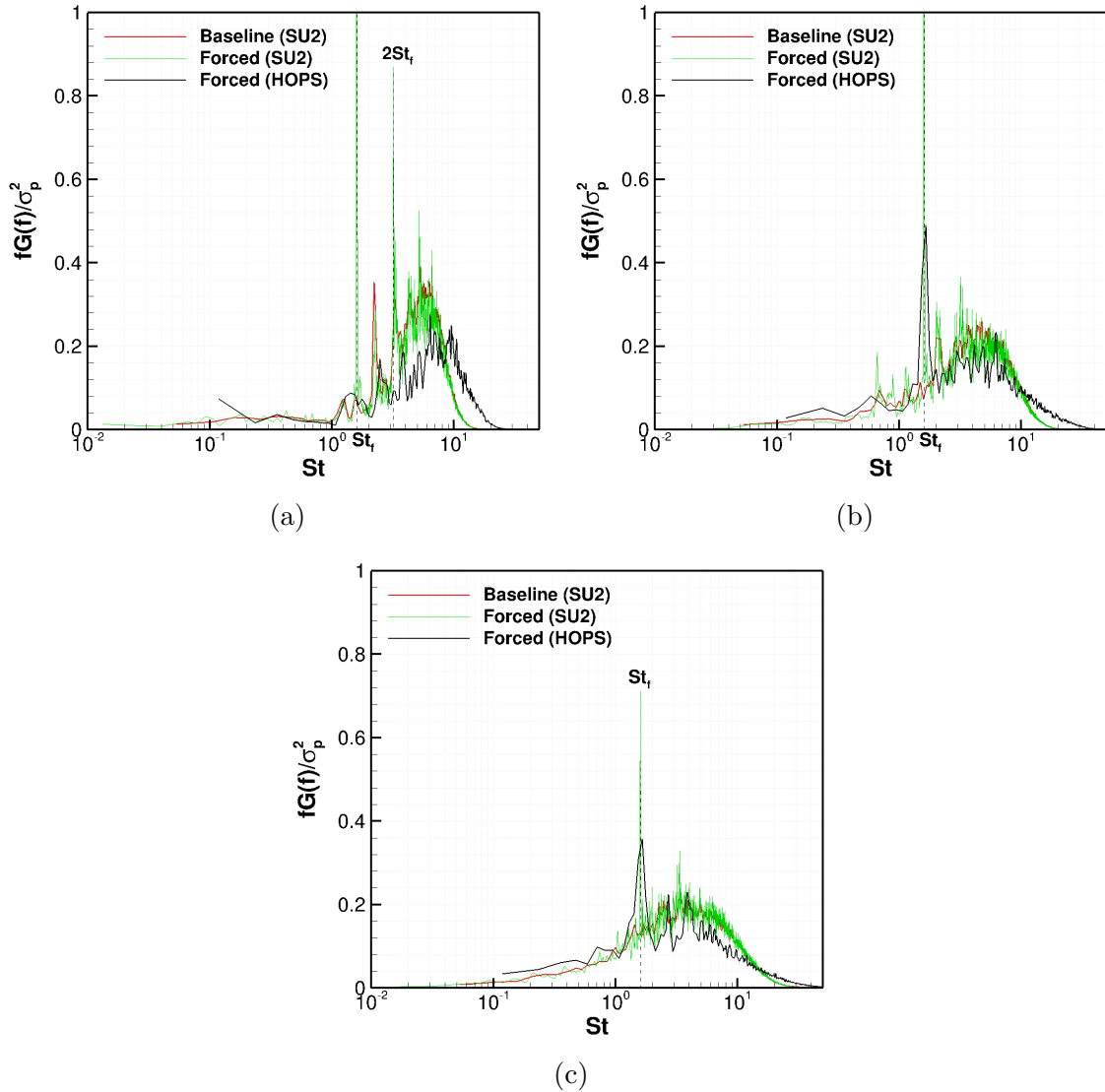
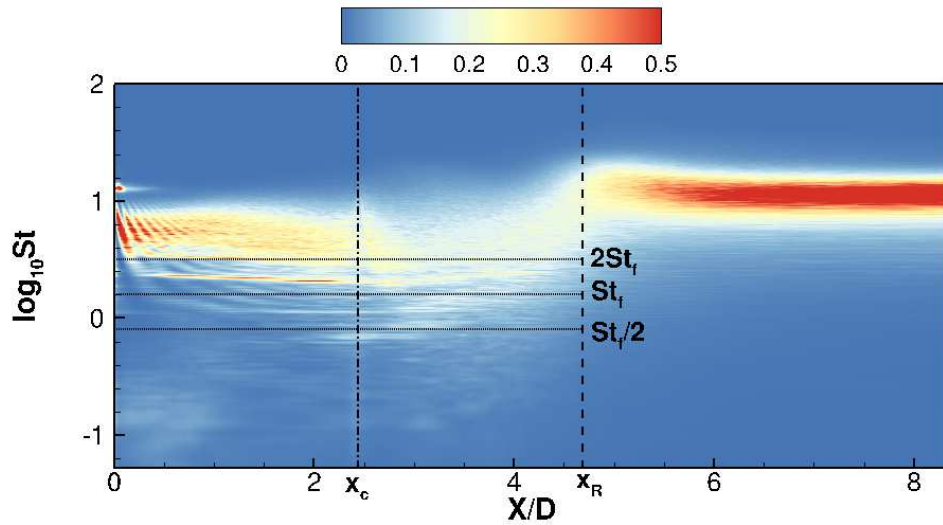


Figure 5.6. Comparison of wall-pressure spectra for the SU2 and HOPS run at (a) $x/D = 1.07$ (b) $x/D = 2.44$ (c) $x/D = 3.81$

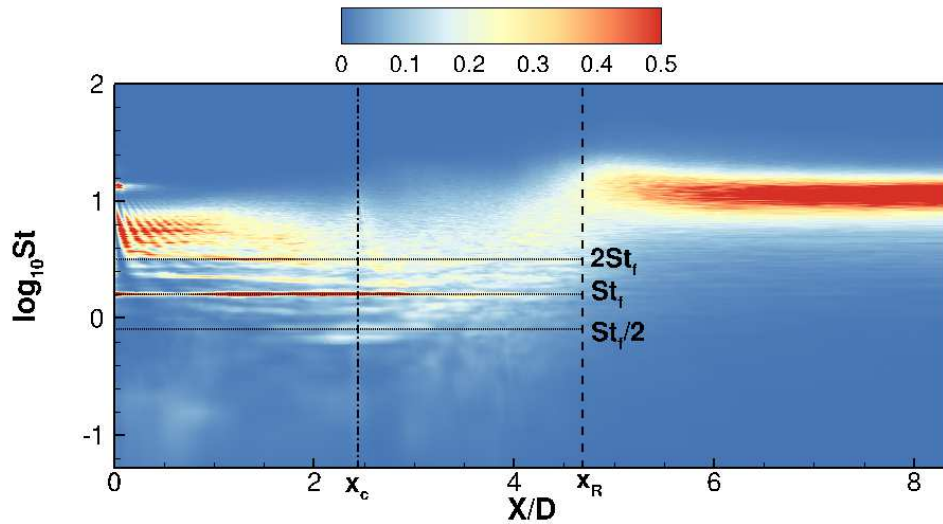
harmonic occurs at $St = 2St_f = 3.2$. The rest of the spectrum remains largely unchanged. On the other hand, the spectrum corresponding to the HOPS run does not show a peak either at the forcing frequency or its higher harmonic. Since this location lies close to the step, it is possible that the large turnover times in the recirculation zone result in slow progression of acoustic disturbances introduced by the actuator, towards the step. At $x/D = 2.44$ in Figure 5.6b, which lies at the cavity-ramp junction, the peak at the higher harmonic present at the upstream location damps out, while the peak value corresponding to the

forcing frequency remains invariant. For the HOPS case, a peak at the forcing frequency now appears in the spectrum.

Farther downstream on the ramp surface at $x/D = 3.81$ in Fig. 5.6c, the peak magnitude corresponding to the forcing frequency in the SU2 spectrum subsides significantly. A similar result occurs in the HOPS spectrum. This observation suggests that the effects of forcing are primarily confined in the cavity region. A detailed view of the spectra shown in Fig. 5.6



(a)



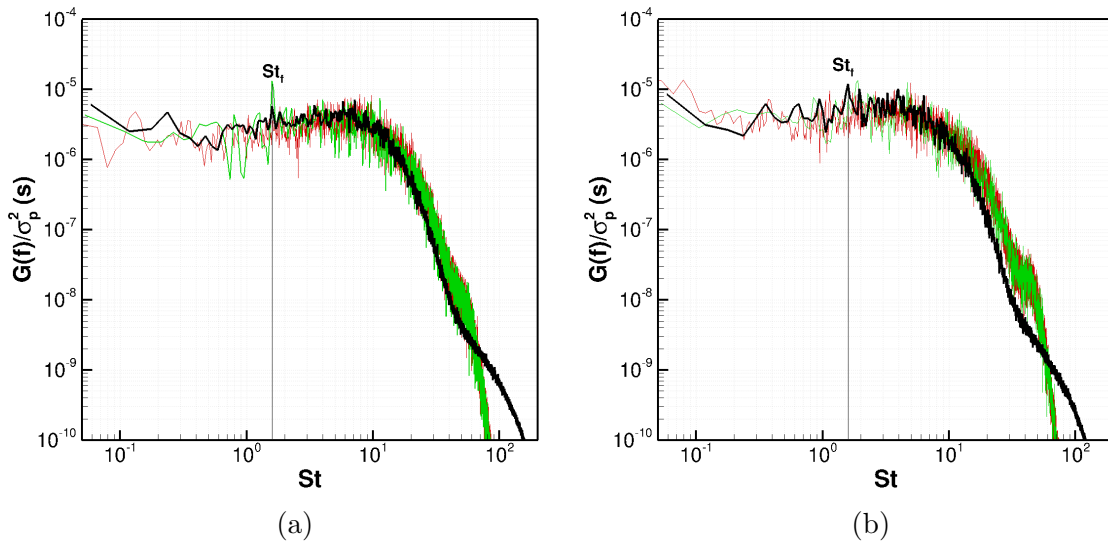
(b)

Figure 5.7. Contours of pre-multiplied wall-pressure spectra corresponding to the SU2 run for (a) Baseline case (b) High-frequency forcing.

is shown in the contour plots presented in Fig. 5.7. The streamwise coordinate is shown on the x -axis and the logarithm of the Strouhal number is plotted on the y -axis.

In this figure, the cavity-ramp junction at $x/D \approx 2.44$ and mean reattachment location at $x/D \approx 4.69$ are labelled as x_c and x_R , respectively. Based on the patterns observed in Figs. 5.6a to 5.6c, the forcing frequency $St_f = 1.6$ and its harmonics $St_f/2$ and $2St_f$ are also marked to track their evolution downstream. The spectra at each streamwise location were calculated using a window size of $N_w = 8192$ samples (~ 16 windows), followed by averaging across the span. The resulting frequency resolution is $\Delta St \approx 0.053$.

The baseline contour plot in Fig. 5.7a is similar to the contour plots corresponding to the OVERFLOW run in Figs. 3.8 and 3.9. The spectral energy residing within the low-mid frequencies ($St \sim \mathcal{O}(0.1)$) is comparatively lower in magnitude due to a shorter run-time. Figure 5.7b clearly highlights the evolution of the forcing frequency and its harmonics. The effect forcing starts immediately downstream of the step at $x/D = 0$ and persists up to the mean reattachment location. The magnitude of spectral energy associated with the forcing frequency (St_f) begins to subside progressively on the ramp. The second harmonic component ($2St_f$) follows a roughly similar pattern. The sub-harmonic component ($St_f/2$) observed in Figs. 5.6b and 5.6b starts developing at $x/D \approx 2.5$ and damps out shortly downstream at $x/D \approx 3.5$.



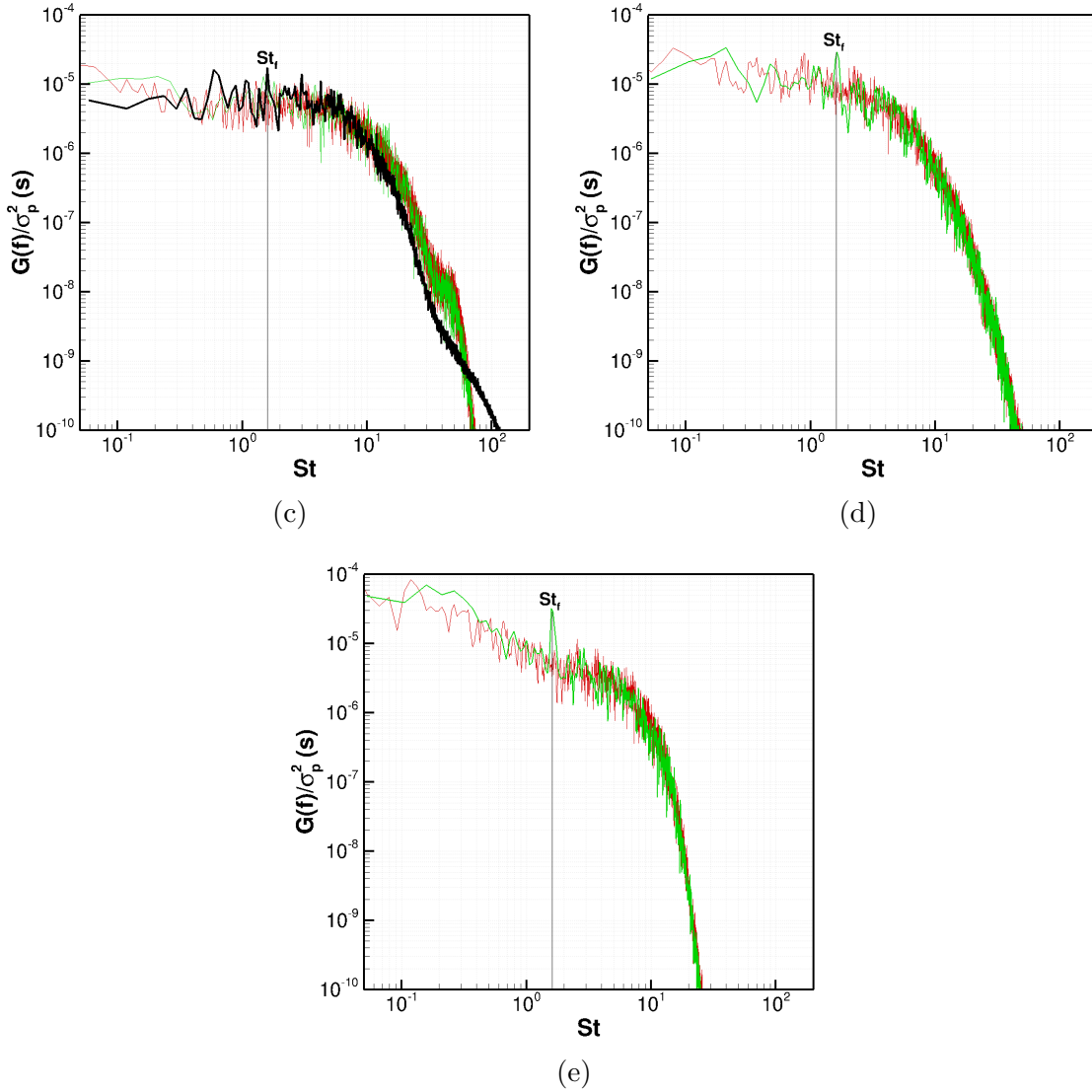


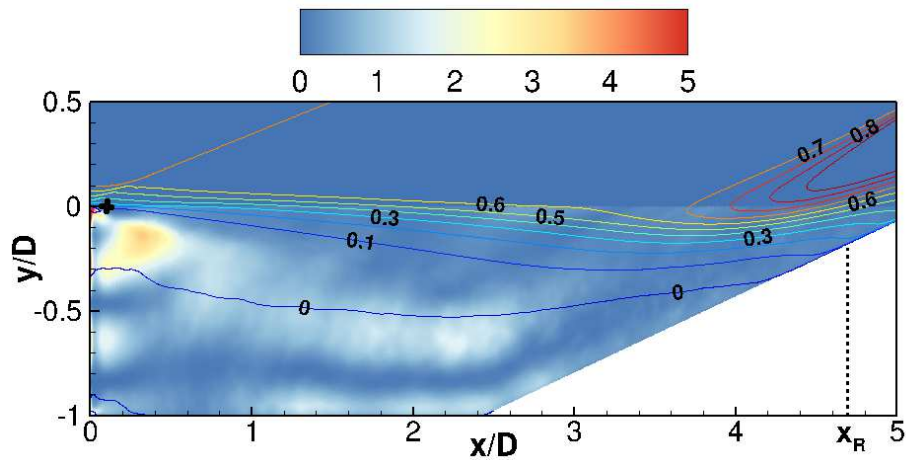
Figure 5.8. Comparison of pressure spectra between SU2 (without forcing) (—), SU2 (with forcing) (—), and HOPS (with forcing) (—) at (a) SH-1 (b) SH-2 (c) SH-3 (d) RZ-1 (e) RZ-2.

Figure 5.8 illustrates the pressure spectra at various stations within the shear-layer and recirculation zone, which were used for the baseline case (see Fig. 3.10 in Chapter 3.) Spectra corresponding to the SU2 and HOPS case are included in the figure. The window segment sizes and the corresponding frequency resolutions for SU2 and HOPS case are $N_w = 32768$ (~ 4 windows), $N_w = 1048576$ (~ 2 windows) and $\Delta St \approx 0.013$, $\Delta St \approx 0.06$, respectively. For reference, the baseline spectrum corresponding to the SU2 run is included in all the

figures. The forcing frequency is labelled in all the cases to discern any peaks that occur at that value. Since the time-step for the HOPS run is smaller, a larger window size is required to capture a longer time-frame, in order to resolve low-mid and mid-frequencies.

At SH-1 in Fig. 5.8a, the spectrum obtained from the SU2 run shows a small peak at the forcing frequency. Compared to the baseline spectrum, the energy magnitude in the vicinity of $St = 1$ are lower in the spectrum corresponding to high-frequency forcing. A peak at the forcing frequency is also observed in the spectrum corresponding to the HOPS run, though it is not well resolved due to an insufficiently long run-time. (This calculation is currently running, and fully converged statistics will eventually be required.) No changes in the spectra are observed in the high-frequency regime.

The peak at the forcing frequency is not as prominent at SH-2 and SH-3 in Figs. 5.8b and 5.8c, which suggests that the effect of forcing in the shear-layer persists only up to SH-1, which lies close to the step. A similar trend is observed in the spectra corresponding to the HOPS case. The peak reappears in the spectra within the recirculation zone at RZ-1 and RZ-2, shown in Figs. 5.8d and 5.8e, respectively. Note that spectra for the HOPS case are not shown since the data were not sampled at those locations. The presence of this peak indicates a relatively stronger influence of forcing in the recirculation zone as compared to the shear-layer. In order to examine this in additional detail, contours of pressure spectra at the frequency component and its sub-harmonic from the SU2 run are shown in Fig. 5.9.



(a)

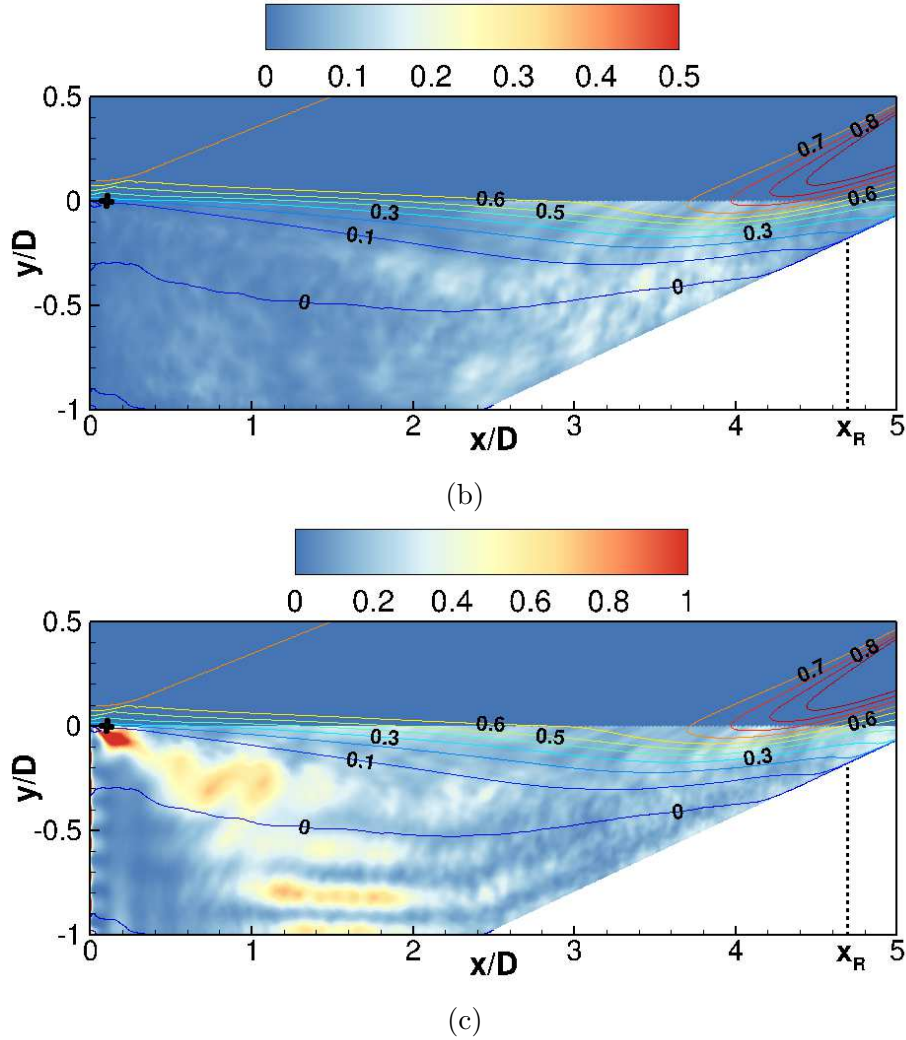


Figure 5.9. Contours of pre-multiplied pressure spectra corresponding to the SU2 run for the frequency components: (a) $St = 1.6$ (b) $St = 0.8$ (c) $St = 3.2$. The mean reattachment location at $x_R/D = 4.69$ is marked for reference. The actuator location at $(x/D, y/D) = (0.1, 0)$ is highlighted using a black marker.

The spectra were determined by using a window size of $N_w = 8192$ samples (~ 16 windows), with a frequency resolution of $\Delta St \approx 0.053$. The contours mean non-dimensional streamwise velocity (u/U_∞) are included in the figure to differentiate between the shear-layer and the recirculation zone. The region above the shear-layer is neglected for ease of analysis. The actuator is located close to the step at $(x/D, y/D) = (0.1, 0)$ and is highlighted using a black marker in each figure.

Figure 5.9a shows the contours for the forcing frequency component of $St = St_f = 1.6$. High magnitudes of spectral energy are present in the immediate vicinity of the actuator location and are skewed towards the recirculation zone. This region approximately follows the contour line of $u/U_\infty = 0$, wherein the magnitude spectral energy decreases progressively downstream. The cavity surface is also characterized by regions high spectral energies distributed unevenly, and which persist up to $x/D \approx 3$. This observation is consistent with the spectra shown in Figs. 5.6 and 5.7. Note that the shear-layer region is populated by moderate to low magnitudes of spectral energy, which confirms that it is not significantly affected by the forcing. This may explain the minimal variation in the growth rates, mean velocity and resolved stress profiles shown in Figs. 5.2, 5.4 and 5.5, respectively.

Figure 5.9b shows the contours for the sub-harmonic of the forcing frequency, $St = St_f/2 = 0.8$. The aft portion of the cavity region consists of low magnitudes of spectral energy associated with this frequency component. It starts to develop towards the cavity-ramp junction and is localized close to the cavity and ramp surfaces. Within the shear-layer, signs of sub-harmonic development are evident downstream of $x/D \approx 2.44$, i.e. the corner. Similar to the fundamental forcing frequency, the effects of the sub-harmonic component is localized to the recirculation zone and does not affect the shear-layer significantly. The contours corresponding to the second harmonic of the forcing frequency ($St = 2St_f = 3.2$) shown in Fig. 5.9c indicate a standing-wave-like pattern along the wall-normal direction.

The effect of forcing on the motion of the reattachment shock and separation bubble breathing is examined by the spectra shown in Figs. 5.10a and 5.10b, respectively. The procedures used to obtain the time histories of shock location and separation bubble mass are described in Sec. 3.4 in Chapter 3. The baseline plots for both the cases are included for reference. In case of the spectra of reattachment shock motion, three distinct peaks are observed at the forcing frequency, $St = 1.6$ and its harmonics, $St = 3.2 = 2St_f$ and $St = 4.8 = 3St_f$. The spectrum of the separation bubble mass history shows a peak at a slightly lower value ($St \approx 0.1$) in the mid-frequency range as compared to the unforced case. The peak in the low-frequency range at $St \approx 0.026$ remains unaffected by forcing. Unlike the spectrum of the reattachment shock motion, peaks at the forcing frequency or any of its higher harmonics are not observed here.

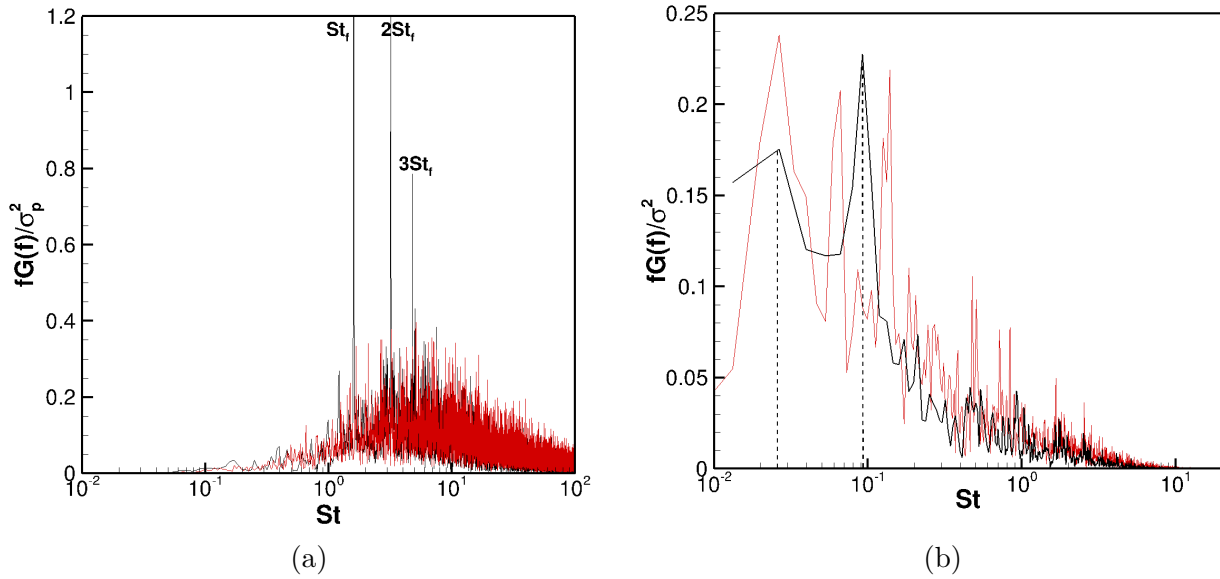


Figure 5.10. Spectra of (a) reattachment shock motion and (b) separation bubble breathing in pre-multiplied coordinates for the baseline (—) and forcing (—) cases using the SU2 code.

To investigate the presence of peaks at the forcing frequency (and its higher harmonics) in the spectrum of reattachment shock location, the contours of phase-averaged pressure fluctuations are plotted in Fig. 5.11. The data are divided into four bins, with the bin edges increasing progressively from 0 to 2π in steps of $\pi/2$. The mean and instantaneous contour levels of $u/U_\infty = 0, 0.15, \text{ and } 0.7$ are used to capture the propagation of pressure fluctuations in the recirculation zone, shear-layer, and the freestream, respectively.

The downstream propagation of disturbances (seen as alternating regions of positive and negative pressure fluctuations) in the freestream and recirculation zone is evident in Figs. 5.11a–5.11d. Based on the magnitude of pressure fluctuations, the disturbances in the freestream get progressively weaker downstream and hence may not affect the shock motion significantly. On the other hand, the disturbances in the recirculation zone seem to traverse along the contour level of $u/U_\infty = 0$ (which is consistent with the trend in Fig. 5.9a) and towards the foot of the reattachment shock. This process can be visualized by focusing on the encircled region at $(x/D, y/D) \approx (2.19, -0.63)$.

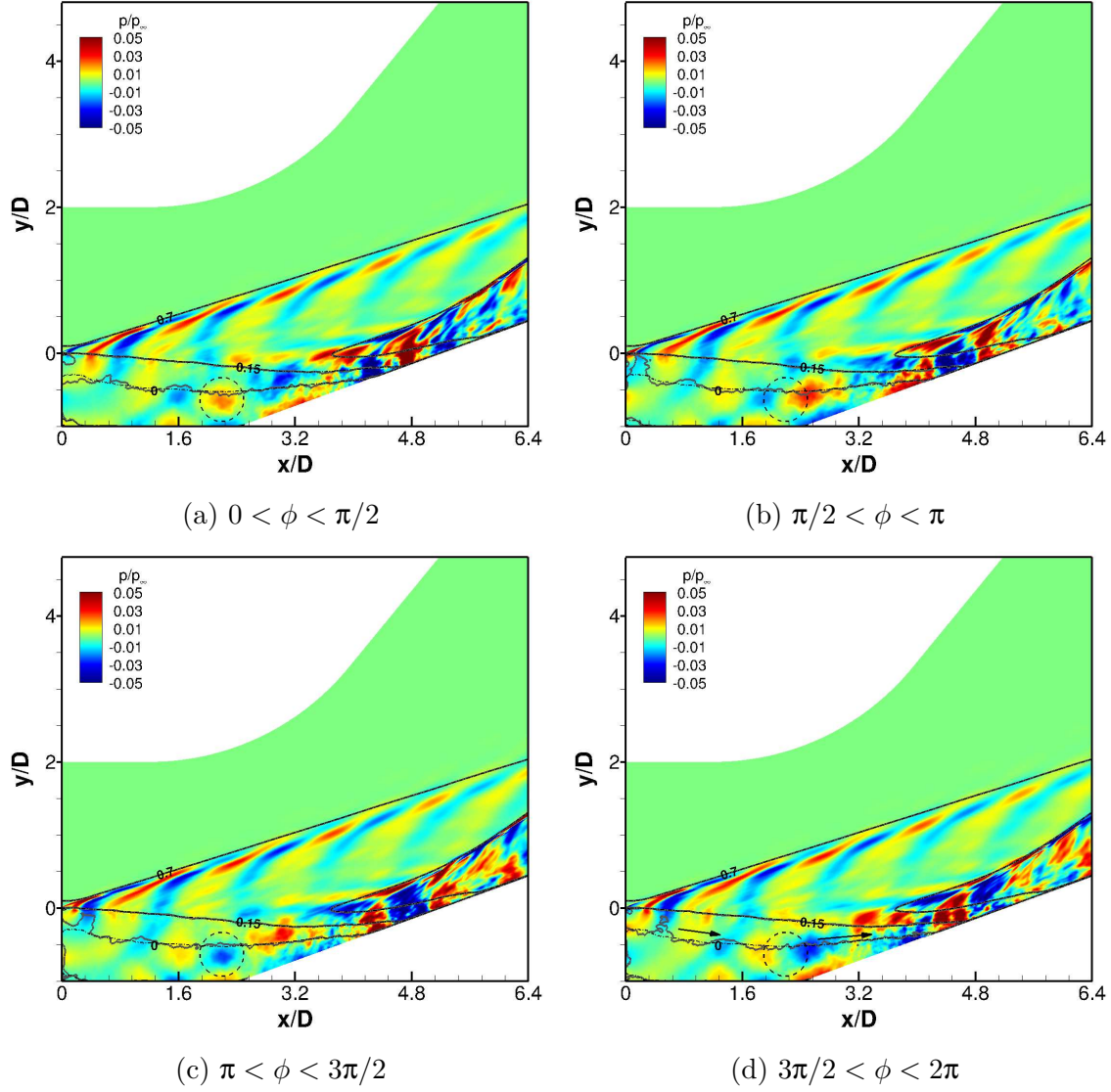


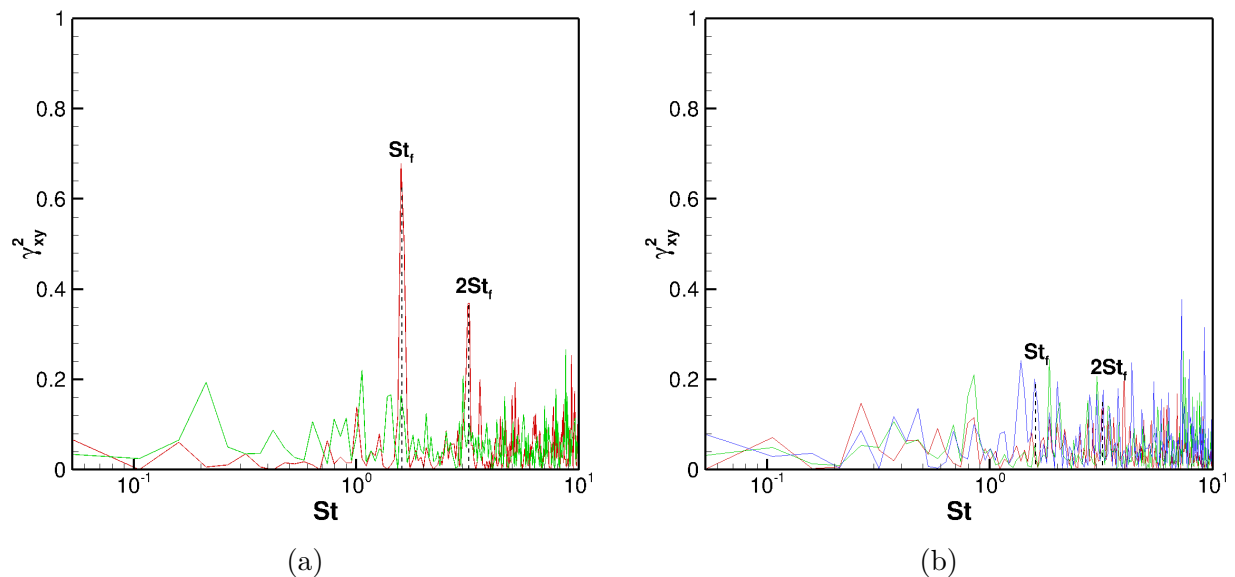
Figure 5.11. Phase-averaged contours of pressure fluctuations corresponding to the SU2 run. Arrows in part (d) indicate the approximate path of disturbances in the recirculation zone.

In Fig. 5.11a when the actuator phase lies between 0 and $\pi/2$, the encircled region captures a downstream propagating packet of positive pressure fluctuations. As observed in Fig. 5.11b, this packet travels along the contour level of $u/U_\infty = 0$. The encircled region is replaced by a packet of negative pressure fluctuations in Fig. 5.11c, which then travels downstream (in Fig. 5.11d) along the same path followed previously by the packet of positive pressure fluctuations in Fig. 5.11b. The packet of positive pressure fluctuations which was

traversing downstream for actuator phase lying in the range: $0 < \phi < \pi$, is now close to the reattachment shock foot. These observations suggest that the peak at the forcing frequency present in the spectrum of reattachment shock position is may be caused by the actuator perturbations propagating through the recirculation zone.

The peaks in the spectrum of reattachment shock location are caused as a result of actuator forcing, as it is only the differentiating factor in comparison to the baseline spectra. It is possible that the high-frequency forcing introduced by the actuator introduces new phenomena in the shear-layer and/or the recirculation zone which have not been addressed previously in this chapter. Considering these points, the influence of perturbations induced by the actuator on the reattachment shock oscillations is investigated by calculating the statistical estimates of coherence. Higher values of coherence indicate a roughly linear relationship between the two signals and in the following discussion, it is assumed that any such observation indicates a stronger influence (and possible causality) of the preceding signal on the phenomenon of interest.

Figure 5.12 illustrates the coherence plots between the reattachment shock oscillations and locations in the recirculation zone and the shear-layer. The coherence estimates were calculated by segment averaging with a window size of $N_w = 8192$ points (~ 16 windows.) The coherence plot corresponding to RZ-1 shown in Fig. 5.12a exhibits two distinct peaks at



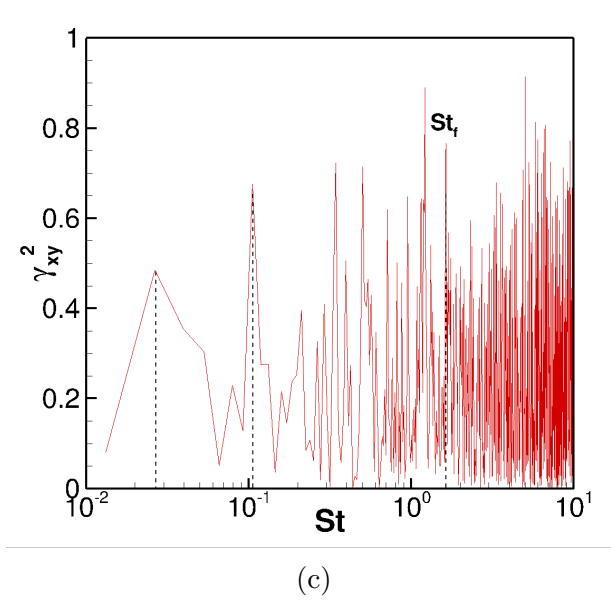


Figure 5.12. Coherence of reattachment shock oscillations with (a) pressure fluctuations in the recirculation zone at RZ-1 (—) and RZ-2 (—) (b) wall-normal velocity fluctuations in the shear-layer at SH-1 (—), SH-2 (—), and SH-3 (—) (c) breathing motion of the recirculation zone, using the SU2 code.

the forcing frequency (St_f) and its harmonic ($2St_f$.) On the other hand, the coherence plot associated with RZ-2 is relatively broadband in nature, suggesting a non-linear relationship with the reattachment shock motion. Unlike RZ-2, RZ-1 lies deep within the recirculation zone (see Fig. 2.4a in Sec. 2.4.1), which according to Figs. 5.9a and 5.11 is influenced by the actuator forcing. This explains presence of peaks in the coherence plot corresponding to this location. Figure 5.12b shows the coherence plots with the wall-normal velocity fluctuations at SH-1, SH-2, and SH-3. The markers corresponding to the forcing frequency and its harmonic are included in the figure for reference. The plots do not show any distinct peaks at any of the three locations, highlighting a weaker effect of flapping motion on the reattachment shock oscillations.

The coherence plot in Fig. 5.12c examines the relationship between the reattachment shock oscillations and separation bubble breathing. A longer window segment of $N_w = 32768$ points was used to resolve the lower frequencies. The locations of the peak in the low and low-mid frequency regimes at $St \approx 0.026$ and $St \approx 0.1$ are similar to the ones in the spectrum of separation bubble breathing in Fig. 5.10b. At mid-frequencies, this plot is broadband in

nature, with one of peaks occurring at the forcing frequency. This plot is similar to the one for the baseline case (see Fig. 3.24 in Sec. 3.5), with peaks occurring at dominant frequencies present in the spectrum of separation bubble mass.

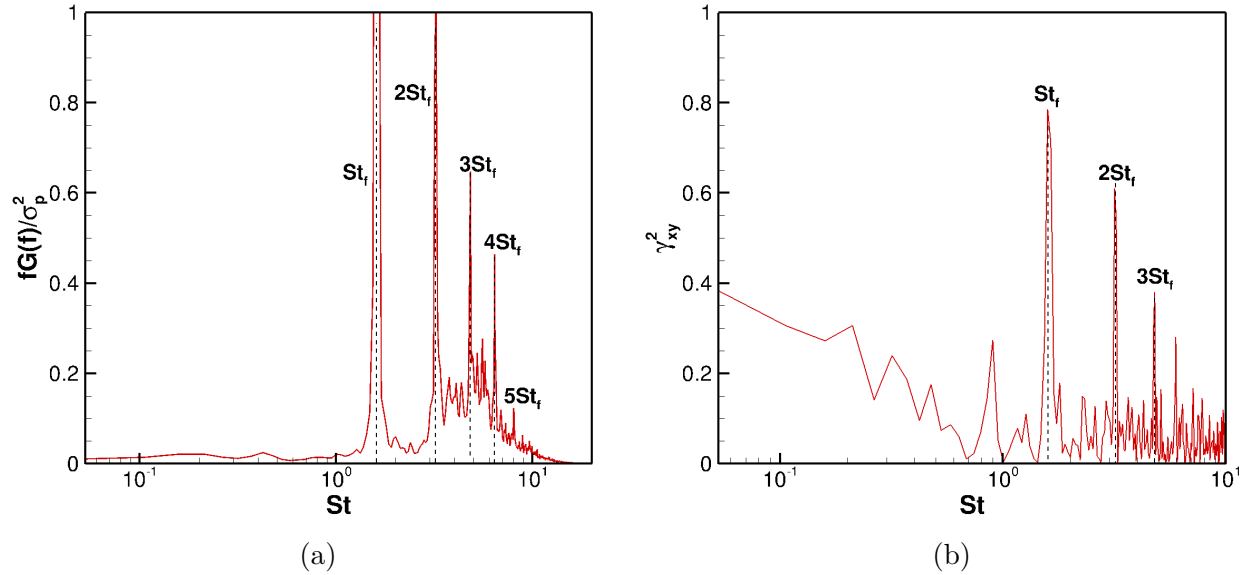


Figure 5.13. (a) Pressure spectrum in the freestream at $(x/D, y/D) \approx (0.71, 0.21)$ (b) Coherence of pressure fluctuations in the freestream with reattachment shock motion, using the SU2 code.

The phase-averaged contours of pressure fluctuations shown in Fig. 5.11 indicated disturbances in the freestream that reach the reattachment shock location farther downstream. In order to determine any influence on its oscillations, a similar exercise of examining the coherence estimates is carried out. Initially, the dominant time-scales in the freestream are quantified by plotting the pressure spectrum at $(x/D, y/D) \approx (0.71, 21)$. The spectrum is plotted in pre-multiplied coordinates and shown in Fig. 5.13a, using a window size of $N_w = 8192$ points (~ 16 windows.) The spectrum consists of peaks at the forcing frequency and its higher harmonics as labelled in this figure. This observation is consistent with a similar result in the work of Samimy et al. [67], who observed several additional peaks at harmonics of the actuation frequency in the near-field pressure power spectra. The coherence plot between this signal and the reattachment shock motions is illustrated in Fig. 5.13b. The window size is similar to the one used in the calculation of pressure spectrum in Fig. 5.13a.

Three peaks occur in the coherence plot at the forcing frequency St_f , and its higher harmonics at $2St_f$ and $3St_f$. The magnitude of peaks decreases monotonically towards higher frequencies. The peak at the third harmonic in the shock position spectrum may therefore be caused due to interaction with freestream disturbances. In case of the peak at second harmonic, based on the coherence magnitudes in this figure and Fig. 5.12a, the influence of freestream disturbances on the reattachment shock motion is relatively more stronger than the disturbances propagating through the recirculation zone.

5.4 Summary

Delayed-Detached Eddy Simulations and Implicit Large-Eddy Simulations of high-frequency forcing applied to the reattaching shear-layer case were carried out, and the corresponding results were described in this chapter. The actuator introduced perturbations of the form that were identified from conditional averages based on the instantaneous reattachment shock position. The actuation frequency and amplitude were set to $St = F^+ = 1.6$ and $\mathcal{A} = 1.5$, respectively. The mean and RMS profiles in the shear-layer did not change significantly, but the forcing did have an effect on the unsteadiness of the flowfield. The wall-pressure spectra indicated development of a sub-harmonic component which damped out shortly downstream. The contours of premultiplied spectra suggested that the effects of forcing were localized to the recirculation zone. The spectrum of reattachment shock location showed three peaks at the forcing frequency and its second and third harmonics. On the other hand, the dominant frequency in the mid-frequency range shifted to a lower value in the spectrum of separation bubble mass. The peak in the low frequency range remained unchanged, thereby suggesting that forcing of this type does not affect the low-frequency breathing motion of the interaction. Based on the coherence plots and phase-averaged contours of pressure fluctuations, the disturbances propagating in the freestream as well as through the recirculation zone drove the oscillations of the reattachment shock.

6. CONCLUSIONS

In this chapter, the main findings from the data analyses carried out on the flowfields corresponding to compressible reattaching shear-layers — with and without forcing — and compression ramp flow with sidewalls, are summarized. Each case generates a unique SWTBLI characterized by events lying in the low, low-mid, and the mid-frequency range. The flowfield corresponding to the compressible reattaching shear-layer was determined using both DDES and ILES calculations. The DDES calculations were carried out using OVERFLOW by Leger et al. [28] and SU2 in the present study. New ILES calculations were also carried out as part of the present study. The ILES computations for the highly confined compression ramp flow were carried by Poggie and Porter [17], [65]. Statistical analysis was performed on the sampled data.

The primary objective of this study was to characterize the separation unsteadiness in each flowfield and determine the possible causes of low-frequency dynamics of the interaction. As mentioned in Chapter 1, separation unsteadiness in a SWTBLI can be caused either due to upstream effects, downstream events, or a combination of both. Huerre and Monkewitz [16] classified flow instabilities in terms of an amplifier, oscillator, or resonator models. These concepts can then be used to model separation unsteadiness in a SWTBLI; the flow behaves as an amplifier when upstream effects are dominant and as a self-sustaining oscillator when downstream effects drive the unsteadiness of the interaction. In some instances, a SWTBLI acts as a resonator wherein the low-frequency dynamics are sustained by perpetual upstream forcing of a particular form. The subsequent sections will summarize the main findings obtained from data analysis of the two flowfields. An attempt is made to classify each flowfield into one of the three models proposed above, based on the nature of its unsteadiness. Avenues for future work are discussed at the end.

6.1 Compressible Reattaching Shear-Layer

A detailed analysis of various unsteady features in a compressible reattaching flow was presented, based on the computations carried out by Leger, Bisek, and Poggie [28]. The computations reproduced all the essential mean flow features of the flowfield, namely a large

recirculation vortex, shear-layer with a concave curvature, and a reattachment shock with a highly smeared shock foot. Visualization of the instantaneous flowfield highlighted the presence of spanwise vortices formed on account of the Kelvin-Helmholtz instability. Shortly downstream of the step, breakdown of these structures to fine-scale turbulence was evident as the DDES simulation transitioned from RANS to LES mode. Farther downstream in the shear-layer, vortical structures resembling the hairpin geometry were observed. The trend of resolved Reynolds stresses agreed with the experimental results of Hayakawa et al. [31].

Premultiplied wall pressure spectra in the cavity region as well as on the ramp surface highlighted events such as low-frequency separation bubble breathing, shear-layer flapping, shedding of vortical structures from the recirculation zone, and the presence of hairpin structures. Local peaks possibly corresponding to Rossiter modes were observed at higher frequency in the spectra, thereby suggesting an acoustic feedback mechanism through the separation bubble. Cavity length was chosen as the length scale to calculate the Strouhal number. This analysis emphasized the broadband nature of unsteadiness in this type of flow, comprising of various events at frequencies ranging from $St \in [0.01, 1]$.

Two-point correlations showed the presence of hairpin structures in the shear-layer, which underwent both streamwise and spanwise elongation downstream. The concomitant non-dimensional convection velocity (U_c/U_∞), determined from space-time correlations, was about 0.61. Correlations in the recirculation zone suggested the presence of similar hairpin structures. The associated length and time-scales were an order of magnitude higher than those present in the shear-layer. This observation is consistent with the results of Kiya and Sasaki [38]. Using the space-time correlations of wall pressure fluctuations on the ramp, the scale dependence of convection velocities was highlighted, and an analogy with the nested hairpin model proposed by Adrian et al. [147] was made. Packets with larger hairpin vortices were present away from the wall and propagated at a higher convection velocity than smaller packets which were present closer to the wall. The time-scale of large-scale structures corresponding to the plot showcasing the scale dependence of convection velocities, and the spectra of wall pressure on the ramp surface showed good agreement.

To study the flapping motion of the shear-layer, wall-normal velocity was used as the representative variable. Space-time correlations with pressure fluctuations in the recircula-

tion zone showed effect of flapping on the local pressure in that region. For some locations in the shear-layer, the disturbances caused by the flapping motion propagated at acoustic speeds. Two-point correlations between wall pressure and wall-normal velocity demonstrated the effect of former on shear-layer flapping, especially close to the step. Low-pass filtered movies¹ of streamwise velocity clearly emphasized the asymmetric flapping motion as well as the breathing cycle of the separation bubble. Reattachment shock location history was extracted using a combination of wall-normal pressure gradient and the Ducros sensor. The corresponding spectra showed evidence of energy concentration at $St \approx \mathcal{O}(10^{-2})$, which was lower in magnitude as compared to the spectra of separation bubble. Additionally, significant energy was also present at higher frequencies $St \approx \mathcal{O}(10^{-1})$ suggesting a broadband nature of reattachment shock motion.

The effects of upstream events on the reattachment shock motion were studied by examining the coherence magnitude. The coherence plots between wall-normal velocity in the shear-layer and reattachment shock location history showed distinct peaks both at frequencies $St \approx \mathcal{O}(10^{-2})$ as well as $St \approx \mathcal{O}(10^{-1})$. The peaks in the latter range had a higher coherence magnitude, indicating a stronger effect of shear-layer flapping and hairpin structures on the reattachment shock motion. In case of coherence plots between pressure fluctuations in the recirculating zone and reattachment shock motion, peaks in $St \approx \mathcal{O}(10^{-2})$ were higher in magnitude, indicating a higher influence of separation bubble breathing. Based on these observations, low-frequency motion of the reattachment shock is affected by frequencies associated with separation bubble breathing, the latter being prevalent in the recirculation zone. Similarly, frequencies associated with flapping and hairpin structures dominant in the shear-layer modulate the high-frequency motion of the reattachment shock.

No definitive phase relationship was obtained for the events occurring at higher frequencies ($St \geq 0.1$). The events occurring at lower frequencies $St \approx \mathcal{O}(10^{-2})$ were 180 deg out of phase with the reattachment shock motion. Coherence between the mass history of separation bubble and reattachment shock motion implied a strong relationship at frequencies $St \approx 0.02$ and 0.03 . Conditionally averaged density gradient demonstrated the effect of separation bubble breathing on the same, which agrees with the model proposed by Pipon-

¹↑see <https://engineering.purdue.edu/jpoggie/RSL/index.html>

niau et al. [25] Coherence between wall pressure fluctuations on the ramp and the motion of the instantaneous reattachment location/shock system (IRSS) was computed. A strong relationship was observed with separation bubble breathing at $St \approx \mathcal{O}(10^{-2})$ and large-scale structures at $St \geq 0.2$. Low values of coherence for frequencies $0.1 < St < 0.2$ suggested a weak effect of shear-layer flapping. In addition to coherence, correlation plots showed negative correlation between shear-layer flapping and motion of the IRSS. On the ramp, shedding of large-scale structures affected the same in the vicinity of the mean reattachment location.

Repeated occurrence of high coherence values at low-frequencies ($St \approx \mathcal{O}(10^{-2})$) suggests a global mode (perhaps weakly damped and driven by shear-layer turbulence) associated with separation bubble breathing. Also, the apparent presence of Rossiter modes may indicate an acoustic feedback mechanism through the separation bubble.

6.2 Compression Ramp Flow with Sidewalls

Statistical analysis of results obtained from the simulations of Poggie and Porter [65] was carried out. The mean and instantaneous flowfields highlighted curving of the shock front due to sidewall effects. Based on the skin-friction contours, flow at the corner separated at a location upstream relative to the separation at the centerline. Critical point analysis on the floor suggested the presence of tornado vortices originating at foci close to the sidewalls. An interaction similar to that produced by a sharp fin was observed on the sidewalls with a λ -shock foot and separation vortex. The separation extent on the sidewalls increased downstream. A vortex system comprised of a pair of corner vortices, a horseshoe vortex, and swept sidewall vortices was observed from the mean density contours. Peak values of RMS pressure fluctuations were observed downstream of mean reattachment on the floor. Based on the instantaneous contours, this was attributed to the reflection of sidewall λ -shock structures at that location.

Spectra of pressure fluctuations for individual frequency components were plotted on the sampled surfaces. For the lowest frequency component ($St = 0.03$), the spectra highlighted the intermittent length of the shock motion on both the floor and sidewalls. The locations corresponding to the sidewall λ -shock feet were comprised of high values of spectral energy

density, which confirmed low-frequency oscillations of the same. At mid-frequencies ($St = 0.12$), regions in the vicinity of foci on the floor showed an increase in the spectral energy density. At higher frequencies ($St = 0.36$), zones within the centerline separation on the floor and separation vortex on the sidewalls were energy dominant. Similar plots on the centerplane characterized the low-frequency shock motion (at $St = 0.03$) and shedding of horseshoe like vortices (at $St = 0.12$) originating at the focus within the centerline separation. At higher frequencies, spectral energy was concentrated in the separated shear-layer, local compression waves, and in the separation zone close to the reattachment.

The shock location histories at the centerline and left juncture were extracted using a pressure based sensor and the corresponding spectra displayed peaks in the low-frequency range. The influence of sidewalls on the flowfield unsteadiness was investigated using coherence and correlations. Initially, the time-history of the centerline shock location was used to calculate coherence with pressure fluctuations in the domain. The corresponding contours were plotted for the lowest frequency components ($St = 0.03$ and 0.06). For $St = 0.03$, the shock oscillations showed a strong linear relationship with pressure fluctuations within the intermittent length on the floor and sidewall, as well as with the λ -shock structure on the sidewalls. This band of high coherence on the floor was skewed in the upstream direction towards the left sidewall, which suggested alternate back and forth movement of the sidewall interactions at lower frequencies. The authors attribute this to the breathing motion of the concomitant separated regions that are out of phase, but a more rigorous analysis is warranted. The spectrum of separation bubble breathing highlighted a dominant frequency component at $St \approx 0.11$. Based on the coherence and correlation plots, this component partly drives the centerline shock oscillations at this frequency. The breathing motion of the centerline separation bubble at lower frequencies seems to have a localized effect, with no significant relationship with the events on the sidewall. The low-pass filtered velocity fields indicated spanwise motion of the interaction (possibly caused by alternating breathing motion of the separated regions on the sidewalls), in addition to the back and forth streamwise motion.

Space-time correlations of wall-pressure fluctuations on the floor were carried out to determine the influence of centerline separation on those at the corners and sidewalls. The

domain of influence of centerline separation encompassed 75% of the span. The corresponding time-scale(s) calculated from the width of the well correlated region lay in the low-frequency range, signifying the presence of shock motion. The domain of influence for corner separations at either junctures extended up to 35% of the span and lay well within the bounds of the centerline separation. Corner separation at one end affected the other after a time delay, which physically may correspond to the transport of fluid in the spanwise direction. A similar exercise was carried out to investigate the relationship between interactions at the centerline and on the sidewalls. The resulting correlations confirmed the asymmetric motion of the sidewall interactions occurring at $St \approx 0.026$, as indicated by the coherence plots as well as the low-pass filtered velocity fields.

Sparsity-Promoting Dynamic Mode Decomposition was also performed on the data set. The eigenspectrum obtained from SPDMD for all the cases indicated a statistically stationary system. Using this observation, the oscillatory part of modes corresponding to a representative frequency from each band were reconstructed and examined at different phase angles. Also, neutral DMD modes suggested that a continuous input of disturbances from the incoming turbulent flow is required to maintain unsteadiness in this flow. This result is consistent with the hypothesis of a weakly-damped global mode. This procedure highlighted several complex phenomena present in the flowfield, which were not readily evident from statistical analysis carried out by Poggie and Porter [65] and Deshpande and Poggie [163].

On the centerplane, the low-frequency mode ($St = 0.03$) highlighted separation bubble breathing coupled with the oscillations of the compression-ramp shock. The shock moved upstream in the bubble expansion phase and downstream when it contracted. The low-mid frequency mode ($St = 0.12$) showed the flapping of the shear layer which responded to the variation in the instantaneous size of the separated zone. The mid-frequency mode indicated vortex shedding ($St = 0.6$) from the separated zone, which also affected the instantaneous reattachment location. Similar analysis on the ramp-normal plane showed in-phase breathing motion of the sidewall separated zones at low-frequency. In addition to the streamwise motion of the λ -shock feet, their spanwise motion was also affected by the aforementioned breathing motion. Asymmetric expansion and contraction of the sidewall separated zones occurred at the low-mid frequency, while the mid-frequency mode showed the spanwise transport of

the vortical structures present on the wall, into the open separation vortex on the sidewalls through the corner vortex system.

The low-frequency mode on the wall and sidewalls highlighted the oscillations of the compression-ramp shock and the reattachment shock-system downstream on the ramp. These oscillations were slightly out of phase. Additionally, oscillations of the portions of the compression-ramp shock closer to the wall and in the freestream were not synchronous. Alternating streamwise motion of the interaction, possibly caused by the asymmetric expansion and contraction of the sidewall separated zones, occurred at the low-mid frequency. The mid-frequency mode showed vortex shedding from the separated region on the floor. The structures shed away from the centerline follow a pattern observed for the mid-frequency mode corresponding to the ramp-normal case, i.e. they are swept away from the midspan and into the sidewall separation vortex. Those that are shed in the vicinity of the centerline are aligned with the core flow.

6.3 High-Frequency Forcing of Reattaching Shear-Layers

Delayed-Detached Eddy Simulations and Implicit Large-Eddy Simulations of high-frequency forcing applied to reattaching shear-layers were carried out using the SU2 and HOPS code. The former was run for longer time (about 343 cycles of actuation) on account of a larger time-step, which allowed for the analysis of low-mid to mid-frequency content in the flowfield. The HOPS run-time was comparatively smaller (about 30 cycles of actuation.)

Since the ILES approach resolves a wider range of scales in the turbulence energy cascade, its time-step is limited by small-scale structures in the dissipation regime. Therefore, longer runs to accurately resolve the low-frequency phenomena are computationally expensive. Whereas DDES approach models the near-wall content, which allows for a larger time-step to determine the evolution of large-scale structures that are resolved. Longer runs to accurately capture the low-frequency events are thus feasible using this approach.

The wall-normal profiles of mean velocity and resolved stresses within the shear-layer did not exhibit significant variation from their baseline counterparts. A similar trend was observed in the case of growth rates and mean wall-pressure and skin-friction coefficient.

The peak RMS value of skin-friction coefficient decreased slightly with the application of forcing. Spectral analysis of the results obtained from the SU2 run indicated effects of forcing localized to the recirculation zone and not affecting shear-layer evolution significantly. This may explain the invariance of the mean and statistical profiles from the baseline case.

The contours of wall-pressure spectra as well as the pressure spectra in the recirculation zone highlighted the development of a sub-harmonic and a harmonic component. The sub-harmonic component persisted only for a short distance since its inception while the harmonic component closely followed the trend of the fundamental forcing frequency. The spectrum of the reattachment shock location showed three peaks at the fundamental frequency and its higher harmonics, which are most likely caused due a combined influence of pressure fluctuations generated by the actuator propagating through the freestream and recirculation zone. The peak value in the mid-frequency range of the separation bubble breathing spectrum shifted to a slightly lower value of $St \approx 0.1$. The actuator forcing did not modulate the low-frequency breathing motion of the interaction.

6.4 Prospects of Future Study

This document has presented a detailed statistical analysis of the unsteadiness present in the flowfields corresponding to reattaching shear-layers and compression ramp flow with sidewalls. A short study on the effects of high-frequency forcing was also carried out. Based on the results presented, certain aspects that require additional efforts are listed below:

1. The flowfield corresponding to the reattaching shear-layer case presents a promising case for a detailed input-output analysis in order to ascertain the frequency response of the system.
2. The application of flow-control did not alter the mean and RMS quantities in the flowfield, but did affect its unsteadiness. For future calculations, modifying the shear-layer evolution by placing the actuator upstream of the shear-layer origin and close to the location of maximum receptivity is worth exploring.

3. Obtaining a more detailed insight on the frequency response of the flowfield via the application of input-output analysis would aid in a more targeted approach in formulating the forcing term.
4. The ILES calculations corresponding to the sidewalls case were not run long enough to accurately resolve the low-frequency events. Based on the comparisons of results between the ILES and DDES calculations carried out for the reattaching shear-layer case in Chapter 3, reasonable agreement was observed in the spectra within the resolved region. Therefore, performing time-resolved DDES calculations of the sidewalls case is another area that needs to be pursued.
5. The DMD analysis presented in this study was memory intensive due to large grid sizes. As a stopgap measure, the data were sub-sampled in space. The streaming DMD algorithm devised by Hemati et al. [167] is an attractive alternative that accounts for both space and time-resolved data.

REFERENCES

- [1] D. S. Dolling, “Fifty years of shock-wave/boundary-layer interaction research: What next?” *AIAA Journal*, vol. 39, no. 8, pp. 1517–1531, 2001.
- [2] N. T. Clemens and V. Narayanaswamy, “Low-frequency unsteadiness of shock wave/turbulent boundary layer interactions,” *Annual Review of Fluid Mechanics*, vol. 46, pp. 469–492, 2014.
- [3] D. V. Gaitonde, “Progress in shock wave/boundary layer interactions,” *Progress in Aerospace Sciences*, vol. 72, pp. 80–99, 2015.
- [4] M. Wu and M. P. Martin, “Analysis of shock motion in shockwave and turbulent boundary layer interaction using direct numerical simulation data,” *Journal of Fluid Mechanics*, vol. 594, pp. 71–83, 2008.
- [5] F. O. Thomas, C. M. Putnam, and H. C. Chu, “On the mechanism of unsteady shock oscillation in shock wave/turbulent boundary layer interactions,” *Experiments in Fluids*, vol. 18, no. 1–2, pp. 69–81, 1994.
- [6] J. Poggie, “Effect of forcing on a supersonic compression ramp flow,” *AIAA Journal*, vol. 57, no. 9, pp. 1–8, 2019.
- [7] J. Poggie and A. J. Smits, “Shock unsteadiness in a reattaching shear layer,” *Journal of Fluid Mechanics*, vol. 429, pp. 155–185, 2001.
- [8] S. Beresh, N. Clemens, and D. Dolling, “Relationship between upstream turbulent boundary-layer velocity fluctuations and separation shock unsteadiness,” *AIAA Journal*, vol. 40, no. 12, pp. 2412–2422, 2002.
- [9] R. A. Humble, F. Scarano, and B. W. Van Oudheusden, “Unsteady aspects of an incident shock wave/turbulent boundary layer interaction,” *Journal of Fluid Mechanics*, vol. 635, pp. 47–74, 2009.
- [10] M. Grilli, P. J. Schmid, S. Hickel, and N. A. Adams, “Analysis of unsteady behaviour in shockwave turbulent boundary layer interaction,” *Journal of Fluid Mechanics*, vol. 700, pp. 16–28, 2012.
- [11] J. W. Nichols, J. Larsson, M. Bernardini, and S. Pirozzoli, “Stability and modal analysis of shock/boundary layer interactions,” *Theoretical and Computational Fluid Dynamics*, vol. 31, no. 1, pp. 33–50, 2017.

- [12] M. A. Mustafa, N. J. Parziale, M. S. Smith, and E. C. Marineau, “Amplification and structure of streamwise-velocity fluctuations in compression-corner shock-wave/turbulent boundary-layer interactions,” *Journal of Fluid Mechanics*, vol. 863, pp. 1091–1122, 2019.
- [13] E. Touber and N. D. Sandham, “Large-eddy simulation of low-frequency unsteadiness in a turbulent shock-induced separation bubble,” *Theoretical and Computational Fluid Dynamics*, vol. 23, no. 2, pp. 79–107, 2009.
- [14] M. C. Adler and D. V. Gaitonde, “Dynamic linear response of a shock/turbulent-boundary-layer interaction using constrained perturbations,” *Journal of Fluid Mechanics*, vol. 840, pp. 291–341, 2018.
- [15] B. Zuchowski, “Air vehicle integration and technology research (AVIATR),” Lockheed Martin Aeronautics Company, Palmdale, CA, Final Report AFRL-RQ-WP-TR-2012-0280, May 2012.
- [16] P. Huerre and P. A. Monkewitz, “Local and global instabilities in spatially developing flows,” *Annual Review of Fluid Mechanics*, vol. 22, no. 1, pp. 473–537, 1990.
- [17] K. Porter and J. Poggie, “Selective upstream influence on the unsteadiness of a separated turbulent compression ramp flow,” *Physics of Fluids*, vol. 31, no. 1, 016104, 2019.
- [18] J. Poggie, N. J. Bisek, R. L. Kimmel, and S. A. Stanfield, “Spectral characteristics of separation shock unsteadiness,” *AIAA Journal*, vol. 53, no. 1, pp. 200–214, 2015.
- [19] K. J. Plotkin, “Shock wave oscillation driven by turbulent boundary-layer fluctuations,” *AIAA Journal*, vol. 13, no. 8, pp. 1036–1040, 1975.
- [20] B. Ganapathisubramani, N. T. Clemens, and D. S. Dolling, “Large-scale motions in a supersonic turbulent boundary layer,” *Journal of Fluid Mechanics*, vol. 556, pp. 271–282, 2006.
- [21] B. Ganapathisubramani, N. Clemens, and D. Dolling, “Effects of upstream boundary layer on the unsteadiness of shock-induced separation,” *Journal of Fluid Mechanics*, vol. 585, pp. 369–394, 2007.
- [22] K. M. Porter and J. Poggie, “Selective upstream influence on the unsteadiness of a separated turbulent compression ramp flow,” *Physics of Fluids*, vol. 31, no. 1, 016104, 2019.

- [23] P. Dupont, C. Haddad, and J. F. Debiève, “Space and time organization in a shock-induced separated boundary layer,” *Journal of Fluid Mechanics*, vol. 559, pp. 255–277, 2006.
- [24] P. Dupont, S. Piponniau, A. Sidorenko, and J. F. Debiève, “Investigation by particle image velocimetry measurements of oblique shock reflection with separation,” *AIAA Journal*, vol. 46, no. 6, pp. 1365–1370, 2008.
- [25] S. Piponniau, J. P. Dussauge, J. F. Debiève, and P. Dupont, “A simple model for low-frequency unsteadiness in shock-induced separation,” *Journal of Fluid Mechanics*, vol. 629, pp. 87–108, 2009.
- [26] S. Pirozzoli and F. Grasso, “Direct numerical simulation of impinging shock wave/turbulent boundary layer interaction at $M = 2.25$,” *Physics of Fluids*, vol. 18, no. 6, 065113, 2006.
- [27] J. Poggie and A. J. Smits, “Large-scale structures in a compressible mixing layer over a cavity,” *AIAA Journal*, vol. 41, no. 12, pp. 2410–2419, 2003.
- [28] T. Leger, N. Bisek, and J. Poggie, “Detached-eddy simulation of a supersonic reattaching shear layer,” *AIAA Journal*, vol. 55, pp. 3722–3733, 2017.
- [29] P. Dupont, S. Piponniau, and J. P. Dussauge, “Compressible mixing layer in shock-induced separation,” *Journal of Fluid Mechanics*, vol. 863, pp. 620–643, 2019.
- [30] G. S. Settles, D. R. Williams, B. K. Baca, and S. M. Bogdonoff, “Reattachment of a compressible turbulent free shear layer,” *AIAA Journal*, vol. 20, no. 1, pp. 60–67, 1982.
- [31] K. Hayakawa, A. J. Smits, and S. M. Bogdonoff, “Turbulence measurements in a compressible reattaching shear layer,” *Physics of Fluids*, vol. 4, no. 6, pp. 1251–1258, 1992.
- [32] J. K. Eaton and J. P. Johnston, “A review of research on subsonic turbulent flow reattachment,” *AIAA Journal*, vol. 19, no. 9, pp. 1093–1100, 1981.
- [33] J. K. Eaton and J. P. Johnston, “Low frequency unsteadiness of a reattaching turbulent shear layer,” in *Turbulent Shear Flows 3*, L. Bradbury, F. Durst, B. E. Launder, F. W. Schmidt, and J. H. Whitelaw, Eds., 1st ed., New York: Springer, 1982, ch. 3, pp. 162–170.
- [34] P. G. Spazzini, G. Iuso, M. Onorato, N. Zurlo, and G. M. Di Cicca, “Unsteady behavior of back-facing step flow,” *Experiments in Fluids*, vol. 30, no. 5, pp. 551–561, 2001.

- [35] F. Scarano, C. Benocci, and M. L. Riethmuller, “Pattern recognition analysis of the turbulent flow past a backward facing step,” *Physics of Fluids*, vol. 11, no. 12, pp. 3808–3818, 1999.
- [36] X. Ma and A. Schröder, “Analysis of flapping motion of reattaching shear layer behind a two-dimensional backward-facing step,” *Physics of Fluids*, vol. 29, no. 11, 115104, 2017.
- [37] M. Kiya and K. Sasaki, “Structure of a turbulent separation bubble,” *Journal of Fluid Mechanics*, vol. 137, pp. 83–113, 1983.
- [38] M. Kiya and K. Sasaki, “Structure of large-scale vortices and unsteady reverse flow in the reattaching zone of a turbulent separation bubble,” *Journal of Fluid Mechanics*, vol. 154, pp. 463–491, 1985.
- [39] J. F. Largeau and V. Moriniere, “Wall pressure fluctuations and topology in separated flows over a forward-facing step,” *Experiments in Fluids*, vol. 42, no. 1, p. 21, 2007.
- [40] R. Camussi, M. Felli, F. Pereira, G. Aloisio, and A. Di Marco, “Statistical properties of wall pressure fluctuations over a forward-facing step,” *Physics of Fluids*, vol. 20, no. 7, 075113, 2008.
- [41] D. S. Pearson, P. J. Goulart, and B. Ganapathisubramani, “Turbulent separation upstream of a forward-facing step,” *Journal of Fluid Mechanics*, vol. 724, pp. 284–304, 2013.
- [42] G. L. Brown and A. Roshko, “On density effects and large structure in turbulent mixing layers,” *Journal of Fluid Mechanics*, vol. 64, no. 4, pp. 775–816, 1974.
- [43] L. P. Bernal and A. Roshko, “Streamwise vortex structure in plane mixing layers,” *Journal of Fluid Mechanics*, vol. 170, pp. 499–525, 1986.
- [44] P. E. Dimotakis and G. L. Brown, “The mixing layer at high reynolds number: Large-structure dynamics and entrainment,” *Journal of Fluid Mechanics*, vol. 78, pp. 535–560, 1976.
- [45] M. Samimy, M. F. Reeder, and G. S. Elliott, “Compressibility effects on large structures in free shear flows,” *Physics of Fluids*, vol. 4, no. 6, pp. 1251–1258, 1992.
- [46] C. Helm, M. P. Martin, and P. Dupont, “Characterization of the shear layer in a Mach 3 shock/turbulent boundary layer interaction,” in *Journal of Physics: Conference Series*, IOP Publishing, vol. 506, 2014.

- [47] W. Hu, S. Hickel, and B. van Oudheusden, “Dynamics of a supersonic transitional flow over a backward-facing step,” *Physical Review Fluids*, vol. 4, no. 10, 103904, 2019.
- [48] W. Hu, S. Hickel, and B. van Oudheusden, “Low-frequency unsteadiness mechanisms in shock wave/turbulent boundary layer interactions over a backward-facing step,” *Journal of Fluid Mechanics*, vol. 915, 2021.
- [49] D. C. Reda and J. D. Murphy, “Shock wave/turbulent boundary-layer interactions in rectangular channels,” *AIAA Journal*, vol. 11, no. 2, pp. 139–140, 1973.
- [50] D. C. Reda and J. D. Murphy, “Sidewall boundary-layer influence on shock wave/turbulent boundary-layer interactions,” *AIAA Journal*, vol. 11, no. 10, pp. 1367–1368, 1973.
- [51] D. M. F. Burton and H. Babinsky, “Corner separation effects for normal shock wave/turbulent boundary layer interactions in rectangular channels,” *Journal of Fluid Mechanics*, vol. 707, pp. 287–306, 2012.
- [52] P. J. K. Bruce, D. M. F. Burton, N. A. Titchener, and H. Babinsky, “Corner effect and separation in transonic channel flows,” *Journal of Fluid Mechanics*, vol. 679, pp. 247–262, 2011.
- [53] X. Xiang and H. Babinsky, “Corner effects for oblique shock wave/turbulent boundary layer interactions in rectangular channels,” *Journal of Fluid Mechanics*, vol. 862, pp. 1060–1083, 2019.
- [54] W. E. Eagle and J. F. Driscoll, “Shock wave–boundary layer interactions in rectangular inlets: Three-dimensional separation topology and critical points,” *Journal of Fluid Mechanics*, vol. 756, pp. 328–353, 2014.
- [55] M. Tobak and D. J. Peake, “Topology of three-dimensional separated flows,” *Annual Review of Fluid Mechanics*, vol. 14, no. 1, pp. 61–85, 1982.
- [56] M. Funderburk and V. Narayanaswamy, “Experimental investigation of primary and corner shock boundary layer interactions at mild back pressure ratios,” *Physics of Fluids*, vol. 28, no. 8, 086102, 2016.
- [57] R. R. Morajkar, R. L. Klomparens, W. E. Eagle, J. F. Driscoll, M. Gamba, and J. A. Benek, “Relationship between intermittent separation and vortex structure in a three-dimensional shock/boundary-layer interaction,” *AIAA Journal*, vol. 54, no. 6, pp. 1862–1880, 2016.

- [58] B. Wang, N. D. Sandham, Z. Hu, and W. Liu, “Numerical study of oblique shock-wave/boundary-layer interaction considering sidewall effects,” *Journal of Fluid Mechanics*, vol. 767, pp. 526–561, 2015.
- [59] I. Bermejo-Moreno, L. Campo, J. Larsson, J. Bodart, D. Helmer, and J. K. Eaton, “Confinement effects in shock wave/turbulent boundary layer interactions through wall-modelled large-eddy simulations,” *Journal of Fluid Mechanics*, vol. 758, pp. 5–62, 2014.
- [60] D. Lushner and N. Sandham, “The effect of flow confinement on laminar shock-wave/boundary-layer interactions,” *Journal of Fluid Mechanics*, vol. 897, A18, 2020.
- [61] A. E. Perry and H. Hornung, “Some aspects of three-dimensional separation. II – Vortex skeletons,” *Zeitschrift für Flugwissenschaften und Weltraumforschung*, vol. 8, pp. 155–160, Jun. 1984.
- [62] P. K. Rabey, S. P. Jammy, P. J. K. Bruce, and N. D. Sandham, “Two-dimensional unsteadiness map of oblique shock wave/boundary layer interaction with sidewalls,” *Journal of Fluid Mechanics*, vol. 871, 2019.
- [63] E. Garnier, “Stimulated detached eddy simulation of three-dimensional shock/boundary layer interaction,” *Shock waves*, vol. 19, no. 6, p. 479, 2009.
- [64] N. Bisek, “Sidewall interaction of a supersonic flow over a compression ramp,” American Institute of Aeronautics and Astronautics, Kissimmee, FL, AIAA Paper 2015–1976, Jan. 2015.
- [65] J. Poggie and K. M. Porter, “Flow structure and unsteadiness in a highly confined shock-wave–boundary-layer interaction,” *Physical Review of Fluids*, vol. 4, no. 2, 024602, 2019.
- [66] H. C-M. and P. Huerre, “Perturbed free shear layers,” *Annual Review of Fluid Mechanics*, vol. 16, pp. 365–424, 1984.
- [67] M. Samimy, N. Webb, and M. Crawley, “Excitation of free shear-layer instabilities for high-speed flow control,” *AIAA Journal*, vol. 56, no. 5, pp. 1770–1791, 2018.
- [68] M. Samimy, J.-H. Kim, J. Kastner, I. Adamovich, and Y. Utkin, “Active control of a mach 0.9 jet for noise mitigation using plasma actuators,” *AIAA Journal*, vol. 45, no. 4, pp. 890–901, 2007.
- [69] J. Dandois, E. Garnier, and P. Sagaut, “Numerical simulation of active separation control by a synthetic jet,” *Journal of Fluid Mechanics*, vol. 574, p. 25, 2007.

- [70] J. M. Wiltse and A. Glezer, “Direct excitation of small-scale motions in free shear flows,” *Physics of Fluids*, vol. 10, no. 8, pp. 2026–2036, 1998.
- [71] B. Vukasinovic, Z. Rusak, and A. Glezer, “Dissipative small-scale actuation of a turbulent shear layer,” *Journal of Fluid Mechanics*, vol. 656, p. 51, 2010.
- [72] M. Stanek, G. Raman, V. Kibens, J. Ross, J. Odedra, and J. Peto, “Control of cavity resonance through very high frequency forcing,” American Institute of Aeronautics and Astronautics, Lahaina, HI, AIAA Paper 2000–1905, Jun. 2000.
- [73] M. Stanek, G. Raman, V. Kibens, J. Ross, J. Odedra, and J. Peto, “Suppression of cavity resonance using high frequency forcing – the characteristic signature of effective devices,” American Institute of Aeronautics and Astronautics, Maastricht, The Netherlands, AIAA Paper 2001–2128, May 2000.
- [74] C. W. Rowley and D. R. Williams, “Dynamics and control of high-reynolds-number flow over open cavities,” *Annual Review of Fluid Mechanics*, vol. 38, pp. 251–276, 2006.
- [75] L. F. Richardson, *Weather prediction by numerical process*. Cambridge University Press, 1922.
- [76] A. N. Kolmogorov, “The local structure of turbulence in incompressible viscous fluid for very large reynolds numbers,” *Cr Acad. Sci. URSS*, vol. 30, pp. 301–305, 1941.
- [77] J. Jiménez, “Cascades in Wall-Bounded Turbulence,” *Annual Review of Fluid Mechanics*, vol. 44, no. 1, pp. 27–45, Jan. 2012.
- [78] A. J. Smits, B. J. McKeon, and I. Marusic, “High–Reynolds Number Wall Turbulence,” *Annual Review of Fluid Mechanics*, vol. 43, no. 1, pp. 353–375, Jan. 2011.
- [79] A. J. Smits, “Some observations on Reynolds number scaling in wall-bounded flows,” *Physical Review Fluids*, vol. 5, no. 11, 110514, Nov. 2020.
- [80] I. Marusic, B. J. McKeon, P. A. Monkewitz, H. M. Nagib, A. J. Smits, and K. R. Sreenivasan, “Wall-bounded turbulent flows at high Reynolds numbers: Recent advances and key issues,” *Physics of Fluids*, vol. 22, no. 6, 065103, Jun. 2010.
- [81] D. R. Chapman, “Computational aerodynamics development and outlook,” *AIAA Journal*, vol. 17, no. 12, pp. 1293–1313, 1979.
- [82] H. Choi and P. Moin, “Grid-point requirements for large eddy simulation: Chapman’s estimates revisited,” *Physics of Fluids*, vol. 24, no. 1, 011702, 2012.

- [83] J. Poggie, N. Bisek, and R. Gosse, “Resolution effects in compressible, turbulent boundary layer simulations,” *Computers & Fluids*, vol. 120, pp. 57–69, 2015.
- [84] K. Ravikumar, D. Appelhans, and P. K. Yeung, “GPU acceleration of extreme scale pseudo-spectral simulations of turbulence using asynchronism,” in *Proceedings of the International Conference for High Performance Computing, Networking, Storage and Analysis*, 2019, pp. 1–22.
- [85] P. K. Yeung and K. Ravikumar, “Advancing understanding of turbulence through extreme-scale computation: Intermittency and simulations at large problem sizes,” *Physical Review Fluids*, vol. 5, no. 11, 110517, 2020.
- [86] C. G. Speziale, S. Sarkar, and T. B. Gatski, “Modelling the pressure-strain correlation of turbulence: An invariant dynamical systems approach,” *Journal of Fluid Mechanics*, vol. 227, pp. 245–272, 1991.
- [87] B. E. Launder, G. J. Reece, and W. Rodi, “Progress in the development of a reynolds-stress turbulence closure,” *Journal of Fluid Mechanics*, vol. 68, no. 3, pp. 537–566, 1975.
- [88] D. C. Wilcox, *Turbulence modeling for CFD*, 3rd ed. DCW industries La Canada, CA, 2006, vol. 2.
- [89] P. R. Spalart, “Comments on the feasibility of les for wings, and on a hybrid rans/les approach,” in *Proceedings of first AFOSR international conference on DNS/LES*, Greyden Press, 1997.
- [90] J. Larsson, S. Kawai, J. Bodart, and I. Bermejo-Moreno, “Large eddy simulation with modeled wall-stress: Recent progress and future directions,” *Mechanical Engineering Reviews*, vol. 3, no. 1, 15–00418, 2016.
- [91] P. R. Spalart, S. Deck, M. L. Shur, K. D. Squires, M. K. Strelets, and A. Travin, “A new version of detached-eddy simulation, resistant to ambiguous grid densities,” *Theoretical and Computational Fluid Dynamics*, vol. 20, no. 3, pp. 181–195, 2006.
- [92] P. R. Spalart, “Detached-eddy simulation,” *Annual Review of Fluid Mechanics*, vol. 41, pp. 181–202, 2009.
- [93] U. Piomelli and E. Balaras, “Wall-layer models for large-eddy simulations,” *Annual Review of Fluid Mechanics*, vol. 34, no. 1, pp. 349–374, 2002.
- [94] N. V. Nikitin, F. Nicoud, B. Wasistho, K. D. Squires, and P. R. Spalart, “An approach to wall modeling in large-eddy simulations,” *Physics of fluids*, vol. 12, no. 7, pp. 1629–1632, 2000.

- [95] S. Ghosal, “An analysis of numerical errors in large-eddy simulations of turbulence,” *Journal of Computational Physics*, vol. 125, no. 1, pp. 187–206, 1996.
- [96] M. R. Visbal and D. V. Gaitonde, “Shock capturing using compact-differencing-based methods,” American Institute of Aeronautics and Astronautics, Reston, VA, AIAA Paper 2005-1265, Jan. 2005.
- [97] J. P. Boris, F. F. Grinstein, E. S. Oran, and R. L. Kolbe, “New insights into large eddy simulation,” *Fluid Dynamics Research*, vol. 10, pp. 199–228, 1992.
- [98] F. F. Grinstein, L. G. Margolin, and W. J. Rider, *Implicit Large Eddy Simulation: Computing Turbulent Fluid Dynamics*. Cambridge University Press, Jan. 2007, vol. 10.
- [99] L. G. Margolin, W. J. Rider, and F. F. Grinstein, “Modeling turbulent flow with implicit les,” *Journal of Turbulence*, no. 7, N15, 2006.
- [100] D. Drikakis, M. Hahn, F. F. Grinstein, C. R. DeVore, C. Fureby, M. Liefvendahl, and D. L. Youngs, “Numerics for ILES,” in *Implicit Large Eddy Simulation: Computing Turbulent Fluid Dynamics*, F. F. Grinstein, L. G. Margolin, and W. J. Rider, Eds. Cambridge University Press, 2007, pp. 94–194.
- [101] C. Fureby, D. D. Knight, and M. Kupiainen, “Compressible turbulent shear flows,” in *Implicit Large Eddy Simulation: Computing Turbulent Fluid Dynamics*, F. F. Grinstein, L. G. Margolin, and W. J. Rider, Eds. Cambridge University Press, 2007, pp. 329–369.
- [102] M. R. Visbal, P. Morgan, and D. Rizzetta, “An implicit les approach based on high-order compact differencing and filtering schemes,” American Institute of Aeronautics and Astronautics, Orlando, FL, AIAA Paper 2003-4098, Jun. 2005.
- [103] S. K. Lele, “Compact finite difference schemes with spectral-like resolution,” *Journal of Computational Physics*, vol. 103, no. 1, pp. 16–42, 1992.
- [104] S. A. Orszag and M. Israeli, “Numerical simulation of viscous incompressible flows,” *Annual Review of Fluid Mechanics*, vol. 6, no. 1, pp. 281–318, 1974.
- [105] R. S. Hirsh, “Higher order accurate difference solutions of fluid mechanics problems by a compact differencing technique,” *Journal of Computational Physics*, vol. 19, no. 1, pp. 90–109, 1975.
- [106] D. J. Garmann, “Characterization of the vortex formation and evolution about a revolving wing using high-fidelity simulation,” PhD thesis, Dept. of Aerospace Engineering and Engineering Mechanics, University of Cincinnati, Cincinnati, OH, Apr. 2013.

- [107] P. R. Spalart and S. R. Allmaras, “A one-equation turbulence model for aerodynamic flows,” American Institute of Aeronautics and Astronautics, Reno, NV, AIAA Paper 1992–0439, Jan. 1992.
- [108] E. Molina, C. Spode, R. G. Annes da Silva, D. E. Manosalvas-Kjono, S. Nimmagadda, T. D. Economon, J. J. Alonso, and M. Righi, “Hybrid rans/les calculations in su2,” Denver, CO, AIAA Paper 2017–4284, Jun. 2017.
- [109] J. Smagorinsky, “General circulation experiments with the primitive equations: I. the basic experiment,” *Monthly Weather Review*, vol. 91, no. 3, pp. 99–164, 1963.
- [110] S. T. Bose, P. Moin, and D. You, “Grid-independent large-eddy simulation using explicit filtering,” *Physics of Fluids*, vol. 22, no. 10, 105103, 2010.
- [111] M. C. Adler, “On the advancement of phenomenological and mechanistic descriptions of unsteadiness in shock-wave/turbulent-boundary-layer interactions,” PhD thesis, Aeronautical and Astronautical Engineering, The Ohio State University, Columbus, OH, 2019.
- [112] M. R. Visbal and D. V. Gaitonde, “High-order-accurate methods for complex unsteady subsonic flows,” *AIAA Journal*, vol. 37, no. 10, pp. 1231–1239, 1999.
- [113] D. V. Gaitonde and M. R. Visbal, “Padé-type higher-order boundary filters for the navier-stokes equations,” *AIAA Journal*, vol. 38, no. 11, pp. 2103–2112, 2000.
- [114] T. D. Economon, F. Palacios, S. R. Copeland, T. W. Lukaczyk, and J. J. Alonso, “SU2: An open-source suite for multiphysics simulation and design,” *AIAA Journal*, vol. 54, no. 3, pp. 828–846, 2016.
- [115] N. J. Georgiadis, D. P. Rizzetta, and C. Fureby, “Large-eddy simulation: Current capabilities, recommended practices, and future research,” *AIAA Journal*, vol. 48, no. 8, pp. 1772–1784, 2010.
- [116] R. Nichols, R. Tramel, and P. Buning, “Solver and turbulence model upgrades to overflow 2 for unsteady and high-speed applications,” American Institute of Aeronautics and Astronautics, San Francisco, CA, AIAA Paper 2006-2824, Jun. 2006.
- [117] R. Tramel, R. Nichols, and P. Buning, “Addition of improved shock-capturing schemes to overflow 2.1,” American Institute of Aeronautics and Astronautics, San Antonio, TX, AIAA Paper 2009-3988, Jun. 2009.
- [118] W. K. Anderson, J. L. Thomas, and B. Van Leer, “Comparison of finite volume flux vector splittings for the euler equations,” *AIAA Journal*, vol. 24, no. 9, pp. 1453–1460, 1986.

- [119] A. Jameson, W. Schmidt, and E. Turkel, “Numerical solution of the euler equations by finite volume methods using runge-kutta time stepping schemes,” American Institute of Aeronautics and Astronautics, Palo Alto, CA, AIAA Paper 1981–1259, Jun. 1981.
- [120] M. L. Shur, P. R. Spalart, M. K. Strelets, and A. K. Travin, “An enhanced version of des with rapid transition from rans to les in separated flows,” *Flow, Turbulence and Combustion*, vol. 95, no. 4, pp. 709–737, 2015.
- [121] A. Jameson, “Time dependent calculations using multigrid, with applications to unsteady flows past airfoils and wings,” American Institute of Aeronautics and Astronautics, Honolulu, HI, AIAA Paper 1991–1596, Jun. 1991.
- [122] A. Jameson and S. Shankaran, “An assessment of dual-time stepping, time spectral and artificial compressibility based numerical algorithms for unsteady flow with applications to flapping wings,” American Institute of Aeronautics and Astronautics, San Antonio, TX, AIAA Paper 2009–4273, Jun. 2009.
- [123] M. R. Visbal and D. P. Rizzetta, “Large-eddy simulation on curvilinear grids using compact differencing and filtering schemes,” *Journal of Fluids Engineering*, vol. 124, no. 4, pp. 836–847, 2002.
- [124] J. S. Bendat and A. G. Piersol, *Random data: analysis and measurement procedures*, 4th ed. John Wiley & Sons, 2010.
- [125] P. J. Schmid, “Dynamic mode decomposition of numerical and experimental data,” *Journal of Fluid Mechanics*, vol. 656, pp. 5–28, 2010.
- [126] P. J. Schmid, L. Li, M. P. Juniper, and O. Pust, “Applications of the dynamic mode decomposition,” *Theoretical and Computational Fluid Dynamics*, vol. 25, no. 1–4, pp. 249–259, 2011.
- [127] S. Pirozzoli, J. Larsson, J. Nichols, M. Bernardini, B. Morgan, and S. Lele, “Analysis of unsteady effects in shock/boundary layer interactions,” in *Proceedings of the Summer Program, Center for Turbulence Research*, (Stanford University, CA), 2010, pp. 153–164.
- [128] V. Pasquariello, S. Hickel, and N. A. Adams, “Unsteady effects of strong shock-wave/boundary-layer interaction at high reynolds number,” *Journal of Fluid Mechanics*, vol. 823, pp. 617–657, 2017.
- [129] V. Statnikov, T. Sayadi, M. Meinke, P. Schmid, and W. Schröder, “Analysis of pressure perturbation sources on a generic space launcher after-body in supersonic flow using zonal turbulence modeling and dynamic mode decomposition,” *Physics of Fluids*, vol. 27, no. 1, 016103, 2015.

- [130] M. R. Jovanović, P. J. Schmid, and J. W. Nichols, “Sparsity-promoting dynamic mode decomposition,” *Physics of Fluids*, vol. 26, no. 2, 024103, 2014.
- [131] A. S. Deshpande and J. Poggie, “Unsteady characteristics of compressible reattaching shear layers,” *Physics of Fluids*, vol. 32, no. 6, 066103, 2020.
- [132] M. Samimy and G. S. Elliott, “Effects of compressibility on the characteristics of free shear layers,” *AIAA Journal*, vol. 28, no. 3, pp. 439–445, 1990.
- [133] J. H. Bell and R. D. Mehta, “Development of a two-stream mixing layer from tripped and untripped boundary layers,” *AIAA Journal*, vol. 28, no. 12, pp. 2034–2042, 1990.
- [134] P. J. Strykowski, A. Krothapalli, and S. Jendoubi, “The effect of counterflow on the development of compressible shear layers,” *Journal of Fluid Mechanics*, vol. 308, pp. 63–96, 1996.
- [135] J. C. Lasheras and H. Choi, “Three-dimensional instability of a plane free shear layer: An experimental study of the formation and evolution of streamwise vortices,” *Journal of Fluid Mechanics*, vol. 189, pp. 53–86, 1988.
- [136] R. Hillier and N. Cherry, “Pressure fluctuations under a turbulent shear layer,” in *Proc. 3rd Symp. on Turbulent Shear Flows*, 1981, pp. 16–23.
- [137] J. E. Rossiter, “Wind tunnel experiments on the flow over rectangular cavities at subsonic and transonic speeds,” Aeronautical Research Council, London, Repts. and Memoranda 3438, Oct. 1964.
- [138] H. H. Heller and D. B. Bliss, “Flow-induced pressure fluctuations in cavities and concepts for their suppression,” *Aeroacoustics: STOL Noise; Airframe and Airfoil Noise*, vol. 45, pp. 281–296, 1976.
- [139] D. Rockwell and E. Naudascher, “Self-sustaining oscillations of flow past cavities,” *Journal of Fluids Engineering*, vol. 100, no. 2, pp. 152–165, 1978.
- [140] Z. H. Shen, D. R. Smith, and A. J. Smits, “Wall pressure fluctuations in the reattachment region of a supersonic free shear layer,” *Experiments in Fluids*, vol. 14, no. 1–2, pp. 10–16, 1993.
- [141] S. Priebe and M. P. Martín, “Low-frequency unsteadiness in shock wave–turbulent boundary layer interaction,” *Journal of Fluid Mechanics*, vol. 699, pp. 1–49, 2012.
- [142] L. Agostini, L. Larchevêque, P. Dupont, J. F. Debiève, and J. P. Dussauge, “Zones of influence and shock motion in a shock/boundary-layer interaction,” *AIAA journal*, vol. 50, no. 6, pp. 1377–1387, 2012.

- [143] D. Weston and S. E. Sherer, “Investigation of shock-boundary layer interaction around wall-mounted hemisphere using DDES and ILES,” Kissimmee, FL, AIAA Paper 2018–1300, Jan. 2018.
- [144] D. Weston and S. E. Sherer, “Comparison of computational and experimental results in the wake region behind a wall-mounted hemisphere in supersonic flow,” Dallas, TX, AIAA Paper 2019–3630, Jun. 2019.
- [145] J. Poggie and A. J. Smits, “Large-scale structures in a compressible mixing layer over a cavity,” *AIAA Journal*, vol. 41, no. 12, pp. 2410–2419, 2003.
- [146] J. Poggie, “On the control of a compressible, reattaching shear layer,” PhD thesis, Dept. of Mechanical and Aerospace Engineering, Princeton Univ., Princeton, NJ, Jan. 1995.
- [147] R. J. Adrian, C. D. Meinhart, and C. D. Tomkins, “Vortex organization in the outer region of the turbulent boundary layer,” *Journal of Fluid Mechanics*, vol. 422, pp. 1–54, 2000.
- [148] S. Pirozzoli, M. Bernardini, S. Marié, and F. Grasso, “Early evolution of the compressible mixing layer issued from two turbulent streams,” *Journal of Fluid Mechanics*, vol. 777, pp. 196–218, 2015.
- [149] M. Bernardini and S. Pirozzoli, “Wall pressure fluctuations beneath supersonic turbulent boundary layers,” *Physics of Fluids*, vol. 23, no. 8, 085102, 2011.
- [150] L. Duan, M. Choudhari, and C. Zhang, “Pressure fluctuations induced by a hypersonic turbulent boundary layer,” *Journal of Fluid Mechanics*, vol. 804, pp. 578–607, 2016.
- [151] L. Agostini, L. Larchevêque, and P. Dupont, “Mechanism of shock unsteadiness in separated shock/boundary-layer interactions,” *Physics of Fluids*, vol. 27, no. 12, 126103, 2015.
- [152] S. Pirozzoli and M. Bernardini, “Direct numerical simulation database for impinging shock wave/turbulent boundary-layer interaction,” *AIAA journal*, vol. 49, no. 6, pp. 1307–1312, 2011.
- [153] A. S. Deshpande and J. Poggie, “Large-scale unsteadiness in a compression ramp flow confined by sidewalls,” *Physical Review Fluids*, vol. 6, no. 2, p. 024610, 2021.
- [154] A. S. Deshpande and J. Poggie, “Dynamic mode decomposition of a highly confined shock-wave/boundary-layer interaction,” American Institute of Aeronautics and Astronautics, Virtual Event, AIAA Paper 2021–1097, Jan. 2021.

- [155] H. Babinsky, J. Oorebeek, and T. Cottingham, “Corner effects in reflecting oblique shock-wave/boundary-layer interactions,” American Institute of Aeronautics and Astronautics, Grapevine, TX, AIAA Paper 2013–0859, Jan. 2013.
- [156] X. Xiang and H. Babinsky, “Corner effects for oblique shock wave/turbulent boundary layer interactions in rectangular channels,” *Journal of Fluid Mechanics*, vol. 862, pp. 1060–1083, 2019.
- [157] J. M. Délery, “Robert Legendre and Henri Werlé: Toward the elucidation of three-dimensional separation,” *Annual Review of Fluid Mechanics*, vol. 33, no. 1, pp. 129–154, 2001.
- [158] A. S. Deshpande and J. Poggie, “Flow control of swept shock-wave/boundary-layer interaction using plasma actuators,” *Journal of Spacecraft and Rockets*, vol. 55, no. 5, pp. 1198–1207, 2018.
- [159] A. E. Perry and M. S. Chong, “A description of eddying motions and flow patterns using critical-point concepts,” *Annual Review of Fluid Mechanics*, vol. 19, no. 1, pp. 125–155, 1987.
- [160] B. Edney, “Anomalous heat transfer and pressure distributions on blunt bodies at hypersonic speeds in the presence of an impinging shock,” Flygtekniska Forsöksanstalten, Stockholm (Sweden), Tech. Rep., 1968.
- [161] B. Ganapathisubramani, N. Hutchins, W. T. Hambleton, E. K. Longmire, and I. Marusic, “Investigation of large-scale coherence in a turbulent boundary layer using two-point correlations,” *Journal of Fluid Mechanics*, vol. 524, pp. 57–80, 2005.
- [162] S. Pirozzoli and F. Grasso, “Direct numerical simulation of impinging shock wave/turbulent boundary layer interaction at $M = 2.25$,” *Physics of Fluids*, vol. 18, no. 6, 065113, 2006.
- [163] A. S. Deshpande and J. Poggie, “Unsteadiness of shock-wave/boundary-layer interaction with sidewalls,” American Institute of Aeronautics and Astronautics, Orlando, FL, AIAA Paper 2020–0581, Jan. 2020.
- [164] A. S. Deshpande and J. Poggie, “Statistical analysis of unsteadiness in a compressible reattaching flow,” American Institute of Aeronautics and Astronautics, Dallas, TX, AIAA Paper 2019–3439, Jun. 2019.
- [165] D. Greenblatt and I. J. Wygnanski, “The control of flow separation by periodic excitation,” *Progress in Aerospace Sciences*, vol. 36, no. 7, pp. 487–545, 2000.

- [166] A. Seifert and L. G. Pack, “Oscillatory control of separation at high reynolds numbers,” *AIAA Journal*, vol. 37, no. 9, pp. 1062–1071, 1999.
- [167] M. S. Hemati, M. O. Williams, and C. W. Rowley, “Dynamic mode decomposition for large and streaming datasets,” *Physics of Fluids*, vol. 26, no. 11, 111701, 2014.